

Mesosopic Modeling and Experimental Investigations of the Last-Stage Solidification of Globular-Equiaxed Grains in Metallic Alloys: Application to the Al-Cu System

THÈSE N° 6681 (2015)

PRÉSENTÉE LE 13 NOVEMBRE 2015

À LA FACULTÉ DES SCIENCES ET TECHNIQUES DE L'INGÉNIEUR
LABORATOIRE DE SIMULATION DES MATÉRIAUX
PROGRAMME DOCTORAL EN SCIENCE ET GÉNIE DES MATÉRIAUX

ÉCOLE POLYTECHNIQUE FÉDÉRALE DE LAUSANNE

POUR L'OBTENTION DU GRADE DE DOCTEUR ÈS SCIENCES

PAR

Christophe MONDOUX

acceptée sur proposition du jury:

Prof. P. Muralt, président du jury
Prof. M. Rappaz, directeur de thèse
Prof. H. Combeau, rapporteur
Dr Ph. Jarry, rapporteur
Dr L. Weber, rapporteur



ÉCOLE POLYTECHNIQUE
FÉDÉRALE DE LAUSANNE

Suisse
2015

Remerciements

Je voudrais, tout d'abord, remercier infiniment Michel Rappaz, mon directeur de thèse, qui m'a accueilli au Laboratoire de Simulation des Matériaux (LSMX). Pendant ces 4 ans de thèse (et déjà pendant mon travail de Master), Michel m'a guidé et a toujours été disponible pour m'aider et me conseiller, tout en me laissant une très grande indépendance dans mon travail de thèse qui m'a tant passionné. J'ai été impressionné par son intelligence et ses connaissances et ai particulièrement apprécié sa capacité à trouver, dans chaque situation, la solution idéale. J'ai en outre pu apprécier ses grandes qualités humaines: la très bonne ambiance qui règne dans le laboratoire en est la preuve la plus visible.

Je tiens à remercier le Fonds National Suisse (FNS) pour avoir financé et soutenu mon projet de thèse. Je remercie les membres du jury qui ont examiné ce travail: Prof. Hervé Combeau, Dr. Ludger Weber et Philippe Jarry pour leurs remarques et les discussions très intéressantes ainsi que Prof. Paul Muralt pour avoir présidé le jury. Je tiens en particulier à remercier Hervé Combeau pour son aide précieuse dans la compréhension des phénomènes de germination et macroségrégation et pour l'aide dans le développement d'un nouveau four Bridgman ainsi que pour les moments toujours très sympas lors de ses visites à Lausanne.

Un grand merci à Anne pour sa disponibilité, son aide pour tout ce qui concerne les tâches administratives et pour toujours penser au moindre détail.

Merci aussi à Jon Dantzig pour ses conseils concernant le modèle mésoscopique et pour m'avoir aidé à améliorer mes présentations.

Je tiens à remercier pour leur curiosité et leur motivation les deux étudiants, Hugo Lavocat et Chatchai Hirunlabh, qui ont décidé de faire un projet sous ma responsabilité. Chatchai a eu la force de persévérer et de faire un deuxième projet avec moi, tout en connaissant mes exigences.

Je tiens à remercier infiniment Jean-Luc Desbiolles pour avoir été toujours disponible et m'avoir aidé à résoudre tout genre de problèmes, en particulier pour tout ce qui avait trait à la modélisation. Sans l'aide précieuse de Jean-Luc, il ne m'aurait pas été possible de faire marcher le modèle multi-champ de phase et de développer le modèle mésoscopique. Accessoirement, merci pour m'avoir aidé quotidiennement à résoudre les mots-fléchés du *20min*.

Remerciements

Merci à Jean-Daniel Wagnière pour m’avoir aidé à faire mes premières coulées d’alliage et à développer un nouveau four Bridgman. Je remercie également Emmanuelle Boehm-Courjault pour son aide en ce qui concerne la microscopie et la préparation d’échantillons et pour les moments sympas pendant la pause de midi. Je tiens aussi à remercier Jean-Marie Drezet avec qui on a proposé le projet Fonds National et Alain Jacot pour les équations du multi-champ de phase. Un grand merci à Julie Fife pour nous avoir initiés à la tomographie rayons-X et pour sa disponibilité et son aide lors des sessions au PSI. Un grand merci aussi au personnel de l’atelier de l’institut des matériaux (ATMX) qui a toujours fait un travail exceptionnel dans des délais pas toujours suffisamment programmés à l’avance.

Au sein du LSMX, je tiens à remercier les personnes suivantes: Alexandre Durussel pour avoir en partie sacrifié ses vacances pour m’aider dans les expériences au PSI et pour s’être soutenus mutuellement lors des dernières phases de la rédaction de la thèse ; Nicolas Chobaut, avec qui j’ai eu le plaisir de partager mon bureau, pour sa bonne humeur quotidienne ; Patrick (Couch-surfer) Schloth pour les soirées à Sat lors de ses séjours à Lausanne ; Bastien Mireux et Paolo Di Napoli pour leur aide concernant la tomographie et pour les nombreuses parties de ping-pong ; Léa Deillon, Jonas Vannod, Jonas Valloton, et Denis Favez pour avoir rendu agréables les pauses-café et, en particulier Léa et Jonas II, pour les match de Jass (avec Alexandre comme partenaire) ; Amin Rostamian pour les discussions jamais banales et pour la nomination officieuse pour le prix “Novamet” ; Jonathan Friedli et Güven Kurtuldu pour m’avoir aidé au début de ma thèse pour les expériences Bridgman, lors des sessions au PSI et aussi pour les moments sympas en conférence ; Luc Rougier pour m’avoir aidé dans le développement de mon modèle et pour les repas partagés à midi ; Kamal Shahim pour les nombreuses parties de tennis, jusqu’à tard le soir ; Meisam Sistaninia pour m’avoir expliqué le fonctionnement du modèle granulaire et Hossein Meidani pour avoir supervisé mon projet de Master et répondu à mes nombreuses questions ; Shuichi Nakamura pour m’avoir appris quelques rudiments de japonais, qui m’ont été bien utiles lors de mon séjour au Japon. Je tiens aussi à remercier les membres du COSMO et FIMAP pour les séminaires toujours intéressants (et pour les croissants) ainsi que les membres du CIME avec qui j’ai interagi.

Un grand merci en particulier à mes potes tessinois Nicola, Lorenzo, Vasco et Gionata, pour leur amitié et pour avoir passé de bon moments lors des nombreuses fêtes, grillades et sorties.

Je tiens à exprimer ma profonde gratitude à ma famille. Merci à mon frère Alexandre, qui, par ailleurs, a choisi la même voie du doctorat, pour m’avoir aidé à orienter mes choix et pour les nombreuses passions que nous avons en commun. Je remercie mes parents, à qui je dédie ce travail de thèse, pour l’éducation et les valeurs qu’ils m’ont transmises, pour m’avoir toujours soutenu et pour l’amour qu’ils m’ont donné.

Abstract

Hot tearing is a major defect of solidification processes and welding. It occurs in metallic alloys while they are in the semi-solid state and is caused by a lack of liquid feeding in the mushy zone to compensate solid network openings due to tensile and shear strains. These strains are localized in the thin liquid films that remain at grain boundaries even in the last stages of solidification. Therefore, it is important to know when the solid grains coalesce and percolate to form a fully coherent solid, i.e., when the material can transmit stresses and strains but also withstand thermal contraction without rupture. It is also important to determine the regions of the mushy zone where liquid feeding is difficult or even impossible due to isolation of liquid pockets. Coalescence is defined as the disappearance of a liquid film in between two distinct grains, forming a solid grain boundary, while percolation is defined as the gradual transition of isolated grains or clusters surrounded by a continuous liquid film to a continuous solid network across a domain, even if some liquid regions remain.

If the simulation of hot tearing has to account for localization of strains and liquid feeding, it is mandatory to use a granular approach. Two previous theses done recently at EPFL have developed such granular models of hot tearing, first in two dimensions (PhD of S. Vernède [1]) and then in three dimensions (PhD of M. Sistaninia [2]). However, these models have used a Voronoi tessellation for the description of globular microstructures in which equiaxed grains were approximated by polygons and polyhedra, respectively. Although some refinement was used to smooth the edges of these grains, these two original contributions to hot tearing did not address specifically the question of the percolation of equiaxed globular grains.

The aim of this thesis is to investigate percolation in inoculated Al-Cu alloys via experimental investigations and refined simulations. More specifically, the goals were to: (i) obtain a globular-equiaxed microstructure under well-controlled conditions by using a modified Bridgman apparatus which after a quench would give access to the whole solidification history in a single sample; (ii) observe the percolation of grains by X-ray tomography, *ex situ* on the samples obtained with the modified Bridgman furnace and *in situ* with a laser-heated furnace; and (iii) provide a new mesoscopic model that considers smooth grains and accounts for solute diffusion as well as grain coalescence in order to predict the various percolation transitions.

From the experimental point of view, an innovative method, based on the Bridgman furnace principle, has been developed. The standard Bridgman furnace has been substantially

Remerciements

modified in order to obtain the desired globular-equiaxed grain structure and reduce macrosegregation in the quenched sample. This modified furnace has been characterized then in terms of thermal measurements and observed final grain size.

The samples obtained with the modified Bridgman furnace were then observed post-mortem by *ex situ* X-ray tomography. In addition, X-ray tomography experiments under similar conditions have been performed *in situ* with the laser-heated furnace installed on the TOMCAT synchrotron beam line of the Paul Scherrer Institute. A postprocessing analysis of the principal curvature distribution (ISD plots) was performed on both *ex situ* and *in situ* observations for various compositions of inoculated Al-Cu alloys. The ISD plots of the X-ray tomography observations indicated the formation of liquid cylinders along triple line and, at a more advanced solidification stage, the formation of liquid pockets at quadruple vertices.

From the modeling point of view, the percolation of a small number of grains has been simulated with a multiphase-field model in 2D. However, due the large computational cost associated with the multiphase-field method, a new mesoscopic model has been developed for both 2D and 3D simulations. This model was inspired by the granular model developed by Phillon *et al.* [3] that considers polyhedral grains based on a Voronoi tessellation of space, but allows to obtain smoother shapes of the grains and more progressive coalescence of the grains.

After its validation with the multiphase-field simulations, the mesoscopic model has been used to predict the various percolation transitions of the solid phase. In addition, by estimating the solid fractions/temperatures at which the liquid starts to form isolated pockets, it was possible to predict the temperatures and solid fractions for which the mushy zone is most vulnerable to hot tearing. The simulations have been performed for various conditions and for different copper compositions, indicating the nominal compositions that are more sensitive to hot tearing. Finally, the 3D mesoscopic model predictions were compared with the X-ray tomography observations.

Key words: Hot tearing, Percolation, Coalescence, Solidification microstructures, X-ray tomography, Curvature distribution, Simulation, Phase-field modeling, Mesoscopic modelling

Riassunto

La fessurazione a caldo è uno dei principali difetti che può apparire durante la solidificazione e la saldatura. Questo difetto si ritrova in determinate leghe metalliche, mentre sono ancora in uno stato semisolido. La fessurazione a caldo è provocata da una non sufficiente alimentazione in liquido della zona semisolido tale da compensare l'apertura della struttura solida a causa di deformazioni di tensione e di taglio. Queste deformazioni sono localizzate nei film liquidi che sussistono ai bordi di grano, anche nelle ultime fasi della solidificazione. Di conseguenza, è importante conoscere il momento a partire dal quale i grani solidi coalescono e percolano in modo da formare un solido totalmente coerente, i.e., il momento a partire dal quale i grani possono trasmettere sforzi e deformazioni, ma anche resistere alla contrazione termica senza rottura. Inoltre, è importante determinare le regioni della zona semisolido nelle quali l'apporto di liquido è difficile o addirittura impossibile a causa dell'isolamento delle sacche di liquido. Il fenomeno di coalescenza è definito come la scomparsa di un film liquido compreso tra due grani, per formare un bordo di grano, mentre il fenomeno di percolazione è definito come la transizione graduale da grani (o clusters di grani) attornati da un film liquido a una rete solida continua attraverso il volume considerato, anche se sussistono delle sacche di liquido.

La simulazione della fessurazione a caldo deve considerare la localizzazione delle deformazioni e dell'apporto di liquido. È dunque necessario utilizzare un approccio granulare. Nel contesto di due lavori di tesi effettuati recentemente all'EPFL, due modelli granulari di fessurazione a caldo sono stati sviluppati, inizialmente in due dimensioni (lavoro di tesi di S. Vernède [1]) e, in seguito, in tre dimensioni (lavoro di tesi di M. Sistaninia [2]). Ciononostante, questi modelli sono basati su una tessellazione di Voronoi in modo da descrivere delle microstrutture globulari et considerano i grani equiassiali come poligoni, rispettivamente poliedri. Nonostante sia stato possibile smussare gli angoli dei grani con un affinamento, queste due contribuzioni, originali nel contesto della fessurazione a caldo, non furono dedicate in modo specifico al fenomeno di fessurazione a caldo di grani globulari equiassiali.

Lo scopo di questa tesi è d'investigare il fenomeno di percolazione dei grani nelle leghe Al-Cu inoculate con uno studio sperimentale e simulazioni più raffinate. In modo più particolare, gli scopi della tesi erano di: (i) ottenere una microstruttura globulare-equiassiale in condizioni controllate con un forno di Bridgman modificato, con il quale, dopo la tempra, permette di accedere a tutta la cronologia della solidificazione, il tutto in un solo campione; (ii) osservare la percolazione di grani per mezzo della tomografia

Remerciements

a raggi-X, *ex situ* su campioni ottenuti con il forno Bridgman e *in situ* con un forno a riscaldamento laser; e (iii) fornire un modello mesoscopico innovativo che considera grani smussati, la diffusione de soluto e la coalescenza dei grani per predire le varie transizioni di percolazione.

Dal punto di vista sperimentale, un metodo innovativo basato sul funzionamento del forno Bridgman è stato sviluppato. Il forno Bridgman standard è stato modificato in modo sostanziale per ottenere la struttura globulare-equiaassiale desiderata e ridurre la macrosegregazione nei campioni temprati. Il forno modificato è stato poi caratterizzato dal punto di vista termico e della grandezza dei grani osservata. In seguito, i campioni sono stati osservati post-mortem con la tomografia a raggi-X *ex situ*. Inoltre, esperimenti di tomografia raggi-X sono stati effettuati in condizioni simili *in situ* con un forno laser installato sul fascio sincrotrone TOMCAT presso l'istituto Paul Scherrer. Un'analisi post-trattamento delle curvature principali (grafici ISD) è stata effettuata su osservazioni *ex situ* e *in situ* di varie composizioni di leghe Al-Cu. I grafici ISD delle osservazioni di tomografia raggi-X indicano la formazione di sacche di liquido con forma cilindrica lungo linee triple e, ad uno stadio di solidificazione più avanzato, la formazione di sacche di liquido in punti quadrupli.

Dal punto di vista della modellazione, la percolazione di un piccolo numero di grani è stata simulata con un metodo di multi-campo di fase in 2D. Ciononostante, dato il lungo tempo di calcolo del metodo di multi-campo di fase, un nuovo modello mesoscopico è stato sviluppato al fine di effettuare delle simulazioni in 2D e 3D. Questo modello è stato ispirato dal modello granulare sviluppato da Phillon *et al.* [3] che considera dei grani poliedrici basandosi sulla tessellazione di Voronoi dello spazio, ma permette di ottenere dei grani maggiormente smussati e una coalescenza più progressiva.

Dopo le validazioni comparando delle simulazioni in multi-campo di fase, il modello mesoscopico è stato utilizzato al fine di predire le varie transizioni di percolazione della fase solida. Inoltre, stimando le frazioni di solido/temperature alle quali la zona semisolida è più sensibile alla fessurazione a caldo, è stato possibile predire la temperature et la frazione di solido in cui la zone semisolida è maggiormente sensibile alla fessurazione a caldo. Le simulazioni sono state effettuate in varie condizioni e diverse composizioni di rame. Questo ha permesso di determinare le composizioni che sono più sensibili alla fessurazione a caldo. Infine, le predizioni del modello mesoscopico 3D sono state confrontate con le osservazioni di tomografia raggi-X.

Parole chiave: Fessurazione a caldo, Percolazione, Coalescenza, Microstrutture di solidificazione, Tomografia a raggi-X, Distribuzione di curvature, Simulazioni, Modellazione con campo di fase, Modellazione mesoscopica

Résumé

La fissuration à chaud est un des défauts majeurs des procédés de solidification et soudage. La formation de ce défaut se produit dans certains alliages métalliques, lorsqu'ils sont encore dans un état pâteux. La fissuration à chaud est due à un manque d'alimentation du liquide dans la zone pâteuse apte à compenser l'ouverture du réseau solide à cause de déformations en tension et en cisaillement. Ces déformations sont localisées dans les films liquides minces qui subsistent aux joints de grain, même dans les derniers stades de la solidification. Par conséquent, il est important de savoir à quel moment les grains solides coalescent et percolent afin de former un solide entièrement cohérent, c.à.d., à quel moment le matériau peut transmettre des contraintes et déformations, mais aussi résister à la contraction thermique sans qu'il y ait rupture. Il est, en outre, important de déterminer les régions de la zone pâteuse pour lesquelles l'alimentation en liquide est difficile, voire impossible à cause de l'isolation des poches de liquide. Le phénomène de coalescence est défini comme étant la disparition d'un film liquide entre deux grains, pour former un joint de grain, tandis que le phénomène de percolation est défini comme étant la transition graduelle d'une situation où les grains (ou des clusters de grains) sont entourés par un film liquide continu à une situation dans laquelle un réseau solide continu s'est formé à travers le domaine, même si des régions liquides peuvent subsister.

La simulation de la fissuration à chaud doit tenir compte de la localisation des déformations et de l'alimentation en liquide, si bien qu'il est essentiel d'utiliser une approche granulaire. Dans le contexte de deux travaux de thèse qui ont été récemment effectués à l'EPFL, des modèles granulaires de fissuration à chaud ont été développés, premièrement en deux dimensions (travail de thèse de S. Vernède [1]) et, par la suite, en trois dimensions (travail de thèse de M. Sistaninia [2]). Cependant, ces modèles sont basés sur une tessellation de Voronoï afin de décrire des microstructures globulaires et considèrent les grains équiaxes comme étant des polygones, respectivement des polyèdres. Bien qu'il fût possible de lisser les angles des grains au moyen d'un affinage, ces deux contributions, originales dans le contexte de la fissuration à chaud, n'étaient pas dédiées de manière spécifique au phénomène de percolation de grains globulaires équiaxes.

Le but de cette thèse est d'investiguer le phénomène de percolation des grains dans des alliages Al-Cu inoculés au moyen d'études expérimentales et de simulations numériques. En particulier, les buts étaient les suivants : (i) obtenir une microstructure globulaire-équiaxe, dans des conditions contrôlées au moyen d'un four Bridgman modifié, qui, après trempe, permet d'accéder à l'historique complet de la solidification, le tout en un seul

Remerciements

échantillon ; (ii) observer la percolation de grains au moyen de la tomographie rayons-X, *ex situ* sur des échantillons obtenus avec le four Bridgman modifié et *in situ* au moyen d'un four avec chauffage laser ; et (iii) fournir un modèle mésoscopique novateur qui considère des grains lisses et tient compte de la diffusion du soluté ainsi que de la coalescence des grains afin de prédire les différentes transitions de percolation.

Du point de vue expérimental, une méthode innovante, basée sur le principe du four Bridgman, a été développée. Le four Bridgman standard a été modifié de manière substantielle afin d'obtenir la structure de grain globulaire-équiaxe désirée et réduire la macroségrégation dans les échantillons trempés. Ce four modifié a été ensuite caractérisé en termes de mesures thermiques et taille finale de grain observée. Les échantillons ont été ensuite observés post-mortem par tomographie rayons-X *ex situ*. En outre, des expériences en tomographie rayons-X ont été effectuées *in situ* dans des conditions similaires au moyen d'un four laser installé sur le faisceau synchrotron TOMCAT de l'institut Paul Scherrer. Une analyse post-traitement des courbures principales (graphes ISD) a été effectuée sur des observations *ex situ* et *in situ* de plusieurs compositions d'alliage Al-Cu. Les graphes ISD des observations en tomographie rayons-X ont indiqué la formation de poches de liquide de forme cylindrique le long des lignes triples et, à un stade de solidification plus avancé, la formation de poches de liquide aux points quadruples.

Du point de vue de la modélisation, la percolation d'un faible nombre de grains a été simulée en multi-champ de phase en 2D. Par contre, du fait du temps de calcul conséquent de la méthode en multi-champ de phase, un nouveau modèle mésoscopique a été développé pour effectuer des simulations en 2D et 3D. Ce modèle a été inspiré par le modèle granulaire développé par Phillon *et al.* [3] qui considère des grains polyédriques en se basant sur une tessellation de Voronoï de l'espace, mais permet d'obtenir des grains plus lisses et une coalescence des grains plus progressive.

Après les validations en le comparant avec des simulations en multi-champ de phase, le modèle mésoscopique a été utilisé afin de prédire les différentes transitions de percolation de la phase solide. De plus, en estimant les fractions de solide/températures auxquelles le liquide commence à former des poches isolées, il a été possible de prédire la température et la fraction de solide auxquelles la zone pâteuse est la plus sensible à la fissuration à chaud. Les simulations ont été faites pour plusieurs conditions et différentes compositions de cuivre, ce qui a permis de déterminer les compositions les plus sensibles à la fissuration à chaud. Enfin, les prédictions du modèle mésoscopique 3D ont été comparées aux observations en tomographie rayons-X.

Mots clefs : Fissuration à chaud, Percolation, Coalescence, Microstructures de solidification, tomographie rayons-X, Distribution de courbures, Simulations, Modélisation en champ de phase, Modélisation mésoscopique

Contents

Remerciements	i
Abstract (English/Français/Italiano)	iii
1 Introduction	1
1.1 Aluminum and its alloys	1
1.2 Solidification processes	2
1.3 Hot tearing percolation and coalescence	4
1.4 Motivation and objective of the thesis	5
1.4.1 Structure of the manuscript	7
2 Literature review	9
2.1 Phase diagrams, microsegregation models and curvature effects	9
2.1.1 Phase diagrams	9
2.1.2 Microsegregation models	10
2.1.3 Curvature effects	14
2.2 Coalescence	15
2.3 Percolation	18
2.4 Hot tearing	21
2.4.1 Experimental investigations	22
2.4.2 Hot tearing models	25
2.5 Thermal conditions for globular-equiaxed grain	29
2.5.1 Columnar-to-equiaxed transition	30
2.5.2 Globular-to-dendritic transition	31
2.5.3 Globular-equiaxed conditions	32
2.6 Nucleation and grain refinement	34
2.6.1 Homogeneous nucleation	34
2.6.2 Heterogeneous nucleation	35
2.6.3 Athermal nucleation and grain refinement	36
2.7 Macrosegregation	38
3 Experimental methods	41
3.1 Materials	41
3.2 Quenched Bridgman furnace	42

Contents

3.2.1	Solidification experiments	46
3.2.2	Temperature measurements	46
3.2.3	Thermal simulation	48
3.2.4	Simulation of grain sizes	51
3.3	Observation techniques	52
3.3.1	Sample preparation	52
3.3.2	Scanning electron microscopy	53
3.3.3	X-ray tomography	54
4	Bridgman furnace results	59
4.1	Introduction	59
4.2	Temperature characterization	59
4.2.1	Furnace I - sample type 1	59
4.2.2	Furnace II - sample type 2	61
4.2.3	Furnace II - sample type 3	64
4.2.4	Measured cooling rates and comparison	66
4.3	Thermal simulation	67
4.3.1	Observed thermal arrests and comparison with experiments	67
4.3.2	Furnace I - sample type 1	68
4.3.3	Furnace II and sample type 2	69
4.4	Grain movement and associated macrosegregation	71
4.5	Grain size and misorientation distributions	72
4.5.1	Misorientation distributions	72
4.5.2	Grain size	73
4.5.3	Simulation with nucleation model	75
5	Modeling	79
5.1	Multiphase-field model	79
5.1.1	Introduction	79
5.1.2	Formulation	79
5.1.3	Implementation and optimization of the code	82
5.2	Mesoscopic model	85
5.2.1	Introduction	85
5.2.2	Method	85
5.2.3	Voronoi meshing and column subdivision	94
5.2.4	Reconstruction of the solid/liquid interface	97
5.2.5	Evaluation of the curvature	99
6	Multiphase-field and mesoscopic model validations	101
6.1	Introduction	101
6.2	Multiphase-field results	101
6.2.1	Validation of the multiphase-field formulation	101
6.2.2	Percolation of grains	105

6.3	Validation of the mesoscopic model	107
6.3.1	Meshing of the Voronoi regions	107
6.3.2	Comparison with multiphase-field predictions	108
6.3.3	Sensitivity to diffusion in the liquid	110
6.3.4	Boundary condition at the Voronoi facet	113
7	X-Ray tomography observations	117
7.1	Introduction	117
7.2	<i>Ex situ</i> tomography	117
7.3	<i>In situ</i> tomography	124
8	Mesoscopic model results	133
8.1	Introduction	133
8.2	2D results	134
8.2.1	Solute diffusion and coalescence	134
8.2.2	Definition of the percolation transitions	135
8.2.3	Percolation transitions for several grains	140
8.3	3D results	143
8.3.1	Grain boundary energy calculation	144
8.3.2	Solute diffusion, coalescence and percolation transitions	145
8.3.3	Percolation of several grains	149
8.3.4	Comparison between experiments and modeling results	153
9	Conclusion and perspectives	157
9.1	Perspectives	159
A	Appendix experimental	161
A.1	Thermal gradient distribution	161
B	Appendix Modeling	165
B.1	Multiphase-field	165
B.1.1	Choice of the multiobstacle potential	165
B.2	Mesoscopic model	168
B.2.1	Discretization of the diffusion equations in the solid	168
B.2.2	Numerical integration in triangular/tetrahedral coordinates	170
B.2.3	Solute conservation equations in the liquid part of the columns	174
B.2.4	Voronoi boundary conditions	177
B.2.5	Meshing of the interface	179
B.2.6	Evaluation of the curvature	182
B.3	Polyhedron associated to regularly arranged edgy grains	184
	Bibliography	185
C	List of symbols	195

Contents

Curriculum Vitae	201
------------------	-----

1 Introduction

1.1 Aluminum and its alloys

Aluminum is one of the most abundant elements of the Earth's crust (8% of the Earth crust). However, since its oxide Al_2O_3 (alumina) is very stable from a chemical point of view, the transformation of Al_2O_3 into metallic aluminum (Hall-Héroult process) requires large quantities of energy. In addition, in nature, alumina is combined with other oxides: it is generally separated from the other undesired oxides in the bauxite ore (which contains up to 60% of Al_2O_3) using the Bayer process [4]. Historically, aluminum production only became significant from an industrial point of view at the end of the 19th century after the invention of the Hall-Héroult (discovered simultaneously by Hall [5] and Héroult [6] in 1886) and the Bayer (1887) processes.

Pure aluminum is a very ductile and malleable metal. Its mechanical properties can be significantly improved by alloying it with other elements. The aluminum alloys are

Table 1.1: Designation of the various aluminum alloys as proposed by the Aluminum Association (AA).

Cast alloys		Wrought alloys	
Series	Major alloying element	Series	
1xx.x	$\text{Al} \geq 99.00\%$	1xxx	
2xx.x	Cu	2xxx	
3xx.x	Si + Cu and/or Mg	3xxx	Mn
4xx.x	Si	4xxx	
5xx.x	Mg	5xxx	
7xx.x	Zn	6xxx	Mg and Si
8xx.x	Sn	7xxx	Zn
9xx.x	other elements	8xxx	
6xx.x	unused series	9xxx	

classified following various systems, but the most widely used is that of the Aluminum Association (AA), shown in Table 1.1. This classification distinguishes cast alloys (designed by three digits followed by a point and a last digit) and wrought alloys (designed by four digits) [7]. Cast alloys are directly shaped in their definitive (or near definitive) shape, while wrought alloys first are cast into simple shapes and then used for further transformations by forging, rolling or extrusion.

1.2 Solidification processes

Casting consists of pouring a liquid metal in a cavity and then cooling it down. The onset of solidification happens when the temperature falls below the liquidus of the alloy and ends, under equilibrium conditions at the solidus temperature (unless other phases nucleate with some eutectic or peritectic reactions). Many types of casting processes exist. However, we will present those related to aluminum production in which hot tearing formation plays an important role, such as semi-continuous casting and welding.

Unlike steel, aluminum alloys, due to their low strength at high temperature and their high thermal conductivity, cannot be produced by truly continuous casting. They are

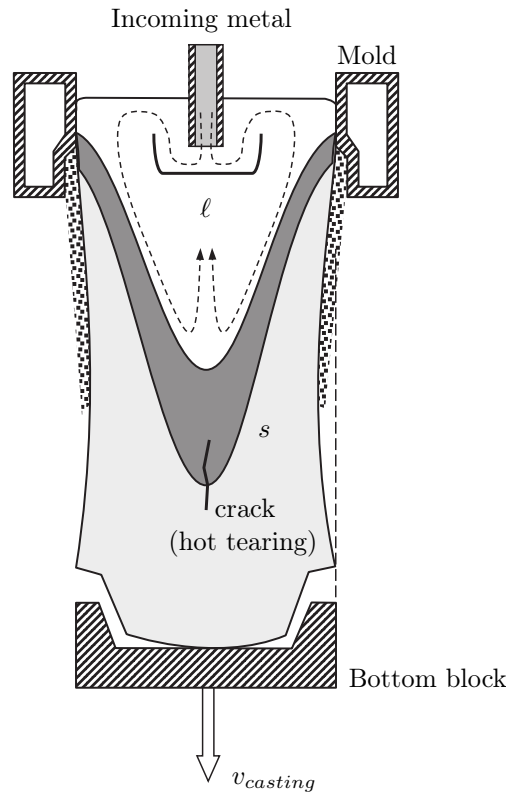


Figure 1.1: Schematic representation of the DC casting process (after [8]). s indicates the solid, ℓ the liquid and $v_{casting}$ the casting speed.

generally produced by a vertical direct chill (DC) casting (see schematic representation in Fig. 1.1). Please note that this is a semi-continuous process due to the limited height of the deep pits used for castings (generally up to 7 meters deep). At the beginning of the process, the mold is closed by a bottom block and the liquid metal is poured via a feeder. Once a sufficient layer of metal has solidified, the bottom block is moved down and withdrawn from the open mold at a pulling speed v_c until the bottom of the cavity pit is reached. During the process, the level of the liquid metal is kept constant by the feeder. The metal is cooled by two mechanisms: by contact with the mould (primary cooling) and by a contact with a water jet (secondary cooling).

Hot tearing generally happens in low-concentration alloys exhibiting a large solidification interval under conditions of high casting speeds [9]. This is due to the high tensile strains that develop at the center of the billet and the fact that the permeability of the mushy zone becomes low at high solid fractions. Various other defects can happen during DC casting, such as microporosity, macrosegregation and macroscopic deformations due to thermal stresses (non exhaustive list).

Welding is one of the most common methods for joining materials that consists in locally melting two pieces in order to join them, once resolidified. Please note that a filler material may be added to control the weld chemistry as well as to fill the gap between the two parts. Hot tearing in welding forms during cooling, when the fusion zone near the end of solidification is subject to tensile stresses associated with high cooling rates. Therefore, in order to reduce the cooling rate experienced in welding (and limit the formation of hot tears) the weldment can be preheated. An alternative way is to use a two-lasers welding process, in which a second heat source that follows the welding source helps reducing the cooling rate [10].

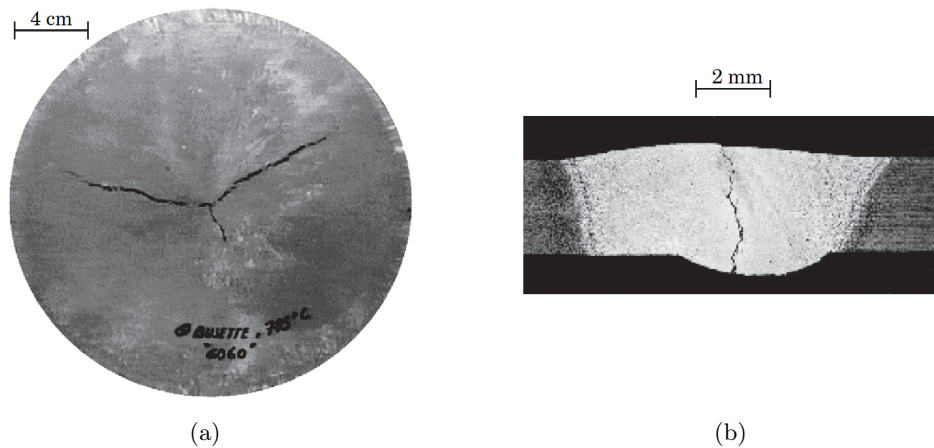


Figure 1.2: Hot tears observed (a) at the center of a DC cast Al 6060 billet (b) at the weld centerline of an aluminum alloy (after [8]).

1.3 Hot tearing percolation and coalescence

As explained above, hot tearing is a spontaneous failure of an alloy during its solidification that generally presents the shape of a ragged branching crack (see Fig. 1.3(a)). As observed by Campbell [14], hot tears propagate mainly in between solid grains (intergranular) and exhibit a fairly smooth surface appearance that existed at the time of fracture (see Fig. 1.3(c)).

The two main phenomena leading to hot tearing are: a lack of liquid feeding at high solid fractions and tensile/shear strains in the mushy zone that tend to pull apart the solid network. These strains, transmitted through the partially coherent solid in the mushy zone, are induced by contraction of the solid in a thermal gradient, and mechanical constraints imposed by the geometry of components. At low solid fraction ($g_s < 0.9$), the permeability of the mushy zone is large enough so that liquid feeding can heal possible grain boundary openings, forming a so-called “healed hot tear”. At high solid fraction

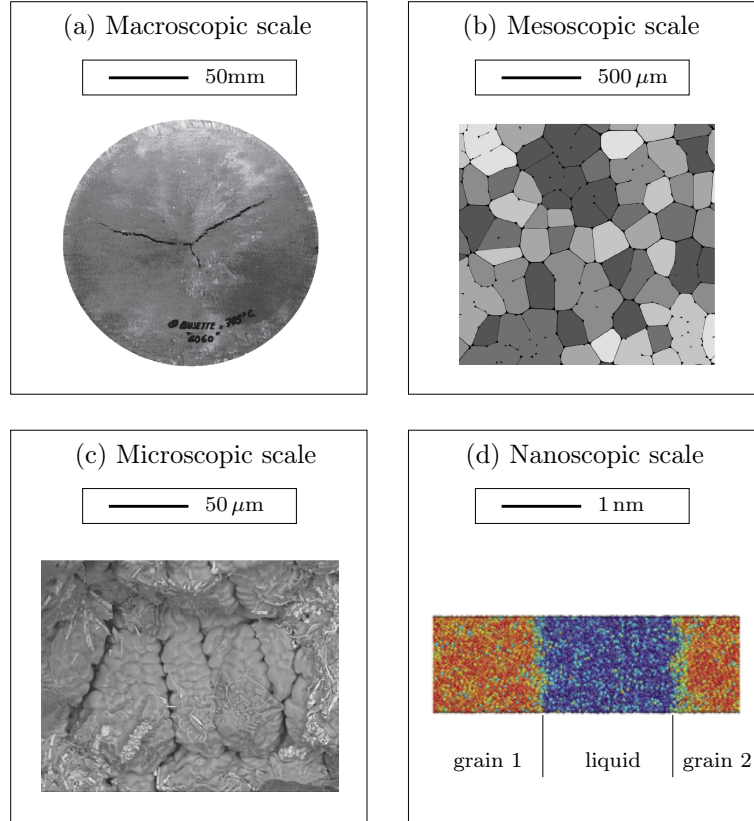


Figure 1.3: Observations of hot tearing and related phenomena at different scales. (a) Hot crack observation in the center of a DC cast Al 6060 billet [8]. (b) Simulation of the solid clusters formation and percolation of globular-equiaxed grains with a granular model [11]. (c) Scanning Electron Microscopy fractography observation of a hot tear surface lip of a crack [12]. (d) Molecular dynamics simulation of the coalescence of two solid liquid interfaces [13].

($g_s > 0.95$), the grains form a continuous solid network with isolated liquid pockets, possessing sufficient mechanical resistance and the mushy material behaves like a ductile solid. However, there is a critical zone for hot tearing (for solid fractions in the range $0.9 < g_s < 0.95$) in which grain boundaries openings, due to the deformation localized in the continuous liquid films, cannot be fed by liquid flow because of the low permeability of the mushy zone [8, 15].

Therefore, it is important to know when the solid grains coalesce and percolate to form a fully coherent solid, i.e., when the material can transmit stresses and strains but also withstand thermal contraction without rupture [15, 16]. Coalescence is defined as the disappearance of a liquid film in between two distinct grains, forming a solid grain boundary, while percolation is defined as the gradual transition of isolated grains or clusters surrounded by a continuous liquid film to a continuous solid network across a domain, even if some liquid regions remain [16, 17].

Coalescence is strongly influenced by the interfacial energies. In the case of a thin liquid film that separates two coalescing grains, as the thickness of the liquid film approaches the solid/liquid interface thickness, δ_{sl} (which is on the order of few nanometers as shown in Fig. 1.3(c)), the excess free energy deviates from the initial value of $2\gamma_{sl}$, (where γ_{sl} is the energy of the solid/liquid interface). When the liquid has completely disappeared, the excess free energy is equal to the grain boundary energy, γ_{gb} . In the case $\gamma_{gb} > 2\gamma_{sl}$, the substitution of two solid/liquid interfaces by a grain boundary is associated with an increase of the excess interface energy: a bridging undercooling, ΔT_b , is thus necessary in order for the two interfaces to coalesce (repulsive case). On the other hand, in the case $\gamma_{gb} < 2\gamma_{sl}$, no undercooling is required for the coalescence of the two interfaces (attractive case) [16].

Simulation of hot tearing and its associated phenomena is not an easy task, since it involves interdependent phenomena occurring at very different length scales, as shown in Fig. 1.3. In order to better predict hot tearing, it is thus important to develop models that account for very different scales.

1.4 Motivation and objective of the thesis

While previous researches in the field of solidification have mainly focused on the dendrite tip kinetics and other topics related to the initial stages of solidification, only few works have been dedicated to the investigation of its final stages, despite its crucial importance for the formation of defects such as hot tearing. The goal of the present research is thus to explore the last-stage solidification, in particular for globular-equiaxed grains in aluminum-copper alloys at the mesoscale but considering also the coalescence phenomenon taking place at the nanoscale (see Fig. 8.5).

The reasons that motivate the choice of this type of microstructure for the present work are multiple. First, since in real castings the alloys are often inoculated in order to promote fine equiaxed microstructures, this project could be interesting from an industrial

point of view. Second, if the grains are globular in shape, it is easier to study their evolution compared to the case in which the instability of the solid/liquid interface leads to dendritic morphologies. Third, the results of the present work can then be used to refine the solidification module of the granular model of Sistaninia *et al.* [18–21], which considers such a microstructure. Therefore, despite the simplicity of the shape of the grains, the main challenge of the present work is to be able to describe the evolution of the shape of globular-equiaxed grains as well as the phenomena of coalescence and percolation from a quantitative point of view.

The novelty of the present work resides in the combination of an experimental approach based on X-ray tomography and the development of a mesoscopic model for simulating the percolation of several grains. The main objectives are the following:

- (i) Obtain the desired globular-equiaxed microstructure in a quenched Bridgman furnace and thus access to the whole solidification history in a single sample. This implies a modification of the furnace and sample designs in order to achieve steady-state conditions and limit macrosegregation, which is generally observed for equiaxed microstructures.
- (ii) Observe the last-stage solidification of inoculated AlCu alloys by synchrotron X-ray tomography at the Paul Scherrer Institut (PSI). Observation will be performed both *ex situ* on samples obtained with the modified Bridgman furnace and *in situ* with a laser-heated furnace. The furnace, installed on the TOMCAT beamline of the Swiss Light Source, was recently developed in collaboration between Paul Scherrer Institut (PSI) and Computation Materials Laboratory (LSMX), thanks to the funding of the Competence Centre of Materials (CCMX) and of several industries. The postprocessing of the 3D microstructures will shed some light on the percolation state evolution and morphology of the solid-liquid interface in the last-stage solidification.
- (iii) Develop a multiphase-field model as well as a less computationally intensive mesoscopic model to simulate grain percolation. The mesoscopic model, developed both in 2D and 3D, is inspired by the granular model developed by Phillon *et al.* [3] that considers polyhedral grains based on a Voronoi tessellation of space. The mesoscopic model will allow to obtain smoother shapes of the grains and a more progressive coalescence of the grains as well as to correctly describe the solid fraction and temperatures of the various percolation transitions.

All the relevant microstructural parameters, such as curvature distribution, solid-liquid interface evolution, percolation parameters and other relevant microstructure features will be deduced from both experimental and simulation approaches.

1.4.1 Structure of the manuscript

The text is organized in 9 chapters.

In chapter 2, the basic knowledge about solidification necessary for this work (phase diagram, microsegregation and curvature effects) is provided. After that, the coalescence and percolation phenomena are explained in the context of hot tearing. The previous works (experimental and modeling) related to hot tearing are then exposed. The last part of the chapter is dedicated to the explanation of the phenomena that can take place in a Bridgman furnace. Conditions under which a desired globular-equiaxed grain structure can be obtained with such an apparatus will be described.

Chapter 3 is dedicated to describing the innovative Bridgman furnace modifications that have been developed in order to obtain the complete solidification history in a single experiment with the desired globular-equiaxed microstructure. In the last part of the chapter, the observation techniques that were used in the context of this work are briefly explained. Chapter 4 is dedicated to the characterization of the standard Bridgman furnace and of the newly developed furnace in terms of temperatures experienced by the sample during directional solidification as well as macrosegregation, grain size and solid fraction evolution observed in the final quenched microstructure.

In chapter 5, the multiphase-field model and the mesoscopic model (for both 2D and 3D geometries) that were developed in the context of this work are explained. In particular, the validation of the mesoscopic model with the phase-field predictions is performed in chapter 6.

Chapter 7 and 8 are dedicated to the study of percolation of grains in the last-stage solidification, from an experimental point of view in chapter 7 and from modeling in chapter 8. More specifically, in chapter 7, the 3D tomography reconstructions, performed both *ex situ* and *in situ*, are analyzed in terms of solid fractions, specific solid-liquid interfacial area and curvature distribution. In chapter 8, the 2D and 3D mesoscopic model results are shown. The various percolation transitions are shown for different nominal compositions. A final analysis indicates the alloy compositions that are vulnerable to hot tearing for various conditions. At the end of the chapter, the 3D mesoscopic model results are compared with the *in situ* X-ray tomography observations.

The conclusion is given in chapter 9, alongside with possible future steps that can be followed to contribute to a better understanding of hot tearing formation.

2 Literature review

2.1 Phase diagrams, microsegregation models and curvature effects

2.1.1 Phase diagrams

In order to be able to describe how an alloy transforms from the liquid to the solid state, it is necessary to introduce the concept of phase diagram. A phase diagram indicates the presence, at equilibrium, of specific phases as a function of temperature and composition for a fixed pressure. During solidification, solute diffusion takes place at a finite rate, thus leading to composition gradients. Consequently, thermodynamic equilibrium is generally not achieved within the phases. However, a good assumption is to consider that the compositions at the interface are given by the phase diagram (so-called *local equilibrium*). The phase diagram of Al-Cu, the alloy used in this project, is presented in Fig. 2.1a. Since

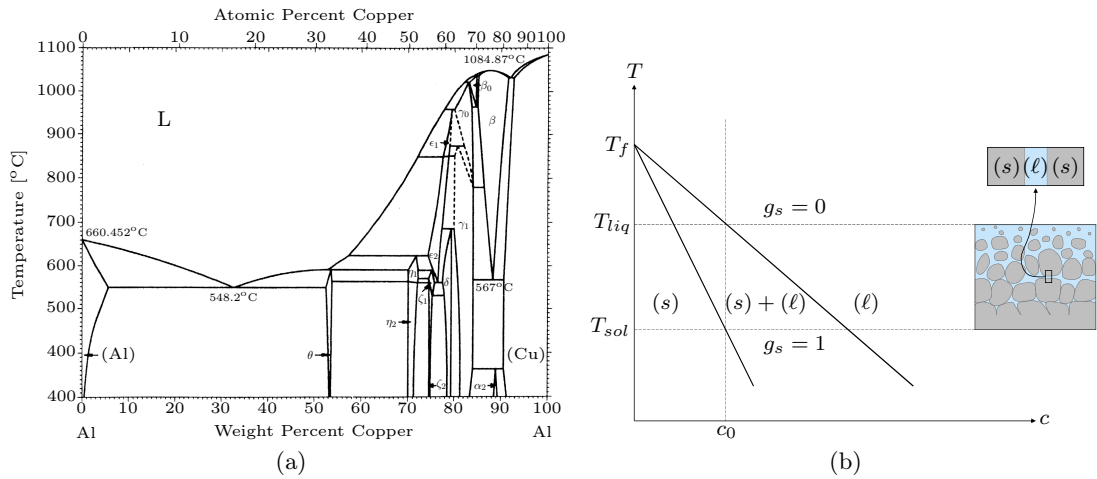


Figure 2.1: (a) Al-Cu equilibrium phase diagram [22]. (b) Schematic enlargement of the low copper composition part of the phase diagram.

we are interested in hypoeutectic alloys, a schematic enlargement of the phase diagram is shown in Fig. 2.1. The liquidus and the solidus are approximated by straight lines, with a constant liquidus slope $m_\ell = -3.4^\circ\text{C}/\text{wt}\%$ and a constant partitioning coefficient $k_0 = m_\ell/m_s = c_s/c_\ell = 0.15$. A list of all the symbols is given in Appendix C.

When the temperature of an alloy of nominal composition c_0 falls under the liquidus temperature, T_{liq} , it is thermodynamically favourable to grow a solid phase. The solid fraction, g_s , increases as the temperature decreases. Solidification is completed ($g_s = 1$) at the solidus temperature, T_{sol} , or eutectic temperature, T_{eut} , depending on the composition and cooling conditions.

In order to study the evolution of solidification, one can use analytical microsegregation models that have been developed, such as the lever rule, the Scheil-Gulliver, or the Clyne and Kurz models. Numerical models have been developed as well. All these models are briefly reviewed hereafter.

2.1.2 Microsegregation models

Solidification can be modeled for a representative elementary volume (REV) that has the size L corresponding to half the secondary dendrite arm spacing, $\lambda_2/2$, for dendritic microstructures or to the final grain radius, R_{g0} , for globular-equiaxed microstructures. Consider a one dimensional domain of length L , where the interface is positioned at x^* . In a closed system, the solute is conserved and thus:

$$\int_0^{x^*} c_s(x, t) x^{P-1} dx + \int_{x^*}^L c_\ell x^{P-1}(x, t) dx = c_0 \int_0^L x^{P-1} dx \quad (2.1)$$

where P is the dimensionality of the problem: $P = 1$ cartesian, $P = 2$ cylindrical (dendrite arm), and $P = 3$ spherical (globular grain).

By derivation of this expression with respect to time for $P = 1$, we get:

$$\begin{aligned} \frac{d}{dt} \int_0^{x^*} c_s(x, t) dx + \frac{d}{dt} \int_{x^*}^L c_\ell(x, t) dx &= 0 \\ \int_0^{x^*} \frac{\partial c_s(x, t)}{\partial t} dx + c_s^* \frac{dx^*}{dt} + \int_{x^*}^L \frac{\partial c_\ell(x, t)}{\partial t} dx - c_\ell^* \frac{dx^*}{dt} &= 0 \end{aligned} \quad (2.2)$$

Please note that one has introduced the compositions at the interface c_s^* and c_ℓ^* , in solid and liquid. Assuming local equilibrium, $c_\ell^* = c_{liq}(T)$ and $c_s^* = k_0 c_\ell^*$. In order to understand the assumptions used in the microsegregation models, we first introduce the dimensionless Fourier number defined as:

$$Fo_i = \frac{D_i t_f}{L^2} = \frac{D_i \frac{\Delta T_0}{|\dot{T}|}}{L^2} \quad \text{with } i = s(\text{solid}) \text{ or } \ell(\text{liquid}) \quad (2.3)$$

where D_i is the diffusion coefficient of the solute in the solid phase (D_s) or in the liquid phase (D_ℓ), t_f the solidification time, ΔT_0 the solidification interval, and \dot{T} the cooling

rate. The Fourier number is nothing but the square of the ratio between the diffusion layer thickness at a given time (proportional to $\sqrt{D_i t}$) and the length of the REV, L . In analytical models, the composition in the liquid is assumed to be uniform (infinite Fo_ℓ) while limited diffusion may occur in the solid phase. Using 2nd Fick's law for the solid phase and dividing by L , Eq. (2.2) becomes after integration:

$$\frac{D_s}{L} \frac{\partial c_s(x^*, t)}{\partial x} + (1 - g_s) \frac{dc_\ell^*}{dt} = (1 - k_0) c_\ell^* \frac{dg_s}{dt} \quad (2.4)$$

where $g_s = x^*/L$ and $dg_s = dx^*/L$ are the fraction of solid, and its increment, respectively.

Analytical models

For the lever rule, thermodynamic equilibrium conditions are assumed, i.e. complete diffusion in both the solid and liquid phases (infinite Fo_s and Fo_ℓ).

It is then possible to rearrange Eq. (2.2) and obtain the lever rule solid fraction as a function of temperature:

$$g_s = \frac{1}{1 - k_0} \left(\frac{T - T_{liq}}{T - T_m} \right) \quad (2.5)$$

where T_m is the melting point of the pure metal.

When a relatively fast solidification takes place, one can assume no diffusion in the solid ($Fo_s = 0$) [23, 24]. The first solid forms at a composition $k_0 c_0$ but, during further cooling, the composition of the solid formed at a given stage of solidification remains unchanged since $Fo_s = 0$. After integration of Eq. (2.4), one obtains the Scheil-Gulliver relation:

$$\begin{cases} g_s = 1 - \left(\frac{T - T_m}{T_{liq} - T_m} \right)^{\frac{1}{(k_0 - 1)}} & \text{for } T > T_{eut} \\ g_s = 1 & \text{for } T \leq T_{eut} \end{cases} \quad (2.6)$$

Here, it is assumed that the eutectic fills the remaining liquid space when T_{eut} is reached. The lever rule and the Scheil-Gulliver model are two extreme cases and do not represent real situations since, in general, limited diffusion takes place in the solid. The assumption of limited diffusion in the solid was initially used by Brody and Fleming [25] to develop a microsegregation model in which a parabolic growth is assumed:

$$x^* = L \sqrt{\frac{t}{t_f}} \quad \frac{dx^*}{dt} = \frac{L^2}{2t_f x^*} \quad (2.7)$$

In their approximation, these authors assumed that the solute gradient in the solid at the interfaces is given by:

$$\frac{\partial c_s(x^*, t)}{\partial x} \approx \frac{dc_s^*}{dx^*} = \frac{dc_s}{dt} \frac{dt}{dx^*} \quad (2.8)$$

Using this relation and Eq. (2.7) in Eq. (2.4), one finally has:

$$((2k_0Fo_s - 1)g_s + 1) \frac{dc_\ell^*}{dt} = (1 - k_0)c_\ell^* \frac{dg_s}{dt} \quad (2.9)$$

This equation can be integrated in order to obtain:

$$\begin{cases} g_s = \frac{1}{1-2k_0Fo_s} \left[1 - \left(\frac{T-T_m}{T_{liq}-T_m} \right)^{\frac{1-2k_0Fo_s}{(k_0-1)}} \right] & \text{for } T > T_{eut} \\ g_s = 1 & \text{for } T \leq T_{eut} \end{cases} \quad (2.10)$$

The assumption made in Eq. (2.9) for the solute gradient in the solid is equivalent to stating that the slope remains about constant during a time increment Δt . If this works for the Scheil-Gulliver model ($Fo_s = 0$), this is not true for the lever rule ($Fo_s = \infty$), reason why the Brody-Fleming's model recovers this limiting case for $Fo_s = 0.5$. For this reason, Clyne and Kurz [26] replaced Fo_s in Eq. (2.10) by the heuristic expression:

$$f(Fo_s) = Fo_s \left[1 - \exp\left(-\frac{1}{Fo_s}\right) \right] - \frac{1}{2} \exp\left(-\frac{1}{2Fo_s}\right) \quad (2.11)$$

such that the lever rule is recovered for $Fo_s = \infty$.

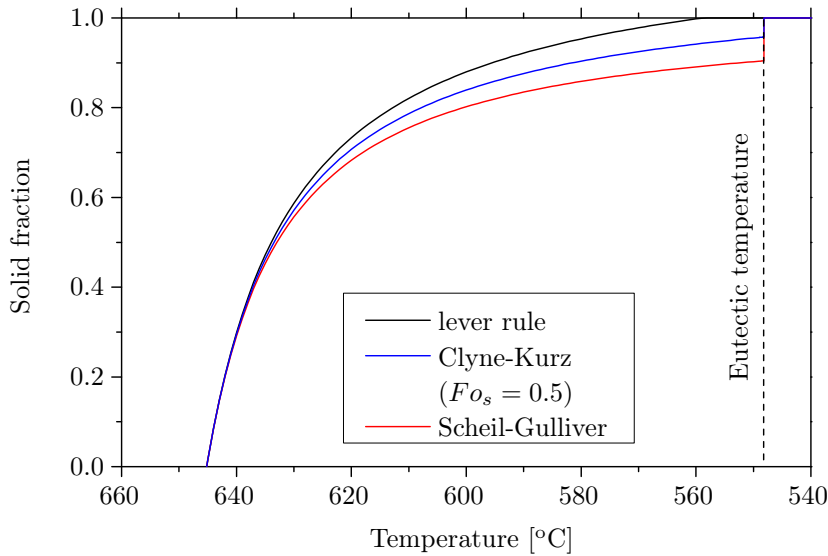


Figure 2.2: Comparison of the predictions of various microsegregation models for Al-4.5wt.%Cu.

In Fig. 2.2, the predictions of the various microsegregation models for an Al-4.5wt.%Cu are compared. The lever rule predicts the fastest evolution of the solid fraction reaching unity when the temperature drops below the solidus (for this specific alloy), while the Scheil-Gulliver predicts the slowest one. The Brody-Fleming model with the Clyne-Kurz correction (in this case with $Fo_s = 0.5$ and thus $f(Fo_s) = 0.248$) gives an intermediate result. Note that when the temperature drops below the eutectic temperature, the solid fraction becomes equal to unity for all the models since the eutectic fills the space of the remaining liquid.

Unfortunately, Brody-Fleming's model does not conserve solute and the Clyne-Kurz correction is only empirical and thus does not solve this problem. Please note that other, more complicated, analytical models can describe more accurately solute diffusion in the solid, by assuming a parabolic profile, as proposed by Ohnaka [27], while an exact solution to Eq. (2.4) has been derived by Kobayashi [28]. Another approach, presented in the following section, is to use a numerical model.

Numerical models

Various numerical approaches have been used to study microsegregation. In this section we review the main assumption of the model developed by Voller and Sundarraaj [29]: a Landau transformation that allows to take into account the motion of the solid-liquid interface. It should be noted that the Landau transformation also allows to take into account the effect of coarsening of the REV size in the case of dendritic microstructures. The diffusion equation in the solid phase in general coordinates is given by:

$$\frac{\partial c_s}{\partial t} = D_s \left(\frac{1}{r^{(P-1)}} \frac{\partial}{\partial r} \left(r^{(P-1)} \frac{\partial c_s}{\partial r} \right) \right) = D_s \left(\frac{\partial^2 c_s}{\partial r^2} + \frac{(P-1)}{r} \frac{\partial c_s}{\partial r} \right) \quad (2.12)$$

where r is the space variable and P the dimensionality of the problem. Eq. (2.12) can be solved by performing a Landau transformation of the domain $[0, r^*(t)]$ into a reference domain $[0, 1]$ such that:

$$c_s(r, t) \rightarrow c_s(\eta, t) \quad \text{with} \quad \eta = \frac{r}{r^*} \quad (2.13)$$

Eq. (2.12) thus becomes:

$$\left(\frac{\partial c_s}{\partial t} \right)_\eta = \frac{D_s}{r^{*2}} \frac{\partial^2 c_s}{\partial \eta^2} + \left(\frac{\eta v^*}{r^*} + \frac{(P-1)D_s}{\eta r^{*2}} \right) \frac{\partial c_s}{\partial \eta} \quad (2.14)$$

where v^* is the velocity of the interface and the term $\frac{\eta v^*}{r^*}$ represents the advection of the mesh. In 1D cartesian coordinates it has the simple following form:

$$\left(\frac{\partial c_s}{\partial t} \right)_\eta = \frac{D_s}{r^{*2}} \frac{\partial^2 c_s}{\partial \eta^2} + \frac{\eta v^*}{r^*} \frac{\partial c_s}{\partial \eta} \quad (2.15)$$

where the $\frac{\partial c_s}{\partial \eta}$ term is only multiplied by the mesh advection term.

As will be seen in Chapter 5 for our granular model, solving Eq. (2.14) with appropriate boundary conditions at $r = 0, r^*$, allows to deduce the solute gradient $dc_s(x^*, t)/dx$ appearing in Eq. (2.4). Knowing $\partial c_\ell/\partial t$ from the imposed cooling rate, the new fraction of solid (and the velocity of the interfaces) can be computed from this equation. The procedure can then be repeated with the new interfacial composition of the solid domain $[0, r^*]$.

2.1.3 Curvature effects

The atoms located near the solid-liquid interface possess an excess free energy, which, after integration over the thickness of the diffuse solid-liquid interface, δ_{sl} , gives the solid-liquid interfacial energy, γ_{sl} (units of Jm^{-2}). This results in a shift of the melting

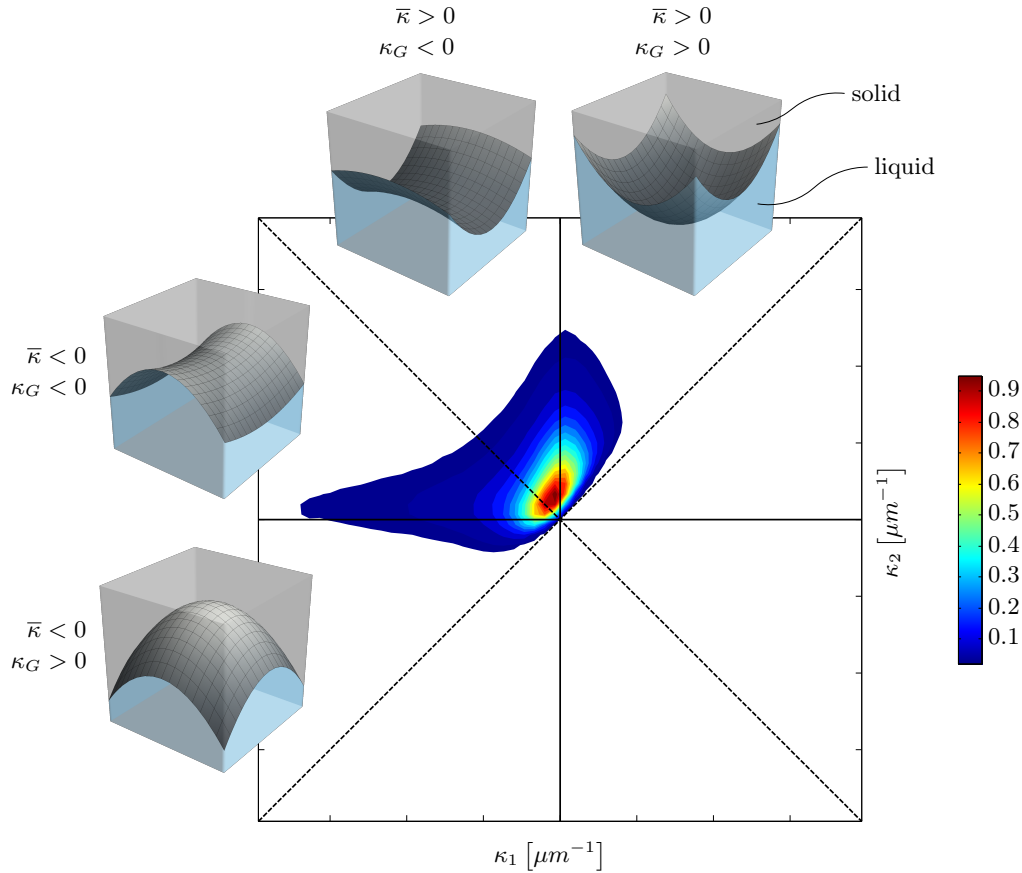


Figure 2.3: Interface shape distribution (or ISD) plot with the constraint that $\kappa_2 \geq \kappa_1$. The color represents the probability of finding a patch of surface with a certain pair of curvatures. The four different regions of the graph correspond to different signs of the mean and Gauss curvature, that are represented in the small cubes [30].

point for a pure system by a curvature undercooling:

$$\Delta T_R = T_m^\infty - T_m^R = 2 \frac{\gamma_{sl}}{\Delta S_f} \bar{\kappa} = 2 \Gamma_{sl} \bar{\kappa} \quad (2.16)$$

where T_m^∞ is the melting point of the pure substance, T_m^R the melting point of the substance for a curved solid/liquid interface of mean curvature $\bar{\kappa}$, and ΔS_f is the volumetric entropy of fusion. The Gibbs-Thompson coefficient, Γ_{sl} , is given by $\gamma_{sl}/\Delta S_f$.

We recall that the mean and Gauss curvatures can be expressed as:

- Mean curvature: $\bar{\kappa} = \frac{1}{2}(\kappa_1 + \kappa_2)$
- Gauss curvature: $\kappa_G = \kappa_1 \kappa_2$

where κ_1 and κ_2 are the principal local curvatures. For a convex solid, the curvature undercooling corresponds to a decrease of the melting point, while for a concave one it corresponds to an increase of the melting point. For a binary alloy, the situation is more complex but for diluted ideal solutions, the curvature contribution can be approximated by a shift of the phase diagram by the quantity ΔT_R . As discussed in section 2.1.1, the compositions at the interface are given by the phase diagram and thus, for a curved interface, they are shifted by an equivalent amount ($\Delta T_R/m_\ell$ and $\Delta T_R/m_s$ for c_ℓ^* and c_s^* , respectively). Please also note that, in general, γ_{sl} is anisotropic and this modifies the expression Eq. (2.16) (Herring's relation [31]). This anisotropy, a few percent for metallic alloys, is important for dendrites but is negligible in our case since we will consider globular-equiaxed microstructures.

In order to better quantify the curvatures, one can compute the interface shape distribution (or ISD) plot [30]. Such graph represents the probability of finding a patch of curvature with a certain pair of principal curvatures. A schematic ISD representation is given in Fig. 2.3, where the different regions corresponding to different values of the mean curvature, $\bar{\kappa}$, and Gauss curvature, κ_G , are illustrated.

2.2 Coalescence

When two solid-liquid interfaces get within interaction distance, a topological change of the local curvature can arise via the formation of a neck. If the two “merging” solids belong to two different grains, i.e., have different crystallographic orientations, two solid-liquid interfaces are replaced by a grain boundary.

Coalescence is defined as the disappearance of a liquid film in between two distinct grains, forming a solid grain boundary (see Fig. 2.4). As the thickness of the liquid film approaches atomic dimensions, the excess free energy deviates from the initial value of $2\gamma_{sl}$. When the liquid has completely disappeared, the excess free energy is equal to the grain boundary energy (denoted by γ_{gb}) [8, 16].

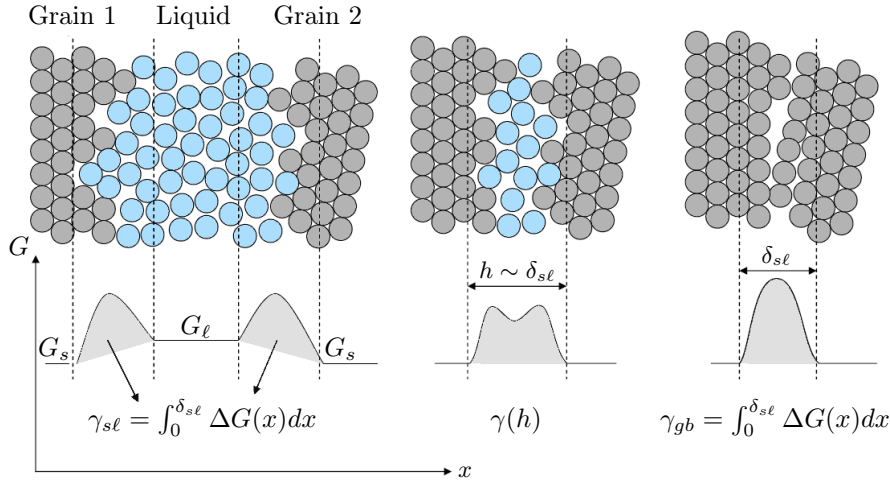


Figure 2.4: Atomistic view of coalescence of two grains of a pure substance with different orientations (upper part) and representation of the Gibbs free energy at a temperature below the melting point (lower part) [16].

As reviewed by Priester [32] and Rohrer [33], finding the grain boundary energy for different configurations is not an easy task. In three dimensions, five parameters should be chosen: three Euler angles describing the relative misorientation of the impinging grains and two director cosines describing the vector normal to the grain boundary plane. However, all the configurations can be simplified by specifying a common direction (2 orientation parameters) and a rotation about that axis ($\Delta\theta$), as well as the vector normal to the grain boundary plane, \mathbf{n} . Special grain boundary plane orientations are referred to as “tilt boundaries” (for \mathbf{n} perpendicular to the axis of misorientation) and “twist boundaries” (for \mathbf{n} parallel to the axis of misorientation). More recently, Bulatov *et al.* [34] derived the grain boundary energy variation in a 5-dimensional space in the particular case of face-centered cubic (FCC) alloys. Their main hypothesis is that, just like the solid-liquid interface energy that can be anisotropic in general, the topography of GB energy function is defined by grooves.

In order to explain how coalescence can be affected by the misorientation between the grains, let us first consider a simple case: a symmetric tilt boundary between two grains. The evolution of the grain boundary energy with respect to the misorientation is represented in Fig. 2.5. For low tilting angles, the grain boundary can be considered as partially coherent with edge dislocations compensating the tilt and the grain boundary energy is well approximated by the Read-Shockley formula [35]. For misorientations greater than approximately 15-20°, the interface is highly disordered and the grain boundary energy is almost constant and equal to γ_{gb}^{max} . The typical values for the maximum grain boundary energy and the solid/liquid interface for aluminum are respectively $\gamma_{gb}^{max} \cong 0.3 \text{ J/m}^2$ and $\gamma_{sl} \cong 0.1 \text{ J/m}^2$ [36].

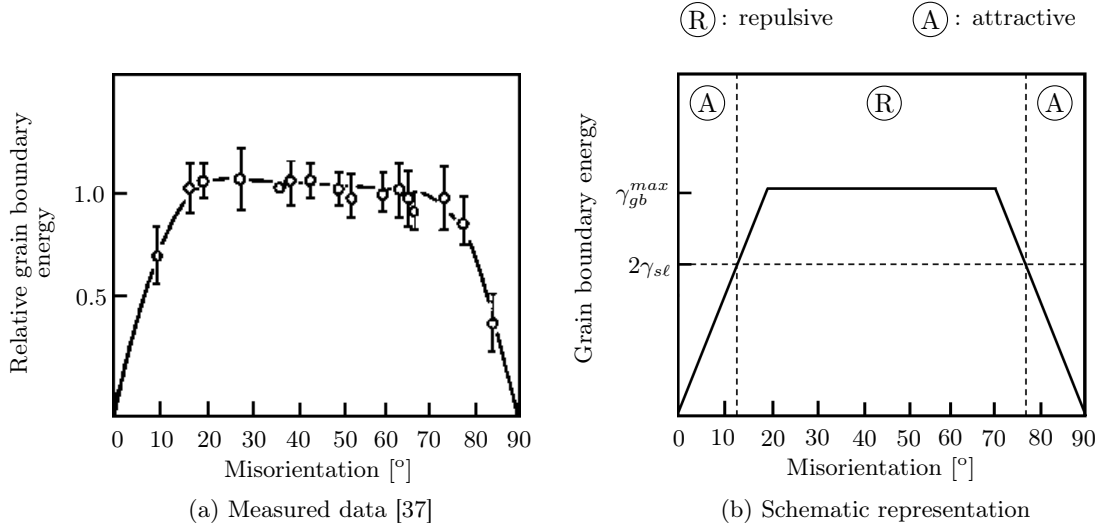


Figure 2.5: (a) Grain boundary energy for a pure symmetric tilt boundary in aluminum when the rotation axis is parallel to $\langle 100 \rangle$, normalized by the maximum grain boundary energy γ_{gb}^{max} . (b) Schematic representation of γ_{gb} with the regions where attractive and repulsive boundaries are found.

As shown in Fig. 2.5(b), for small values of the tilt angle, γ_{gb} is smaller than $2\gamma_{sl}$. This corresponds to an attractive case and no undercooling is required for coalescence [16]. However, for larger misorientations, γ_{gb} is larger than $2\gamma_{sl}$, corresponding to a repulsive grain boundary. Let us first assume that the excess energy, γ has the following dependence with respect to the liquid width h [16]:

$$\gamma(h) = 2\gamma_{sl} + (\gamma_{gb} - 2\gamma_{sl}) \exp\left(-\frac{h}{\delta_{sl}}\right) \quad (2.17)$$

where δ_{sl} is the thickness of an isolated and diffuse solid-liquid interface. According to this approximation, one can compute the excess Gibbs free energy (per unit area) of the situation in which there are two solid-liquid interfaces, coming into close contact:

$$G(h) = \Delta S_f \Delta T h + \gamma(h) = \Delta S_f \Delta T h + 2\gamma_{sl} + (\gamma_{gb} - 2\gamma_{sl}) \exp\left(-\frac{h}{\delta_{sl}}\right) \quad (2.18)$$

In the case of a repulsive interface and a positive undercooling, one can then find the minimum of Eq. (2.18) and thus the dependence between the undercooling, ΔT , and the liquid film width, h , that remains in between. It is then possible to find the bridging undercooling needed for coalescence of two repulsive solid-liquid interface, i.e., when the liquid width becomes nil. It is given by [16]:

$$\Delta T_b = \frac{\gamma_{gb} - 2\gamma_{sl}}{\Delta S_f} \frac{1}{\delta_{sl}} \quad (2.19)$$

Please note the analogy between Eq. (2.16) and Eq. (2.19): the curvature undercooling can be expressed as a different Gibbs-Thompson coefficient multiplied by the curvature, while the coalescence undercooling can be expressed as a differential Gibbs-Thompson factor ($\frac{\gamma_{gb}-2\gamma_{sl}}{\Delta S_f}$) multiplied by the inverse of δ_{sl} . For a binary alloy, the situation is more complex, because the solute element can alter the grain boundary energy but also mainly because coalescence is influenced by the solute composition of the liquid film. The rejection and diffusion of solute in the liquid parallel to the film as well as backdiffusion perpendicular to the impinging interfaces can thus play an important role. Coalescence will occur when the temperature and the concentration of the liquid film reaches a so-called *coalescence line*, which is parallel to the liquidus line, but shifted down by ΔT_b [16,17].

2.3 Percolation

For equiaxed microstructures, percolation is defined as the gradual transition from isolated grains or clusters surrounded by a continuous liquid film to a continuous solid network across a domain. In fact, percolation consists of a succession of several coalescence events. The arrangement and the crystallographic orientations of the grains being random, repulsive and attractive boundaries are also randomly distributed. The closure of liquid films will depend on these orientations, but also on the local size of the grains via back-diffusion. Consequently the remaining liquid films that will have a complex morphology, especially in three dimensions [8,16,17]. In this section we will introduce the basic concepts of percolation theory related to the present project (a more exhaustive review is given in [38]).

The most simple model of percolation considers a square lattice in which each site randomly and independently belongs to one of the two phases (gray or white, solid or liquid). Each site is occupied at random by the gray phase with a probability p , or to the white phase with a probability $(1 - p)$. A group of nearest neighbors that are gray is defined as a cluster. As shown in Fig. 2.6, for small p , isolated clusters appear, but, as p increases, the clusters become larger until the percolation threshold p_c is reached, at which point the gray phase becomes continuous over the whole domain (in the example of Fig. 2.6 the largest cluster percolates through the lattice from left to right when $p \geq 0.59$). For p larger than p_c , the gray phase progressively thickens and occupies more space. It should be noted that p_c is uniquely defined for an infinite lattice but may vary when considering a finite one. In 2D, the percolation threshold (0.59) is larger than 0.5 and thus for a certain range of p no one of the two phases is continuous. In 3D, the percolation threshold for a cubic lattice is 0.31 and thus allows the possibility of having the continuity of both gray and white phases.

One can then introduce some quantities such as the correlation length ξ (that represents the average gyration radius of the clusters) or the average number of sites per cluster S .

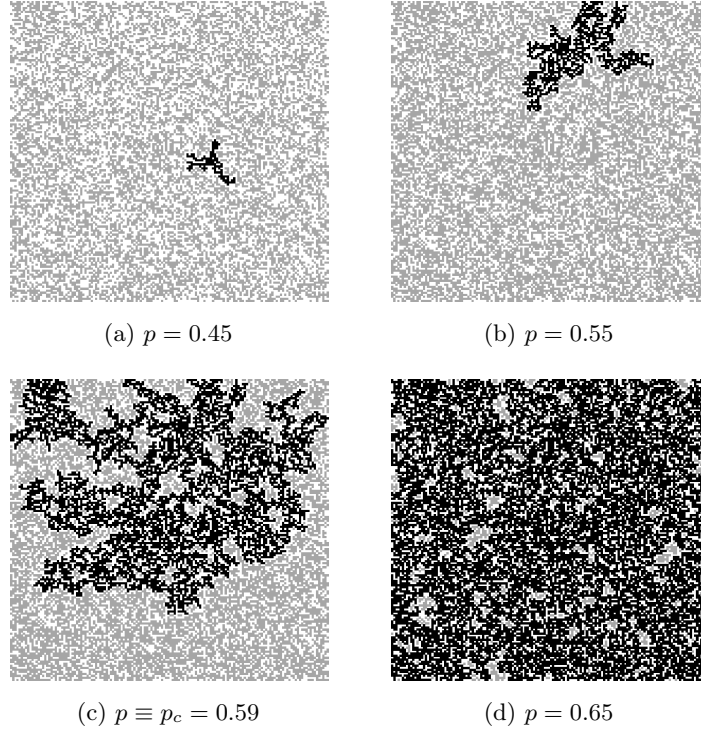


Figure 2.6: Simulation of the percolation of a 2D square lattice (150x150 cells) with increasing probability that the cells are occupied by the gray phase from the left figure to the right figure (the largest cluster is represented in black) [39].

These quantities can be expressed as a function of p in scaling laws [38]:

$$\xi \propto |p - p_c|^{-\nu} \quad (2.20)$$

$$S \propto |p - p_c|^{-\gamma} \quad (2.21)$$

where $\nu, \gamma > 0$ are constants. Eqs. 2.20 and 2.21 show that ξ and S increase with p for $p < p_c$ and diverge at $p = p_c$. Note that for $p > p_c$, the continuous percolated cluster is not included. The surprising result is that the two exponents ν and γ do not depend on the microscopic details of the lattice, but depend only on the dimensionality of the problem. For example, γ is equal to 4/3 in 2D and 0.88 in 3D [1, 38].

Note that the exact definition of the percolation threshold is the probability at which an infinite cluster appears for the first time in an infinite lattice. For example, the scaling law given in Eq. (2.21) is valid when considering an infinite lattice, but for a finite lattice of size L it may not be the case. For $L \gg \xi$, the quantity S does not depend on the lattice size, while for $L \ll \xi$, it does. In order to correctly describe percolation, one should thus choose a representative volume element (RVE) whose dimensions are larger than ξ . However, at the percolation threshold, no RVE can be found as the correlation length become infinite. This is one of the limitations of average methods [1].

For the case $L \ll \xi$, one can perform several (different) simulations for a given L . Each of these simulations will give a slightly different value of the observed percolation threshold $p_{c,L}$. Then, the standard deviation between $p_{c,L}$ and the average observed percolation threshold $\langle p_{c,L} \rangle$ can be expressed as a scaling law [1, 40]:

$$\sqrt{\langle (p_{c,L} - \langle p_{c,L} \rangle)^2 \rangle} \propto L^{-1/\nu} \quad (2.22)$$

The standard deviation thus vanishes as L increases. Furthermore, $\langle p_{c,L} \rangle$ tends to p_c as the number of simulations increases. Therefore, in order to find an accurate value of the percolation threshold, one can either perform a small number of simulation in a large domain or a large number of simulations in a small domain.

In order to describe the evolution of more complex situations, continuous percolation theories can be used. One of those is the “Swiss cheese model” [41] that considers randomly located holes growing in a uniform transport media (see Fig. 2.7). Since it can be based on a Voronoi tessellation of the space, this model is very close to the solidification model of Vernède *et al.* [1] that will be presented in section 2.4.2, with the difference that the holes of the first correspond to the solid grains of the second. In order to be consistent with the other sections of the present paper, the space occupied by the circles will be defined as the solid fraction g_s .

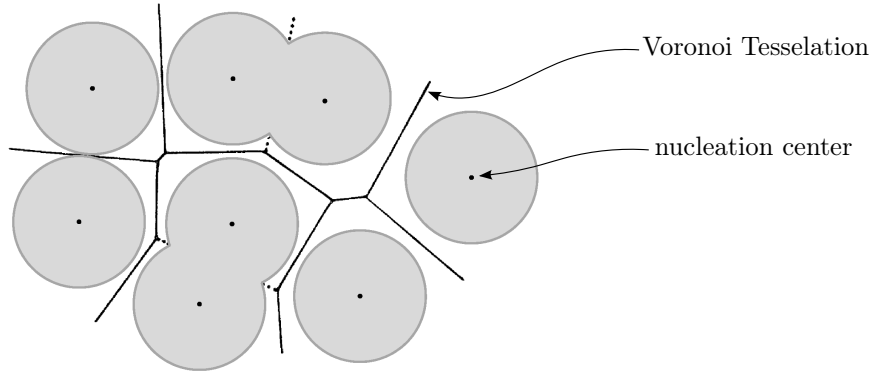


Figure 2.7: Swiss cheese model [41]. The black segments represent the Voronoi tessellation of nucleation centers of the holes (in gray).

An interesting result is that continuum percolation follows the same laws as lattice percolation. In addition, the geometrical percolation properties (such as the value of the exponent ν appearing in Eq. (2.20)) are unchanged with respect to lattice percolation. Provided there is no strong local correlation, the correlation length in the “Swiss cheese model” can thus be expressed as a function of the solid fraction:

$$\xi \propto |g_s - g_{sc}|^{-\nu} \quad (2.23)$$

where g_{sc} is the solid fraction at percolation.

2.4 Hot tearing

Hot tearing, or hot cracking, is a spontaneous failure of an alloy during its solidification that generally presents the shape of a ragged branching crack (see Fig. 2.8). As observed by Campbell [14], hot tears propagate mainly between solid grains (intergranular) and exhibit a fairly smooth surface appearance that existed at the time of fracture (see Fig. 2.8(b)).

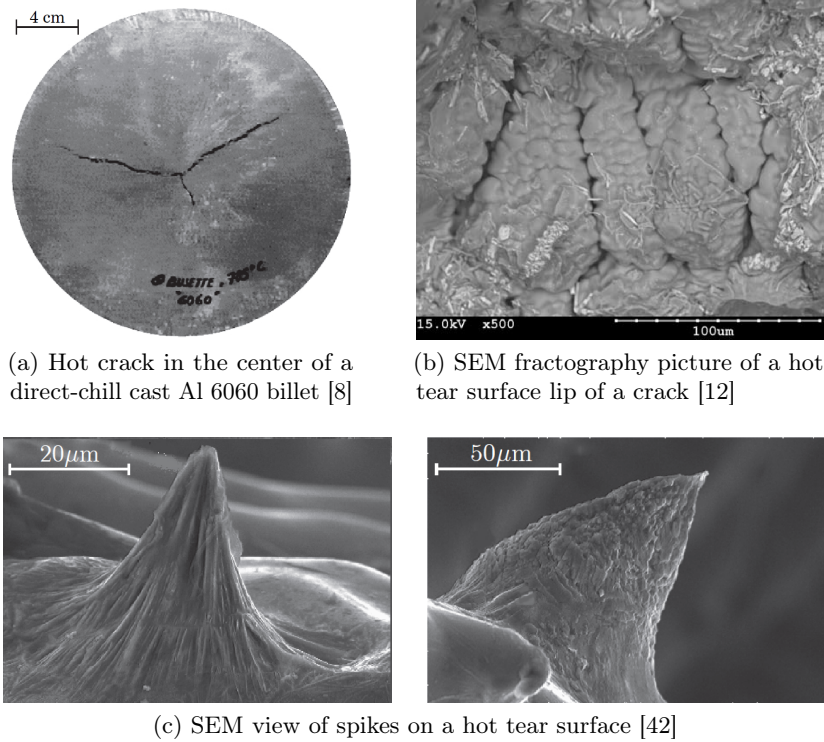


Figure 2.8: Observations of hot tearing formation at different scales.

The two main phenomena leading to hot tearing are: a lack of liquid feeding at high solid fractions and tensile and shear strains in the mushy zone that tend to pull apart the solid network. The strains, transmitted through the partially coherent solid in the mushy zone, are induced by contraction of the solid in a thermal gradient, and mechanical constraints imposed by the geometry of components. At low solid fraction ($g_s < 0.9$), the permeability of the mushy zone is large enough so that liquid feeding can heal possible grain boundary openings, forming a so-called “healed hot tear”. At high solid fraction ($g_s > 0.95$) the grains form a continuous solid network with isolated liquid pockets possessing sufficient mechanical resistance and the mushy material behaves like a ductile solid. However, there is a critical zone for hot tearing (for solid fractions in the range $0.9 < g_s < 0.95$) in which grain boundaries openings, due to the deformation localized in the continuous liquid films, cannot be fed by liquid flow because of the low permeability of the mushy zone [8, 15, 18].

The previous works related to hot tearing can be subdivided into two basic approaches: experimental investigations and hot tearing models. These aspects will be presented in the next sections, by always emphasizing the importance of coalescence and percolation phenomena presented in the previous sections.

2.4.1 Experimental investigations

In order to study hot tearing, different types of experiments can be performed. One of those is the ring mold test (see Fig. 2.9(a)), realized by Farup *et al.* [42], that consists in introducing a liquid alloy in a preheated annular mould and then to cool it down from a central pipe. In this way, important stresses develop in both tangential and longitudinal directions, inducing hot tears.

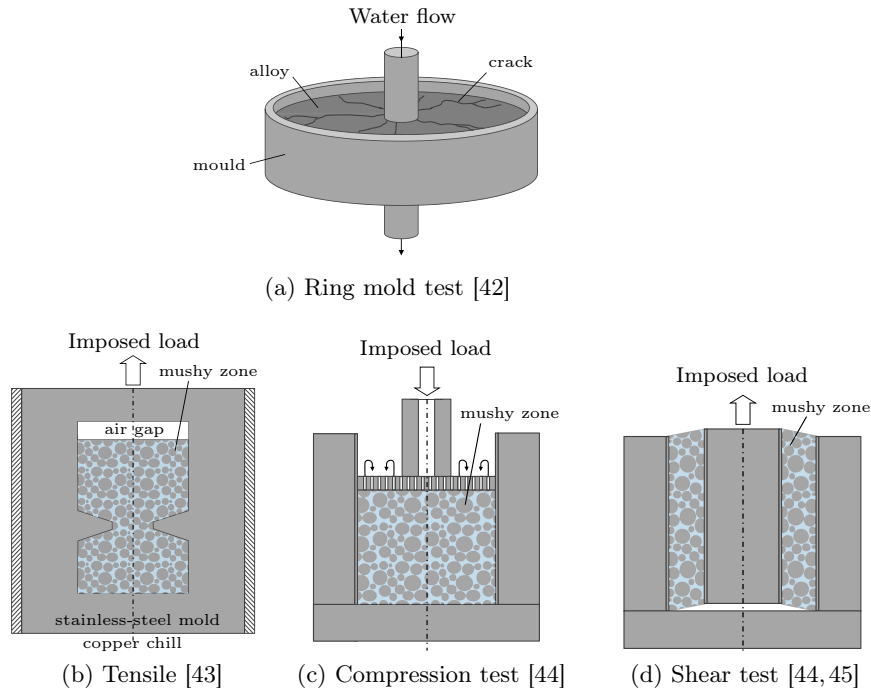


Figure 2.9: Schematic drawings of (a) a ring mould test as well as (b)-(d) some of the common devices used to perform mechanical tests on mushy zones.

Another type of test consists in studying the mechanical properties of a semi-solid alloy. This test can be either performed in tension, compression or shearing and upon solidification or remelting conditions (in Fig. 2.9(b)-(d) a non-exhaustive list of tests is presented). The main difficulty of these experiments is the low ductility and strength of semi-solid alloys [46]. As shown in Fig. 2.10, the tensile tests performed by Mathier *et al.* [43] on Al-Cu alloys have shown that the semi-solid material presents a sharp increase of tensile strength for solid fractions larger than 0.95, solid fraction at which grains coalesce, leading to percolation.

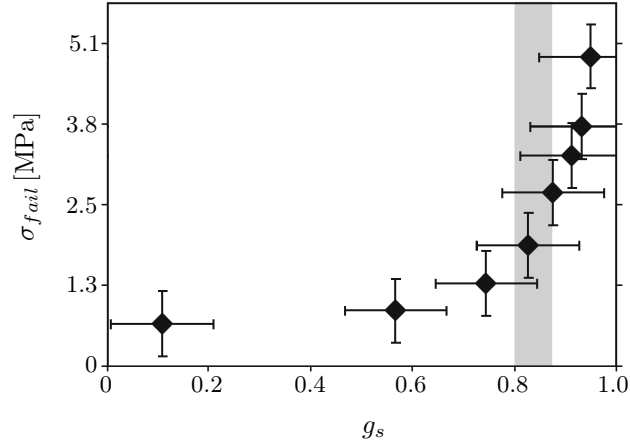


Figure 2.10: Tensile strength of a mushy Al-1.0wt.%Cu alloy as a function of the solid fraction performed with the apparatus shown in Fig. 2.9(b) [43].

In situ optical microscope observations of hot tearing in a transparent succinonitrile-acetone alloy have been performed by Farup *et al.* [42] and Grasso *et al.* [47]. In these experiments, the alloy is directionally solidified and hot tears are induced by pulling apart, transversely to the thermal gradient, the columnar dendrites near a grain boundary. When the dendrites are pulled at low solid fractions ($g_s < 0.9$), the permeability of the mushy zone is large enough so that liquid feeding can heal grain boundary openings, forming a "healed hot tear" (see Fig. 2.11). At higher volume fraction of the solid (typically $g_s > 0.95$), the permeability of the mushy zone is too low to allow feeding. The strain localized at wet grain boundaries (repulsive type) is accommodated in a first step by drainage of the remaining liquid. When this is no longer possible, a void is nucleated

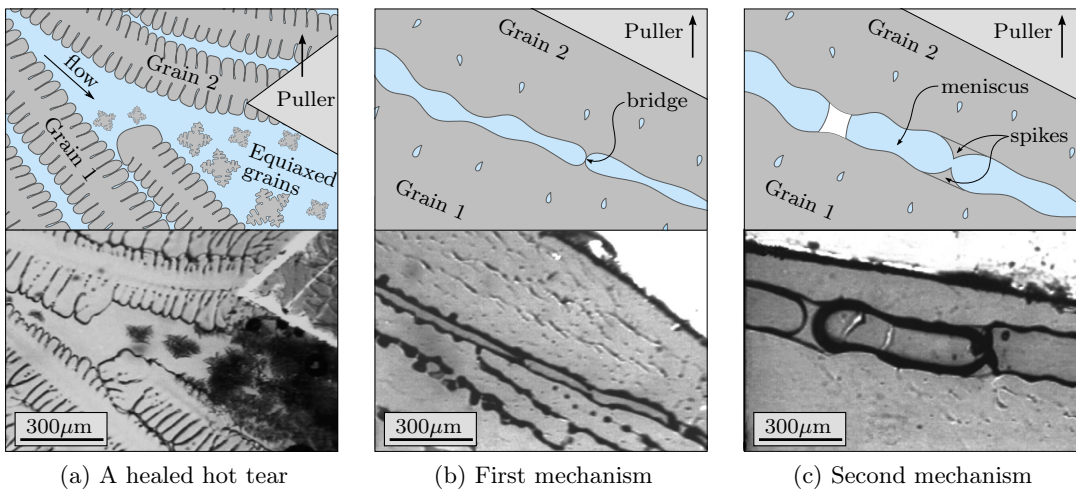


Figure 2.11: Hot tears formation observations in succinonitrile analog made by Farup *et al.* [42].

and grows. While the grain boundary becomes cracked, it leaves the two surfaces of the grains with a fairly smooth aspect where dendrite arms that have not yet bridged. But some spikes have been also observed at the cracked surface (see Fig. 2.8(c)).

The first mechanism of spikes formation results from the plastic deformation and rupture of solidified bridges due to local coalescence between the grains (see Fig. 2.11(b) and right picture of Fig. 2.8(c)). The second mechanism is the formation of liquid menisci, between the two grains resulting from the accumulation of the remaining liquid, that are pulled apart and eventually brake-up at the same time they solidify (see Fig. 2.11(c) and left picture of Fig. 2.8(c)). Hot tear surfaces scanning electron microscope (SEM) observations of an Al-4.5wt%Cu alloy solidified with the apparatus shown in Fig. 2.9(a) revealed the presence of a few spikes at the surface of an otherwise smooth landscape showing secondary dendrite arms (see Fig. 2.8(c)). From observations of a large number of spikes, it seems that the second mechanism is prominent, thus indicating that intergranular coalescence is often not fully reached and that thin liquid films can persist at repulsive grain boundaries even at a last-stage solidification [42, 47].

From such observations, it appears that a better prediction of hot tearing as well as of the mechanical behavior of the mushy zone, requires to account for the mechanisms of coalescence and percolation.

More recently, Terzi *et al.* [48] performed *in situ* X-ray tomography observations during tensile deformation of semi-solid specimens at the European Synchrotron Radiation Facility (ESRF) in Grenoble. The Al-8wt.%Cu cylindrical sample of 8mm length and 2mm diameter was locally notched to reduce the diameter to 1.5mm in order to localize the deformations in the observation region. The specimen was initially heated at 0.5°C/s up to 555°C (induction coil heating) and then held at this temperature. After three minutes, the upper part of the sample was pulled at a velocity of 0.1µm/s with a tensile testing machine, specifically designed to fit in the beamline. As shown in Fig. 2.12, the deformation of the sample induces liquid flow towards the deformed region while the grains deform and rearrange. When drainage of the liquid from the surrounding zones can

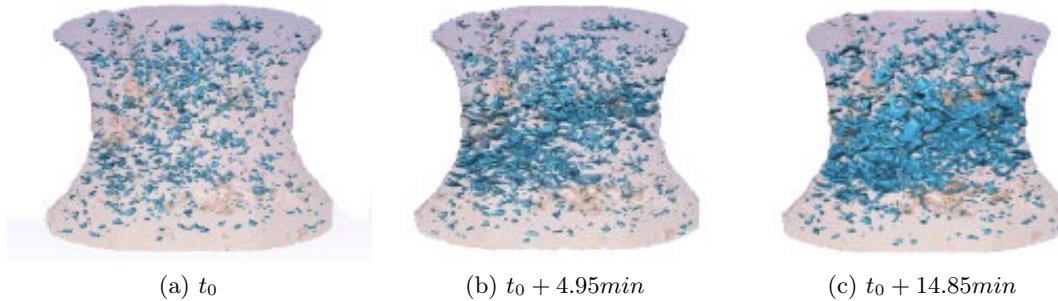


Figure 2.12: Sequence of 3D images of the notched region of an Al-8.0wt.%Cu sample in a tensile test performed at 10^{-4}s^{-1} strain rate by Terzi *et al.* [48]. The blue regions correspond to the voids.

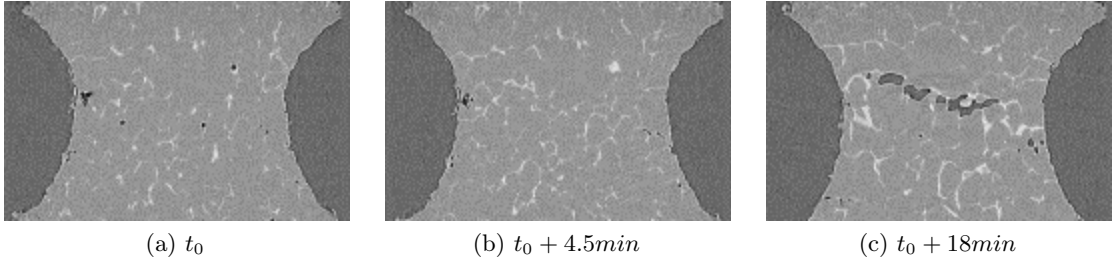


Figure 2.13: Sequence of 2D longitudinal section obtained the 3D tomography stacks shown in Fig. 2.12 [48].

no longer compensate for the local strain, voids grow inward from the external surface within the widest liquid channels.

2.4.2 Hot tearing models

We will now introduce some of the models that were developed in the past for hot tearing (a more exhaustive review may be found in [46]). The most simple models assume that the hot cracking sensitivity (HCS) index of an alloy is proportional to its freezing range (for equilibrium or non-equilibrium conditions depending on the Fourier number) [14]. Since hot tearing occurs in a specific range of solid fractions in the last stages of solidification when liquid films remain at grain boundary and feeding is difficult, Clyne and Davies [49] proposed a simple criterion. This criterion is based on the time spent in this vulnerable state of the mushy zone, normalized by the time during which stress in the mushy zone can be relaxed. Considering the lack of liquid feeding, Feurer *et al.* [50] developed a model for hot tearing predictions. However, this model cannot take into account the effect of the deviatoric strains acting on the mushy zone. More advanced studies led to the so-called Rappaz-Drezet-Gremaud (RDG) criterion [15] which considers the two phase nature of the mushy zone: such criterion takes into account both the pressure drop in the liquid and the strain rate applied to the mushy zone perpendicularly to the thermal gradient. This simple two-phase RDG criterion led other researchers, in particular M’Hamdi *et al.* [51] and Mathier *et al.* [9, 52], to develop average approaches which specifically consider in a general formalism the two-phase nature of the mushy zone. In such models, the microscopic quantities are averaged over a representative volume element (RVE), which must be smaller than the size of the entire system but larger than the microstructural features (such as the grain size). One of the main limitations of average models is their inability to account for the localization of deformation (and feeding) in the liquid films that persist at grain boundaries, and thus they cannot accurately predict the appearance of hot tears.

In order to account for the inhomogeneity of mushy zones and try to describe its mechanical behavior, “granular models” have been proposed. Early granular models considered a

regular hexagonal arrangement of grains [53]. The main drawback of such arrangements is that the solid structure does not become interconnected until $g_s = 1$, solid fraction at which all the solid grains suddenly percolate.

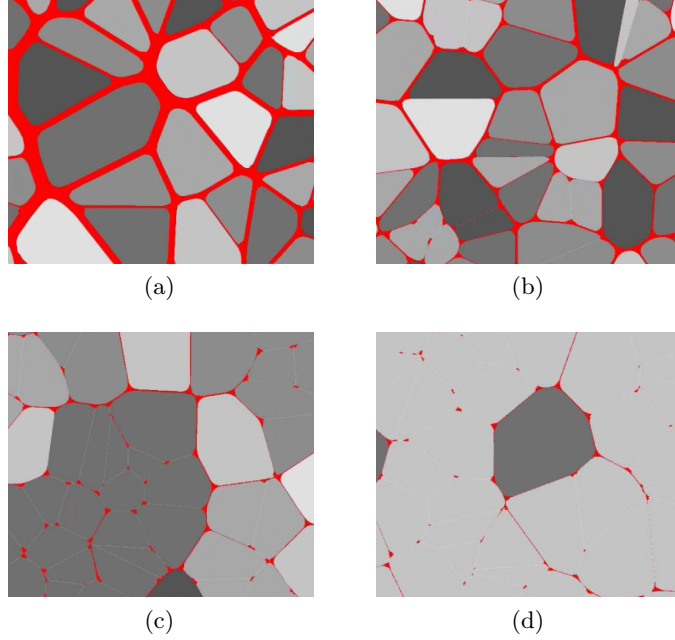


Figure 2.14: Simulations of solidification with a granular model in 2D (the solid fraction increases from left to right). The liquid phase is represented in red, while the grains with the same gray level belong to the same cluster ((d) represents a fully percolated network) [17].

A more realistic model, based on the prior work of Mathier *et al.* [36], was developed by Vernède *et al.* [17, 40, 54] and considers a 2D arrangement of polygonal equiaxed grains derived from a Voronoi tessellation associated with randomly distributed nucleation centers. The model computes the solidification in each polygon taking into account solute backdiffusion and coalescence. Then, the fluid flow in the network of liquid channels, caused by solidification shrinkage and grain movement, is computed assuming a Poiseuille flow, while the grains are considered to be perfectly rigid bodies. The solidification model was further improved by smoothing the shape of polygonal grains based on the Gibbs-Thomson effect as represented in Fig. 2.14. This leads to predictions that are close to phase-field models results [11].

The fact that the granular model of Vernède *et al.* assumes a 2D configuration introduces some inaccuracies. First, the fluid flow in a network of liquid channels as well as the semi-solid deformation are intrinsically 3D problems. Second, as explained in section 2.3, 3D geometry allows to have both continuous solid and liquid networks at the same time, while in 2D only one phase can be percolated through the domain at a given time. Furthermore, deformation of the solid grains should be part of the model. Recently,

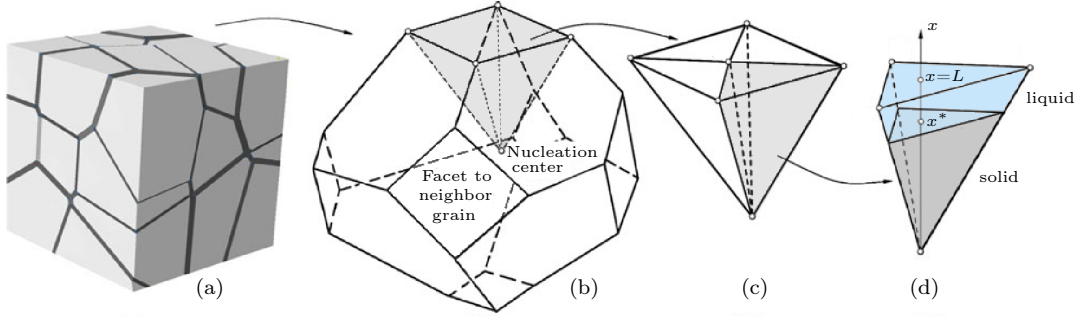


Figure 2.15: Detailed description of the 3D granular solidification model of Sistaninia *et al.* [18, 19, 55]: (a) calculation domain made of polyhedral grains, (b) a polyhedral grain, (c) a pentahedral volume element of a grain, (d) a single tetrahedral element in which both the solid portion (gray) and liquid portion (light blue) are represented.

Sistaninia *et al.* [18, 19, 55] extended the granular model of Vernède *et al.* to 3D and removed the assumption of rigid grains.

This 3D model consists of four modules: a solidification model based on the work of Phillon *et al.* [3] (schematized in Fig. 2.15), a fluid flow model consisting of an extension of the 2D model developed by Vernède [19], a semi-solid deformation model based on a combined Finite Element/Discrete Element Method [18], and the coupling of the fluid flow and the semi-solid deformation models. Please note that the 3D solidification module considers the smoothing of the shape of the grains, but only with an analytical correction of the solute flux similar to the work done by Vernède *et al.* [17, 40, 54]. The smoothing operation is much more complex in 3D than in 2D in particular because the grains are slightly curved along the edges (cylindrical type of curvature) and highly curved near the corners (spherical type of curvature). The 3D granular solidification model has thus to be improved by comparison with more refined methods such as phase-field.

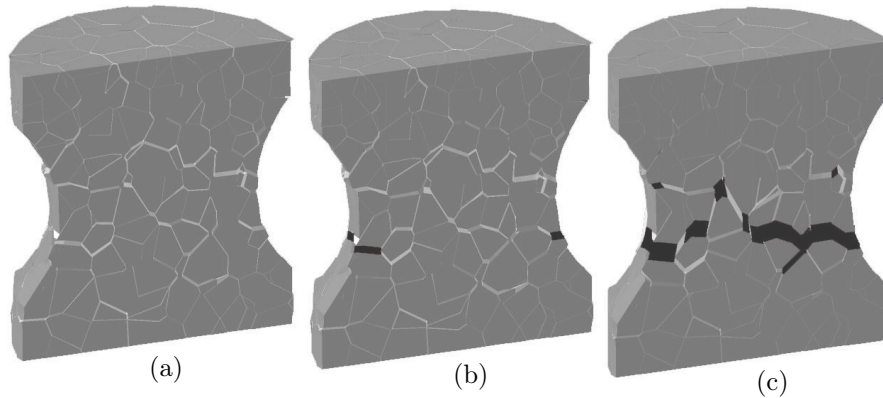


Figure 2.16: Simulation performed by Sistaninia *et al.* of the *in situ* experiment performed by Terzi *et al.* [48] (see Fig. 2.12). Remaining liquid in white, grains are gray and cracks are black.

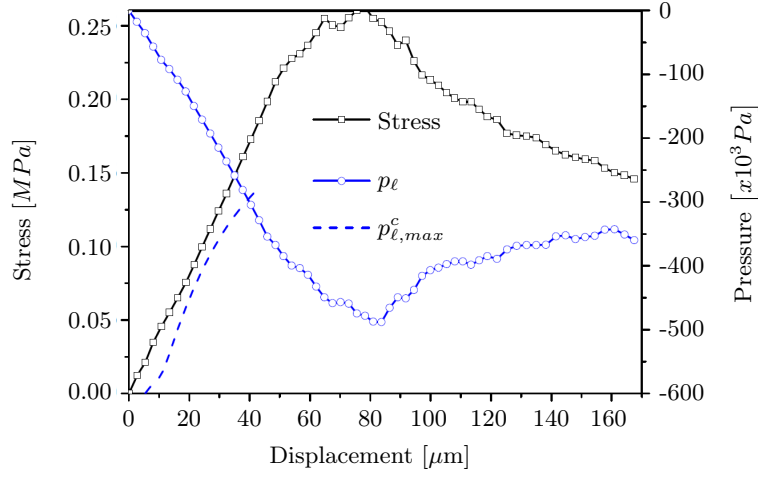


Figure 2.17: Stress as function of displacement (black curve) in a tensile test simulated by the 3D granular model of Sistaninia *et al.* [2] shown in Fig. 2.16. The pressure in the liquid, p_ℓ , as well as the cavitation pressure, $p_{\ell,max}^c$, are also plotted (blue curves).

As shown in Fig. 2.16, the experiment performed by Terzi *et al.* [48] (see section 2.4.1) was simulated with the 3D granular model. Fig. 2.17 shows the simulated behaviour of the semi-solid material subjected to a tensile strain (the same as in the experiment). The stress increases with increased displacement (and thus increased strain) and reaches a maximum value, σ_{fail} , after about $70\mu\text{m}$ displacement before overall failure occurs. In the same graph, the liquid pressure is shown to decrease while the imposed stress increases. The dashed curve corresponds to the capillary pressure, $p_{\ell,max}^c$, associated with the air-liquid meniscus in the largest channel connected to the ambient air. As can be seen, crack initiation occurs when these two curves cross, prior to attaining the value σ_{fail} . However, only when σ_{fail} is reached, the crack propagation is sufficient to relax

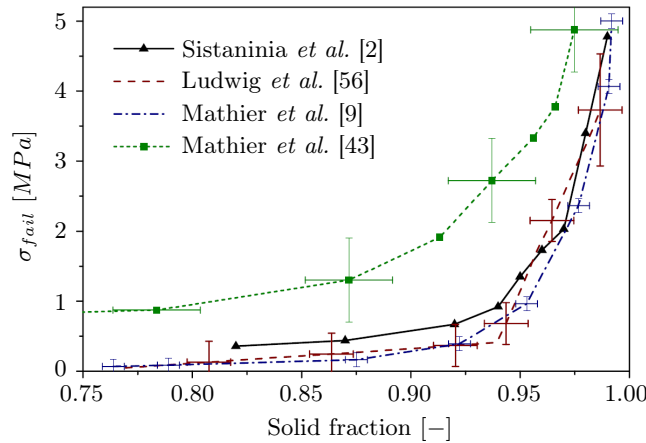


Figure 2.18: Tensile strength as a function of the solid fraction curve simulated by the 3D granular model of Sistaninia *et al.* [2] and comparison with experimental results [9, 43, 56].

2.5. Thermal conditions for globular-equiaxed grain

the pressure drop.

Several simulations of tensile tests were performed by Sistaninia *et al.* on cubic domains containing approximately 1000 grains at different solid fractions. The tensile strength, σ_{fail} , was then plotted as a function of the solid fraction and compared with experimental results of Ludwig *et al.* [56] and Mathier *et al.* [9, 43] (see Fig. 2.18). Except for the result of Mathier *et al.* [43], for which the compliance of the test device (Fig. 2.9(b)) might play a role, all the curves are well superimposed and exhibit a sharp increase of σ_{fail} at a solid fraction of approximately 0.95.

As a general conclusion, simulation of hot tearing and of the deformation behavior of the mushy zone is not an easy task, since it involves interdependent phenomena occurring at very different length scales, as shown in Fig. 2.8. It appears that granular models are required to account for the intergranular nature of hot tearing and for localization of strains and feeding at grain boundaries.

2.5 Thermal conditions for globular-equiaxed grain

The hot tearing model of Vernède *et al.* [17, 40, 54] and Sistaninia *et al.* [18, 19, 55], as well as the present percolation study focus on globular-equiaxed grains. The present section describes the conditions under which such microstructures are obtained under fixed thermal gradient and cooling rate (Bridgman conditions). The first aspect that has to be considered is the columnar-to-equiaxed transition (or CET). The second aspect is linked to the fact that the growth of a spherical particle in a undercooled melt is unstable with respect to morphological perturbations thus leading to equiaxed dendrites.

Note that the physical values used in this section are summarized in Tab. 2.1. In addition, in this section, we assume that we know a priori the final grain size d_{g0} and thus the nucleation site density n_g , but, as will be seen in section 2.6, it can depend on the cooling conditions, namely the cooling rate, and inoculation conditions. We recall the following relationship between the nucleation site density and the grain radius/diameter:

$$n_g \frac{4}{3} \pi R_{g0}^3 = n_g \frac{\pi}{6} d_{g0}^3 = 1 \quad (2.24)$$

Table 2.1: Summary of the physical values used for the calculation. L_f is the latent heat of fusion and c_p the specific heat per unit volume.

Parameter/constant	value
D_ℓ	$3.0 \cdot 10^{-9} \text{m/s}$
Γ_{sl}	$1.0 \cdot 10^{-7} \text{Km}$
L_f	$1.0 \cdot 10^9 \text{J/m}^3$
c_p	$2.4 \cdot 10^6 \text{J}/(\text{m}^3 \text{K})$

2.5.1 Columnar-to-equiaxed transition

It is well known that equiaxed grains can be obtained under isothermal conditions, but it is also possible to obtain them in a thermal gradient, provided in general the alloy is inoculated (see section 2.6). The CET can be described with the help of Hunt's criterion [57]. Please note that another criterion derived by Rappaz *et al.* [58], describing the shape of equiaxed eutectics grains growing in a thermal gradient, is also able to predict the CET.

Hunt's criterion is based on the fact that, ahead of a columnar front, an undercooled melt is present in which equiaxed grains can nucleate and grow. When the fraction of equiaxed grains in front of the columnar front is sufficient to block the advance of the columnar front, the CET occurs.

The velocity of the isotherms v_T , assumed to be equal to the velocity of the columnar front, can be related to the dendrite tip undercooling, ΔT_{col} , by the simple law (parabolic dendrite tip):

$$v_T = \frac{A'}{c_0} \Delta T_{col}^2 \quad (2.25)$$

where A' is a constant and c_0 is the nominal composition of the alloy [57]. The growth velocity of the envelope of the equiaxed grains, v_g , is given by that of the dendrite tips and assumed to follow the same law:

$$v_g(\Delta T) = \frac{A'}{c_0} \Delta T^2 \quad (2.26)$$

where ΔT is the local undercooling. In addition, it is assumed that the grains nucleate at a fixed undercooling ΔT_n , with a density n_g and that they do not move (as will be seen in section 2.7 this is not always the case).

The radius of an equiaxed grain, R_g , can thus be expressed as:

$$\begin{aligned} R_g(t_n, t_{col}) &= \int_{t_n}^{t_{col}} v_g(t) dt = \frac{A'}{c_0(Gv_T)} \int_{\Delta T_n}^{\Delta T_{col}} \Delta T^2 d(\Delta T) \\ &= \frac{A'}{3c_0(Gv_T)} (\Delta T_{col}^3 - \Delta T_n^3) \end{aligned} \quad (2.27)$$

where t_n is the time at which grains nucleate, t_{col} the time at which the columnar front arrives, and G is the thermal gradient.

The extended volume fraction of grains, g_{ge} , is defined as the volume that would be occupied by the grains if there were no impingement between each other. At the position of the columnar front, it can be expressed as $g_{ge} = n_g 4/3\pi R_g^3(t_n, t_{col})$. The link between g_{ge} and the volume fraction of grains with consideration of their impingement is given by: $g_g = 1 - \exp(-g_{ge})$.

As assumed by Hunt, a fully equiaxed microstructure is considered to occur when

2.5. Thermal conditions for globular-equiaxed grain

$g_{ge} > 0.66$ and thus when:

$$G > \left(\frac{4\pi n_g}{0.66 \cdot 81} \right)^{1/3} \frac{A'}{c_0 v_T} \left(\left(\frac{c_0}{A'} v_T \right)^{3/2} - \Delta T_n^3 \right) \quad (2.28)$$

while a columnar microstructure is expected when $g_{ge} < 0.0066$ and thus when:

$$G < \left(\frac{4\pi n_g}{0.0066 \cdot 81} \right)^{1/3} \frac{A'}{c_0 v_T} \left(\left(\frac{c_0}{A'} v_T \right)^{3/2} - \Delta T_n^3 \right) \quad (2.29)$$

Hunt's criterion (taking into account Eq. (2.28) and Eq. (2.29)) is shown in Fig. 2.19 for an Al-4.5wt.%Cu: it shows that an equiaxed microstructure is favoured by a low G and high v_T .

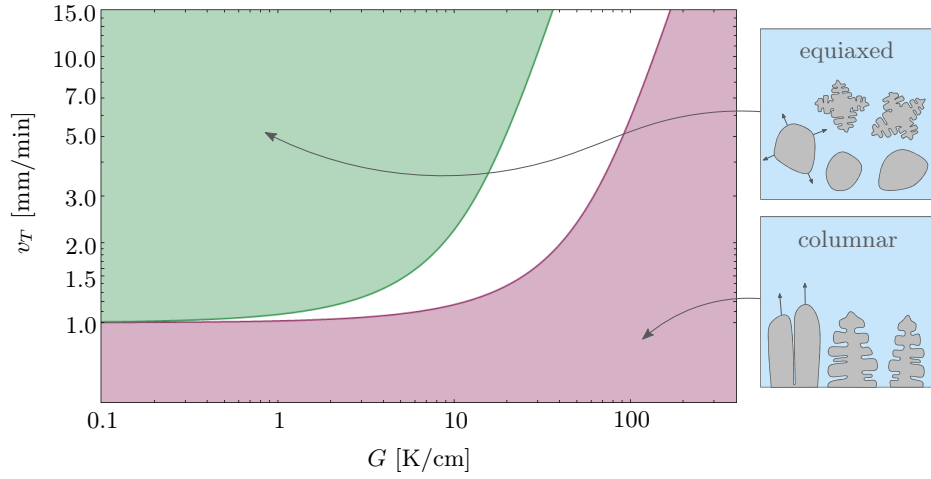


Figure 2.19: Graphical map of the CET in terms of v_T as a function of G for an Al-4.5wt.%Cu alloy with $n_g = 3.0 \cdot 10^{10} \text{m}^{-3}$, $\Delta T_n = 0.5 \text{K}$ and $A' = 3 \cdot 10^{-6} \text{ms}^{-1} \text{K}^{-2}$ (green: equiaxed, red: columnar). The other parameters are given in Tab. 2.1.

2.5.2 Globular-to-dendritic transition

The globular-to-dendritic transition (abbreviated GDT) is a consequence of the fact that the spherical growth of a grain in an undercooled melt is unstable with respect to morphological perturbations. According to the analysis of Mullins and Sekerka [59], a spherical grain becomes unstable when its radius exceeds a critical value given by [8]:

$$\left(\frac{(m+1)(m+2)}{2} + 1 \right) R_c \quad (2.30)$$

where $R_c = 2\Gamma_{sl}/\Delta T_R$ is the critical radius of nucleation and m is the disturbance mode. For a FCC crystal structure, such as Al, the 4-fold symmetry instability is given by $m = 4$: the grain becomes unstable when R_g is larger than $16R_c$.

By assuming that the solute layer around the spherical grain is much smaller than the final grain size and that it can be approximated as being piece-wise linear (Zener approximation), one can obtain the critical final grain radius $R_{g0,c}$ characteristic of the GTD transition as a function of the principal solidification parameters:

$$R_{g0,c} = \left(-96 \frac{D_\ell \Gamma_{sl}}{k_0 \Delta T_0} \frac{L_f}{c_p} \frac{1}{\dot{T}} \right)^{\frac{1}{3}} \quad (2.31)$$

where L_f is the latent heat of fusion and c_p the specific heat per unit volume. A globular microstructure will be obtained if $R_{g0} < R_{g0,c}$, otherwise a dendritic microstructure is expected. Alternatively, one can express Eq. (2.31) in terms of a critical cooling rate:

$$|\dot{T}_c| = 96 \frac{D_\ell \Gamma_{sl}}{k_0 \Delta T_0} \frac{L_f}{c_p} \frac{4}{3} \pi n_g \quad (2.32)$$

Since $|\dot{T}| = |Gv_T|$, the GDT is represented by a line with a negative slope in the log-log map of v_T as a function of G in Fig. 2.20. As shown in Fig. 2.20, grains with a fixed density n_g remain globular if $|\dot{T}| < |\dot{T}_c|$.

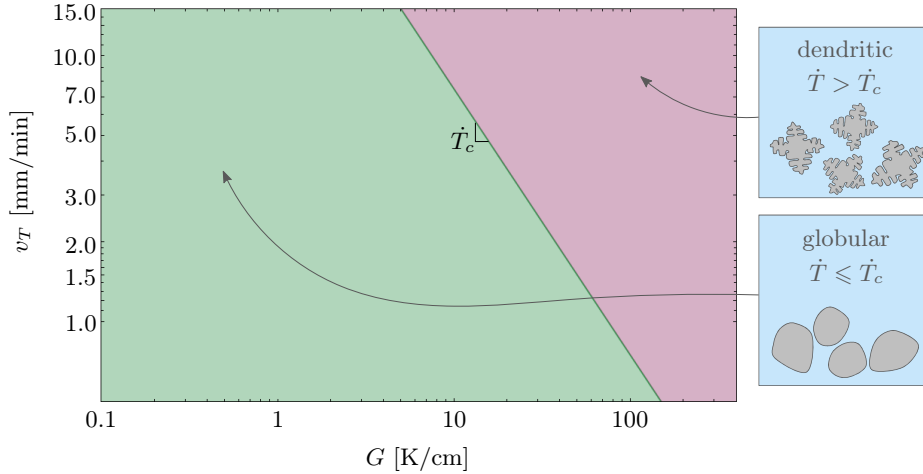


Figure 2.20: Graphical map of the GDT in terms of v_T as a function of G for an Al-4.5wt.%Cu alloy with $n_g = 3.0 \cdot 10^{10} \text{m}^{-3}$ (green: globular, red: dendritic). The other parameters are given in Tab. 2.1.

2.5.3 Globular-equiaxed conditions

The two criteria for the CET and GDT can be combined in a unique graph (Fig. 2.21), which reveals that globular-equiaxed grains form for low G and intermediate v_T .

In order to optimize the choice of G and v_T , one can plot the maximum admissible gradient (points in orange in Fig. 2.22) for different values of n_g that still result in a globular-equiaxed microstructure. For example, for a thermal gradient of $G = 10 \text{K/cm}$,

2.5. Thermal conditions for globular-equiaxed grain

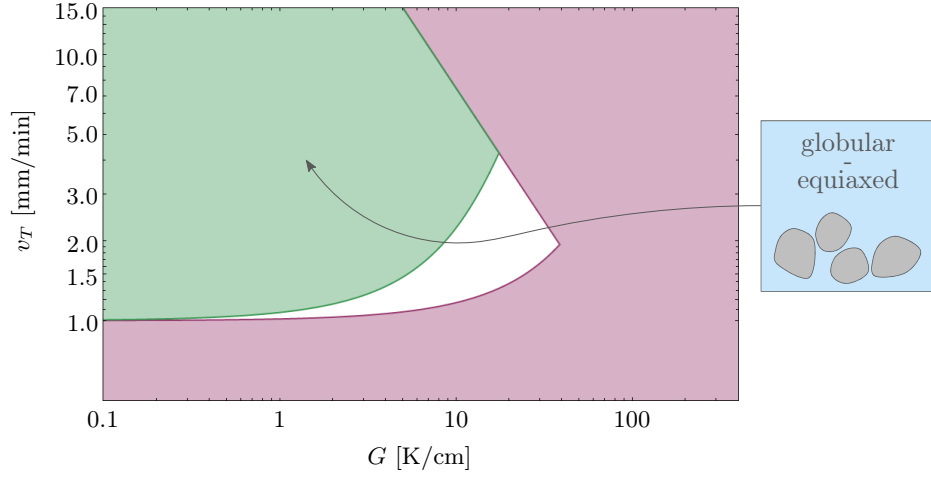


Figure 2.21: Graphical map of the grain structure formation in terms of v_T as a function of G for an Al-4.5wt.%Cu alloy with $n_g = 3.0 \cdot 10^{10} \text{m}^{-3}$, $\Delta T_n = 0.5 \text{K}$ and $A' = 3 \cdot 10^{-6} \text{ms}^{-1} \text{K}^{-2}$. The other parameters are given in Tab. 2.1. Globular-equiaxed grains form in the green region.

the optimal speed of the isotherms for an Al-4.5wt.%Cu alloy is on the order of 3 mm/min. One can also evaluate the conditions under which a globular-equiaxed microstructure is obtained for different alloy nominal compositions c_0 (see Fig. 2.23). The interesting result is that the the maximum admissible gradient leading to a globular-equiaxed microstructure does not vary with the nominal composition.

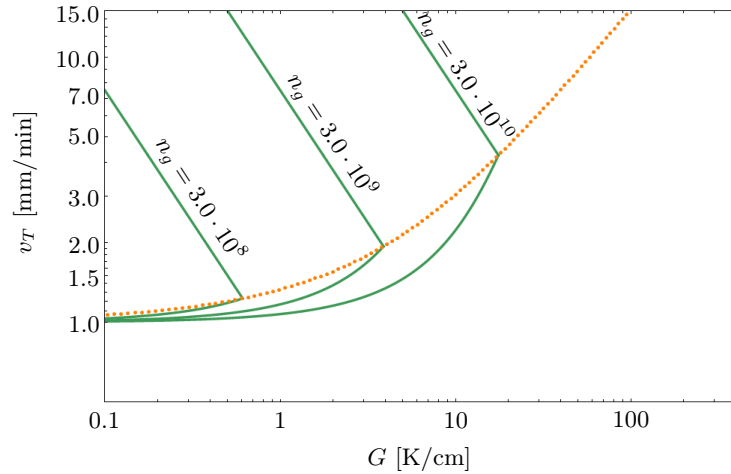


Figure 2.22: Graphical representation of the (G, v_T) conditions under which globular-equiaxed grains form for an Al-4.5wt.%Cu alloy, with different values of the grain density n_g (values given in m^{-3}).

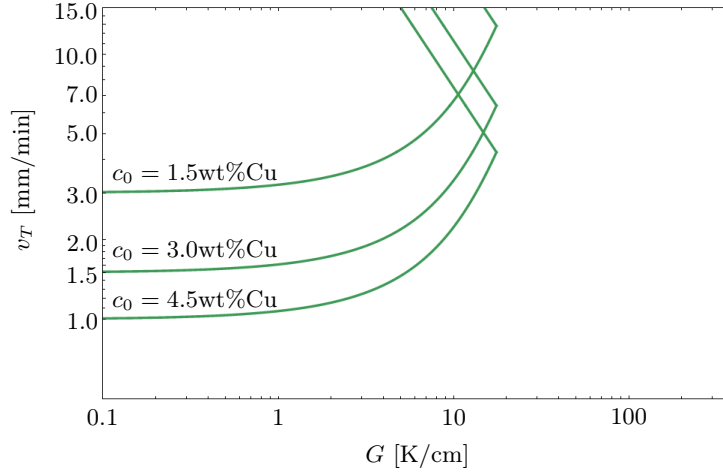


Figure 2.23: Graphical representation of the (G, v_T) conditions under which globular-equiaxed grains form for Al-Cu alloys of various composition c_0 , with $n_g = 3.0 \cdot 10^{10} \text{ m}^{-3}$.

This analysis is clearly limited by the assumptions used in the calculations of the CET and GDT. However, they give a first indication of the order of magnitude of the thermal gradient and velocity of the isotherms that lead to the desired microstructure.

2.6 Nucleation and grain refinement

In this section we will see how solid grains nucleate from the liquid (in most cases with the help of foreign particles) and how it is possible to decrease the final grain size of the microstructure by grain refining (or inoculating) the alloy.

2.6.1 Homogeneous nucleation

When the temperature of a pure material falls under its melting point, T_m , the material is expected to solidify since there is a driving force due to the difference between the Gibbs free energies of the solid and liquid phases. For small undercoolings, $\Delta T = T_m - T$, the driving force can be approximated as $\Delta S_f \Delta T$. However, from an energetic point of view, there is also a price to pay for the formation of the solid/liquid interface, corresponding to the interfacial energy, γ_{sl} . By assuming that the solid cluster that forms in the liquid has the shape of a sphere of radius R , the difference in Gibbs free energy between a system containing a cluster and a fully liquid system is:

$$\Delta G = -\Delta S_f \Delta T \frac{4}{3} \pi R^3 + \gamma_{sl} 4 \pi R^2 \quad (2.33)$$

One can then find the critical radius, R_c , at which the solid cluster radius begin to be stable, since an increase of dR would lead to a decrease of $d(\Delta G)$:

$$R_c = \frac{2\Gamma_{s\ell}}{\Delta T_n} \quad (2.34)$$

where ΔT_n is the nucleation undercooling. The homogeneous nucleation barrier, ΔG_n^{homo} , defined as ΔG for a critical radius, is then:

$$\Delta G_n^{homo} = \Delta G(R_c) = \frac{16\pi}{3} \frac{\gamma_{s\ell}^3}{(\Delta S_f \Delta T)^2} \quad (2.35)$$

2.6.2 Heterogeneous nucleation

Homogeneous nucleation is very rare in practice, since there are very often heterogeneous nucleation sites in the melt that can lower the nucleation barrier and significantly lower the nucleation undercooling, as observed by Turnbull [60].

Instead of growing as a sphere, we assume that the solid forms a spherical cap on a foreign substrate, as represented in Fig. 2.24. γ_{fs} and $\gamma_{f\ell}$ are the foreign/solid and foreign/liquid interfacial energies respectively. These quantities are linked with $\gamma_{s\ell}$ by the Young-Laplace's equation:

$$\gamma_{f\ell} = \gamma_{fs} + \gamma_{s\ell} \cos \theta \quad (2.36)$$

By doing the same analysis than in section 2.6.1, one can find that the critical radius remains unchanged with respect to homogeneous nucleation. However, the energy barrier of heterogeneous nucleation, ΔG_n^{hetero} , is smaller than ΔG_n^{homo} by a factor $f(\theta)$:

$$\Delta G_n^{hetero} = \Delta G_n^{homo} f(\theta) \quad \text{with} \quad f(\theta) = \frac{(2 + \cos \theta)(1 - \cos \theta)^2}{4} \leq 1 \quad (2.37)$$

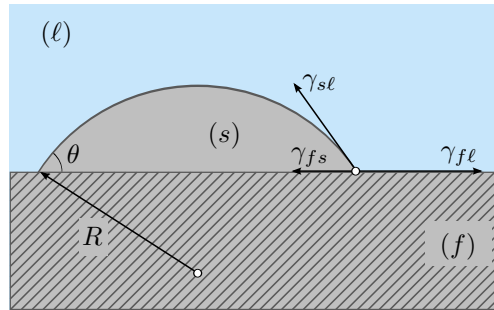


Figure 2.24: Nucleation of a spherical cap on a substrate.

2.6.3 Athermal nucleation and grain refinement

Heterogeneous nucleation can explain that in practice the nucleation undercoolings are much smaller than predicted by homogeneous nucleation. However, a more detailed analysis can show that, based on thermally activated processes, both models predict that the final grain density is independent of the cooling conditions, while in reality it is well known that the grain density strongly increases with the cooling rate. Therefore, it is better to treat heterogeneous nucleation as an athermal process in which the grain density depends on undercooling, but not on time. This is referred to as athermal nucleation, since it does not consider the thermal activation of atoms over an energy barrier.

When $\gamma_{f\ell} > \gamma_{fs} + \gamma_{sl}$, there is no value of θ that satisfies Young-Laplace's equation (see Eq. (2.36)) and it is always favourable for the system to have a solid layer that separates the foreign substrate from the liquid, even at negative undercoolings. It is possible to show that the thickness of the solid increases until $\Delta T = 0$ where the thickness is undetermined but would in fact be limited by growth [8]. If the substrate has a limited size, by decreasing the temperature, the solid becomes more and more curved in order to accommodate the curvature undercooling (see Eq. (2.16)). As shown in Fig. 2.24(a), this happens until its radius of curvature, R , is half the diameter of the disk, d_f (assuming that the substrate has a circular disk shape). Beyond that point, grain growth leads to a

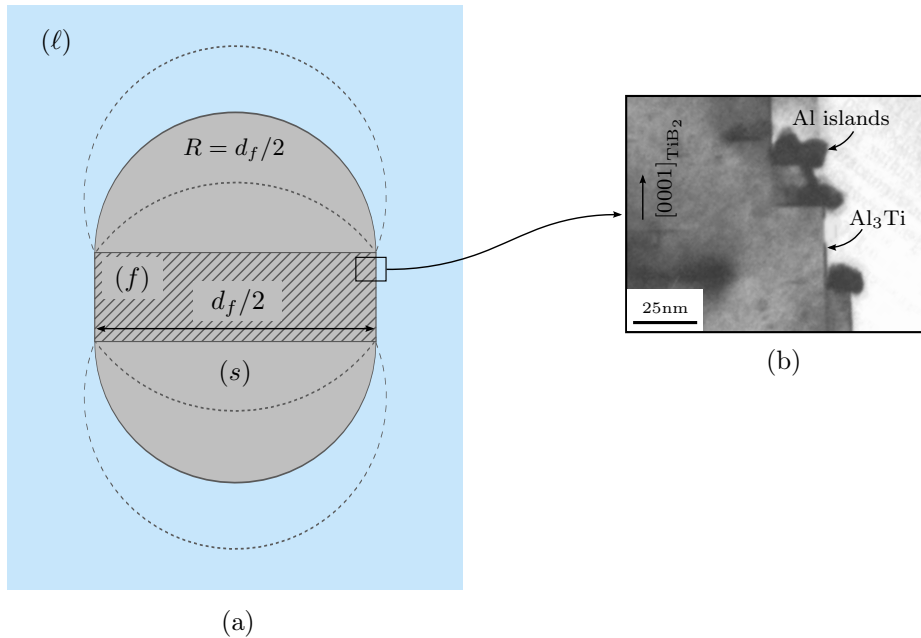


Figure 2.25: (a) Nucleation of a spherical cap on a foreign substrate. (b) Electron micrograph of Al₃Ti layer grown epitaxially on a TiB₂ particle over which small Al island nucleated [61].

decrease of the curvature of the grain. The critical undercooling is thus given by [62]:

$$\Delta T_n = \frac{2\Gamma_{sl}}{\frac{d_f}{2}} = \frac{4\Gamma_{sl}}{d_f} \quad (2.38)$$

Unlike homogeneous and standard heterogeneous nucleation theories, growth of the grain in this case is only determined by the temperature and the geometry of the substrate, and thus nucleation is not a thermally activated process.

Such a nucleation mechanism was evidenced by Greer *et al.* [64] in the solidification of Al alloys inoculated by TiB_2 particles. These authors showed that Al does not form directly on the surface of the TiB_2 particles: initially, a thin layer of Al_3Ti first grows epitaxially from the basal plane of the TiB_2 particles. After that, many islands of Al form on this layer and merge as they grow. This explains why an excess of Ti is necessary to correctly inoculate the alloy, since an AlTi_3 layer has to form first around the TiB_2 particles (see Fig. 2.24(b)). In industry, it is common to add between 1kg/ton and 10kg/ton of a master alloy (Al-5wt%Ti-1wt%B) in order to inoculate or grain refine the alloy [64].

An interesting result is also that only a very small portion of the size distribution of TiB_2 particles acts effectively as nucleation substrates. The largest ones, possessing the lowest athermal nucleation undercooling (see Eq. (2.38)), are the first to be activated while smaller ones get incorporated by grain growth. In order to reach higher undercoolings and thus activate more particles, the growth rate of the grains, and the subsequent entrapment of other nucleation sites, should be limited as much as possible. As seen in the CET section, growth of the grains is limited by the diffusion of solute species in the liquid. It is recalled that the growth constant A'/c_0 appearing in Eq. (2.26) is proportional to the

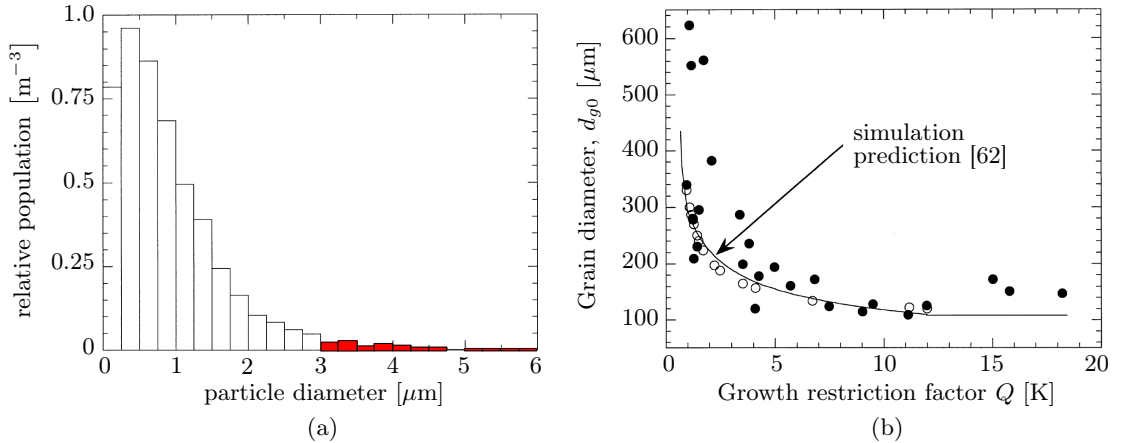


Figure 2.26: (a) Size distribution of TiB_2 particles (the red rectangles correspond to the activated classes) [62]. (b) Final grain diameter as a function of the growth restriction factor for an alloy with the addition of 2kg/ton Al-5Ti-B refiner (black points: experimental data [63] and white points: simulated data [62])

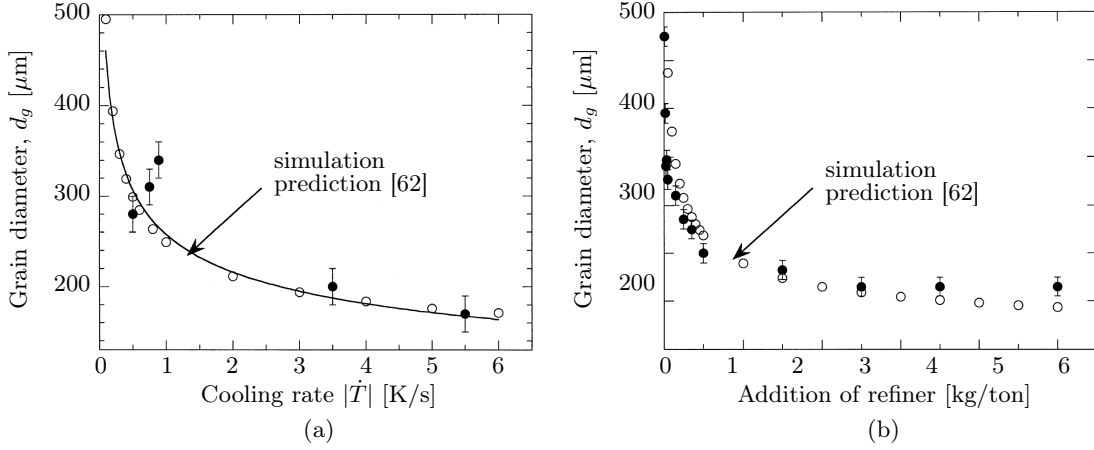


Figure 2.27: Grain diameter (a) as a function of the cooling rate (with 5kg/ton of refiner addition) and (b) as a function of the amount of refiner (for a cooling rate of -3.5K/s). Black points represent experimental data and white points simulated ones [62].

diffusion coefficient D_ℓ , and inversely proportional to the growth restriction factor, Q , defined as:

$$Q = m_\ell(1 - k_0)c_0 \quad (2.39)$$

Therefore, in order to obtain a smaller grain size, it is important to increase the growth restriction factor.

Other important conditions, for grain refinement, are the cooling rate and the amount of refiner. As shown in Fig. 2.27, a small grain size is favoured by a high cooling rate and a large amount of refiner. These effects however reach a saturation level: the addition of refiner over 4kg/ton does not significantly affect the final grain size for the given conditions, namely cooling rate.

2.7 Macroseggregation

Macroseggregation is defined as an inhomogeneous solute distribution at the scale of the sample (or at the scale of the product in an industrial context). These macroseggregations are due to two combined elements: microseggregations caused by the rejection of chemical species due to the different solubility between the solid and the liquid phases and the relative movement of both phases on large length scales [68]. As explained by Appolaire *et al.* [68], while most of the studies considered the influence of liquid movement in relation to solutal and thermal buoyancy, the relative movement of equiaxed crystal is also important.

As shown in Fig. 2.28, Ganesan *et al.* [67] calculated the evolution of the solid and liquid

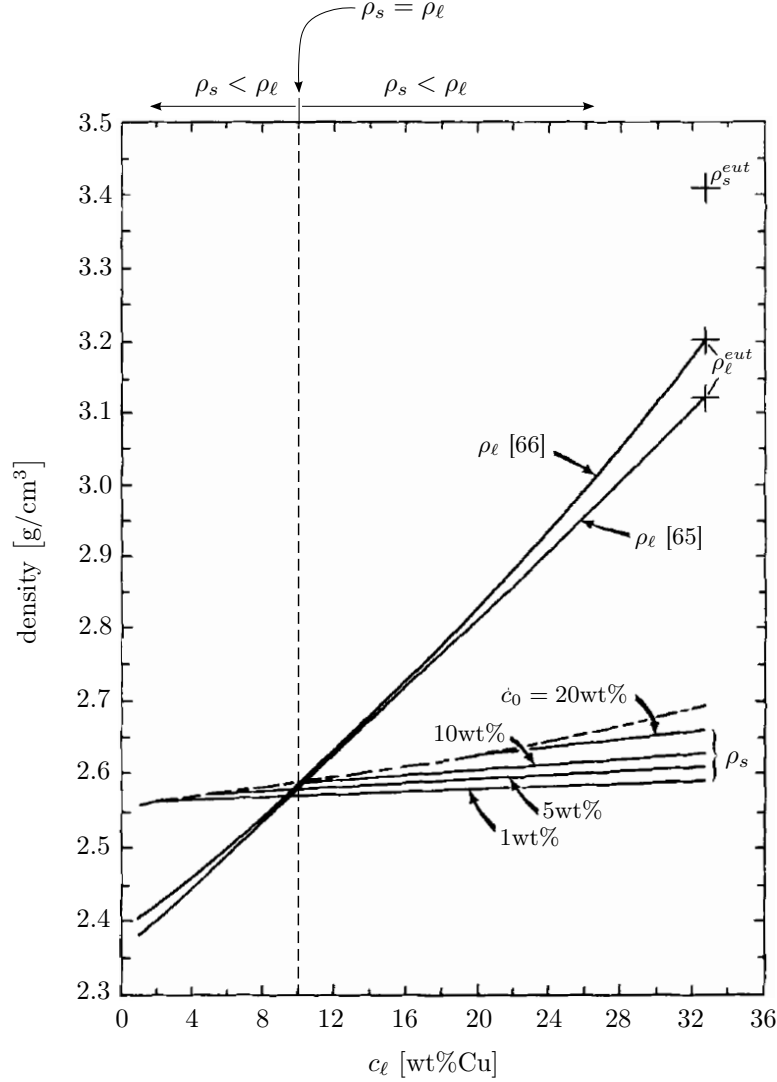


Figure 2.28: Density of the solid and liquid phases during solidification of Al-Cu alloys as a function of the liquid concentration, c_ℓ [67]. The dotted line corresponds to the solid density at equilibrium (complete mixing). The vertical dotted line corresponds to the nominal composition (around 10wt%Cu) for which the first solid that solidifies possesses the same density as the liquid.

densities as a function of the composition of the liquid. The density of the liquid was calculated from references [65] and [66] respectively, while the solid density was found as a function of c_ℓ with the Scheil-Gulliver equation (see Eq. (2.6)), with the reference density given by [69]. This is represented in Fig. 2.28, in which the continuous lines correspond to the density of the liquid respectively the solid possessing different nominal compositions. The dotted line corresponds to composition in the solid at equilibrium (and thus the composition of the first solid nucleus).

The vertical dotted line in Fig. 2.28 corresponds to the nominal composition (around

10wt%Cu) for which the first solid that solidifies possesses the same density as the liquid. For higher nominal composition alloys, the grains will always tend to float ($\rho_s < \rho_\ell$), while for lower nominal compositions the grain will initially tend to sediment ($\rho_s > \rho_\ell$), but floating can then be induced by the advance of solidification and the consequent increase of liquid Cu compositions.

3 Experimental methods

3.1 Materials

In this work, aluminum-copper (Al-Cu) alloys were used for several reasons. The first, and main reason, is that it is important to have a good knowledge of the last-stage solidification of Al-Cu alloys, since they are sensitive to hot tearing. Second, these alloys were already extensively studied in the literature and the fact that their physical properties are well known (used as model system) can help in using accurate physical values either to interpret the experimental data or to compare the experimental results with the simulated ones. The third reason is that Al-Cu alloys yield an excellent contrast in X-Ray tomography. All these reasons establish AlCu alloys as excellent candidates for the purpose of this work.

Various Al-Cu alloys were used in this work (see Tab. 3.1). All the alloys were produced from a base Al-4.5wt.%Cu alloy, the copper content being adjusted by the addition of high purity copper shots (AlfaAesar® 99.999% purity) or pure aluminium (99.99% purity). As mentioned in section 2.6.3, it is usual to add a master alloy, at typical levels of 0.1wt% to 1.0wt%, to the liquid alloy before casting in order to grain refine it. In this work, we inoculated the alloy by the addition of 0.4wt% and 2.0wt% of a master AlTi5B alloy

Table 3.1: Compositions of the alloys used in this study.

No.	Copper content [wt%]	Master alloy content [wt%]
1	1.5	0.4
2	3.0	
3	4.5	
4	6.0	
5	1.5	2.0
6	3.0	
7	4.5	
8	6.0	

(containing 5wt%Ti and 1wt%B, i.e., TiB_2 particles with an excess titanium), in order to study the grain refining effect of alloys containing different amounts of refiner. 2.0wt% of inoculant can appear as a high value, but, as shown in section 2.6.3 and in particular in Fig. 2.27, the inoculation strongly depends on the cooling rates, especially in our case where it is about -0.05°C/s . Note that during casting, the master alloy was added to the liquid AlCu alloy just before pouring it in the mould in order to avoid a loss of efficiency of the inoculant. The alloys were cast in a brass mold ($25 \times 25 \times 250 \text{ mm}^3$) and then machined and turned to rods of two different diameters, 3.6 mm and 1.1 mm, for Bridgman experiments.

3.2 Quenched Bridgman furnace

The Bridgman furnace is generally used for crystal growth or for oriented solidification. Such a furnace typically consists of two temperature zones, a hot and a cold zone, establishing a temperature gradient in the sample (shown schematically in Fig. 3.1(a)). The 250 mm long and 3.6 mm diameter sample is fitted in an alumina crucible of 4 mm diameter and initially molten in the hot zone. It is then pulled from the hot to the cold zone. After a given travel length, the sample is quenched (by releasing it in a water bath) at room temperature in the semisolid state. It is then possible to access to the whole

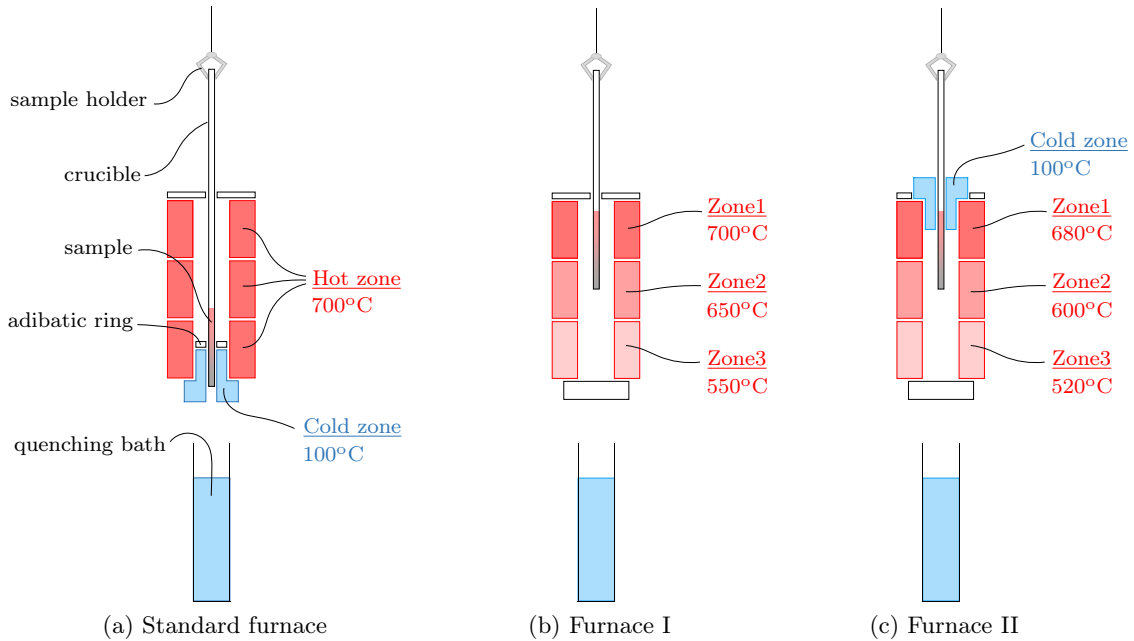


Figure 3.1: Schematic representation of the different furnace setups. They all possess a hot zone consisting of three sets of heating coils. The thermal gradient is either formed by using a copper chill cooler (cold zone) or by setting different parts of the furnace at specific temperatures.



Figure 3.2: Picture of furnace II configuration.

solidification history in space (equivalence between the position at moment of the quench and temperature).

In this work, we wanted to obtain the complete solidification history in space in a single experiment and thus use the principle of the Bridgman furnace. However, the typical gradient of 100 K/cm obtained in such an apparatus is improper for obtaining the desired globular-equiaxed microstructure: according to the calculations performed in section 2.5 and summarized in Fig. 2.21, for a Al-4.5wt%Cu alloy and a final grain size of $200\text{ }\mu\text{m}$ (corresponding to a nucleation site density of $3.0 \cdot 10^{10}\text{m}^{-3}$), the gradient should be, at maximum, on the order of 20 K/cm. Therefore, the standard Bridgman furnace (see Fig. 3.1(a)), was substantially modified in order to obtain a reduced gradient while keeping its principle: by setting the appropriate temperatures for each part of the furnace (that consists of three distinct parts and is closed at the bottom), the natural gradient that develops in the furnace (in the order of 10-15 K/cm) was used to solidify the samples (see Fig. 3.1(b)).

The results obtained with this furnace configuration and 250 mm long / 3.6 mm diameter samples were still not fully satisfying since large macrosegregation profiles were observed in the quenched sample. As shown in section 2.7, for compositions lower than 10 wt%Cu, the grains tend to sediment, while for compositions higher than 10 wt%Cu there is an opposite effect. With this sample and furnace configurations, it is always preferable to have sedimentation of the grains such that the grains move in the direction of the lower temperature in order to prevent their remelting. The sample configuration was thus modified and consisted in smaller pellets separated by ceramic separators in order to limit grain movement (see Fig. 3.3(b)). In addition smaller diameter samples were prepared

in order to limit convection within each pellet (see Fig. 3.3(c)). The fact of having separated pellets has another advantage: since the separators possess a lower thermal conductivity and the separator/pellet interfaces add a thermal resistance, the average conductivity of the sample is reduced. This helps achieving steady state conditions in the furnace since each portion of the sample exchanges heat radially while axial conductivity is substantially reduced. However, the fact of having separated samples has a disadvantage: the pellets do not remain liquid for the same amount of time: in particular the pellets at the top can remain liquid for longer times before reaching the liquidus temperature and starting solidifying. It is known in industry that the inoculant tends to fade as the melt is maintained at high temperature. In order to avoid fading of the inoculant, each pellet

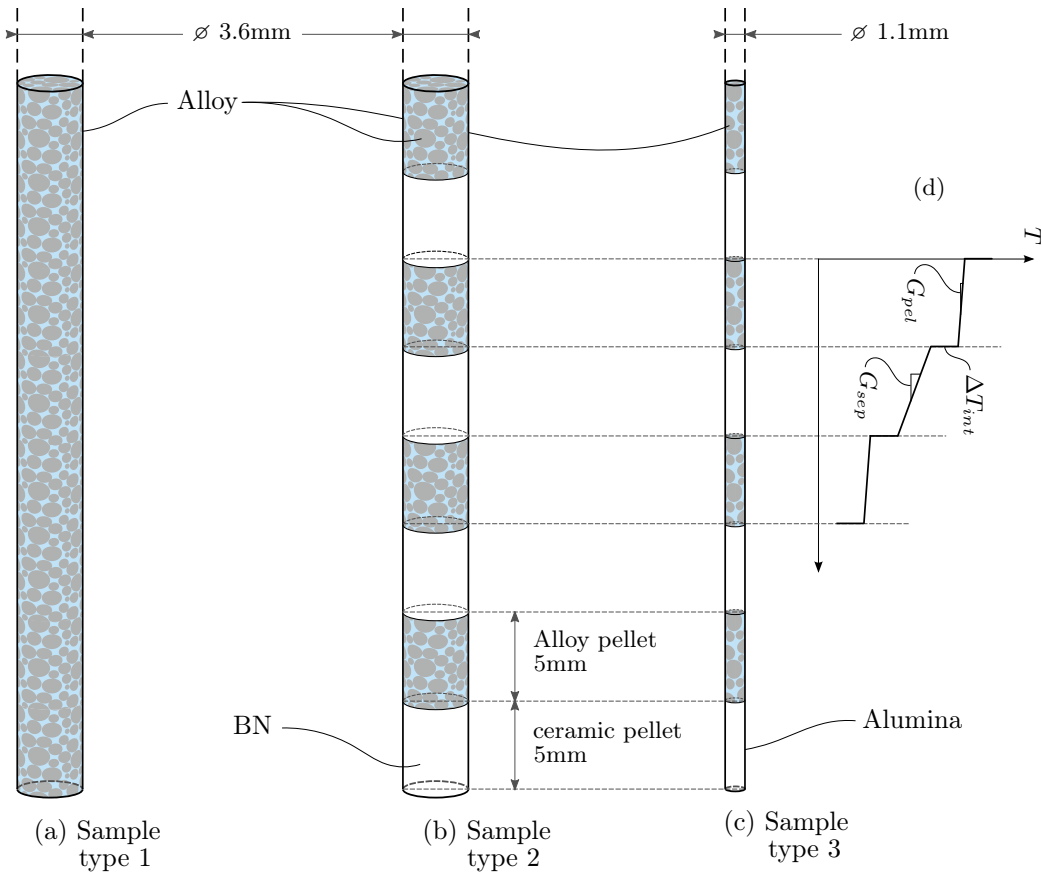


Figure 3.3: Schematic representation of the different samples used in this project. (a) sample type 1: monolithic sample of 3.6 mm diameter and 250 mm length. (b) sample type 2: 5 mm height alloy pellets separated by 5 mm height BN separators all of 3.6 mm diameter. (c) sample type 3: 5 mm height alloy pellets separated by 5 mm height alumina separators all of 1.1 mm diameter. Please note that samples type 2 and 3 consist of 13 alloy pellets and 13 separators and thus have a total length of 130 mm. (d) Schematic representation of the temperature profile inside (b) and (c): G_{pel} , G_{sep} and ΔT_{int} represent the gradient in the alloy pellet, the gradient in the ceramic separator and the temperature drop at the interface, respectively.

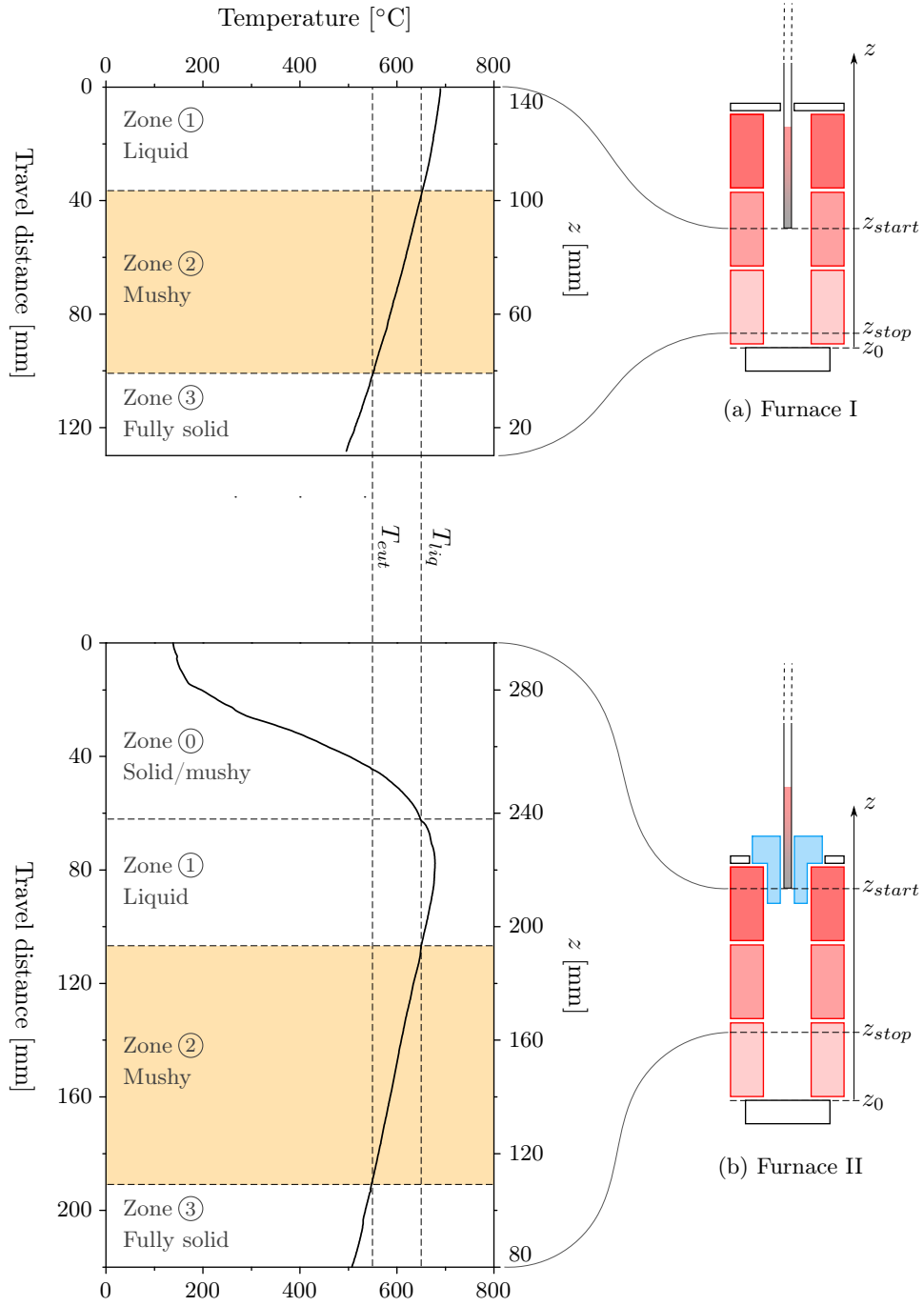


Figure 3.4: Typical temperature profiles as a function of the travel distance and the absolute position in the furnace z (reference z_0). The samples are initially positioned at z_{start} and the quench is performed at z_{stop} . For furnace I, there are three distinct zones where the sample is respectively liquid, mushy, or fully solid. For furnace II, there is an additional zone (zone 0) where the sample initially heats up. At the moment of the quench, the portion of the sample that is in the mushy zone is highlighted in orange. Ideally the sample length should cover this zone in order to have access to the whole solidification history after the quench.

needs to remain liquid for a short amount of time and in order to have a homogeneous final grain size they have to remain liquid for the same amount of time. This is the reason why furnace II was developed (Fig. 3.1): a cooler was added at the top of the furnace so that the pellets are all initially solid and then remain liquid only for a specific (and short) amount of time. A schematic representation of the temperature profile inside furnace I and II is given in Fig. 3.4.

3.2.1 Solidification experiments

The alloy samples or the alloy pellets/separators are first inserted in alumina, Al_2O_3 , crucibles. The 3.6 mm diameter samples (sample type 1 and 2) are introduced in a 4.0 mm(interior)/6.0 mm(exterior) diameter crucibles, while the 1.1 mm diameter samples (type 3) are introduced in a 1.4 mm(interior)/1.8 mm(exterior) diameter crucibles.

The furnace is preheated for 40 minutes in order to establish a steady-state thermal gradient. After that, the sample is introduced from the top of the furnace and placed at the starting position and heated for 50 minutes. The sample is then pulled through the thermal gradient and finally quenched at the desired position. Please note that in the furnace I configuration, the sample remains molten during the initial 50min heating, while in the case of furnace II the sample only melts when the experiment effectively starts, namely when the sample is pulled down and reaches the higher temperature zone. The quench (at the end of the pulling process) allows to “freeze” the microstructure at a given time.

The sample and furnace associations are the following:

- Furnace I and sample type 1
- Furnace II and sample type 2 or sample type 3

The experiments were then performed for different alloy compositions.

3.2.2 Temperature measurements

Temperature measurements were performed in order to characterize the temperature profiles and thermal gradient in the different configurations and to assess under which conditions it is possible to obtain globular-equiaxed grains. The alloy used in this case is an Al-4.5wt%Cu inoculated by the addition of 2wt% of master alloy. The thermal measurements are similar to the solidification experiments, except that the sample is not quenched at the end.

As shown in Fig. 3.5, in order to characterize the temperature profile of furnace I, the specimen named O was prepared as sample type . For furnace II, the specimens named A and B (prepared as sample type 2) as well as the specimen named C (prepared as sample type 3) were made. The specimens O, A, and B were then machined as hollow cylinders

(2mm internal diameter). After that, two K-type integrated standard thermocouples (Thermocoax[®]) inserted in an alumina sheath were inserted through the hole of the hollow cylinder samples. As for the solidification experiments (see section 3.2.1), the samples were placed in an alumina crucible. All the assembly was then sealed with a ceramic paste in order to prevent the movement of the sheath in the crucible. In contrast, because of the reduced diameter of specimen C, it was not possible in this case to insert the thermocouples inside the sample. Therefore, the specimen C was prepared exactly as for the solidification experiments (see section 3.2.1), the two K-type thermocouples being directly fixed outside the sample crucible with a ceramic paste. The thermocouples were connected to a NetDAQ data acquisition system, in order to record the temperature evolutions.

In order to assess whether the experimental conditions correspond to steady-state, the two thermocouples of each specimen were placed at different positions as shown in table 3.2. Furthermore, in order to check the reproducibility of the experiments, two similar but distinct specimens, A and B, were tested under the same conditions.

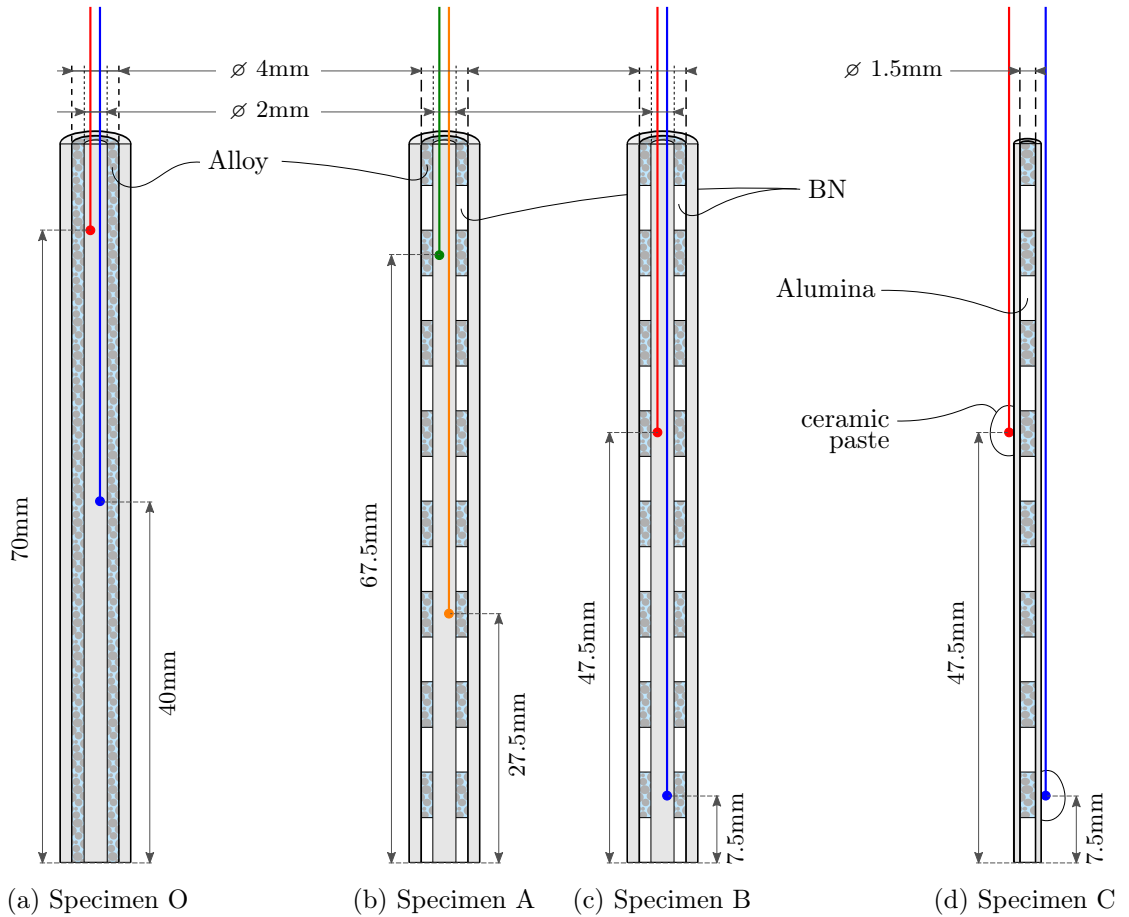


Figure 3.5: Schematic representation of the three specimens that were chosen for the thermal measurement experiments.

Table 3.2: Position of the thermocouples (distance from the bottom of the crucible) for each specimen. Please note that specimens A and B are exactly the same, the only difference being the position of the thermocouples.

Specimen	Sample type	Furnace	Themocouple 1 distance [mm]	Themocouple 1 distance [mm]
O	1	I	40.0	70.0
A	2	II	7.5	47.5
B	2	II	27.5	67.5
C	3	II	7.5	47.5

3.2.3 Thermal simulation

With the specimens instrumented with thermocouples (see section 3.2.2), it is possible to measure the temperature evolution (and the cooling rate) at a specific position in the sample. If the sample was only laterally heated with no influence of the conductivity of the sample, it would be possible to calculate the thermal gradient, G , by knowing the pulling speed of the sample, v_{pull} (assumed to be equal to the velocity of the isotherms, v_T , under steady-state conditions) as well as the absolute cooling rate $|\dot{T}|$, since they are linked by the following relationship:

$$|\dot{T}| = G v_T \quad (3.1)$$

However, the axial conductivity can play a significant role and affect the profile in the sample. In the case of a monolithic alloy sample (sample type 1), the axial conductivity tends to lower the thermal gradient inside the sample. For samples made of alloy pellets and separators (sample type 2 and 3), a temperature discontinuity can occur at each interface and the temperature gradient inside the pellets can be significantly smaller than within the separators, as explained in appendix A.1. For sample type 2 and 3, since the gradient curve is not continuous, Eq. (3.1) is applicable only if the average gradient over a RVE (shown in appendix A.1) is considered and not the local gradient.

Figure 3.6 shows the typical mesh used for the thermal simulation of the type 2 sample and of the crucible. A regular rectangular meshing is performed inside the alloy pellets and the ceramic separators, while a free mesh is used for the crucible. The calculation of the temperature field, $T(r, z', t)$ (where r and z' are the spatial coordinates and t the time), is performed in cylindrical coordinates using the software CalcoSoft® [70]. Please note that the z' axis is fixed to the sample (unlike z which is fixed to the furnace, as shown in Fig. 3.4) and the calculation is performed in a Lagrangian reference frame. The temperature profile imposed by the furnace, T_{ext} , is dependent on z' and time.

For the exterior boundary conditions, one should account for both convection and radiation exchange. For simplicity, both terms are included in a single, and constant, heat transfer coefficient, h_{ext} .

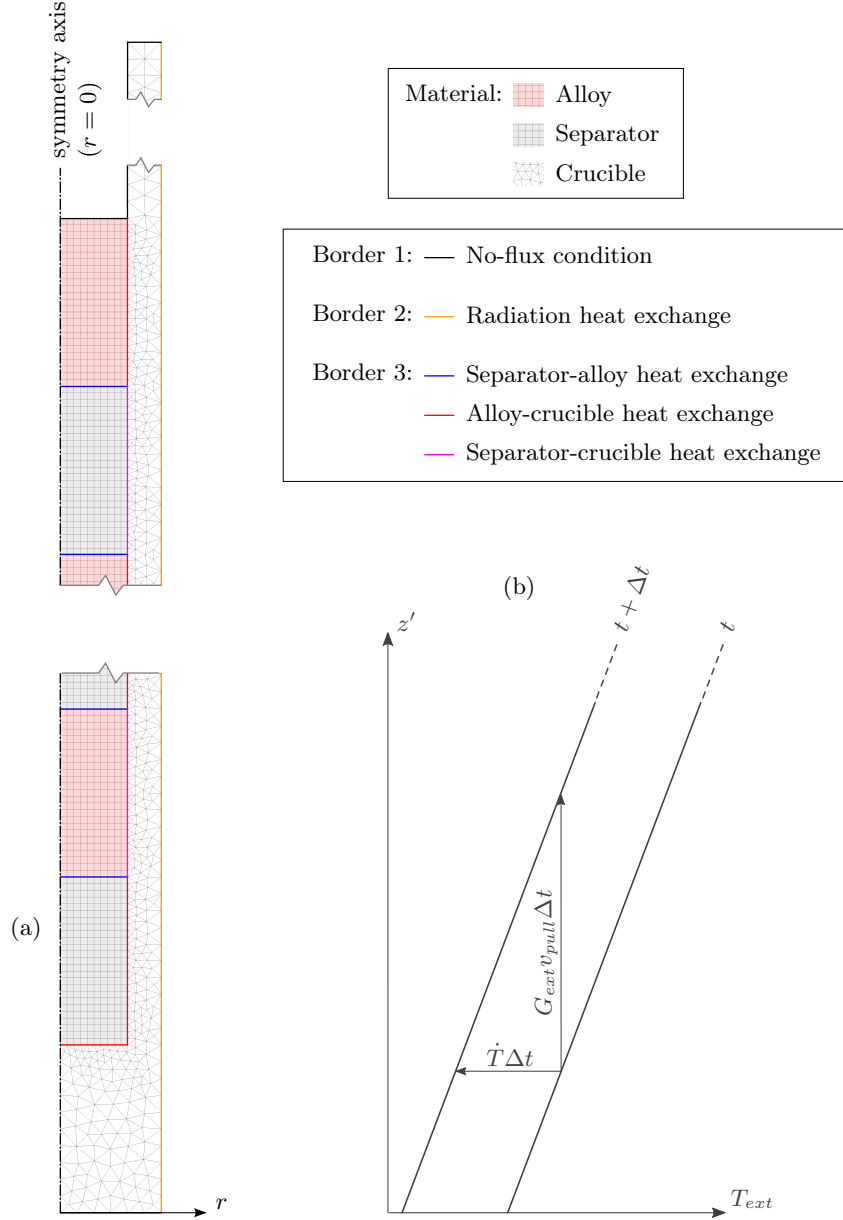


Figure 3.6: Schematic representation of the thermal simulation. (a) Meshing of the sample (in this case: alloy pellets alternated with separators). (b) Schematic temperature profile of the furnace $T_{ext}(z', t)$: the profile is shown at two different times.

The external temperature imposed by the furnace is given by the following expression:

$$T_{ext}(z, t) = T_{bottom} + G_{ext}z' + \dot{T}_{ext}t = T_{bottom} + G_{ext}(z' + v_{pull}t) \quad (3.2)$$

where $T_{bottom} = T_{ext}(z' = 0, t)$, G_{ext} the thermal gradient of the furnace (assumed to be constant), and v_{pull} the pulling velocity of the sample in the furnace. By performing several calculations and comparing them with experimental measurements, G_{ext} was adjusted in order to have a cooling rate close to the liquidus temperature in good agreement with

experiments.

On the other boundaries, a no-flux condition is applied:

$$\frac{\partial T}{\partial n} = 0 \quad (3.3)$$

where $\frac{\partial T}{\partial n}$ is the derivative along the normal (and outside pointing), \mathbf{n} , of the surface. This condition applies in particular at the center for symmetry reasons.

At the interfaces between different materials (between the alloy pellets, ceramic separators and crucible), a heat balance is performed:

$$\left(\kappa_- \frac{\partial T_-}{\partial n} \right) = \left(\kappa_+ \frac{\partial T_+}{\partial n} \right) = -h_{int}(T_- - T_+) \quad (3.4)$$

where κ_- , T_- , κ_+ and T_+ are the conductivities and the temperatures of the material on the left, respectively right side, h_{int} being the heat transfer coefficient of the interface and \mathbf{n} points from the left (-) to the right (+).

The boundary and interface conditions can be summarized as follows:

Border 1 No-flux condition:

$$\frac{\partial T}{\partial n} = 0 \quad (3.5)$$

Border 2 Heat exchange with the furnace:

$$\kappa \frac{\partial T}{\partial n} = -h_{ext}(T - T_{ext}) \quad (3.6)$$

with $T_{ext}(z, t) = T_{bottom} + G_{ext}(z' + v_{pull}t)$

Border 3 Interface heat exchange:

$$\left(\kappa_- \frac{\partial T_-}{\partial n} \right) - \left(\kappa_+ \frac{\partial T_+}{\partial n} \right) = -h_{int}(T_- - T_+) \quad (3.7)$$

As initial condition, the temperature in the sample is supposed to be equal to the external imposed temperature $T(r, z, t = 0) = T_{ext}(z, t = 0)$.

All the parameters used for the calculation are summarized in Table 3.3. Please note that CalcoSoft® uses an enthalpic method in order to take into account latent heat release during solidification [70].

The heat transfer coefficients are summarized in Tab. 3.4. Please note that the separator-crucible coefficient is set to a lower value compared to that of the alloy-separator and alloy-crucible since there is an air gap between the separator and the crucible, while the alloy has a good thermal contact (especially when it is liquid) with the other parts.

3.2. Quenched Bridgman furnace

Table 3.3: Physical values of the materials used for the calculation. c_p is the volumetric specific heat, κ the thermal conductivity, and L_f the volumetric latent heat of fusion. The values are taken from the CalcoSoft® database.

Material	Physical parameter	Value	Unity
Al-4.5wt.%Cu	c_p	$3.3 \cdot 10^6$	J/(m ³ K)
	κ (liquid)	100	W/(mK)
	κ (solid)	185	W/(mK)
	L_f	$9.58 \cdot 10^8$	J/(m ³)
Alumina	c_p	$3.18 \cdot 10^6$	J/(m ³ K)
	κ	9.0	W/(mK)
BN	c_p	$3.06 \cdot 10^6$	J/(m ³ K)
	κ	30.0	W/(mK)

Table 3.4: Heat transfer coefficients.

Interface	h_{ext} [W/(m ² K)]
external	60
Interface	h_{int} [W/(m ² K)]
alloy-separator	2000
alloy-crucible	2000
separator-crucible	500

3.2.4 Simulation of grain sizes

In order to simulate the final grain sizes obtained in the modified sample setup (see samples 2 and 3 in Fig. 3.3) a Lagrangian 1D model proposed by Appolaire *et al.* [68,71] was used. This model can simulate the nucleation and growth in multicomponent alloys and takes into account the globular-to-dendritic transition (see section 2.5.2). Please note that this model can also account for the grain movement. However, this feature was not used since this model was mainly used to simulate the effect of solute, inoculation content and heat transfer coefficients in the furnace II and sample 2 and 3 setup, where we assume that convection is limited to the scale of each single pellet and thus no macrosegregation is observable at the scale of the full sample, which is composed by several pellets.

Various simulations were performed with the model of Appolaire *et al.* [71] by considering a cylindrical pellet of 5mm of height. Two pellet diameters (sample type 2 and 3) were considered. In the furnace II setup, a heat transfer of $h_{ext} = 60 \text{ W/(m}^2\text{K)}$ between the exterior of the crucible and the furnace was considered. Please note that the model of Appolaire *et al.* [71] requires the heat transfer coefficient at the surface of the alloy pellet. This value was found by taking into account the thermal conductivity of the alumina crucible as well as geometry factors (such as the exterior and interior diameters of the crucible).

Another simulation was performed in order to predict the grain size in the case of the *in situ* X-ray tomography experiment (see section 3.3.3). In this experiment, the temperature is directly imposed in order to follow a predefined cooling ramp. This situation corresponds to a large heat transfer coefficient. Therefore, the simulation of this case was performed by using a heat transfer coefficient of $h_{ext} = 10'000\text{W}/(\text{m}^2\text{K})$.

Because of the large addition of master alloy (aluminum matrix containing 5wt% of titanium and 1wt% of boron) the titanium addition has to be taken into account. The master alloy contains TiB_2 particles and an excess of titanium. By assuming that all the boron is in the TiB_2 particles, the master alloy contains 2.21wt% of Ti in the TiB_2 particles and 2.79wt% of excess titanium (corresponding to the 5wt% of titanium minus the 2.21wt% of Ti in the TiB_2 particles). For the alloy containing 2.0wt% of master alloy, it corresponds to $2.0\text{wt}\% \times 2.79\text{wt}\% = 0.056\text{wt}\%$ of excess titanium. For the alloy containing 0.4wt% of master alloy, the excess titanium is 0.011wt%. Even if relatively small, these quantities are not negligible since the presence of titanium influences the growth restriction factor Q . In addition, titanium forms a peritectic reaction with Al-rich alloys and possesses a large liquidus slope of $25.6^\circ\text{C}/\text{wt}\%\text{Ti}$ (compared to the liquidus slope of $-3.4^\circ\text{C}/\text{wt}\%\text{Cu}$ in hypoeutectic AlCu alloys) and thus affects liquidus temperature of the alloy. Please note that, in the model, the TiB_2 particle distribution of Greer *et al.* (shown in Fig. 2.26(a)) is considered.

3.3 Observation techniques

In order to characterize the grain shape and size, two main techniques have been used in this work: chemical etching followed by optical microscopy or scanning electron microscopy (SEM). Note that in order to find the grain orientation and grain sizes, electron back-scattered diffraction (EBSD) was performed in a SEM. In order to observe the microstructure in 3D and follow the evolution of the percolation state and interface curvature along the solidification history, *ex situ* X-ray tomography experiments were performed post-mortem on the quenched samples. Similar experiments were also performed *in situ* in order to directly observe the evolution of the grain structure in 4D (3D evolution as a function of time). This was done using a laser-heated furnace directly mounted on the X-ray tomography beamline at the Paul Scherrer Institute (PSI) [72].

3.3.1 Sample preparation

In order to observe the microstructure of the AlCu samples by optical or electronic microscopy, their surface had first to be mechanically polished. The samples were first embedded in a conductomet® resin and then polished with SiC paper of increasing grades (sequence of FEPA standard grit sizes: P500, P1200, P2400 and P4000), i.e., decreasing particle sizes. This was followed by a mirror polish using diamond particles sprayed on

a DP-Nap felt from Struers[®] installed on a polishing plate (decreasing particle sizes of $6\mu\text{m}$, $1\mu\text{m}$ and $0.25\mu\text{m}$). Because of the relative lack of hardness of the AlCu alloys, some polishing particles can get incorporated at the surface of the sample during these operations. The samples had to be washed with ethanol and then put in an ultrasound ethanol bath for 60 s between each polishing step in order to eliminate them.

For the optical microscopy observations, the surface was etched in a Keller solution [73], consisting of 5 mL HF, 7.5 mL HNO₃, 2.5 mL HCl and 475 mL distilled water, for 15 seconds to reveal the microstructure. For the EBSD analysis, vibrating polishing was performed for 3 hours on a soft cloth with a Struers[®] silica colloidal solution, in order to remove the hardened layer that forms at the surface during the previous polishing stages.

Preliminary optical imaging investigations were performed with a Reichert-Jung MeF3 A optical microscope, using the software Fiji[®] for further analysis. A median filter was first applied in order to reduce the noise and the picture was then binarized. The solid fraction was then calculated by the ratio between the pixels belonging to the solid divided by the total amount of pixels (assuming the area fraction to be equal to the volume fraction).

3.3.2 Scanning electron microscopy

Electron backscattered diffraction (EBSD)

The crystallographic orientation of grains can be determined with EBSD. Backscattered electrons of the incident beam, after interaction with the crystalline solid grains of the specimen, are diffused in all the directions. In the proximity of the surface, the backscattered electrons form a divergent source of electrons. The interaction of these electrons with the crystal lattice can be diffracted by atomic layers, according to Bragg's equation $2d_{hkl}\sin(\theta) = n\lambda$, where d_{hkl} is the interplanar distance of (hkl) planes, θ the angle between the diffracted and the incident beam, n the order of the diffraction and λ the wavelength of the incident beam. Each crystallographic plane leads to a pair of large angle cones. The impingement of these diffracting cones on a phosphorous detector generate characteristic pseudo-Kikuchi bands, producing an electron backscattered diffraction pattern. The width of the Kikuchi lines is inversely proportional to the distance separating the planes, while their centers correspond to the projection of the diffracting plane and their intersection define the zone axis. With all this information, it is possible to access to the crystal orientation (as well as indexing different phases). A map can then be constructed by identifying the orientation of the grains associated to a specific region.

EBSD maps were done with a NordlysS II EBSD detector mounted on a Philips XL-F30 SEM at the Interdisciplinary Centre for Electron Microscopy (CIME) at EPFL. The samples were tilted at 70° with respect to the direction of the incident beam in order to maximize the intensity.

Energy dispersive X-ray spectrometry (EDX)

Chemical analysis of the specimens was performed with the Energy Dispersive X-ray Spectroscopy (EDX) technique. This technique is based on the detection of X-rays emitted by the sample subjected to an electron beam. The electrons of the beam can eject electrons from inner shells of the atoms and X-rays are emitted when another electron of the outer shells fills the vacancy. The X-ray energy spectrum being characteristic of each element under the beam, the intensity of the lines allows to perform a chemical analysis. Please note that this technique is in fact only semi-quantitative. However, it allows to characterize relative composition changes.

A Philips XL-F30 SEM was used for EDX analyses. The chemical analyses were performed at different positions in the sample in order to find the occurrence of macrosegregations in the quenched sample, in particular for the monolithic sample of type 1 (see Fig. 3.3(a)).

3.3.3 X-ray tomography

Basic principles

X-ray tomography is a non-destructive technique that allows to observe the microstructure in 3D. As explained hereafter, it can either be performed *ex situ* on quenched microstructures, or *in situ* in order to observe the evolution of the microstructure in real time.

The technique is based on two basic principles: the Beer-Lambert law and the Radon theorem [74–76]. The Beer-Lambert law relates, for a given energy of the incident rays, the number of transmitted photons N_1 for a number of incident photons N_2 possessing an energy E [77]:

$$\frac{N_1}{N_2} = \exp \left[- \int_{s \in \text{ray}} \mu(E, s) ds \right] \quad (3.8)$$

where μ is the attenuation coefficient and $s \in \text{ray}$ denotes the trajectory of the rays (or optical path) through the sample. Note that for a polychromatic beam, equation 3.8 has to be integrated also over the energy spectrum. The attenuation coefficient μ can be expressed as follows [77]:

$$\mu = K \rho \frac{Z^4}{E^3} \quad (3.9)$$

where K is a constant, ρ and Z are respectively the density and the atomic number of the material. Since each ray follows a distinct optical path through which the integral of μ is different, the signal captured by each pixel of the detector is potentially different leading to a contrast.

The Radon transform then consists in the integral of a function through straight lines, in our case the integral of the absorption coefficient μ along the optical path. Therefore,

by using the inverse of the Radon transform of projections recorded at different angular positions, the 3D distribution of the absorption coefficient μ can be retrieved. Since the solid and the liquid exhibit different solute compositions (in hypoeutectic AlCu alloys, the liquid is copper-enriched), it is possible to reconstruct the 3D microstructure of the sample in a non-destructive manner. Please note that, in general, an inverse contrast picture is produced, such that the most absorbing elements appear brighter in the image, in a way similar to backscattered electron microscopic images. The best results, in terms of spatial resolution and signal-to-noise ratio, can be obtained with synchrotron radiation.

The X-ray tomography experiments were performed at the TOMCAT (TOmographic Microscopy and Coherent rAdiology experimenTs) at the Swiss Light Source (SLS) of the Paul-Scherrer Institute in Villigen (Switzerland). The X-rays that are transmitted through a rotating cylindrical sample hit a $25\mu\text{m}$ thick LuAG:Ce scintillator, which converts X-rays to visible light recorded by a 2048×2048 CCD camera. The visible light then goes through interchangeable objective (4x, 10x or 20x). The sample is rotated through 180° at a constant angular speed. The selected voxel size was $0.667\mu\text{m}$ (the resolution being on the order of 3 times the voxel size, i.e., about $2\mu\text{m}$).

Ex situ X-ray tomography

Quenched Al-Cu samples obtained with the Bridgman furnace were observed post mortem (or *ex situ*) by X-ray tomography. The samples were inserted into a BN hollow tube (of $2.0\mu\text{m}$ exterior diameter) to hold them during tomography. Note that the diameter of the samples type 1 and 2 was previously reduced to $1.1\mu\text{m}$ in order to be inserted in the BN tubes.

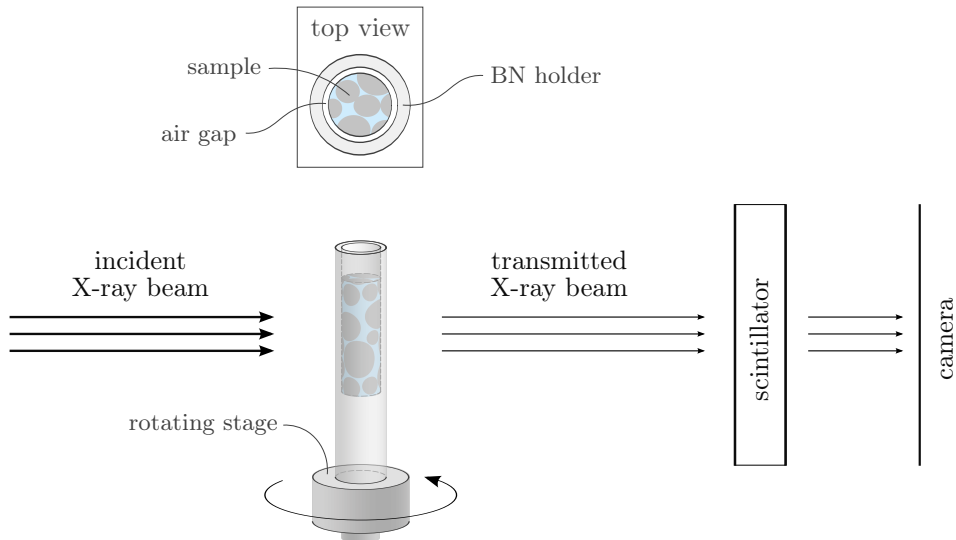


Figure 3.7: Schematic representation of the *ex situ* tomography experiment.

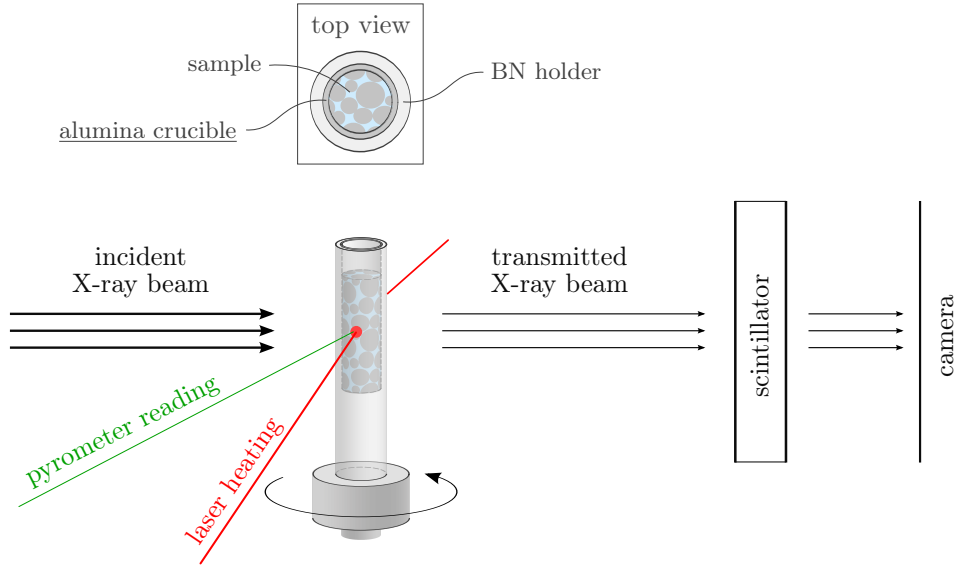


Figure 3.8: Schematic representation of the *in situ* tomography experiment. Please note that, unlike *ex situ* experiments, the sample is inserted in a composite alumina-BN crucible.

In situ X-ray tomography

As a complement, *in situ* X-ray tomography observations were performed. As shown in Fig. 3.8, the experiment uses the setup as for the *ex situ* observations, the main difference being the fact that solidification takes place during tomography observations.

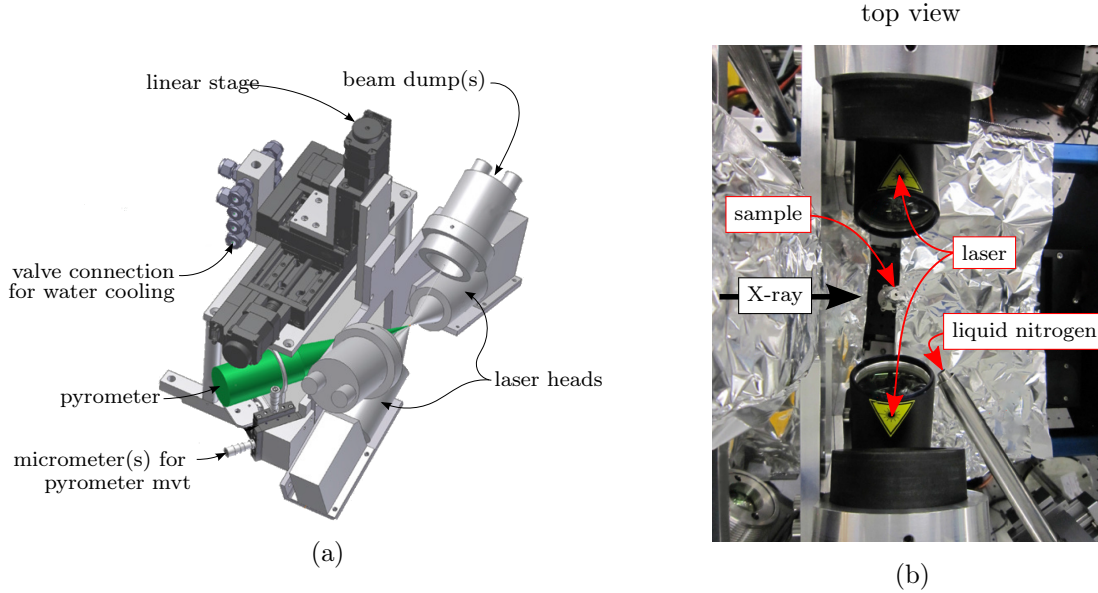


Figure 3.9: (a) Technical drawing of the laser furnace mounted on the X-ray tomography beamline. (b) Top view picture showing the laser furnace (after [72]).

Heating and remelting of the sample is provided in this case by a laser-heating furnace, developed by Fife *et al.* [72]. As shown in Fig. 3.9, two near-infrared diode lasers of 150W power output each, operating at a wavelength of 980nm, allow to heat the sample in the range 400-1700°C. The temperature is controlled by the measurement of a pyrometer, while temperature calibration can be made by observing *in situ* melting of the specimen. The alloy samples used for this experiment had a diameter of 1.1mm. They are not directly inserted in the BN holder. As emphasized in the top view of Fig. 3.8, the alloy sample is inserted in an alumina crucible, which itself is fitted inside the BN holder. This composite alumina-BN crucible was developed because the inner alumina crucible provides good wetting conditions and prevent the sample from exhibiting a broken meniscus, while the BN (outer holder) has a higher emissivity and thus allows a better control of the sample temperature and heating. As for the *ex situ* experiment, the exterior diameter of the BN holder is 2.0mm.

As shown in Fig. 3.10, the temperature cycle consisted in a fast heating ramp followed by a “plateau” at a constant temperature of 700°C in order to completely melt the sample and then followed by a slow cooling ramp, with the desired cooling rate \dot{T} . Two different cooling rates of -0.05°C/s and -0.1°C/s were used. When the temperature falls below the liquidus temperature, T_{liq} , the tomography scan are started and taken at regular intervals. When the temperature falls below the eutectic temperature, T_{eut} , the lasers are turned off, resulting in a fast quench of the sample.

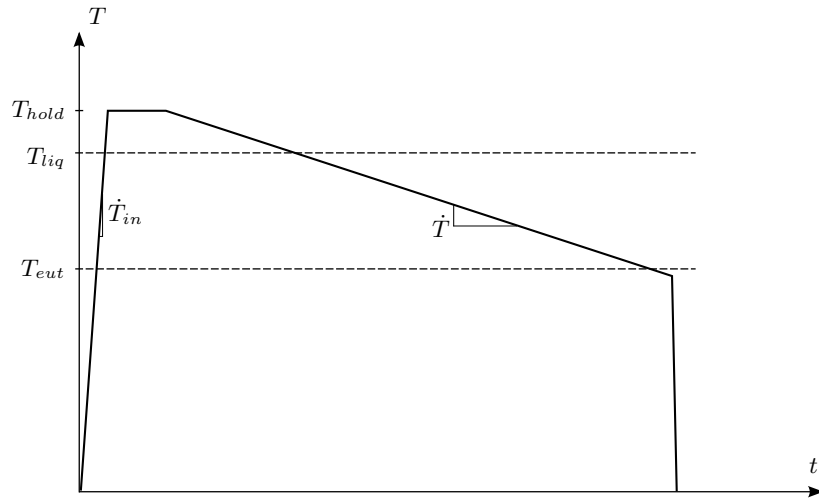


Figure 3.10: Temperature cycle followed in *in situ* experiments.

In fact, Bridgman furnace II setup (described in Fig. 3.4), tried to replicate the temperature cycle done in the *in situ* experiment.

Image reconstruction

For the image reconstruction, the stack of images were first cropped to the desired size. After the application of a median filter in order to reduce the noise, the images of the stack were segmented with the software Fiji®. With the software Avizo®, it was then possible to visualize the microstructures in 3D and to extract the solid/liquid interface surface and deduce its curvature. The solid-liquid interface was smoothed with the application of a gaussian smoothing algorithm of the binarized image stack and a subsequent smoothing algorithm available in Avizo®. Finally, it was possible to plot the interface shape distribution (ISD) diagram (explained in section 2.1.3) as well as the interfacial area per unit volume S_V with a Matlab® code developed by Meidani *et al.* [78].

4 Bridgman furnace results

4.1 Introduction

As explained in section 3.2.2, it is of crucial importance to measure the thermal gradient of the furnace in order to determine the conditions for obtaining the desired, globular-equiaxed, microstructure. A comparison between the cooling rates experienced in the various furnace/sample configurations was performed in order to explain the differences in the observed grain size. This was complemented by simulation of the temperature profiles inside the samples (see section 3.2.3) and of the grain nucleation (see section 3.2.4). Finally, the grain structure evolution, in particular the solid fraction evolution as a function of temperature, was characterized.

4.2 Temperature characterization

The aim of this section is to set up the appropriate temperature for each zone of the various furnace setups that yield a constant thermal gradient and that allows to have the solidification interval within the sample at the moment of the quench.

4.2.1 Furnace I - sample type 1

Several temperature characterization tests were necessary to determine the appropriate settings. The final selected setup is summarized in Table 4.1.

Table 4.1: Appropriate temperature setting for each zone of the furnace I.

Zone 1 [°C]	Zone 2 [°C]	Zone 3 [°C]
700	650	550

Figure 4.1 shows the temperature profile and the temperature gradient G measured by two thermocouples in specimen O. The thermal gradient is lower than $20^{\circ}\text{C}/\text{cm}$, over the

Chapter 4. Bridgman furnace results

whole history of the sample. Therefore, as shown by Fig. 2.21, it is possible to obtain a globular-equiaxed microstructure provided that the pulling speed is in the order of 2-3 mm/min.

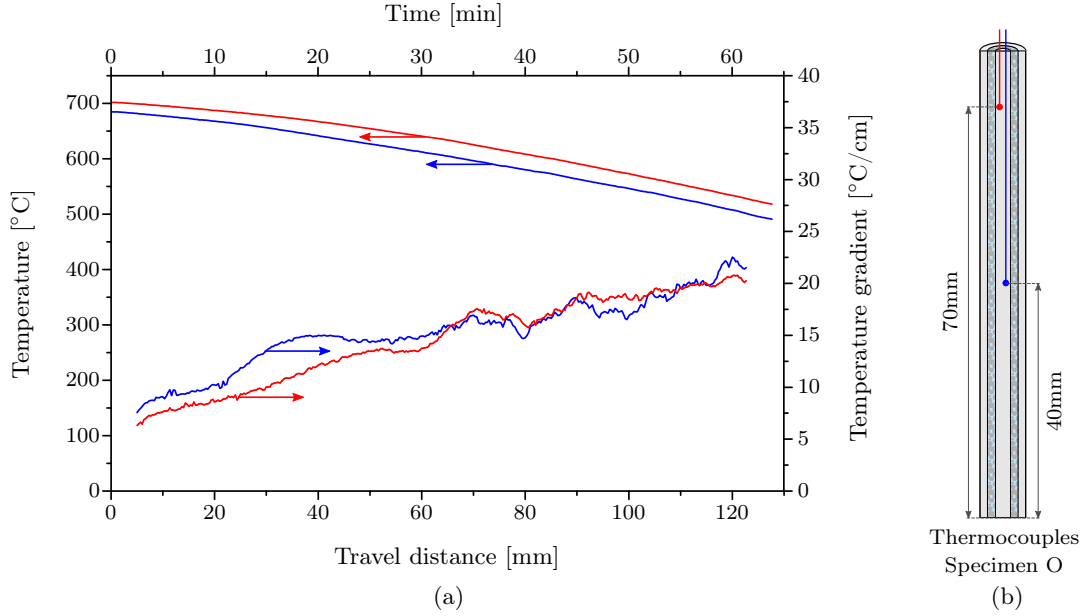


Figure 4.1: (a) Temperature curves and thermal gradients, G , of sample type 1 in furnace I measured by two thermocouples, $v_{pull} = 2$ mm/min. (b) Detail of the thermocouple positions, with colors corresponding to the measured curves in (a).

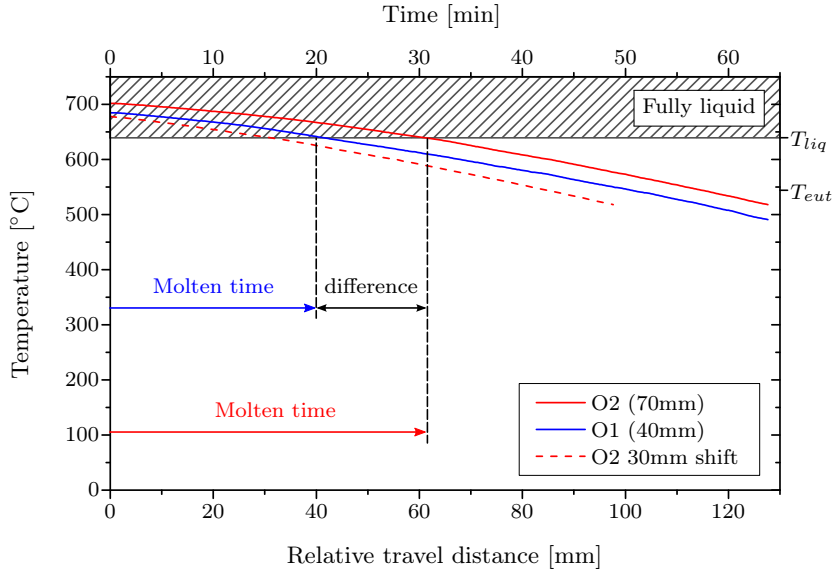


Figure 4.2: Same temperature curves of Fig. 4.1, showing the molten region. The red dotted line corresponds to the curve of thermocouple O2 shifted by 3cm (i.e., the distance separating the two thermocouples).

If steady-state conditions were achieved in the furnace, the curve of thermocouple O2 shifted by the distance separating the two thermocouples (dotted red curve in Fig. 4.2) would coincide with the curve of thermocouple O1 (blue curve in Fig. 4.2). One can clearly see that this is not the case, indicating that, in this configuration, steady-state conditions are not achieved. As mentioned in section 3.2.3, the conductivity of the sample plays an important role: the sample is not simply laterally heated by the furnace but longitudinal conduction acts as well.

Another aspect is that different parts of the sample do not share the same thermal history: as emphasized in Fig. 4.2, the part of the sample that is further away from the bottom of the sample (for example thermocouple O2 with respect to O1), remains liquid for a longer time. This can affect the efficiency of the inoculant as a function of the height of the specimen.

4.2.2 Furnace II - sample type 2

The main problem with the furnace and sample configuration presented in the previous section was the difficulty of achieving steady-state conditions. Sample type 2 (consisting of several alloy pellets alternated with ceramic separators) was engineered to address this issue as well as to limit macrosegregation (shown in section 4.4). In addition, furnace II (similar to furnace I but with the addition of a copper cooler at the top as shown in Fig. 3.1(c)) was developed. With this configuration, each alloy pellet remains liquid for a short and comparable amount of time. Furthermore, the mushy zone length should be reasonable to reduce the quantity of pellets necessary to cover the solidification history. Several thermal measurements tests (summarized in Table 4.2) were performed by fine-tuning the temperature settings for each zone of the furnace, in order ensure the appropriate temperature profile over the whole solidification domain.

Table 4.2: Test of the temperature settings for furnace II and sample type 2.

Test	Zone 1-2-3 [°C]	Molten time [min]	Mushy zone length [mm]	\bar{G} [°C/cm]	σ_G [°C/cm]
1	750-650-550	48	96	14.6	1.6
2	700-625-550	38	84	11.8	1.7
3	680-600-550	26	104	10.1	1.4
4	680-580-550	22	104	9.5	2.5
5	680-600-520	26	88	11.7	0.8

The settings of test No 5 were chosen because they provide a short melting time and the lowest gradient standard deviation σ_G . In addition, they provide a reasonable mushy zone length (that can be covered by the 130 mm long sample) and average gradient, \bar{G} . Figure 4.3 shows the temperature and gradient curves for sample 2 in furnace II. Unlike sample 1 in furnace I, the gradient remains constant over the cooling part of the curve. In addition, the time during which the pellets are molten is similar for each of them (as

Chapter 4. Bridgman furnace results

shown in Fig. 4.4).

In order to have a systematic approach and also the test the reproducibility of the

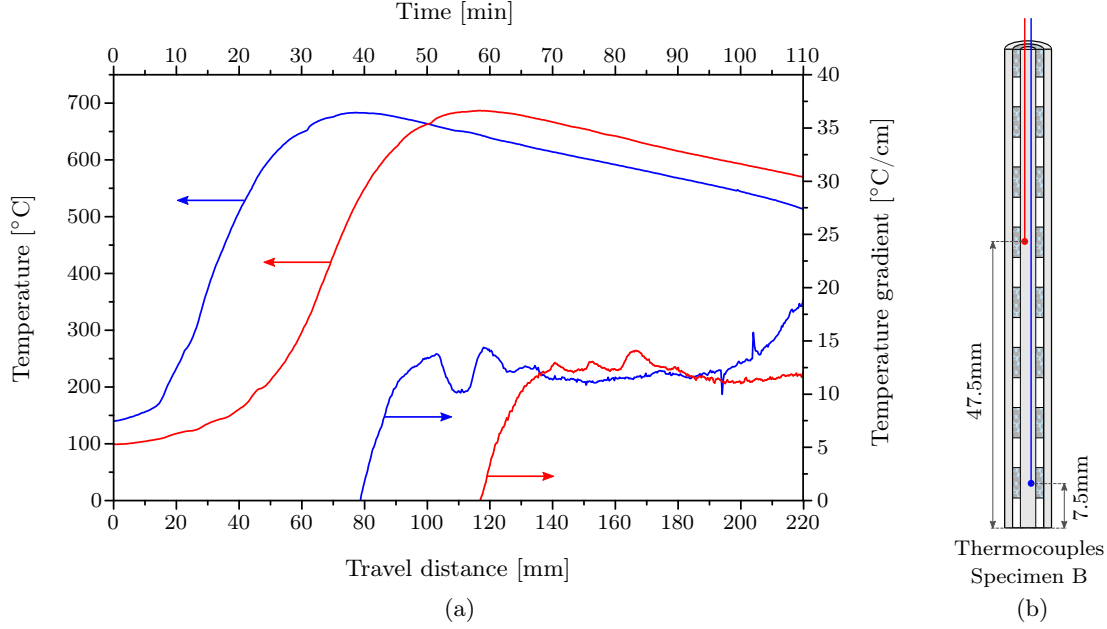


Figure 4.3: (a) Temperature curves and thermal gradients, G , of sample 2 in furnace II measured by two thermocouples, $v_{pull} = 2$ mm/min. (b) Detail of the thermocouple positions, with colors corresponding to those of the curves in (a).

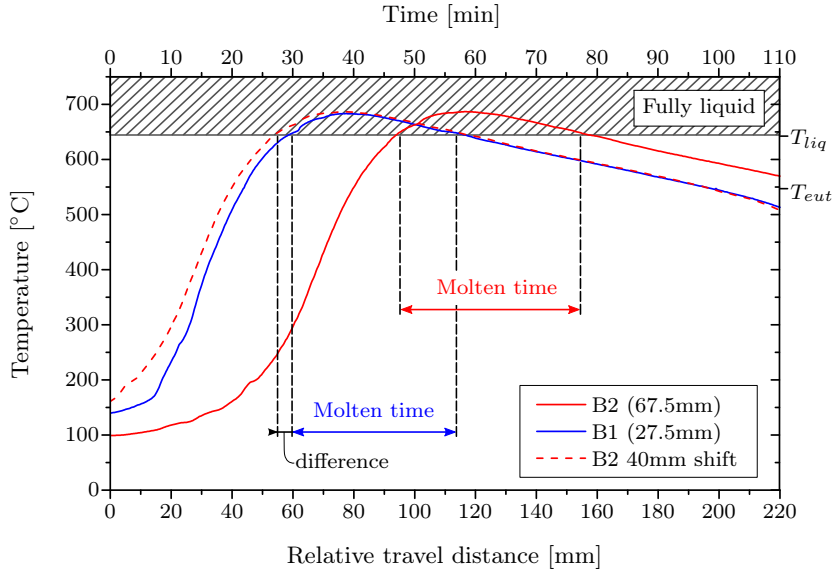


Figure 4.4: Same temperature curves of Fig. 4.3 showing the molten region. The red dotted line corresponds to the curve of thermocouple B2 shifted by 4 cm, the distance separating the two thermocouples.

4.2. Temperature characterization

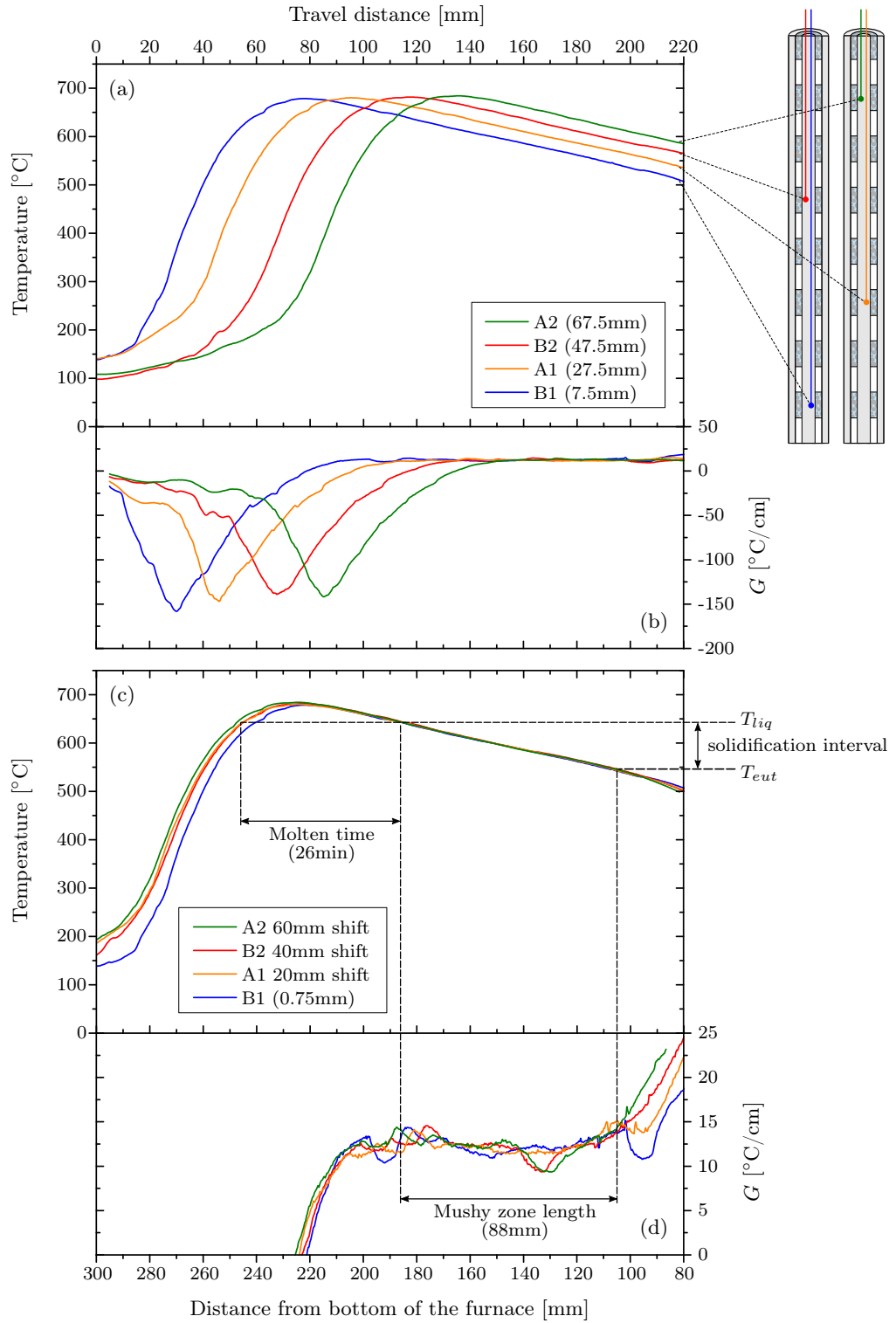


Figure 4.5: (a) Temperature curves and (b) respective thermal gradients, G , of sample type 2 in furnace II obtained from four thermocouples placed in two specimens A and B. In (c) and (d) the temperature and gradient curves are shifted by their corresponding height difference for comparison.

experiment, the temperature curves were measured with two different specimens, A and B. As shown in Fig. 4.5(c), once shifted, all the temperature curves, measured with thermocouples placed at different positions within the sample, are well superimposed, especially in the cooling region. The time during which the pellets are molten is similar for all of them (about 26 min). Only thermocouple B1 exhibits a slightly different heating curve. This can be explained by the fact that B1 is in the proximity of the bottom of the sample and thus, when the sample enters in the hot part of the furnace, there is an initial transient. However, this effect is not seen for the other thermocouples, and this suggests that steady-state conditions are nearly achieved with furnace II and sample type 2. The experiment is also reproducible, since the curves were obtained from two distinct specimens. When compared to furnace I and sample type 1, furnace II and sample type 2 allow to obtain a lower average gradient ($11.7^{\circ}\text{C}/\text{cm}$ instead of $17.0^{\circ}\text{C}/\text{cm}$) with less variations. In addition, with furnace II and sample type 2, it was possible to obtain steady-state conditions, which was unfortunately not possible with the previous configuration.

4.2.3 Furnace II - sample type 3

The aim of this section is to compare the two different sizes of sample (3.6 mm diameter for type 2 and 1.1 mm for type 3) both used in furnace II. The temperatures measured in specimen C (Fig. 3.5(d)) were compared with those of specimen B (Fig. 3.5(c)), with the same thermocouples positions. The temperature of the furnace zones remained unchanged (see Table 4.2, No 5 settings) and the main results are summarized in Table 4.3.

Table 4.3: Main results for furnace II and sample type 3.

Molten time [min]	\overline{G} [$^{\circ}\text{C}/\text{cm}$]	σ_G [$^{\circ}\text{C}/\text{cm}$]
35	10.4	1.1

The temperature curves and thermal gradients measured in specimen C (reduced diameter of 1.1mm) are shown in Fig. 4.6. Compared to the experiment performed with larger diameter, the time during which the sample remains molten is significantly larger (35 min instead of 26 min), while the average thermal gradient is smaller ($10.4^{\circ}\text{C}/\text{cm}$ instead of $11.7^{\circ}\text{C}/\text{cm}$). Also, as shown in Fig. 4.7, steady-state conditions are achieved, since the two cooling curves shifted by the distance separating the two thermocouples are superimposed (red dotted and blue curves). However, the data collected with specimen C are less reliable than those previously measured for samples A and B since the thermocouples were outside of the crucible and no longer at the center of the sample.

The comparison of the temperature curves and gradients of sample type 3 and type 2 is shown in Fig. 4.8. During the cooling part of the curves for temperatures between 675°C and 600°C , the temperature curves of the sample possessing different diameters are well superimposed, while they deviate outside of this range. The fact that the peak

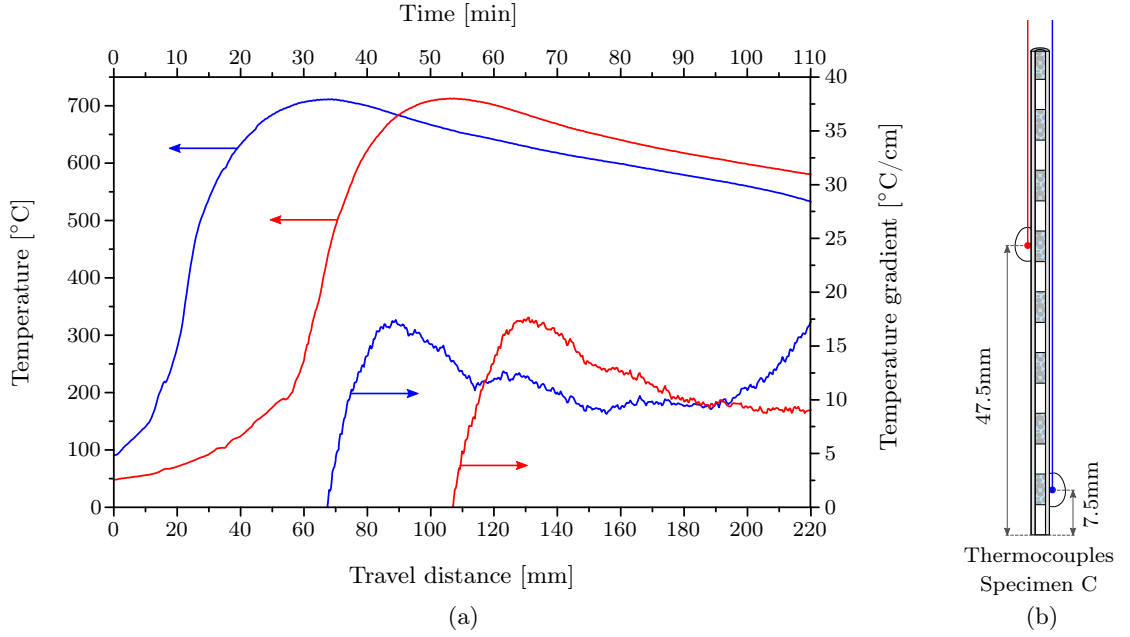


Figure 4.6: (a) Temperature curves and thermal gradients, G , measured for sample type 3 in furnace II, $v_{pull} = 2$ mm/min. (b) Detail of the thermocouple positions, which colors corresponding to those ones of the curves in (a).

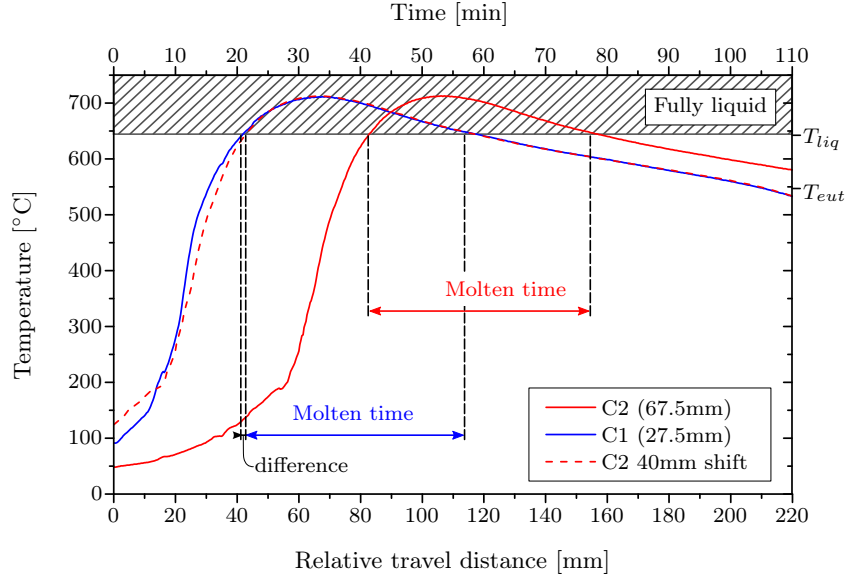


Figure 4.7: Same temperature curves of Fig. 4.6, showing the molten region. The red dotted line corresponds to the curve measured by thermocouple C2 shifted by 4cm, the distance separating the two thermocouples.

temperature is higher for the smaller diameter sample could be explained by the fact that the efficiency of the water-cooled copper chill installed at the top of the furnace is decreased, since there is larger distance separating the sample and the cooler. The

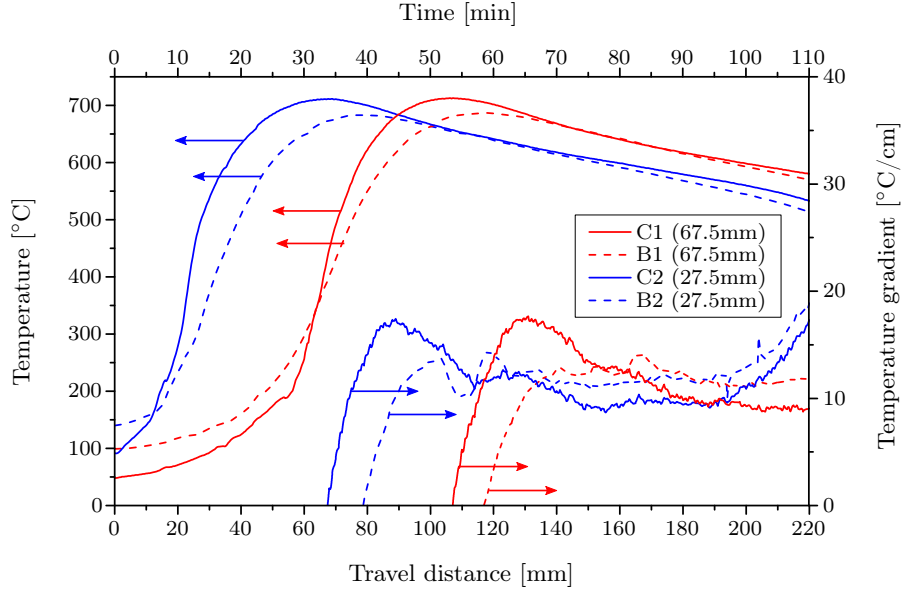


Figure 4.8: Temperature curve of sample type 3 (solid lines) and sample type 2 (dotted lines) in furnace II measured by two thermocouples in each sample (C1 and C2 respectively B1 and B2), $v_{pull} = 2 \text{ mm/min}$.

other reason, as explained before, can be the higher sensitivity of the specimen C to the external temperature imposed by the furnace, due to the positioning of the thermocouples outside of the crucible.

4.2.4 Measured cooling rates and comparison

The thermal exchanges between a specimen and Bridgman furnace are complex, as explained in [79, 80]. It is thus not surprising that the cooling rate of the specimen is affected by the latent heat release during solidification of the alloy. This can result in a significant change of cooling rate, defined hereafter as “thermal arrest”. By comparing the cooling rates observed in different samples configuration, it is then possible to explain the differences in grain size observed in section 4.5.

Figure 4.9 shows the absolute value of the cooling rate, $|\dot{T}|$, as a function of time for sample type 1-furnace I and sample type 2-furnace 2. In order to compare them, the time axis has been adjusted for each curve in such a way that the liquidus temperature is reached at around the same time (200s). It can clearly be observed that sample type 1 (thermocouples O1 and O2) experiences virtually no thermal arrest, while in sample type 2 (thermocouples A1, A2, B1 and B2) it is much more pronounced. In addition, the measured cooling rate curves of sample type 2 show two subsequent thermal arrests. These are delayed by approximately 400s or 13.3mm when converted in a distance with

the pulling velocity of 2 mm/min. This distance is on the same order of the distance separating the centers of the pellets. This indicates that the thermocouples can “feel”, not only the thermal arrest of the pellet in which they are inserted, but also that of the neighbouring upper pellet.

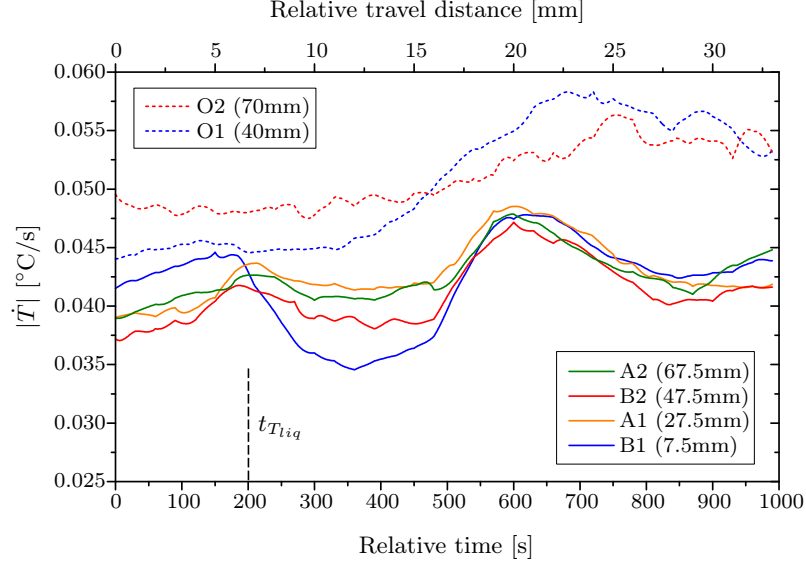


Figure 4.9: Absolute cooling rate as a function of time near the liquidus temperature. All the curves are shifted in order to superpose them and the thermocouple reaches the liquidus temperature at approximately 200s.

4.3 Thermal simulation

With the thermal simulations performed with CALCOSOFT® [70], it is possible to access to the temperature profile within the whole sample, including for example the ceramic separators. In addition, it is then possible to obtain the cooling curves at specific locations in the sample and compare them with the experimental results.

4.3.1 Observed thermal arrests and comparison with experiments

In order to compare the results with the experiments, the external thermal gradient of the furnace in the simulation, G_{ext} , is set accordingly to the measured cooling rate experienced by the sample above the liquidus temperature. A good agreement with the experiments was found for G_{ext} set to 15.5°C/cm for furnace I (associated to sample type 1) and 13.5°C/cm for furnace II (associated with sample type 2). One can also observe in Figs. 4.10 and 4.11 that the general behaviour of the simulated curves is in good agreement with the experiments for both specimen types. The only noticeable difference is the fact that the second thermal arrest in Fig. 4.11 (due to the solidification of a neighbouring pellet) is less pronounced in the simulations.

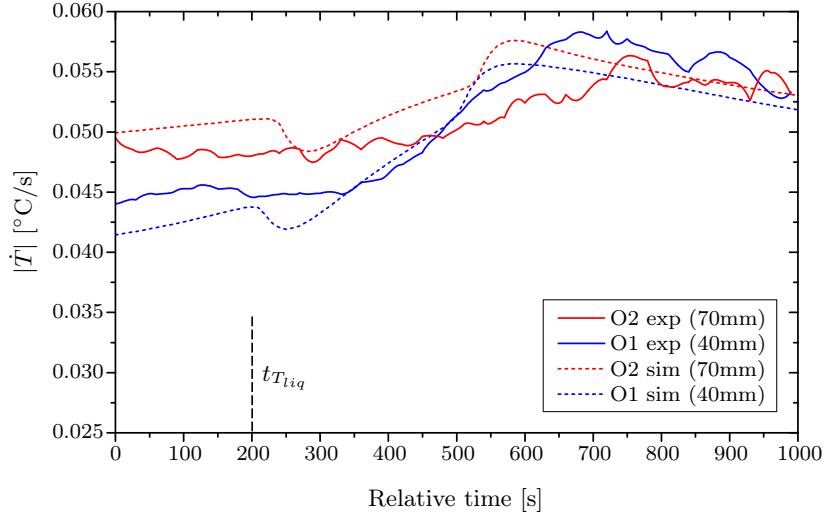


Figure 4.10: Simulated and measured absolute cooling rate as a function of time near the liquidus temperature for sampe type 1 in furnace I.

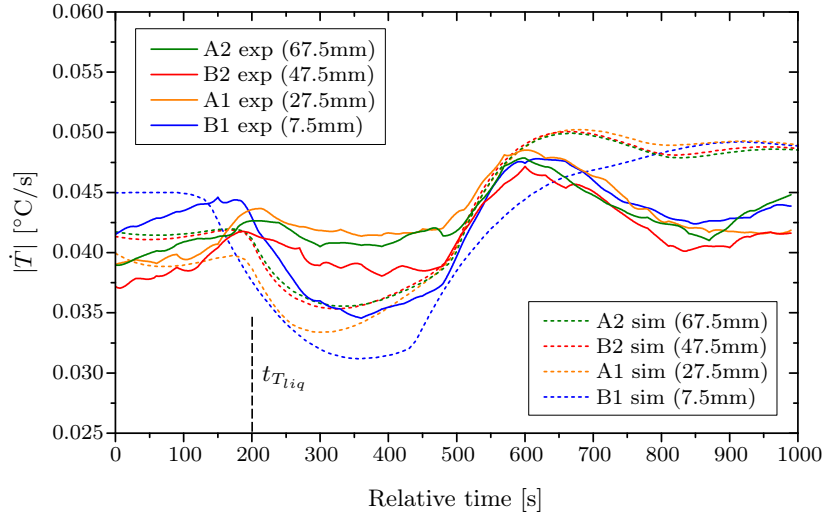


Figure 4.11: Simulated and measured absolute cooling rate as a function of time near the liquidus temperature for sample type 2 in furnace II.

4.3.2 Furnace I - sample type 1

The simulated temperature profile at the center of the sample type 1 is shown in Fig. 4.12 at different times. The dotted line represents the imposed thermal gradient of the furnace set to $15.5^{\circ}\text{C}/\text{cm}$. It is clearly visible that the profile within the sample deviates from the imposed curve, due to the thermal conductivity of the sample. The thermal conductivity tends to lower the gradient inside the sample compared to the imposed one: the longitudinal thermal gradient at the center of the sample is on the order of $10.5^{\circ}\text{C}/\text{cm}$ (measured on the simulated curve at 4000s between from 40 mm and 200 mm from the

bottom) compared to the imposed value of $15.5^\circ\text{C}/\text{cm}$. This corresponds to a relative decrease of 32% of the thermal gradient.

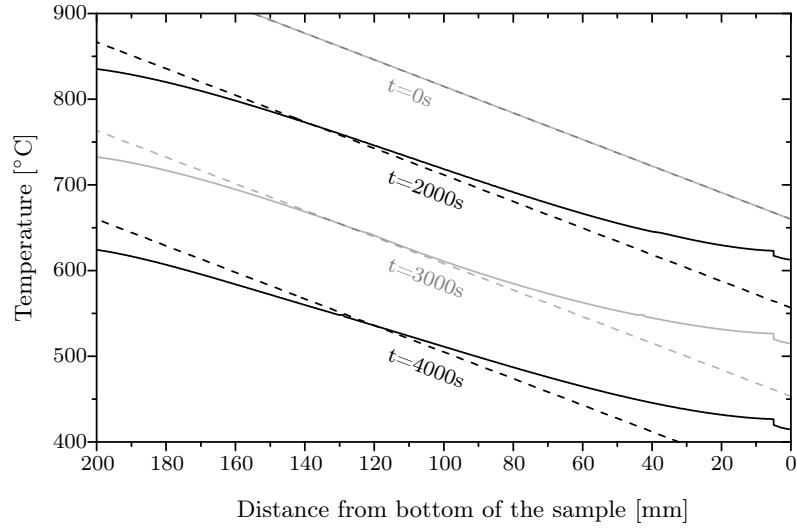


Figure 4.12: Temperature profiles for sample type 1 in furnace I with an imposed external thermal gradient, $G_{imp} = 15.5^\circ\text{C}/\text{cm}$ (dotted line), at four different instants.

4.3.3 Furnace II and sample type 2

In Fig. 4.13, the simulated profile at the center of sample type 2 in furnace II for different times is shown. As shown in more details in Fig. 4.14, the temperature profile exhibits jumps at each interface between the alloy and the separator. As expected, the gradient in the alloy, due to its higher thermal conductivity, is smaller compared to the ceramic.

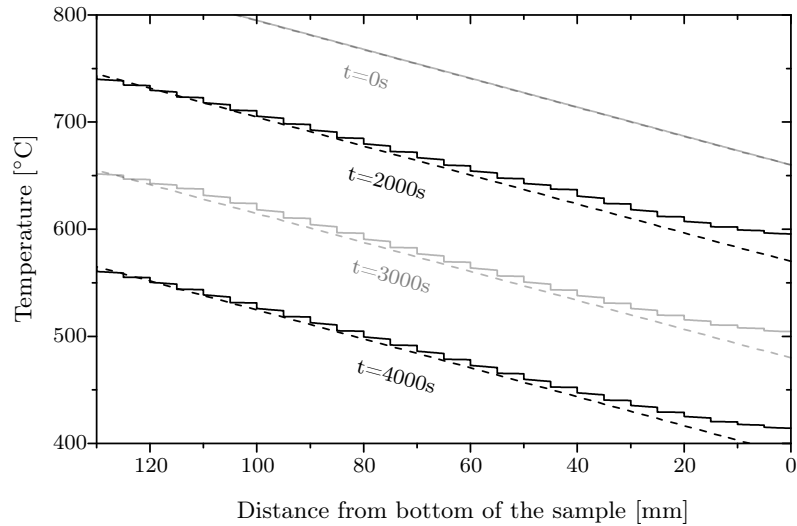


Figure 4.13: Temperature profiles for sample type 2 in furnace II with an imposed external thermal gradient, $G_{imp} = 13.5^\circ\text{C}/\text{cm}$ (dotted line), at four different instants.

Like in the simulation of sample type 1 in furnace I, it can be observed that the thermal conductivity tends to lower the average gradient in the center of the sample as compared with the imposed temperature profile: inside the sample the gradient is on the order of $12.5^{\circ}\text{C}/\text{cm}$ (measured on the simulated curve at 3000s in the region 20 mm to 130 mm from the bottom) while the imposed value is $13.5^{\circ}\text{C}/\text{cm}$. This corresponds to a small decrease of 7% of the thermal gradient, compared to the 32% decrease of sample type 1 (section 4.3.2).

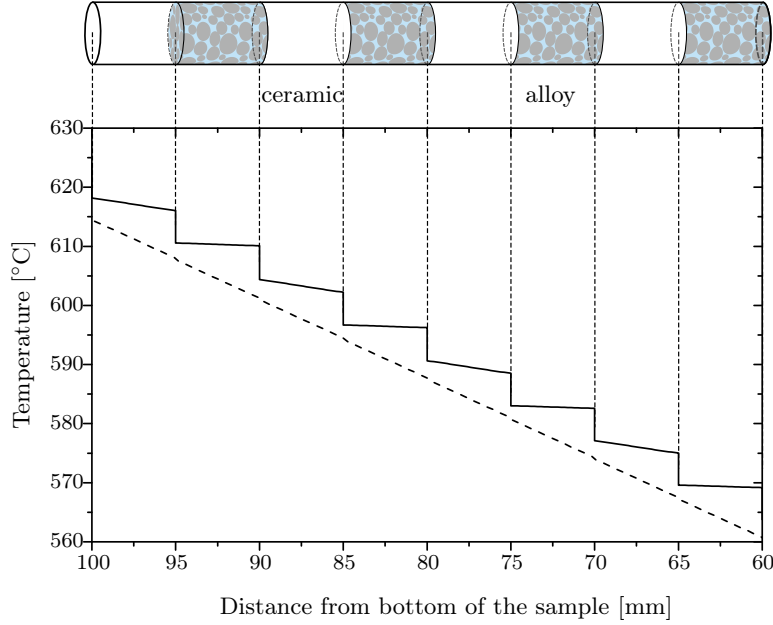


Figure 4.14: Detailed zoom of Fig. 4.13 showing the temperature profile at $t=3000\text{s}$. In addition, a schematic drawing of the sample is shown.

The average gradient measured at the center of the sample cannot be predicted by an analytical calculation. However, once the final average gradient in the center of the sample is known, with a simple heat conservation equation (see Appendix A.1), it is possible to know how the gradient and temperature jumps are distributed. In the portion of the sample shown in Fig. 4.14, the average gradient, \overline{G} , is equal to $13.5^{\circ}\text{C}/\text{cm}$, i.e., the same value as the gradient imposed by the furnace. It is then possible to find the temperature drop at the interface ΔT_{int} as well as the thermal gradient in the pellet and in the separator, noted as G_{pel} and G_{sep} , respectively. All these values are summarized

Table 4.4: Comparison of a thermal simulation result and the respective analytical calculation (based on the expressions found in Appendix A.1) for sample type 2 and an average thermal gradient of $13.5^{\circ}\text{C}/\text{cm}$.

	ΔT_{int} [$^{\circ}\text{C}$]	G_{pel} [$^{\circ}\text{C}/\text{cm}$]	G_{cer} [$^{\circ}\text{C}/\text{cm}$]
Simulation	5.43	0.57	3.87
Analytical	5.65	0.63	3.77

in Table 4.4 and compared with the analytical calculation developed in Appendix A.1. The analytical calculation results are in good agreement with the simulation ones.

4.4 Grain movement and associated macrosegregation

In this section, we present the macrosegregation profiles measured by EDX in sample type 1 solidified in furnace I. As explained in section 2.7, the grains tend to sediment in Al-Cu alloys containing less than 10wt%Cu (leading to a negative macrosegregation at the bottom of the sample), while they tend to float for compositions larger than 10wt%Cu (leading to a positive macrosegregation at the bottom of the sample).

In Fig. 4.15 is shown the composition profile of an Al-9.0wt.%Cu sample. Even if the alloy composition is lower than 10wt%, the sample exhibits a positive macrosegregation at its bottom. This can be explained by the fact that the sample is initially kept in the liquid state for 40min. During this amount of time, the copper can redistribute towards the bottom of the sample, where the composition can locally exceed 10wt%. The first solid grains that solidify at the bottom of the sample will have the tendency to float and remelt since they then attain temperatures that are potentially higher than the liquidus. In addition, please note that, as shown in Fig. 2.28, even if the first solid that nucleates possesses a slightly larger density than the liquid (and thus initially tends to sediment), at more advanced solidification stage, this relation is inverted and thus grain flotation is induced.

Because of the floating and remelting of grains, the bottom of the sample consists in fact of eutectic only (confirmed by the fact that the composition is on the order of the eutectic composition at 33wt%Cu).

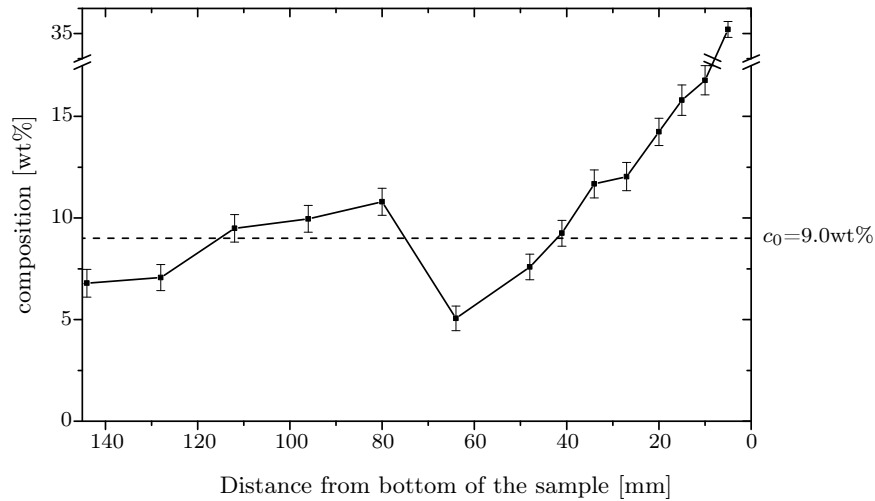


Figure 4.15: Mean Cu composition of the sample type 1 (furnace I) as a function of the position from the bottom. The nominal composition of the sample is 9wt% and the sample was inoculated with 2.0wt% AlTi5B master alloy.

The composition profile of an Al-4.5wt.%Cu alloy is shown in Fig. 4.16. For this sample there is no evidence of significant macrosegregation. The small positive macrosegregation that can be observed at the bottom is due to the fact that, as explain before, the sample is initially kept in the molten state for 40min. From 25mm from the bottom upwards the composition is slightly lower than the nominal composition: because of the sedimentation of grains (that contain less copper than the liquid phase), the bottom of the sample is impoverished in copper.

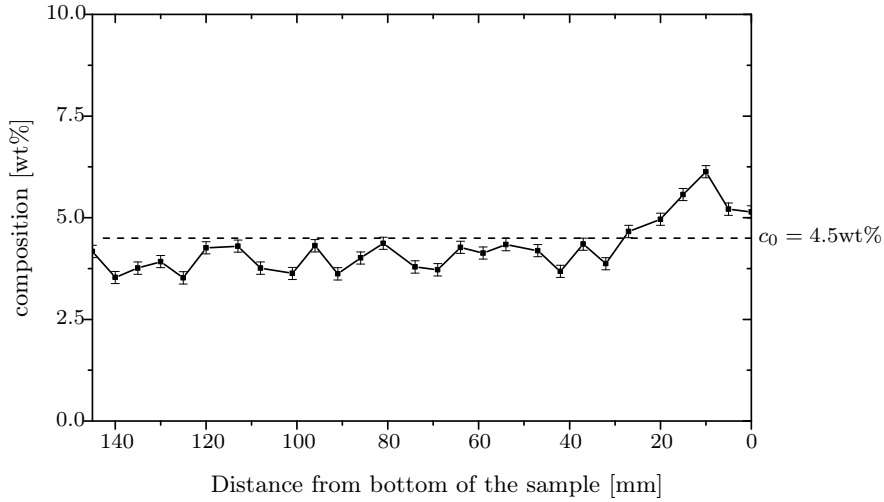


Figure 4.16: Mean Cu composition of sample type 1 (furnace I) as a function of the position from the bottom. The nominal composition of the sample is 4.5wt% and the sample was inoculated with 2.0wt% AlTi5B master alloy.

As a conclusion a slight sedimentation is always preferred (observed in practice for Cu content on the order of 6wt% or lower) in order to avoid having grain remelting as well as a strong positive macrosegregation at the bottom of the sample.

4.5 Grain size and misorientation distributions

In this section, the final grain sizes of the different sample types and alloy materials are measured by EBSD analysis in longitudinal sections. This was performed in order to benchmark the effects of solute content, inoculant addition and sample type. The results are also compared with EBSD measurements performed on sample solidified *in situ*. The distribution of misorientation angles was measured and compared to theoretical data in order to assess whether the structure is fully equiaxed.

4.5.1 Misorientation distributions

Figure 4.17 shows the misorientation distribution of the grain boundaries measured in a sample type 3 obtained in furnace II. These experimental distributions can be compared

4.5. Grain size and misorientation distributions

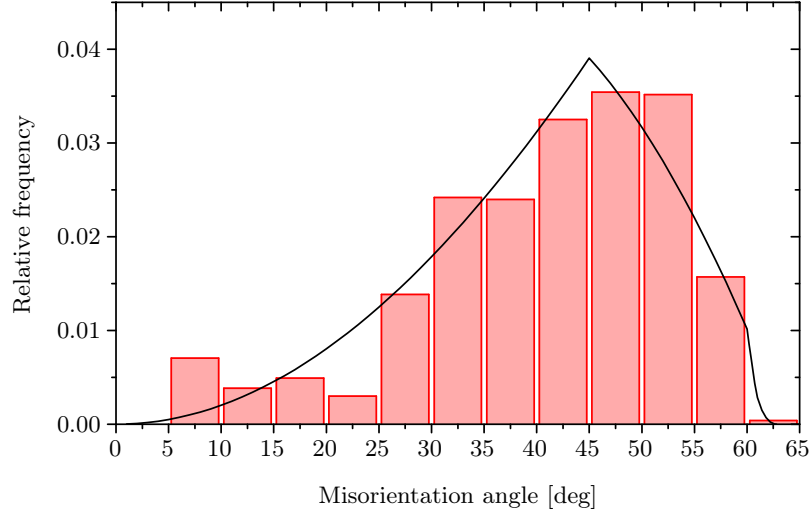


Figure 4.17: Misorientation angle distribution for an Al-4.5wt.%Cu (with 2wt% of inoculant) sample type 2 obtained in furnace II. The black solid line corresponds to a fully random distribution, given by the Mackenzie plot [81].

with the so-called Mackenzie plot [81], consisting in the misorientation distribution of randomly oriented grains of cubic symmetry. The experimental distributions follow fairly well the random distribution, thus indicating that the structure is fully equiaxed and that there is no particular texture in the sample. All the other samples exhibit a similar distribution and do not show a strong deviation from the Mackenzie plot.

4.5.2 Grain size

The various final grain sizes, were observed for different copper compositions, inoculant additions, and solidification conditions, as shown in Fig. 4.18. The results are summarized in Table 4.5. The tests are numbered from 1 to 5, the reference being noted “R”.

Table 4.5: Final average grain size, d_{90}^{2D} (the 2D superscript indicates that the grain size results from a surface cut measurement), measured by EBSD as a function of composition, sample type and furnace, with respect to the reference test noted “R”. Please note that the *in situ* sample was also analyzed for comparison.

Test	Alloy	inoculant [wt.%]	Sample	Furnace	d_{90}^{2D} [μm]
R	Al-4.5wt.%Cu	2.0	3	II	249
1	Al-6.0wt.%Cu	2.0	3	II	288
2	Al-3.0wt.%Cu	2.0	3	II	229
3	Al-4.5wt.%Cu	0.4	3	II	423
4	Al-4.5wt.%Cu	2.0	2	II	211
5	Al-4.5wt.%Cu	2.0	<i>In situ</i>		150
6	Al-4.5wt.%Cu	2.0	1	I	109

Chapter 4. Bridgman furnace results

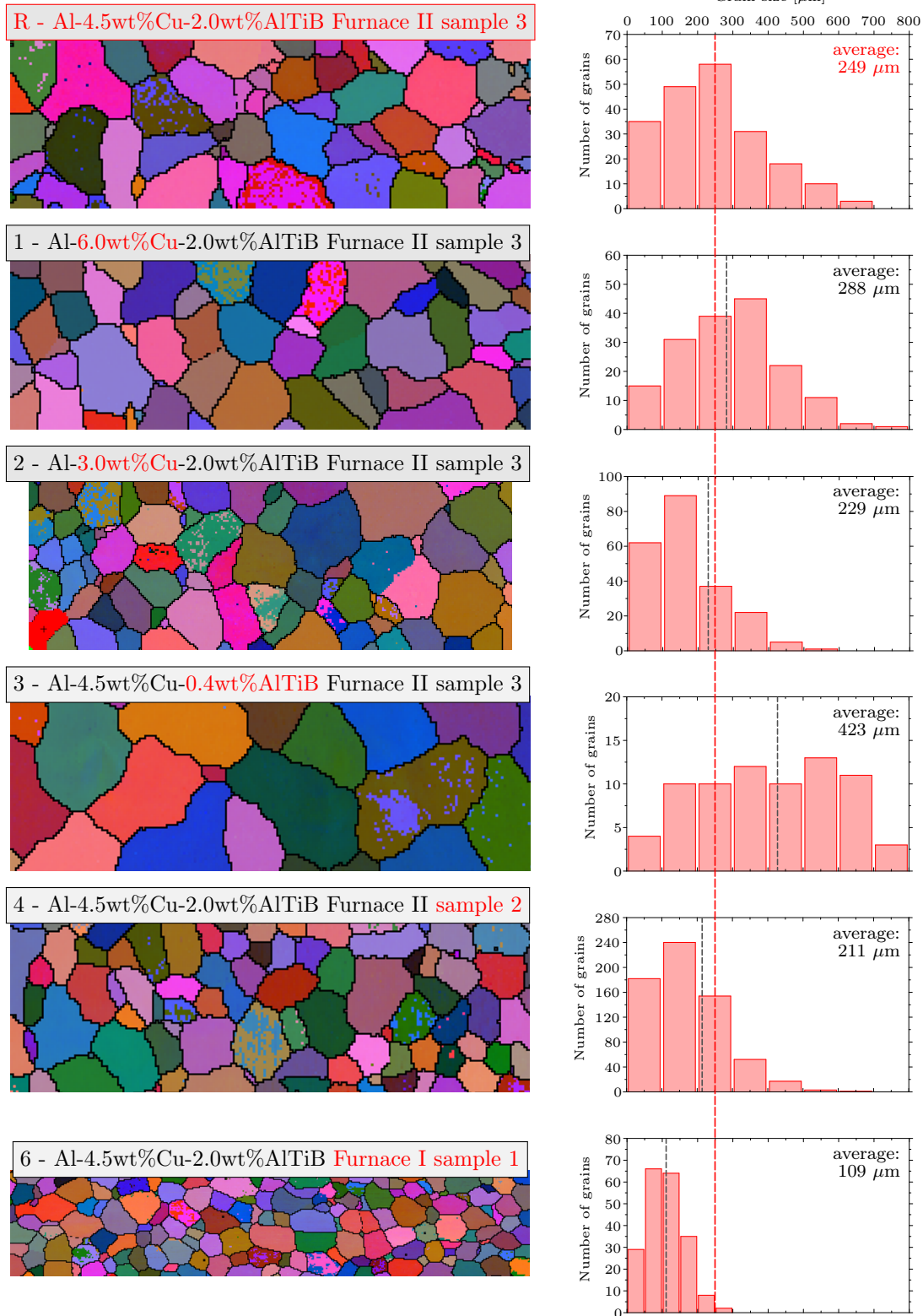


Figure 4.18: (a) EBSD image and (b) grain size distribution of various samples (the average grain sizes are represented by a gray dotted line, the reference being in red).

4.5. Grain size and misorientation distributions

The following tendencies have been observed:

Composition The final grain size slightly increases with increasing nominal composition. However, the variation is small and it can be stated that the alloy composition has virtually no effect on the final grain size.

Inoculant content The inoculant content however has a strong influence on the final grain size: the grain size is almost divided by a factor two when the inoculant content is increased from 0.4wt% to 2.0wt%. The ratio of the grain sizes between test 3 and the reference test R is $423\mu\text{m}/249\mu\text{m} = 1.7$. This ratio scales exactly as the cubic root of the inverse of the ratio of the inoculant content: $\sqrt[3]{2.0\text{wt.}\%/0.4\text{wt.}\%} = 1.7$. This indicates that, for this conditions (namely low cooling rates), the nucleation site density increases with the inoculant content, i.e., the inoculant has not reach a saturation level.

Sample diameter The diameter of the sample has virtually no effect on the final grain size.

In situ In the *in situ* experiment the cooling rate is fixed and imposed by the laser-heated furnace. Therefore, there is virtually no thermal arrest. This allows to activate more nucleation sites (i.e. nucleation particles that require higher undercoolings) and results in a finer final grain size.

Monolithic sample The finest grain size of all the experiments is observed in sample type 1 solidified in furnace I. Since the larger diameter sample was used for this experiment, it is more accurate to compare it with test 4, similar to the reference experiment but with the larger diameter. The comparison of test 6 with test 4 shows that the grain size obtained in sample type 1 is significantly lower by a factor 2. This can be explained by the fact that the thermal arrest that takes place during solidification is much less pronounced in sample type 1, compared to the samples in which the alloys are separated where it prevents further activation of the inoculant particles. However, the explanation is more complex, since in test 6 the grain is even finer than for the *in situ* experiment, which should result in the finest grain size by taking into account thermal aspects only. The more plausible explanation is that the sedimentation that takes place in the monolithic sample yields a finer grain size.

4.5.3 Simulation with nucleation model

In this section, the results of the grain sizes simulations performed with the model proposed by Appolaire [68, 71] are presented. The simulation results are compared with the EBSD analysis (shown in Table 4.5). Please note that, in the EBSD analysis, the observed grain size, d_{g0}^{2D} , corresponds to the diameter of the circle that fits the surface

Chapter 4. Bridgman furnace results

(number of pixels) associated to each grain. On the other hand, the grain size obtained with the simulations corresponds to the diameter of an equivalent sphere, d_{g0} . In order to perform a comparison between the simulations and the experiments, it is needed to convert the diameter to a common measure.

The average observed grain radius in a 2D cut, R_{g0}^{2D} , can be linked with the radius of an equivalent sphere, R_{g0} :

$$\pi [R_{g0}^{2D}]^2 = \frac{1}{R_{g0}} \int_0^{R_{g0}} \pi(R_{g0}^2 - z^2) dz = \frac{2\pi}{3} R_{g0}^2 \quad (4.1)$$

Therefore, the following relationship can be found:

$$d_{g0} = \sqrt{\frac{3}{2}} d_{g0}^{2D} \quad (4.2)$$

The simulated values and the converted experimental ones are summarized in Table 4.6.

Table 4.6: Final average grain size, d_{g0} , measured by EBSD (surface measurement converted into an equivalent 3D grain size) and by the model proposed by Appolaire *et al.* [68, 71].

Test	Alloy	inoculant [wt. %]	Sample	Furnace	EBSD d_{g0} [μm]	Simulation d_{g0} [μm]
R	Al-4.5wt.%Cu	2.0	3	II	305	383
1	Al-6.0wt.%Cu	2.0	3	II	353	378
2	Al-3.0wt.%Cu	2.0	3	II	280	385
3	Al-4.5wt.%Cu	0.4	3	II	518	446
4	Al-4.5wt.%Cu	2.0	2	II	258	393
5	Al-4.5wt.%Cu	2.0	<i>In situ</i>		184	203

The same tendencies are observed for the EBSD measurements and the simulated results when the inoculant content is changed (test 3 versus R) and for the comparison between the *in situ* experiment and the solidification with sample type 3 and Furnace II configuration (test 5 versus R). However, stronger variations are observed between the EBSD measurements of the various cases. Please note that the ratio of the grain sizes between test 3 and the reference test R does not scale as the cubic root of inverse of the ratio of the inoculant content. The simulation results thus indicate that the inoculant is closer to achieving a saturation level, while the EBSD measurements suggested that this was not the case.

The simulation predicts an inverse tendency for the final grain size dependence with respect to the alloy nominal composition (decrease of d_{g0} for an increased nominal composition for the simulation and inverse tendency for the EBSD measurement as shown in test 1 and 2 versus R) and with respect to the sample diameter (test 4 versus R). However, the variations between the various cases are small, especially in the simulation results.

4.5. Grain size and misorientation distributions

Test 6 was not simulated since the aim of this section was to perform calculation by considering only thermal and solute diffusion aspects and relate them to final grain size, without taking into account grain sedimentation/floatation.

5 Modeling

5.1 Multiphase-field model

5.1.1 Introduction

The phase-field method is an effective approach for describing the solidification of metallic alloys. However, in the case of equiaxed grains, since the standard phase-field method considers only two phases (solid and liquid), the grain boundary energy due to the misorientation between impinging grains, and the associated coalescence undercooling, cannot be taken into account: the last-stage solidification is thus not correctly described. In order to account for coalescence undercooling, two approaches can be performed. The first one is the orientational method [82–87], in which, in addition to the phase-field, an orientation-field is introduced. The second is the multiphase-field method [88–90], in which each solid grain is described by a different phase in order to take into account these misorientations, even though all the grains have the same thermodynamic properties. In the present work, since a multiphase-field code [91] was already available, the second method has been chosen.

5.1.2 Formulation

The present model can handle the evolution of an arbitrary number N of phases. Each phase-field varies smoothly from zero to unity with the constraint that $\sum_{i=1}^N \phi_i = 1$ everywhere. The liquid phase is represented by the phase-field ϕ_1 , while each phase-field ϕ_i with $i \in [2, N]$ indicates a solid grain with its own crystallographic orientation. The phase-fields can be seen as local fractions of a specific phase, the interface between two phases being located where the two phase fields are equal to 0.5. One can define a vector ϕ of dimension N , whose components ϕ_i represent the various phase-field variables.

First, in order to obtain an evolution equation, a free energy functional has to be defined. The functional, based on the work of Steinbach *et al.* [88], has the following form:

$$\mathcal{F} = \int_{\Omega} \left(\sum_{i,j>i} \frac{\epsilon_{ij}^2}{2} |\phi_i \nabla \phi_j - \phi_j \nabla \phi_i|^2 + g_{mo}(\phi, T) + f_{tr}(\phi_1, c, T) + \Lambda \left[\sum_i \phi_i - 1 \right] \right) d\Omega \quad (5.1)$$

where c is the solute composition, T is the actual temperature and ϵ_{ij} is associated with the first interfacial energy contribution. Note that Λ is a Lagrange multiplier added to the equation in order to ensure that $\sum_{i=1}^N \phi_i = 1$. The second interfacial energy contribution is accounted for in the term g_{mo} which consists in the following multiobstacle potential:

$$g_{mo}(\phi, T) = \underbrace{\sum_{i<j} W_{ij} \phi_i \phi_j}_{g_{mo,1}} + \underbrace{\sum_{i<j<k} 9(W_{ij} \phi_k + W_{ik} \phi_j + W_{jk} \phi_i) \phi_i \phi_j \phi_k}_{g_{mo,2}} \quad (5.2)$$

where the $g_{mo,1}$ term can be related to the height of the multiobstacle potential between two phases, while the $g_{mo,2}$ term is added in order to avoid the spontaneous appearance of “ghost” phases at the interface between two other phases. Details about the choice of the multiobstacle g_{mo} potential are given in section B.1.1. Please note that the $g_{mo,2}$ term can lead to negative values of the phase-field variables. This is avoided with a numerical algorithm, similar to the one originally proposed by Cogswell *et al.* [92], that projects back the phase-field values in the Gibbs simplex, defined by $\Sigma := \{\phi \in \mathbb{R}^N \mid \sum_{i=1}^N \phi_i = 1, \phi_i \geq 0\}$.

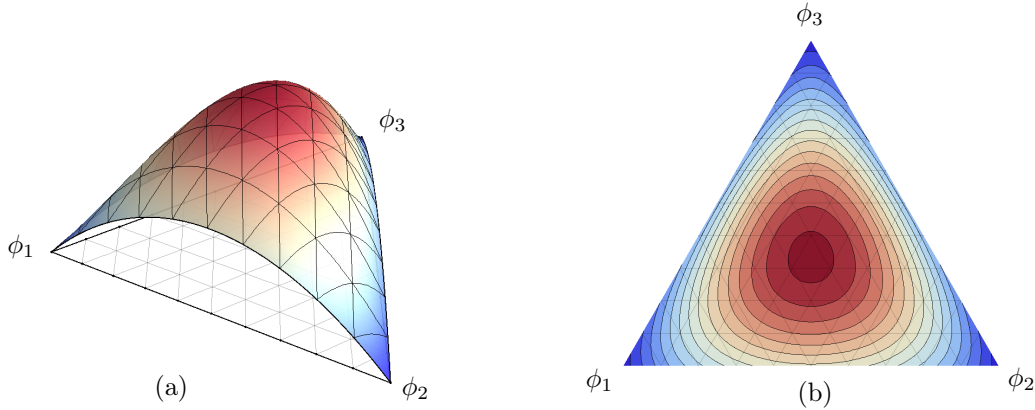


Figure 5.1: (a) Multiobstacle potential of $g_{mo}(\phi)$ for $W_{12} = 1.8$ and $W_{13} = W_{23} = 1$ and (b) relative colormap plot in the Gibbs simplex.

The Gibbs free energy per unit volume associated with the phase transformation, f_{tr} , is a function of solute composition and temperature and a function of the liquid phase-field variable ϕ_1 only, since the bulk Gibbs free energies of the $(N - 1)$ solid phases are identical.

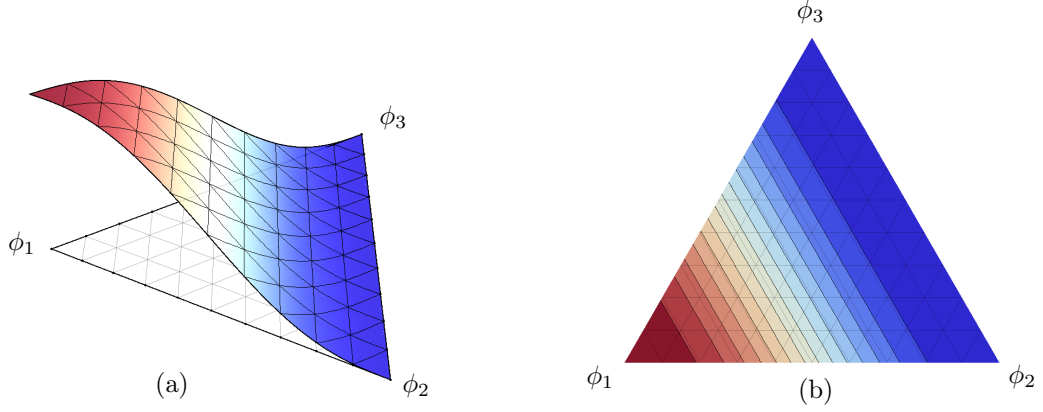


Figure 5.2: (a) Ternary plot of the interpolation function $p(\phi_1)$ and (b) relative colormap.

For a binary alloy it has the following form:

$$f_{tr}(\phi_1, c, T) = \Delta S_f \Delta T(\phi_1, c) p(\phi_1) \quad (5.3)$$

$$\text{with } \Delta S_f = L_f/T_m, \quad \Delta T = T_{liq} - T, \quad \text{and } p(\phi_1) = \phi_1^3(6\phi_1^2 - 15\phi_1 + 10)$$

where ΔS_f is the volumetric entropy of fusion, ΔT the undercooling, L_f the volumetric latent heat, T_m the melting temperature, and T_{liq} the liquidus temperature. Since ϕ_1 can be considered as a local liquid fraction, the liquidus temperature is defined as:

$$T_{liq} = T_m + m_\ell c_\ell = T_m + m_\ell \frac{c}{\phi_1 + k_0(1 - \phi_1)} \quad (5.4)$$

By taking the functional derivative with respect to an arbitrary phase-field variable ϕ_i and considering the Ginzburg-Landau theory, one can obtain the phase equation:

$$\begin{aligned} \frac{1}{M_{ij}} \frac{\partial \phi_i}{\partial t} = -\frac{\delta \mathcal{F}}{\delta \phi_i} = & \left(\sum_{j \neq i} \epsilon_{ij} [\phi_j^2 \nabla^2 \phi_i - \phi_i \phi_j \nabla^2 \phi_j - 2\phi_i (\nabla \phi_j)^2 + 2\phi_j \nabla \phi_i \nabla \phi_j] \right) \\ & - \left(\sum_{j \neq i} W_{ij} \phi_j + 9 \sum_{j < k, j \neq i, k \neq i} \phi_j \phi_k (W_{ij} \phi_k + W_{ik} \phi_j + 2W_{jk} \phi_i) \right) \\ & - \left(30 \sum_{j \neq i} \Delta G_{ij} \phi_j^2 (1 - \phi_j)^2 \right) - \Lambda \end{aligned} \quad (5.5)$$

$$\text{with } \Delta G_{ij} = \begin{cases} +\Delta S_f \Delta T & \text{if } j = 1 \\ -\Delta S_f \Delta T & \text{if } i = 1 \\ 0 & \text{else} \end{cases}$$

where the M_{ij} term corresponds to a mobility coefficient of the diffuse interface between

two phases i and j . The phase-field parameters can be linked to the interfacial energy γ_{ij} , the interface thickness δ_{ij} and the interface mobility μ_{ij} with the following formula [93]:

$$W_{ij} = \frac{4}{\pi} \frac{\gamma_{ij}}{\delta_{ij}} \quad \epsilon_{ij}^2 = 2W_{ij}\delta_{ij}^2 \quad M_{ij} = \frac{\mu_{ij}}{\delta_{ij}}$$

As shown by Kim *et al.* [94], the dynamics of the phase field model is independent of the choice of the multi-well/obstacle potential (in our case the multiobstacle potential g_{mo}) and of the interpolation function for the Gibbs free energy p , as long as the phase-field parameters are correctly derived from physical parameters.

The phase equation is then coupled with the solute conservation equation:

$$\frac{\partial c}{\partial t} = \nabla \cdot \left[\overline{D}(\phi_1) \left(\nabla c - \frac{(1-k_0)c}{\phi_1 + k_0(1-\phi_1)} \nabla \phi_1 \right) \right] \quad (5.6)$$

$$\text{with } \overline{D}(\phi_1) = D_s + \frac{\phi_1}{\phi_1 + k_0(1-\phi_1)} (D_\ell - D_s)$$

where D_ℓ and D_s are the diffusion coefficients of solute in the liquid and solid phases, respectively. Note that only the phase-field variable of the liquid, ϕ_1 , is considered in this equation.

5.1.3 Implementation and optimization of the code

Eq. (5.5) and Eq. (5.6) are discretized using a finite volume method and an explicit time-discretization scheme. A regular and orthogonal arrangement of nodes is considered. Since the time-discretization is explicit, the time step is limited by a Fourier condition on both Eq. (5.5) and Eq. (5.6):

$$\frac{M_{ij}\epsilon_{ij}\Delta t}{h_{mesh}^2} < \frac{1}{2P} \quad \frac{\max(D_\ell, D_s)\Delta t}{h_{mesh}^2} < \frac{1}{2P} \quad (5.7)$$

where h_{mesh} is the mesh spacing and P the dimensionality of the problem.

One of the main limiting factors of the phase-field approach is its computational cost. This is in general critical for 3D calculations, but in our multiphase case corresponding to several grains the computational cost is already quite significant in 2D: in order to correctly catch the coalescence phenomenon (see Eq. (2.19)), the interface thickness, $\delta_{s\ell}$, has to match the physical one of the order of 1nm. As a rule of thumb one should consider a mesh size, h_{mesh} , at least 3 times smaller than $\delta_{s\ell}$. By taking a reasonable grain size of $d_{g0} = 100\mu\text{m}$, this means that for a regular square mesh one should have:

$$\frac{d_{g0}}{\frac{1}{3}\delta_{s\ell}} = \frac{10^{-4}m}{\frac{1}{3}10^{-9}m} = 3 \cdot 10^5 \text{ nodes (in 1D)}$$

This corresponds to $9 \cdot 10^{10}$ in 2D and $2.7 \cdot 10^{16}$ in 3D just for a single grain. Trying to simulate the solidification of a large number of grains is thus clearly not feasible with such parameters. Phase-field simulations are generally performed by using an interface thickness 2 to 3 orders of magnitude greater than the physical one (with the addition of an anti-trapping current in order to limit solute trapping induced by a large interface thickness as proposed by Karma [95]), in order to significantly reduce the number of nodes. However, with this approximation, the last-stage solidification would not be correctly described. Another way of reducing the computational cost is to use an adaptive mesh, but unfortunately the multiphase-field code running on a multiple-processors machine that was developed in our laboratory only considers regular meshes. The high computational cost associated with the multiphase-field technique is the main reason why a new mesoscopic model has been developed (see section 5.2). However, the multiphase-field model was used to validate the results of the mesoscopic model in a few simple situations. For that purpose, it was optimized as explained in the following sections.

Optimizations for the phase equations: Parallel computations

One possible way of reducing the computational cost is to use parallel computations, which is based on the principle that large problems can be solved by subdividing them into smaller ones, solved simultaneously on distinct CPUs. Therefore, in a parallel calculation, the computational domain is broken down into a certain number of smaller subdomains and each part is calculated on a single CPU. At each time step, neighboring subdomains (processors) communicate with each other.

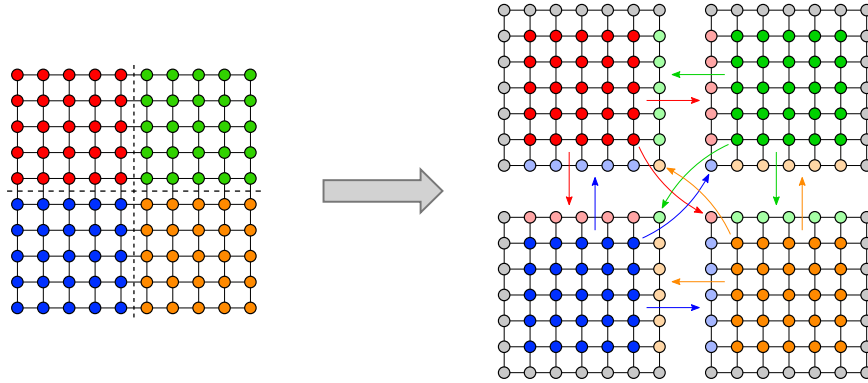


Figure 5.3: Schematic representation of the subdivision of a 2D domain made of 10×10 nodes into 4 subdomains of 7 nodes (red, green, blue and orange). The colored arrows represent data exchange. Phantom nodes possess the same color, but shaded, as the node they duplicate. The gray nodes are used to impose boundary conditions.

In the multiphase-field code developed at EPFL and used in the present project, the domain is split into blocks of equal size and the phase and solute equations (Eq. (5.5) and Eq. (5.6)) are solved on separate CPUs. At each time step, the outer layer of nodes of a block is transmitted to the neighbouring CPUs and stored as an additional layer of

so-called phantom nodes. Communication between the processors is done through the Message Passing Interface (MPI) language. For the blocks positioned near a boundary of the simulation domain, the phantom nodes that are not linked to another block (nodes in gray in Fig. 5.3) are used to impose boundary conditions. Since they do not correspond to any neighbour, they receive no data (except in the case of periodic boundary conditions). The code, initially written in C++ language, was then parallelized using the *MPI library* [96], allowing to perform calculations on a high performance computing machine.

Optimization for the phase equations: Voronoi tessellation and position of the interface

In Eq. (5.5), all the interaction terms between phases have to be calculated. For a system of N phases this corresponds to $N(N - 1)$ terms. One can clearly see that this would be detrimental for the computational cost when considering a large number of grains. In order to limit the number of interaction terms, one has to consider the topology of the grains position. By considering that all the grains nucleate at the same time and the temperature is homogeneous, the final grain structure is given by a Voronoi tessellation of the domain (see Fig. 5.4(a)). For each node of a 2D mesh, only the interaction terms between the three closest grains and the liquid phase are considered (see Fig. 5.4(b)). Therefore, only $4 \times 3 = 12$ interaction terms will be calculated at each node independently of the total number of grains. Note how in Fig. 5.4(b) the final triple junctions fall within a specific zone of the third order Voronoi diagram.

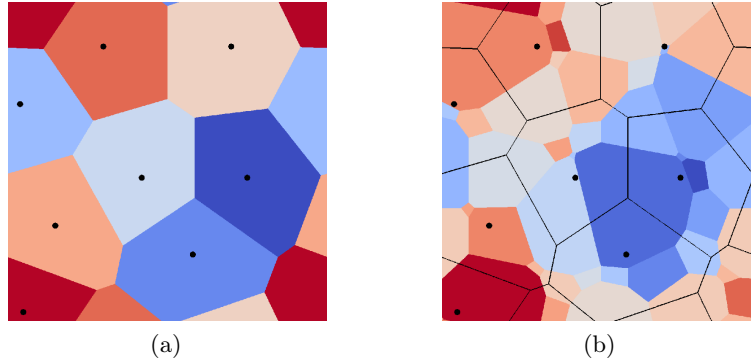


Figure 5.4: (a) First-order Voronoi diagram with periodic boundary conditions, representing the final grain structure. Each color corresponds to a different grain (thus to a different phase-field) and nucleation centers are represented in black. (b) Third-order Voronoi diagram. Each color corresponds to a different triplet of the three closest nucleation centers (indicated by the black points). In this figure, the first order Voronoi diagram is represented with a black line.

An additional optimization consists in evaluating Eq. (5.5) only for nodes that are, or have a neighbour, “within” a diffuse interface (i.e., where $\phi_i \in]0, 1[$).

5.2 Mesoscopic model

5.2.1 Introduction

Despite all the optimizations explained in the previous section, the multiphase-field method is very CPU intensive and thus does not allow considering many grains. Therefore, in the present work, we propose a new mesoscopic model inspired from the 3D granular model developed by Phillion *et al.* [55] and Sistaninia *et al.* [18–21]. The model is developed in order to obtain smoother grain morphologies, thus allowing to predict more accurately the percolation for a large population of grains.

5.2.2 Method

As for the granular model, a Voronoi tessellation is generated from randomly distributed nucleation centers. Up to this point, the steps are identical to the granular model developed by Phillion *et al.* [55]. It is just recalled that this model considers tetrahedra in 3D (triangles in 2D) formed by the nucleation centers as summits and the Voronoi facets to calculate solidification. In the present mesoscopic model, each tetrahedron (triangle) is subdivided into various columns (see Fig. 5.5c) and Fig. 5.5(d)). By connecting the

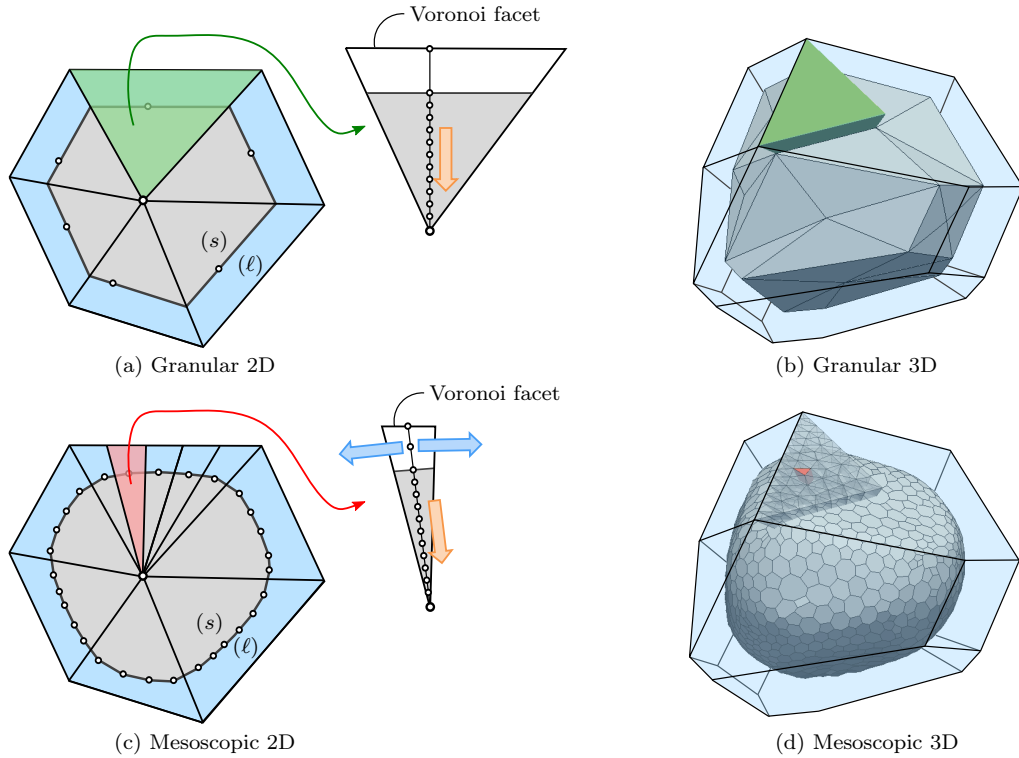


Figure 5.5: Schematic representation of the granular model of Phillion *et al.* [55]: (a) in 2D, (b) in 3D, compared to the new mesoscopic model: (c) in 2D, (d) in 3D.

positions of the solid-liquid interface within the columns, this allows to obtain smoother morphologies and to take into account two important phenomena for coalescence and percolation: (i) back-diffusion in the solid perpendicular to the interface (orange arrow in Fig. 5.5(c)) which was already considered in [55]; (ii) diffusion in the liquid parallel to the interface (light blue arrow in Fig. 5.5(c)). Please note that the exchange of solute between the solid parts of different columns is neglected. The various components of this model are described in the following subsections.

Compositions at the interface and boundary conditions

The granular model of Pillion *et al.* [55], considers a non-uniform solute composition in the solid and complete mixing in the liquid. In the mesoscopic model, non-uniform compositions of solute in both the solid and liquid phases, respectively $c_{s,i}$ and $c_{\ell,i}$, are considered. Within each column, a 1D coordinate system r is defined for the position. The position of the solid/liquid interface and of the facet in a column i are designed by $r_i^*(t)$ and L_i , respectively (see Fig. 5.6 and Fig. 5.7). As shown in Fig. 5.8, the compositions at the Voronoi facet position, $c_{\ell,i}^\infty = c_{\ell,i}(r = L_i)$, are initiated at the nominal composition, c_0 , while the compositions of the liquid at the interface, $c_{\ell,i}^*$, are given by:

$$c_{\ell,i}^*(T, \bar{\kappa}_i) = \frac{T - T_m + 2\Gamma_{s\ell}\bar{\kappa}_i}{m_\ell} \quad (5.8)$$

where T_m is the melting temperature of pure aluminum and $\bar{\kappa}_i$ the mean local curvature of the interface in the i -th column (evaluated from a fitting circle in 2D or sphere in 3D as explained in section 5.2.5). Then, the interfacial solid compositions are simply given by:

$$c_{s,i}^* = k_0 c_{\ell,i}^* \quad (5.9)$$

Diffusion in the solid

Within each column i , backdiffusion in the solid is calculated radially by using a Landau transformation of the domain $r \in [0, r_i^*(t)]$ into a reference domain $\eta \in [0, 1]$, as explained in section 2.1.2 and already done in [55]. The diffusion equation in the solid is given by:

$$\left(\frac{\partial c_{s,i}}{\partial t} \right)_\eta = \frac{D_s}{r_i^{*2}} \frac{\partial^2 c_{s,i}}{\partial \eta^2} + \left(\frac{\eta v_i^*}{r_i^*} + \frac{(P-1)D_s}{\eta r_i^{*2}} \right) \frac{\partial c_{s,i}}{\partial \eta} \quad , \quad \text{with} \quad \eta = \frac{r}{r_i^*(t)} \quad (5.10)$$

where v_i^* is the velocity of the interface, D_s the diffusion coefficient in the solid phase and P the dimensionality of the problem (3 for 3D and 2 for 2D). Eq. (5.10) is solved using an implicit finite difference scheme as explained in section B.2.1.

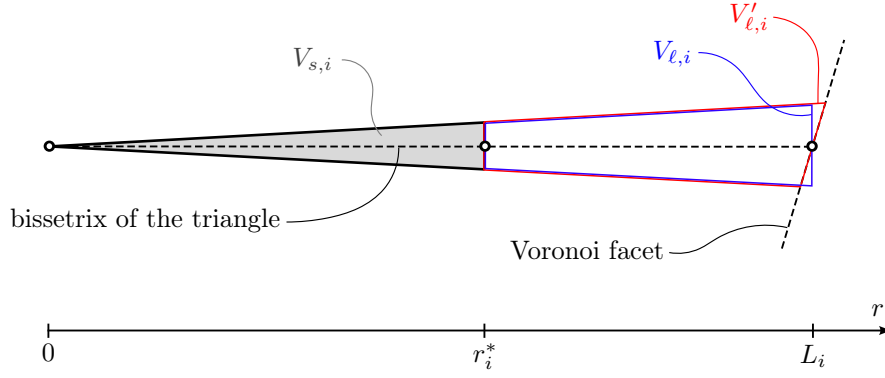


Figure 5.6: Representation of a single 2D column and the associated volume of the solid $V_{s,i}$ and the liquid $V_{\ell,i}$. The positions of r_i^* and L_i are noted on the r -axis.

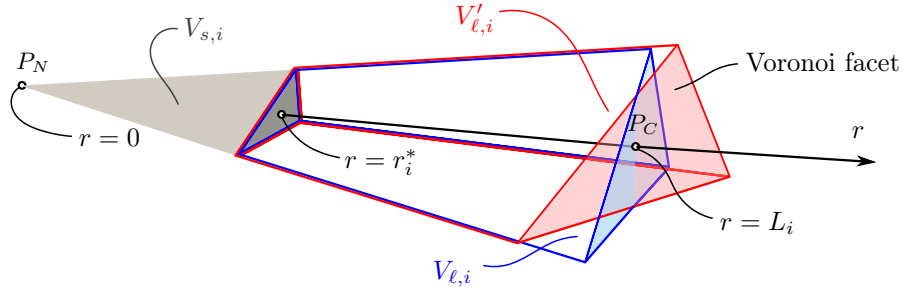


Figure 5.7: Representation of a single 3D column with the associated volumes of solid $V_{s,i}$ and liquid $V_{\ell,i}$. The positions of r_i^* and L_i are noted.

Flow of solute between the solid and the liquid part of the columns

Since it is assumed that there is no direct solute exchange through the solid parts of neighbouring columns, the differentiation over time of the volume integral of the composition of the solid, gives the flow of solute pumped by the solid within one column, Φ_i^* :

$$\Phi_i^* = \frac{d}{dt} \int_0^{r_i^*(t)} c_{s,i} dV = \int_0^{r_i^*(t)} \frac{\partial c_{s,i}}{\partial t} dV + c_{s,i}^* \frac{dr_i^*}{dt} S_i^* \quad (5.11)$$

where S_i^* is the area of the surface separating the liquid and the solid parts of the column i . The average composition in the solid can be calculated as follows:

$$\langle c_{s,i} \rangle = \frac{P}{r_i^{*P}} \int_0^{r_i^*} c_{s,i} r^{(P-1)} dr \quad (5.12)$$

where P is the dimensionality of the problem. Eq. (5.12) is then integrated numerically as explained in section B.2.2. After calculating back-diffusion and the new average

composition, the flow of solute pumped by the solid Φ_i^* at each time step is given by:

$$\Phi_i^* = \frac{\langle c_{s,i} \rangle^t V_{s,i} |t - \langle c_{s,i} \rangle^{t-\Delta t} V_{s,i} |t-\Delta t}{\Delta t} \quad (5.13)$$

where Δt is the time step and $V_{s,i} |t$ and $V_{s,i} |t-\Delta t$ are the volumes of the solid part of column i at time t , respectively $t - \Delta t$. Please note that $V_{s,i}$ is show in Fig. 5.6 and Fig. 5.7 for the 2D and 3D cases, respectively.

Composition profile in the liquid part of the columns

In the liquid part of the columns, the liquid composition, $c_{\ell,i}$, is assumed to be a piecewise parabolic-constant function (see red profile in Fig. 5.8):

$$c_{\ell,i}(r) = \begin{cases} c_{\ell,i}^\infty + (c_{\ell,i}^* - c_{\ell,i}^\infty) \left(\frac{\lambda_i - (r - r_i^*)}{\lambda_i} \right)^2 & \text{if } r < r_i^* + \lambda_i \\ c_{\ell,i}^\infty & \text{if } r \geq r_i^* + \lambda_i \end{cases} \quad (5.14)$$

where λ_i is the diffusion layer thickness. As shown in Fig. 5.6, the r axis, aligned with the bisectrix of the aperture angle of the triangle in 2D, is not necessarily perpendicular to the Voronoi facet. The solute gradient in the liquid being aligned with the r -axis, the conservation equations in the liquid are calculated in the volume $V_{\ell,i}$, instead of $V'_{\ell,i}$ (see Fig. 5.6). In 3D, the centroid (or geometric center) of the Voronoi facet triangle associated to the column is first found (noted as P_C in Fig. 5.7). After that, the r -axis is set to originate from the nucleation center (P_N in Fig. 5.7) and to pass trough P_C . As for the 2D case, the conservation equations in the liquid are calculated in the volume $V_{\ell,i}$, instead of $V'_{\ell,i}$.

As shown in Fig. 5.8, the solute profile in the liquid exhibits 3 typical stages:

- Stage 1: before the diffusion layer reaches the Voronoi facet, $c_{\ell,i}^\infty$ is set to the nominal composition and λ_i can be found by knowing $\langle c_{\ell,i} \rangle$ and using Eq. (B.35) in 2D and Eq. (B.39) in 3D.
- Stage 2: once the diffusion layer has reached the Voronoi facet, λ_i is equal to $L_i - r_i^*$ while $c_{\ell,i}^\infty$ is unknown and can be found by knowing $\langle c_{\ell,i} \rangle$ and using Eq. (B.36) in 2D and Eq. (B.40) in 3D.
- Stage 3: when Eq. (B.36) or Eq. (B.40) result in $c_{\ell,i}^\infty > c_{\ell,i}^*$, complete mixing in the liquid part of the column is assumed.

Note that the approximation of the solute profile in the liquid by a piecewise parabolic-linear function does not correspond to the solution of the diffusion equation in cylindrical or spherical coordinates. However, in all the three stages, the derivative at $r = L_i$ is zero and it is thus consistent with the fact that there is a symmetric column on the other side

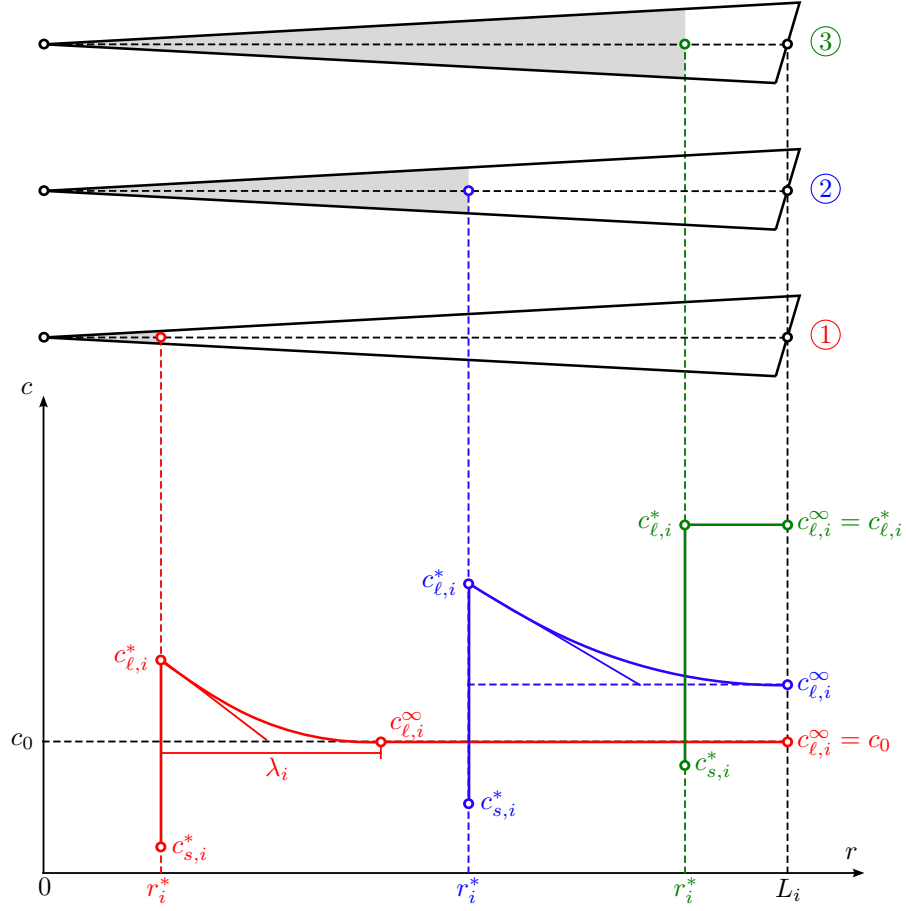


Figure 5.8: Solute profile in the liquid at different stages. Stage 1 in red ($c_{\ell,i}^\infty = c_0$), stage 2 in blue ($c_{\ell,i}^\infty > c_0$), and stage 3 in green (complete mixing).

of the Voronoi facet imposing a no-flux condition. In fact, it is more complex since the r axis is not necessarily normal to the Voronoi facet. In section 6.3.4, the error associated with this approximation, i.e., taking $V_{\ell,i}$ instead of $V'_{\ell,i}$, is evaluated.

Flow of solute between the columns

The flow of solute exchanged between the liquid parts of two adjacent columns can be first calculated in 2D. Let us define μ as the distance with respect to the nucleation center along the surface separating the two columns (see Fig. 5.9). The flow of solute is evaluated by calculating the gradient in liquid composition between the columns, perpendicularly to the μ -axis. In 2D, the flow of solute leaving the liquid part of column i and going into the adjacent liquid part of column j is given by:

$$\Phi_i^j = - \int_{\mu_{start}}^{\mu_{stop}} D_\ell \frac{c_{\ell,j}(\mu') - c_{\ell,i}(\mu')}{l_{\mu'}} d\mu' \quad (5.15)$$

where D_ℓ is the diffusion coefficient in the liquid, $d\mu'$ corresponds to the lateral surface distance parameter through which solute is exchanged and $l_{\mu'}$ is the distance between the positions at which the compositions are evaluated in the adjacent columns. μ_{start} and μ_{stop} are defined as follows: the two positions corresponding to r_i^* and r_j^* are projected onto the μ axis. The projected position that is the furthest away from the nucleation center is set as μ_{start} . In a similar way, μ_{stop} is defined as the position of the projection of $r_i^* + \lambda_i$ and $r_j^* + \lambda_j$ that is the closest to the nucleation center.

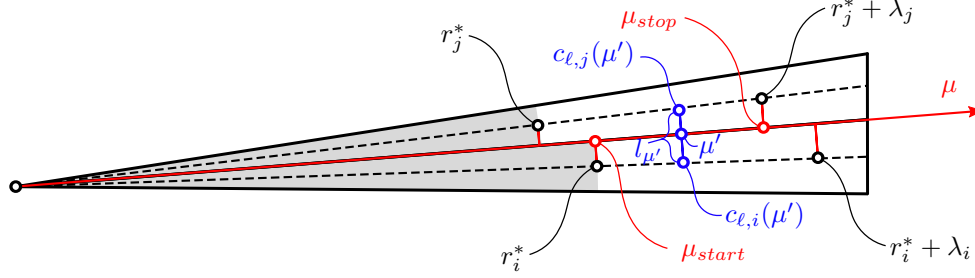


Figure 5.9: Schematic representation of the calculation of diffusion in the liquid between two adjacent columns in 2D. Please note that exchange of solute between the solid and liquid parts of adjacent columns is neglected.

In 3D, the method is similar. Let us call P_NKL the plane separating two adjacent columns and P_NMN the plane defined by the central lines of the columns (Fig. 5.10). The intersection between these two planes define the μ axis. The points located on the two central lines of the columns (dotted lines in Fig. 5.10) are projected onto the μ axis and μ_{start} and μ_{stop} are determined as in 2D. Since the planes P_NKL and P_NMN are not necessarily perpendicular, the composition gradients have to be weighted by a factor $\sin(\omega)$, where ω is the angle between these planes. Therefore, in 3D, the flow of solute leaving the liquid part of column i and going into the adjacent liquid part of column j is

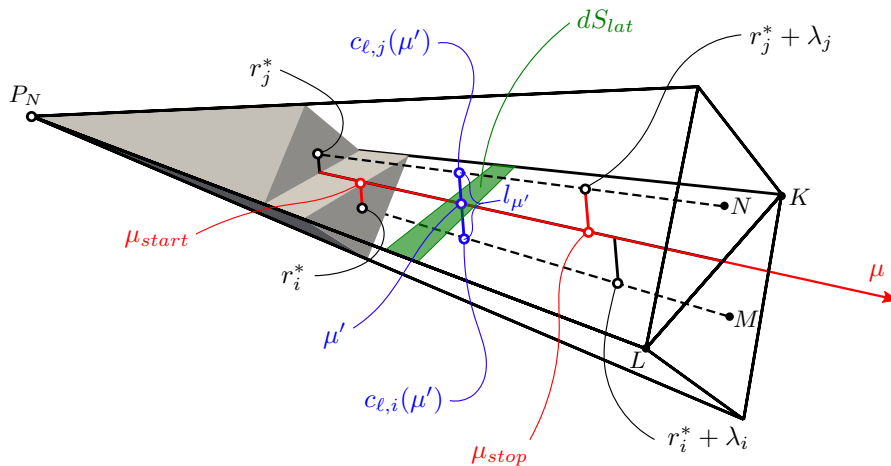


Figure 5.10: Schematic representation of the calculation of diffusion in the liquid between two adjacent columns in 3D.

thus given by:

$$\Phi_i^j = - \int_{\mu_{start}}^{\mu_{stop}} D_\ell \frac{c_{\ell,j}(\mu') - c_{\ell,i}(\mu')}{l_{\mu'}} \sin(\omega) dS_{lat} \quad (5.16)$$

where dS_{lat} is shown in Fig. 5.10.

Change of composition of the liquid

The change of the average composition in the liquid part of a column is given by subtracting all the flows of solute leaving it by back-diffusion, partitioning due to solidification and diffusion with the liquid parts of the adjacent columns:

$$\frac{d}{dt} \int_{r_i^*}^{L_i} c_{\ell,i} dV = \int_{r_i^*(t)}^{L_i} \frac{\partial c_{\ell,i}}{\partial t} dV - c_{\ell,i}^* \frac{dr_i^*}{dt} S_i^* = - \left(\Phi_i^* + \sum_{j=\text{neighbour}} \Phi_i^j \right) \quad (5.17)$$

where Φ_i^* is given in Eq. (5.13) and Φ_i^j in Eq. (5.16) (or Eq. (5.15) in 2D). The change of the average composition in the liquid is evaluated by estimating the time derivative as in Eq. (5.13):

$$\frac{\langle c_{\ell,i} \rangle^t V_{\ell,i} |t - \langle c_{\ell,i} \rangle^{t-\Delta t} V_{\ell,i} |t-\Delta t}{\Delta t} = - \left(\Phi_i^* + \sum_{j=\text{neighbour}} \Phi_i^j \right) \quad (5.18)$$

where $V_{\ell,i} |t$ and $V_{\ell,i} |t-\Delta t$ are the volumes of the liquid parts of column i at time t , respectively $t - \Delta t$.

Interface velocity

At each time step, the advance of the solid-liquid interface position, $r_i^*(t)$, is calculated from the interface velocity, v_i^* , given by the interfacial solute balance calculated with the solute profiles in the solid and liquid phases:

$$v_i^* = \frac{1}{(1-k_0)c_{\ell,i}^*} \left(D_s \left[\frac{\partial c_{s,i}}{\partial r} \right]^* - D_\ell \left[\frac{\partial c_{\ell,i}}{\partial r} \right]^* \right) \quad (5.19)$$

$[\partial c_{s,i}/\partial r]^*$ is estimated numerically (with a 4-th order derivative as explained in section B.2.1) and $[\partial c_{\ell,i}/\partial r]^*$ can be found analytically (as derived in B.2.3):

$$\left[\frac{\partial c_{\ell,i}}{\partial r} \right]^* = \begin{cases} \frac{c_{\ell,i}^* - c_{\ell,i}^\infty}{\frac{\lambda_i}{2}} & \text{in stage 1} \\ \frac{c_{\ell,i}^* - c_{\ell,i}^\infty}{\frac{L_i - r_i^*}{2}} & \text{in stage 2} \end{cases} \quad (5.20)$$

Once the velocity is known, the diffusion equation in the solid can be solved in the next time step using Eq. (5.10) and appropriate boundary conditions. When the composition in the liquid becomes uniform in a column (i.e., when stage 3 is reached), the exact position of the interface can be calculated from a solute balance equation:

$$\langle c_i \rangle \frac{L_i^P}{P} = \langle c_{\ell,i} \rangle \frac{L_i^P - r_i^{*P}}{P} + \langle c_{s,i} \rangle \frac{r_i^{*P}}{P} \quad (5.21)$$

$$r_i^* = L_i^P \sqrt{\frac{\langle c_i \rangle - \langle c_{\ell,i} \rangle}{\langle c_{s,i} \rangle - \langle c_{\ell,i} \rangle}} \quad (5.22)$$

Coalescence undercooling

Near the end of solidification, i.e., when the distance separating the solid-liquid interfaces of two neighbouring grains becomes small, coalescence is accounted for. When this distance becomes lower than $\delta_{sl} = 1$ nm, the liquid layer thickness is fixed to δ_{sl} and the composition of the liquid is assumed to be uniform and is not anymore linked to the phase diagram with Eq. (5.8). Essentially, the liquid composition decreases by backdiffusion of solute in the solid (perpendicularly to the interface), diffusion of solute between the remaining liquid of adjacent columns (parallel to the interface) becoming negligible. Once the coalescence line (located at an undercooling $\Delta T_b = (\gamma_{gb} - 2\gamma_{sl})/(\Delta S_f \delta_{sl})$ below the liquidus line, as explained in section 2.2) is reached, the two interfaces are considered to be coalesced.

In 2D, a random orientation θ is assigned to each grain. The grain boundaries are approximated as being pure tilt boundaries with the rotation axis parallel to $\langle 100 \rangle$. The

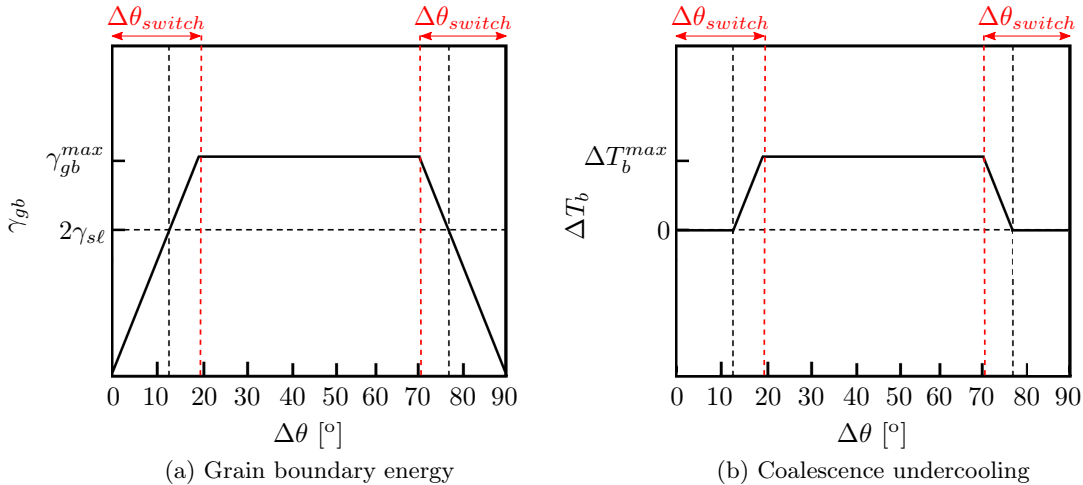


Figure 5.11: Grain boundary energy and coalescence undercooling for a $[100]$ symmetric tilt grain boundary. $\Delta\theta_{switch}$ is defined as the $\Delta\theta$ at which there is a transition between the Read-Schockley formula and the saturated value γ_{gb}^{max} .

grain boundary energy as a function of the misorientation can be approximated as shown in Fig. 5.11(a). The misorientation $\Delta\theta_{switch}$ corresponds to the value at which the grain boundary energy becomes maximal and equal to γ_{gb}^{max} . The coalescence undercooling ΔT_b can be then directly deduced from it. We recall that, in the case $\gamma_{gb} < 2\gamma_{sl}$, $\Delta T_b = 0$. In 3D a random orientation matrix, describing its orientation, is assigned to each grain. The grain boundary energy is then calculated for each boundary between two Voronoi regions with the code developed by Bulatov *et al.* [34], using the orientations of the two grains and the vector perpendicular to the grain boundary plane .

Time stepping scheme

The time stepping scheme can be summarized as follows:

1. The temperature (or the cooling rate) is given and is homogeneous over the whole domain. The interfacial compositions in the liquid and in the solid phases ($c_{\ell,i}^*$ and $c_{s,i}^*$) are given by Eq. (5.8) and Eq. (5.9), respectively.
2. All the solid nuclei are initiated at a given radius (same for all the grains) and with an initial undercooling. The solid composition is initially homogeneous and equal to c_s^* . One can thus find the solute layer thickness in the liquid, λ_i , by knowing the total volume of solid, respectively liquid, of one grain.
3. The flow of solute pumped by the solid part of the column, Φ_i^* , can be found with Eq. (5.13), while the flow of solute leaving the column, $\sum_{j=\text{neighbour}} \Phi_i^j$, can be estimated with Eq. (5.15) in 2D or Eq. (5.16) in 3D. Based on Eq. (5.18), one can then find the change of average liquid composition in the column.
4. The layer thickness λ_i is calculated with Eq. (B.35) in 2D or Eq. (B.39) in 3D. Once the solute layer reaches the Voronoi facet, the composition $c_{\ell,i}^\infty$ is increased and calculated with Eq. (B.36) in 2D or Eq. (B.40) in 3D.
5. Finally, the actual velocity of the interface, $v_i^*(t)$, is calculated from Eq. (5.19) (or Eq. (5.21) if the liquid composition is uniform). Once two interfaces get in close contact, coalescence is considered. In the case of attractive boundaries, closure of the grain boundary will be made once the remaining liquid thickness within a given column falls below a preset value. In the case of repulsive boundaries, it is only achieved once the coalescence line is reached.
6. The interface velocity is then used as an input in order to calculate the diffusion in the solid with equation Eq. (5.10). The value of λ_i or the new value $c_{\ell,i}^\infty$ when the solute layer thickness has reached the Voronoi facet is updated. After that, the calculation of the next time step starts again from point 3.

Note that, since an explicit formulation is used, the time step used for the calculation is limited by the Fourier criterion in the liquid.

5.2.3 Voronoi meshing and column subdivision

The *QHull* software [97] is used to perform a Voronoi tessellation of space from pseudo-randomly distributed nucleation centers (a minimum separation distance of the nucleation centers is imposed). The pseudo-randomly positioning avoids having two initial grains for which the solute layers might already interact at the time of nucleation, leading to an incorrect grain growth dynamic. The 2D and 3D meshes are created in a slightly different way, reason why they are presented in two separate sections.

2D meshing

The Voronoi tessellation of the domain is shown in Fig. 5.12(a). Each region associated with a grain consists of a polygon (represented by a specific color in Fig. 5.12(a)) and can be subdivided into triangles (as shown in Fig. 5.12(b)), which can be further subdivided

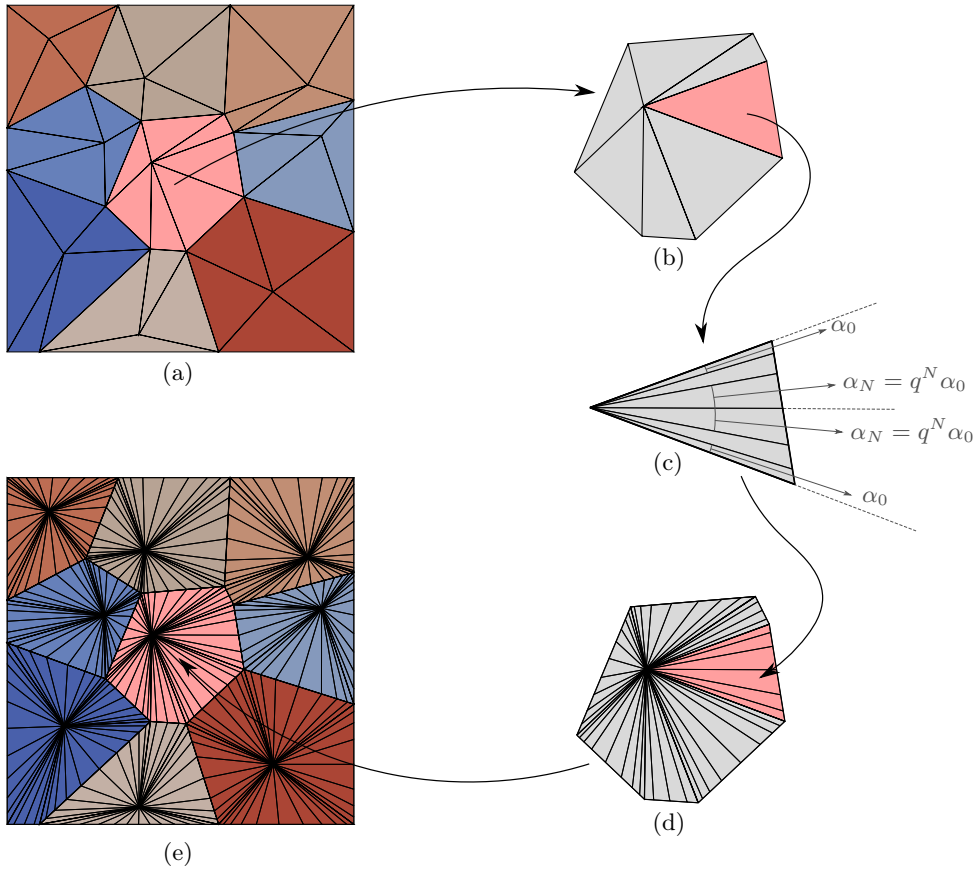


Figure 5.12: 2D meshing of the Voronoi tessellation into columns. (a) Voronoi tessellation of the REV, (b) detail of the region associated with one grain and subdivided into triangles, (c) detail of the subdivision of a triangle into columns, (d) region associated with one grain and subdivided into columns, and (e) REV subdivided into triangular columns.

into columns (as shown in Fig. 5.12(c)). Please note that, as shown in Fig. 5.12(c), the column division is based on their opening angles, α_i , which are set in a geometrical progression of ratio q (fixed for all the triangles) in order to have finer columns near the corners of the polygons (see Fig. 5.12(d)), i.e. where a higher curvature of the solid/liquid interface is expected. A minimum opening angle, that α_0 should exceed, is also fixed for all the triangles. At the end, it is possible to obtain the REV subdivided into triangular columns (see Fig. 5.12(e)).

3D meshing

The 3D Voronoi tessellation of a domain, performed with *QHull* [97], is shown in Fig. 5.13(a). Each region associated with a grain consists of a polyhedron (represented by a specific color in Fig. 5.13(a)) and can be subdivided into tetrahedra (as shown in Fig. 5.13(b)). Each tetrahedron is constructed from the connection of the nucleation center P_N , the centroid of a face of the Voronoi polyhedron, U , and two vertices of the Voronoi polyhedron, R and S , belonging to the same face as U .

It is possible to transform the face URS (shown in red in Fig. 5.13(c)), by applying a rotation transformation with a matrix $[A]$, and obtain the triangle $U'R'S'$ (where $U' = [A]U$, $R' = [A]R$, and $S' = [A]S$) in the x' and y' plane coordinates (shown in Fig. 5.13(d)). As for the 2D meshing, a geometrical progression is introduced in order to have a finer mesh where a higher curvature of the solid/liquid interface is expected (shown in Fig. 5.13(f)). First, the RS segment is divided in halfway in two parts by the point V . After that, the mesh points at the boundary of the triangle are determined: in the vicinity of R' and S' the spacings Δr_0 , Δs_0 and Δu_0 are set such that they are larger than a minimum distance Δh . The mesh points at the boundary of the surface are positioned with a geometrical progression such that:

$$\Delta u_m = q_1 \Delta u_{m-1} = q_1^m \Delta u_0 \quad \text{with } m = [1, N] \quad (5.23)$$

$$\Delta r_m = q_2 \Delta r_{m-1} = q_2^m \Delta r_0 \quad \text{with } m = [1, N] \quad (5.24)$$

$$\Delta s_m = q_2 \Delta s_{m-1} = q_2^m \Delta s_0 \quad \text{with } m = [1, N] \quad (5.25)$$

where q_1 and q_2 are the ratios of the geometrical progressions. Please note that, as shown in Fig. 5.13, there is a geometrical progressions from the points R and S towards V . Once the points at its boundary are set, the triangle $U'R'S'$ is meshed with the commercial code *modulef* [98, 99].

All the nodes of the mesh can be transformed back in the original xyz coordinates with the inverse transformation $[A]^{-1}$ (an example of the inverse transformation of a mesh point T' into T is shown in blue in Fig. 5.13). The tetrahedron $P_N U R S$ can then be subdivided into columns by connecting the nucleation center P_N with all the mesh points of the face as shown in Fig. 5.12(e)). At the end, it is possible to obtain the REV subdivided into a set of tetrahedral columns (see Fig. 5.13(g)).

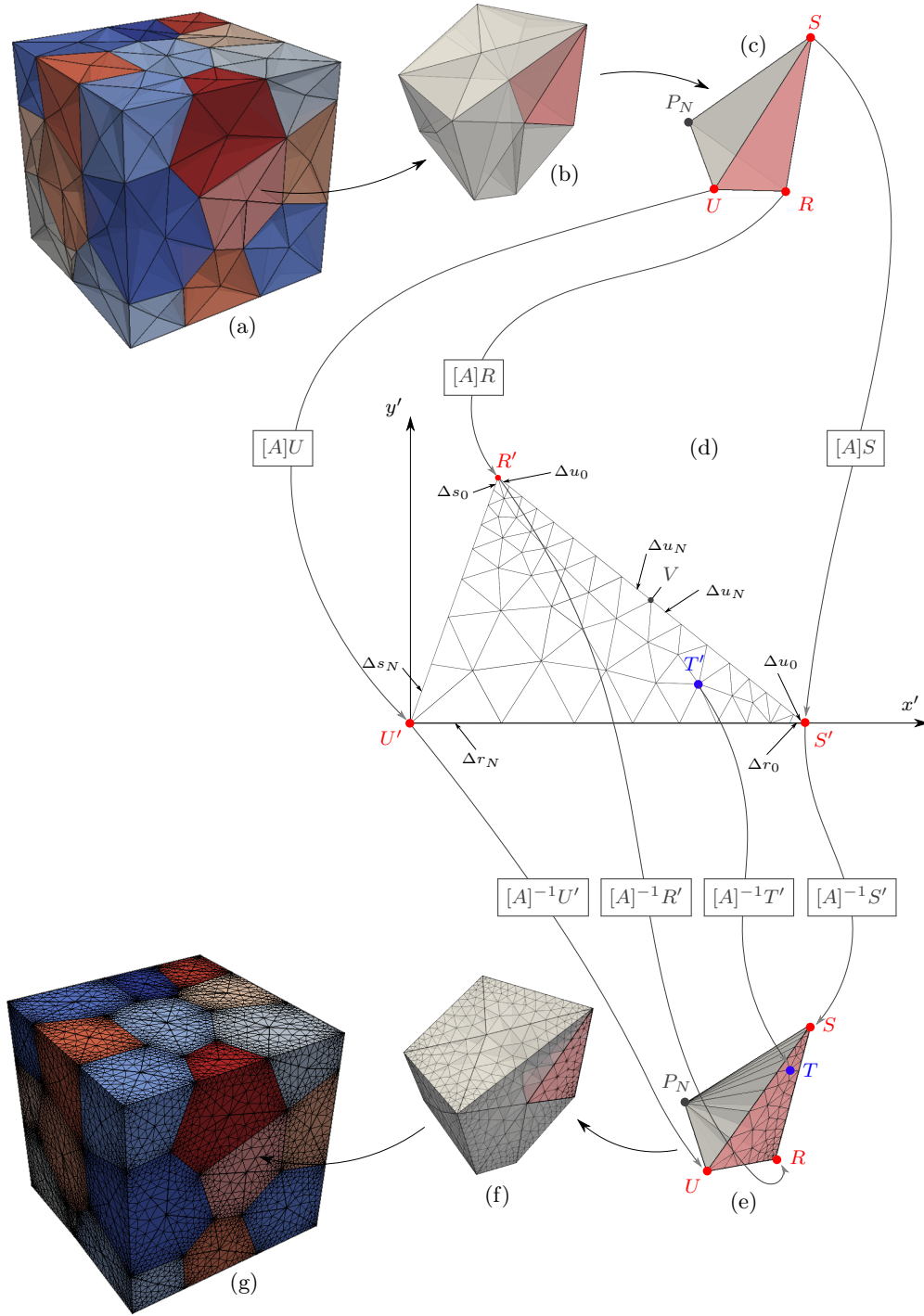


Figure 5.13: 3D meshing of the Voronoi regions into columns. (a) Voronoi tessellation of the REV, (b) detail of the region associated with one grain subdivided into tetrahedra, (c) detail of one tetrahedron (with the face to be meshed highlighted), (d) representation of the meshing of one face, (e) tetrahedron subdivided into columns, (f) Voronoi region associated with one grain and subdivided into columns, and (g) REV subdivided into tetrahedral columns.

Please note that, in the code, each Voronoi region associated with one grain can be treated independently, except when it is needed to evaluate whether two columns of neighbouring grains are coalesced. Therefore, in order to optimize the calculations, they were performed in parallel using a shared memory parallelization (*openMP* API [100]).

5.2.4 Reconstruction of the solid/liquid interface

Once the position of the interface in each column is known (at each time step), it is necessary to reconstruct a smooth surface and enmesh it. As for the Voronoi meshing of a column subdivision shown in the previous section, the reconstruction/meshing of the solid/liquid interface is far easier in 2D than in 3D. Hereafter, we present how this operation is performed, in particular how coalescence is taken into account for the interface reconstruction.

2D reconstruction

The points that represent the position r_i^* inside the columns are shown in Fig. 5.14. The points for which the two neighbours are not coalesced are coloured in red. Columns where

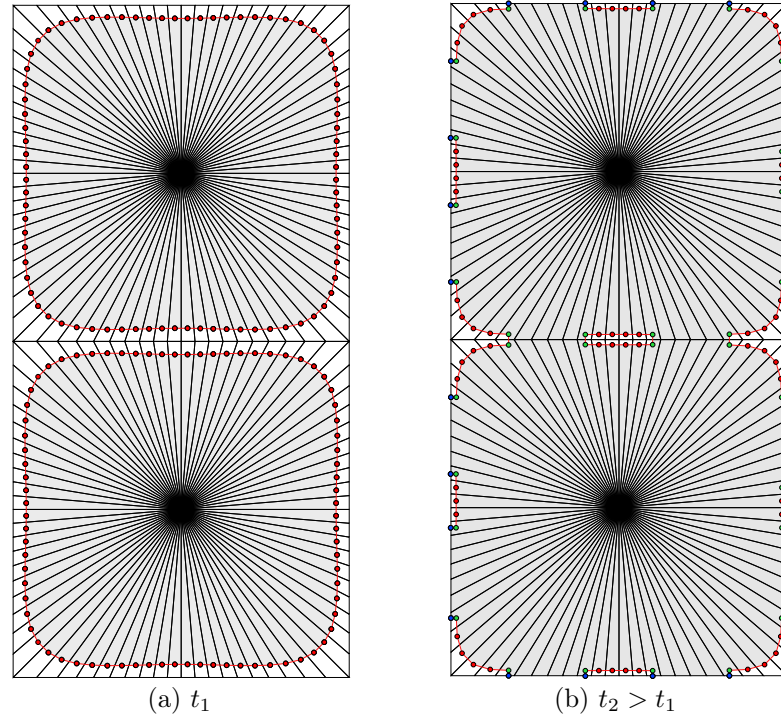


Figure 5.14: 2D solid/liquid interface (red line) at different stages of solidification. The points define the positions of the interface within one column: red if no neighbours are coalesced or green if one or more neighbours are coalesced. The blue points correspond to the green points orthogonally projected on the RVE external boundary.

coalescence has occurred are not considered, while those having one or more coalesced neighbours are coloured in green. Until no coalescence takes place, the solid/liquid interface consists in the connection of the neighbouring points belonging to the same grain (see Fig. 5.14(a)). However, when the grains start to coalesce, the situation becomes more complex. Additional segments connecting the green points in Fig. 5.14 with its symmetric counterparts are created. For green points located at the boundary of the calculation domain, the segments connect these points to their orthogonal projections on the boundary (blue points in Fig. 5.14).

3D reconstruction

In 3D, the reconstruction is performed in a similar way, but the meshing of the surface (see explanation in section B.2.5) is more complex: this is due to the fact that the points are not only linked together by segments as in 2D, but the interface mesh consists of several polygons as shown in Fig. 5.15.

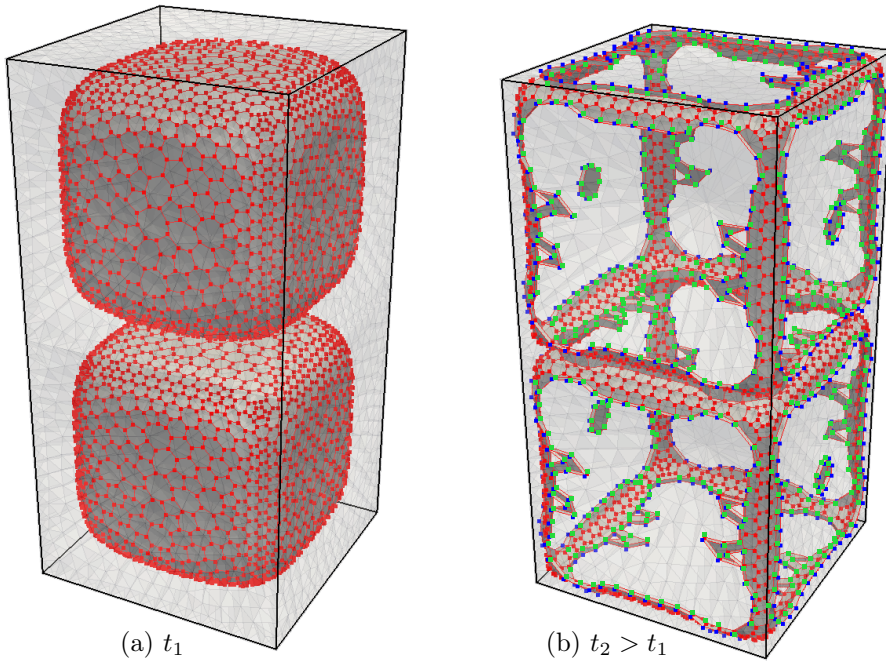


Figure 5.15: 3D Solid/liquid interface (gray surface formed by the red lines connection) at different stages of solidification. Each point defines the position of the interface within one column: red if no neighbours are coalesced or green if one or more neighbours are coalesced. The blue points correspond to the green points orthogonally projected on the RVE external boundary.

5.2.5 Evaluation of the curvature

While the radii of curvature for the ISD plots are measured with the software Avizo®, in Eq. (5.8), only the local mean curvature of the interface $\bar{\kappa}_i$ needs to be evaluated. This was performed by considering the position of the interface in the column as well as the position of the interface in the neighbouring columns (2 neighbours in 2D and 3 neighbours in 3D). These points define a common circle (Fig. 5.16) or sphere (Fig. 5.17) in 2D, respectively 3D.

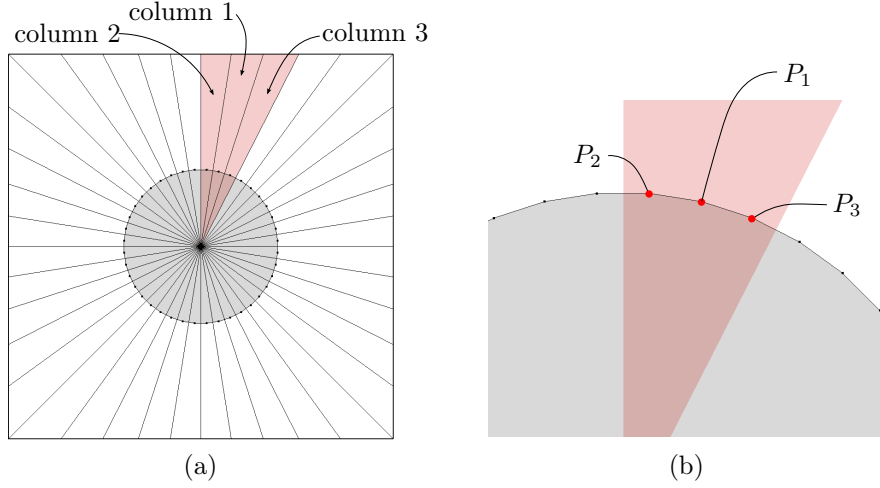


Figure 5.16: (a) Square domain subdivided into columns. (b) Detail of the interface positions in three neighbouring columns used to evaluate the curvature in column 1.

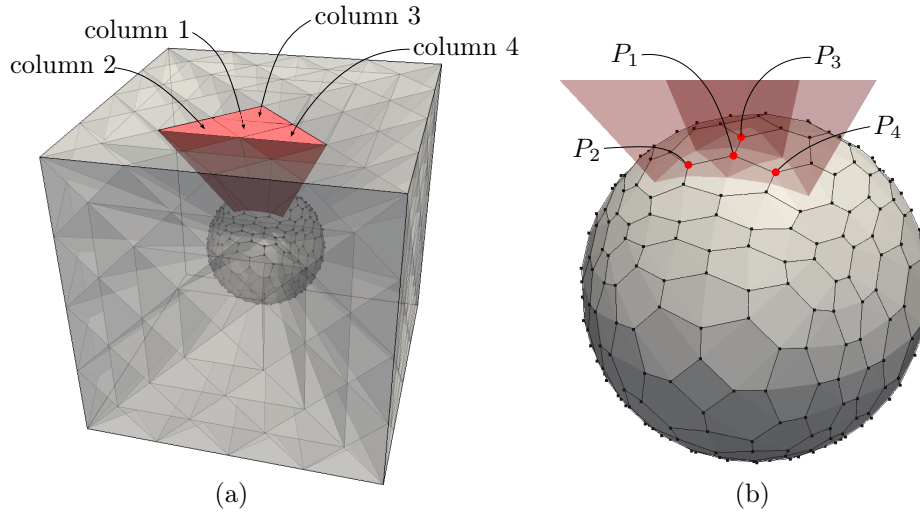


Figure 5.17: (a) Cubic domain subdivided into columns. (b) Detail of the interface positions in four neighbouring columns used to evaluate the curvature in column 1.

Detailed calculations are performed in section B.2.6. In order to calculate the sign of the curvature at point P_1 , the angle $\gamma = \widehat{P_N P_1 P_R}$ is evaluated. Please note that P_N is

the position of the nucleation center, P_1 the position of the interface within a specified column, and P_R the center of the fitted circle in 2D (see Eq. (B.54)) or sphere in 3D (see Eq. (B.61)). As shown in Fig. 5.18, if γ is larger than $\pi/2$, the curvature is positive, while it is negative in the other case.

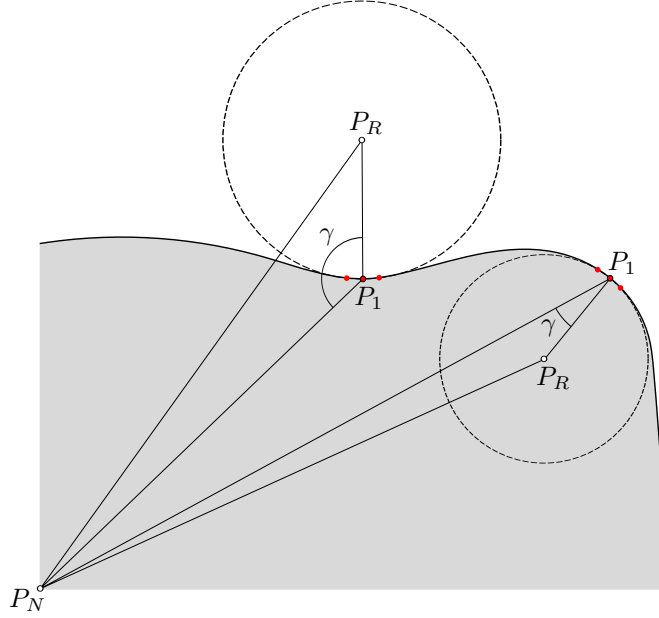


Figure 5.18: Schematic drawing of the calculation of the sign of the curvature at point P_1 . P_N is the position of the nucleation center, P_1 the position of the interface within a specified column, and P_R the center of the fitted circle in 2D or sphere in 3D.

6 Multiphase-field and mesoscopic model validations

6.1 Introduction

The formulation of the multiphase-field model, presented in section 5.1.2, was first validated in a simple 1D case in order to test the predicted coalescence undercoolings obtained with this method. In addition, the behaviour of a triple junction was evaluated in 2D. The multiphase-field code was then used to perform simple 2D grain percolation calculations.

After that, the mesoscopic model (presented in section 5.2) was validated with the multiphase-field predictions for simplified geometries, such as a single grain growing in a square arrangement of grains in 2D or a cubic arrangement of grains in 3D. The sensitivity of the model with respect to the diffusion in the liquid was also assessed, by enhancing or suppressing the diffusion in the liquid in the direction parallel to the solid-liquid interface (for a fixed diffusion in the solid perpendicularly to the interface). At the end, the choice of the boundary condition at the Voronoi facet is discussed.

6.2 Multiphase-field results

6.2.1 Validation of the multiphase-field formulation

The multiphase-field model was run in a simple 1D case of two coalescing solid-liquid interfaces. This was performed in the simplest case of a pure system, namely pure aluminum. As shown in Fig. 6.1(a), when no undercooling is applied, the solid-liquid interfaces do not move, while when an undercooling (even slight) is applied, there is a driving force that tends to close the liquid film. As explained in section 2.2, in the case of a repulsive grain boundary, a liquid film may persist (see Fig. 6.1(b)). In a similar simulation performed by Rappaz *et al.* [16], the authors used a different multiphase-field formulation leading to the presence of undesired phases at interfaces: for example ϕ_3 was

always present at the interface between ϕ_1 and ϕ_2 and viceversa. This is not the case for the present formulation derived in section 5.1.2, as shown in Fig. 6.1(a).

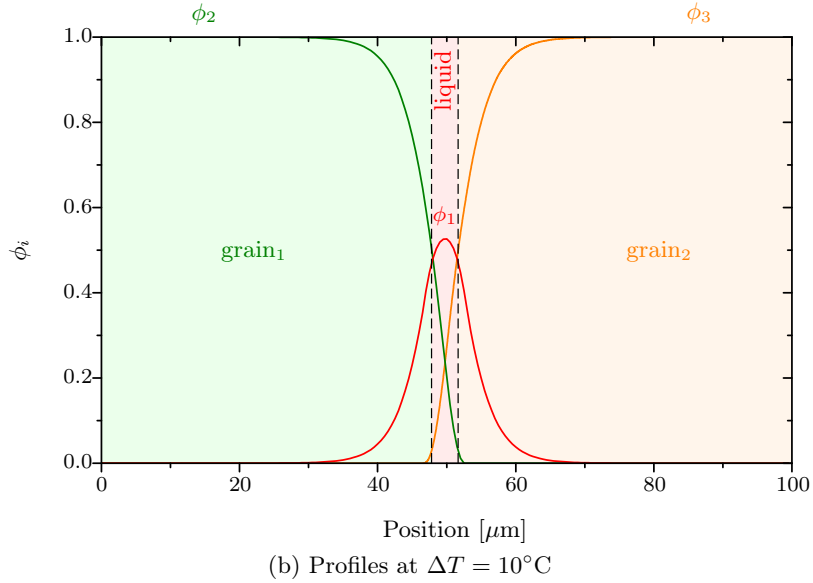
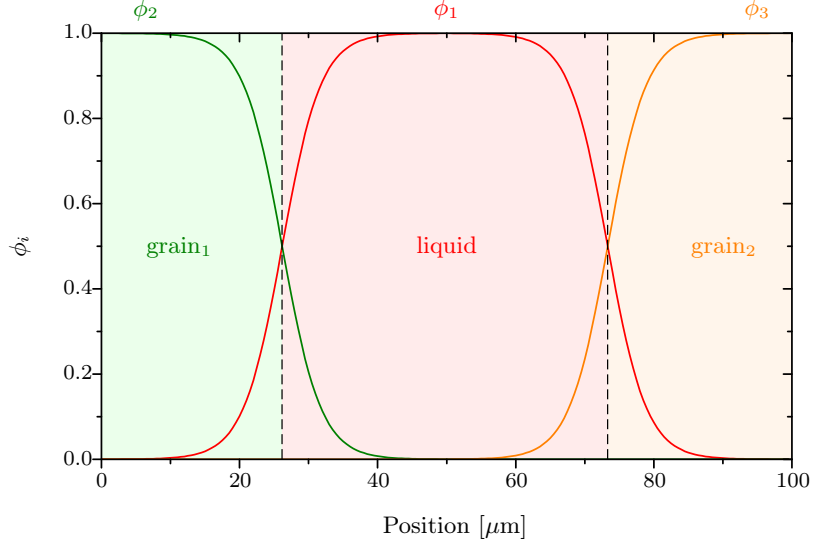


Figure 6.1: 1D profile of the phase fields in the case of two coalescing solid-liquid interfaces in pure Al. The represented case is repulsive since $\gamma_{gb} > 2\gamma_{sl}$ ($\gamma_{gb} = 0.3 \text{ J/m}^2$ and $\gamma_{sl} = 0.1 \text{ J/m}^2$). In (a) and (b) different undercoolings are set and the system is allowed to relax in order to find its position at equilibrium. $\Delta S_f = 10^6 \text{ J/(m}^3\text{K)}$ and $\delta_{sl} = 8 \text{ nm}$.

Since, $\phi_1 = \phi_2$ at the center of the grain boundary, one can consider that a thin liquid film persists when $\phi_1 > 1/3$. When $\phi_1 < 1/3$, the two interfaces can be considered as coalesced. Several multiphase-field simulations were performed with various values of

the parameter $(\gamma_{gb} - 2\gamma_{sl})$. As shown in Fig. 6.2, the undercooling necessary to coalesce the two solid-liquid interfaces is reported as a function of $(\gamma_{gb} - 2\gamma_{sl})$. As explained in section 2.2, we recall that the coalescence undercooling of a repulsive grain boundary is given by the following relationship:

$$\Delta T_b = \frac{\gamma_{gb} - 2\gamma_{sl}}{\Delta S_f} \frac{1}{\delta_{sl}} \quad (6.1)$$

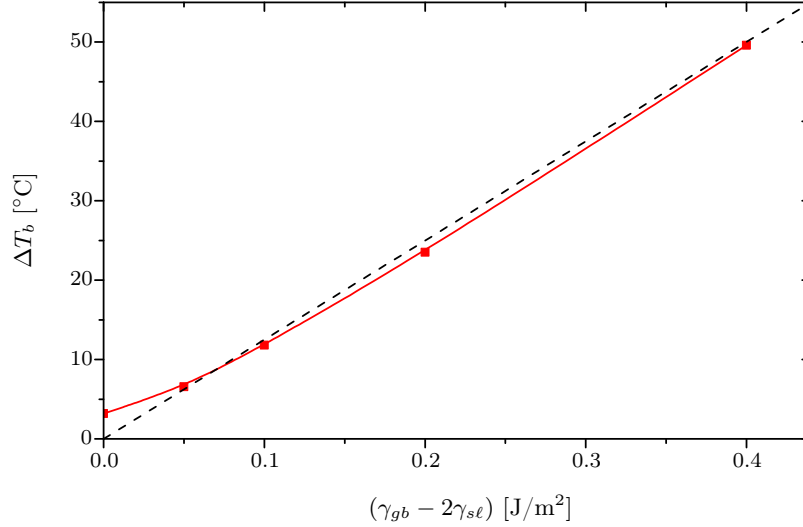


Figure 6.2: Multiphase-field simulated coalescence undercooling, ΔT_b , as a function of the excess grain boundary energy, $\gamma_{gb} - 2\gamma_{sl}$ (in red). The black dotted line represents the analytical curve calculated with Eq. (6.1). $\gamma_{sl} = 0.1$ J/m², $\Delta S_f = 10^6$ J/(m³K) and $\delta_{sl} = 8$ nm.

The simulated coalescence undercoolings are in very good agreement with the analytical curve given by Eq. (6.1). A slight deviation from the analytical calculation is found near $\gamma_{gb} - 2\gamma_{sl} \cong 0$, where a coalescence undercooling of 3.2°C is found while it should be zero. This is due to the term $g_{mo,2}$ that was added to the multiobstacle potential in the multiphase-field formulation (see Eq. (5.2)) in order to eliminate the presence of undesired phases at interfaces. For all the attractive grain boundary cases (when $\gamma_{gb} - 2\gamma_{sl} < 0$), as expected, no coalescence undercooling is necessary.

As explained before, since the additional term in the multiobstacle potential can slightly modify the coalescence undercooling, it is important to verify that, for example in the case of a triple junction between three grains, the angles determined between the interfaces are in good agreement with analytical predictions (similarly to validations performed by Garcke *et al.* [101]).

Several simulations were performed in order to find the conformation of a triple junction at zero undercooling, the position of the triple junction being determined by the interfacial energies. As shown in Fig. 6.3, the shape of the triple junction was simulated for various

grain boundary energy configurations. Please note that, since there is no undercooling, no driving force for solidification is present. The three grains can thus be considered as equivalent and are simply noted as 1, 2 and 3. Since the system tends to lower its energy, the position of the interface can be found analytically by minimizing the following expression (boundaries considered as straight lines and no anisotropy of the interface energies):

$$\gamma_{12} \|\mathbf{x}_3 - \mathbf{x}_{\text{triple}}\| + \gamma_{13} \|\mathbf{x}_2 - \mathbf{x}_{\text{triple}}\| + \gamma_{23} \|\mathbf{x}_1 - \mathbf{x}_{\text{triple}}\| \quad (6.2)$$

where the positions \mathbf{x}_1 , \mathbf{x}_2 , \mathbf{x}_3 and $\mathbf{x}_{\text{triple}}$ are indicated in Fig. 6.3 and $\|\cdot\|$ represents the L_2 norm. However, it is possible to obtain a simpler relationship by setting $\gamma_{12} = \gamma_{13}$. By assuming that interface tensions are equivalent to interface energies (i.e., neglecting anisotropy of the interface energies), the equilibrium of forces allows to find the theoretical

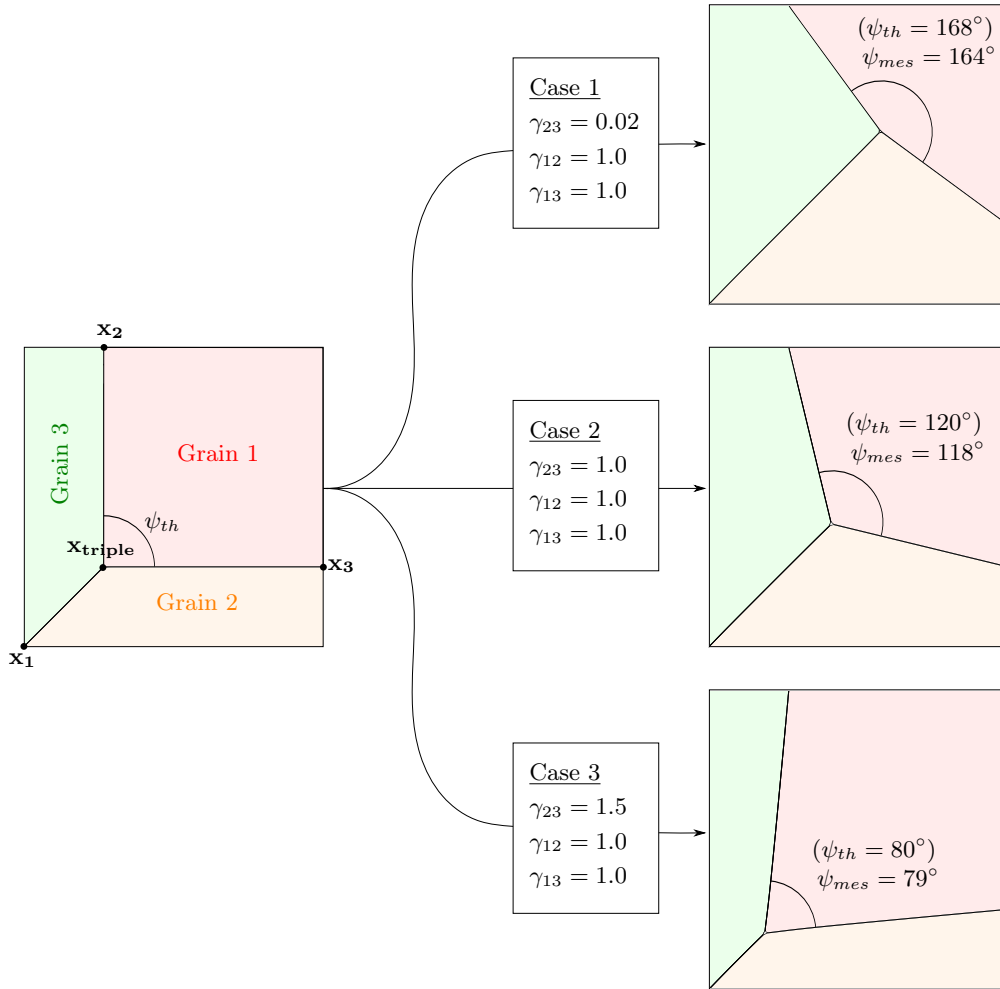


Figure 6.3: Simulated triple junction in 2D with no undercooling. On the right side is indicated the theoretical dihedral angle, ψ_{th} calculated with Eq. (6.3) as well as the dihedral angle measured from simulations, ψ_{mes} .

dihedral angle, ψ_{th} (as shown in Fig. 6.4):

$$\psi_{th} = 2 \arccos \left(\frac{\gamma_{23}}{\gamma_{12} + \gamma_{13}} \right) \quad (6.3)$$

As shown in Fig. 6.3, the dihedral angles measured from simulations are in good agreement with the theoretical values, thus validating the choice of the multiobstacle potential.

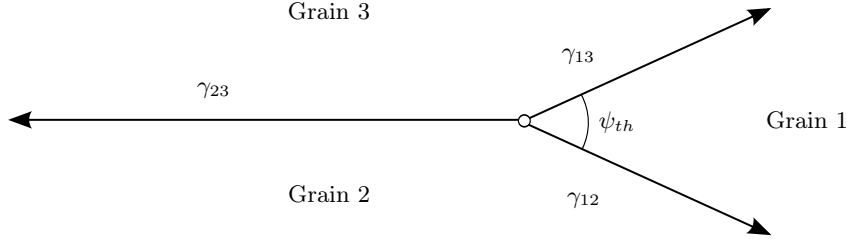


Figure 6.4: Schematic representation of the symmetric dihedral angle at a triple junction.

6.2.2 Percolation of grains

The progressive percolation of 8 grains with randomly distributed nucleation centers and periodic boundary conditions in 2D was simulated with the multiphase-field model. As explained in section 5.1.3, it is very difficult to simulate the percolation of several grains with a reasonable grain size (on the order of $100\mu\text{m}$) while capturing the coalescence effect at the same time, which requires a realistic solid-liquid interface thickness (on the order of a few nanometers). A compromise was found by using a domain of $10\mu\text{m}$ side containing 8 grains. Based on a surface average, the grain size is thus on the order of $3.5\mu\text{m}$. The interface thickness, δ_{sl} , was set to 60nm , while the interfacial energies were set to $\gamma_{sl} = 1.0\text{ J/m}^2$ and $\gamma_{gb} = 3.0\text{ J/m}^2$, respectively. Please note that, since δ_{sl} was set to a value one order of magnitude larger than the physical value, γ_{sl} and γ_{gb} were also increased by a factor 10 in order to lead to a realistic coalescence undercooling (see Eq. (6.1)). The alloy considered was Al-3.0wt.%Cu and the cooling rate was set to -50°C/s , which allows to obtain globular grains for the specified grain size.

In figure 6.5(b), a simulation in which each grain has a specific and random orientation is represented. The grain boundary energies are related to the misorientations of the impinging grains with the dependence represented in Fig. 5.11(b). In figures 6.5(a) and 6.5(c), other simulations have been performed assuming that all the grain boundary energies are respectively neutral ($\gamma_{gb} = 2\gamma_{sl}$) or repulsive ($\gamma_{gb} = \gamma_{gb,max}$). The diffusion coefficients were set to $D_\ell = 3 \cdot 10^{-9}\text{ m}^2/\text{s}$ and $D_s = 3 \cdot 10^{-13}\text{ m}^2/\text{s}$.

The solid fraction at percolation $g_{s,pcoal}$ for the different configurations are the following: 0.94 for the neutral case, 0.95 for the random case, and 0.97 for the repulsive case. Therefore, we observe that the solid fraction at percolation is significantly influenced by the grain boundary energies. The highest value of $g_{s,c}$ is given by the repulsive case, while the value of $g_{s,pcoal}$ for the random case is intermediate. However, note that in

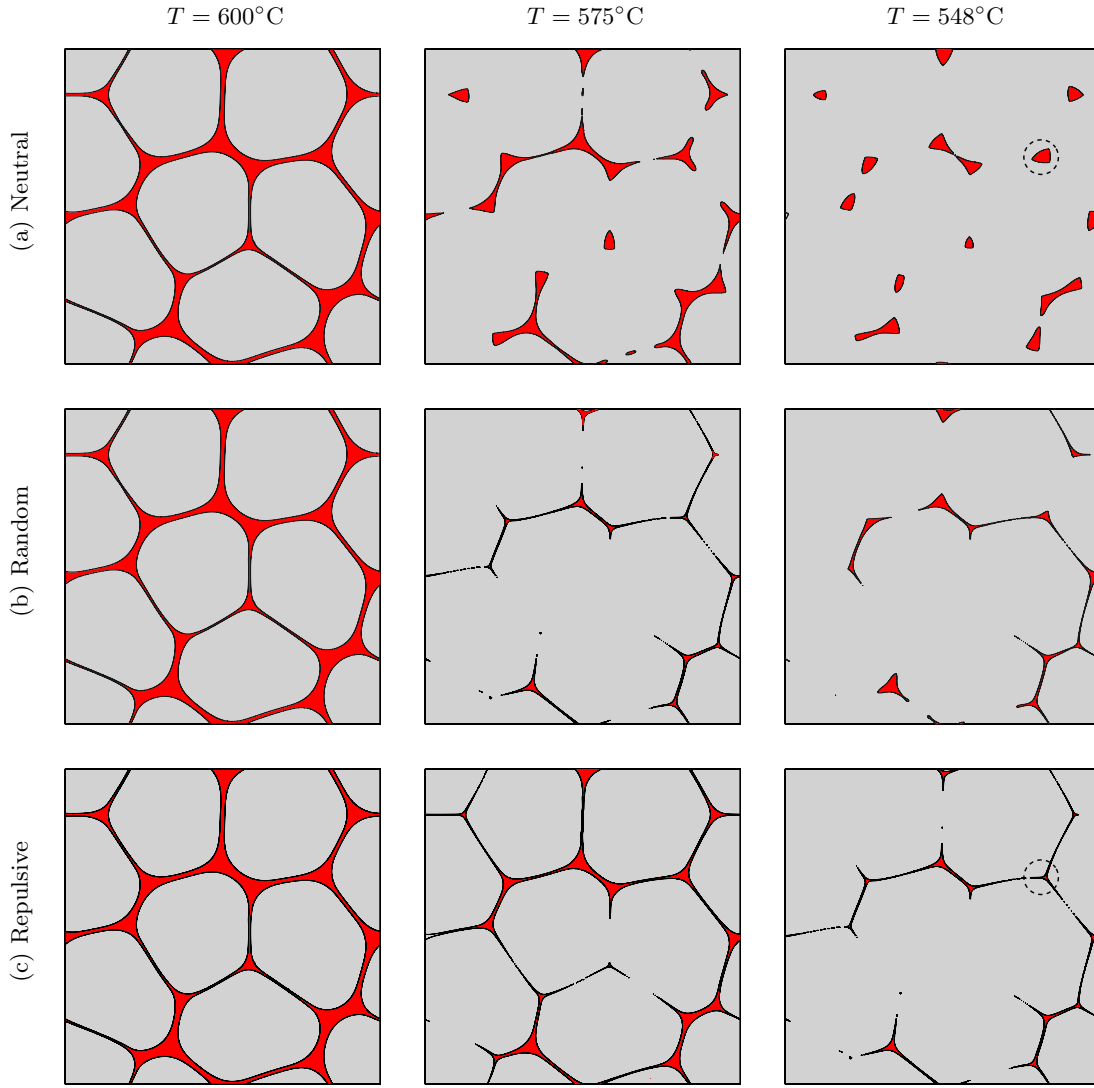


Figure 6.5: Progressive percolation within a volume containing 8 grains with different grain boundary energy configurations at specific temperatures. In the random case, all grain boundary energies are dependent on the misorientation between the grains, while in the neutral/repulsive case all the grain boundaries are set to $\gamma_{gb} = 2\gamma_{sl}$ and $\gamma_{gb} = \gamma_{gb,max}$, respectively. The two dotted circles indicate the different behaviour of a liquid pocket for the neutral versus the repulsive case.

the random case, there is the possibility of having very small (even nil) grain boundary energies. Therefore, the lowest value of solid fraction at percolation would be given by the case in which all grain boundary energies are nil. As evidenced by the dotted circles in Fig. 6.5(a), one can also observe that when low energy grain boundaries are coalesced, the liquid pocket that has formed at the triple junction does not evolve much (its volume is slightly decreasing but not its shape). This is due to the equilibrium of forces at the triple junction that tends to open the liquid pockets because of the large dihedral angle

in the liquid. On the other hand, for larger coalescing grain boundaries (see Fig. 6.5(c)), the equilibrium of forces at the triple junction tends to close the liquid pocket.

As explained before, the parameters chosen for the multiphase-field simulations are a compromise between a “reasonable” solid-liquid interface thickness as well as a “reasonable” grain size. However, the values depart from the physical ones, the physical value of δ_{sl} being on the order of 2 nm and a typical grain size on the order of 100 μm . By decreasing the interface thickness by a factor $1/N$, the mesh size should be decreased by the same factor, leading to an increase of the number of mesh points of a factor N^2 in 2D (N^3 in 3D). An increase of the grain size, d_{g0} by a factor M would further increase the number of mesh points of a factor M^2 in 2D (M^3 in 3D). Please note that, since the multiphase-field formulation is explicit, the time step should be decreased by a factor N^2 in both 2D and 3D (see Eq. (5.7)). Since, the critical cooling of the globular-to-equiaxed transition is proportional to d_{g0}^{-2} in 2D (d_{g0}^{-3} in 3D), an increase of the grain size by a factor M would force to reduce the cooling rate by a factor M^2 in 2D (M^3 in 3D). Finally, taking the physical values of the grain size and of the interface thickness would lead to an increase of the computational cost of the 2D calculation by a factor (assuming that one wants to cover an unchanged temperature range):

$$M^4 \times N^4 = \left(\frac{100\mu\text{m}}{3.5\mu\text{m}} \right)^4 \left(\frac{60\text{nm}}{2\text{nm}} \right)^4 = 5.4 \cdot 10^{11} \quad (6.4)$$

while in 3D the increase of the computational scales as:

$$M^6 \times N^5 \quad (6.5)$$

Considering that the computational cost of each of the 2D simulations shown in Fig. 6.5 is approximately 3 hours when run on 32 processors, the time needed to perform the same calculation but with realistic physical values would be prohibitive even for a reasonable amount of grains. This is the reason why the mesoscopic model was developed.

6.3 Validation of the mesoscopic model

6.3.1 Meshing of the Voronoi regions

The mesoscopic model described in section 5.2 was initially run with simple grain configurations such as a square arrangement of regular grains in 2D (or a cubic arrangement of regular grains in 3D). In such configurations, it is only needed to simulate a single grain growing in a square box in 2D (or a cubic box in 3D) thus allowing a comparison with multiphase-field predictions (next section). As shown in Fig. 6.6, the free meshing in both 2D and 3D is more refined where needed, i.e. in the regions where a high curvature is expected in the last-stage solidification such as the corners and the edges of the cube in 3D (or the corners of the square in 2D).

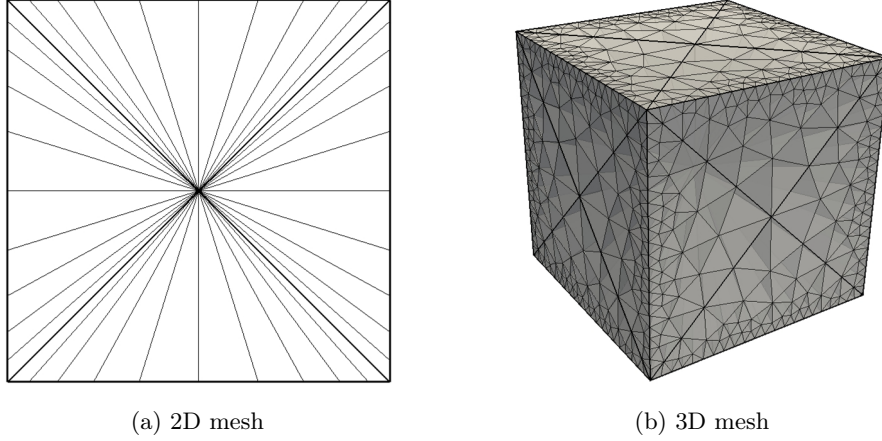


Figure 6.6: (a) 2D mesh of a square box and (b) 3D mesh of a cubic box.

6.3.2 Comparison with multiphase-field predictions

In this section, the mesoscopic model predictions are compared with the multiphase-field results for simple configurations. For both 2D and 3D, an Al-1.0wt.%Cu alloy of $50\mu\text{m}$ grain size was chosen. The physical parameters are summarized in Table 6.1. Please note that the multiphase-field simulation is performed on a larger domain, i.e., by taking into account the neighbouring grains that have a repulsive boundary with the grain at the center of the domain (all the grain boundary energies are set to $\gamma_{gb} = 0.32 \text{ J/m}^2$). However, as explained in section 6.2.2, the multiphase-field can run only under very specific conditions to have an acceptable computational times. Therefore, as summarized in Table 6.2, some of the conditions and physical parameters had to be adapted.

Table 6.1: Realistic physical parameters used in the mesoscopic and multiphase-field models.

Physical parameter	Value
γ_{sl}	0.135 J/m^2
γ_{gb}	0.32 J/m^2
ΔS_f	$10^6 \text{ J/(m}^3\text{K)}$
D_ℓ	$3 \cdot 10^{-9} \text{ m}^2/\text{s}$
D_s	$3 \cdot 10^{-13} \text{ m}^2/\text{s}$

Table 6.2: Parameters used for the comparison between the mesoscopic model and the multiphase-field model.

Model or physical parameter	2D models	3D models
δ_{sl}	$0.2 \mu\text{m}$	$1.0 \mu\text{m}$
\dot{T}	-20.0°C/s	-8.0°C/s

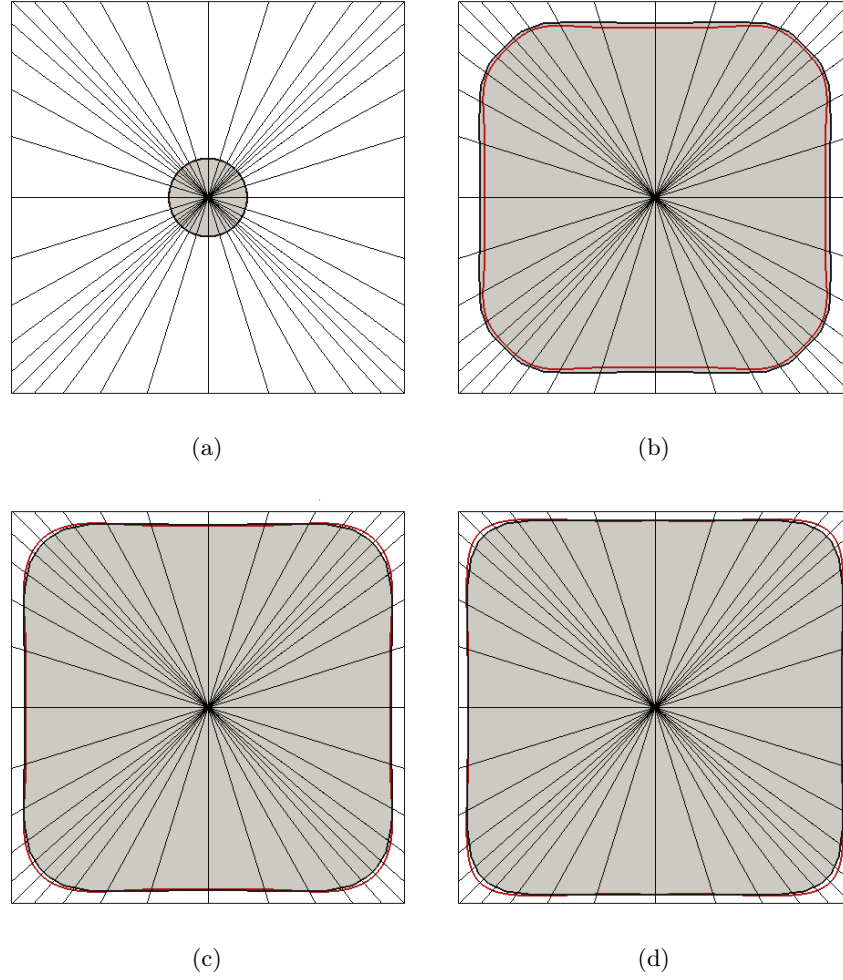


Figure 6.7: Comparison of the mesoscopic model (in gray) and the multiphase-field model (in red) for different times of a 2D single grain growing in a square box.

As shown in Fig. 6.7 and Fig. 6.8, the mesoscopic model correctly captures the physics of solute diffusion both in 2D and 3D, since the shapes of the grains are very close, as long as there is no deep instability of the solid-liquid interface (i.e., small grain size) [102]. In addition, like the multiphase-field method, the mesoscopic model predicts the fact that, at the center of the flat parts of the grains, the interface is slightly negatively curved. The only small differences that can be noticed are: solidification is more advanced for the mesoscopic model at low solid fractions (see Figs. 6.7(b) and 6.8(b)), while, at higher solid fractions (see Figs. 6.7(d) and 6.8(d)), the curvature of the interface near the grain corners is slightly more pronounced for the multiphase-field model.

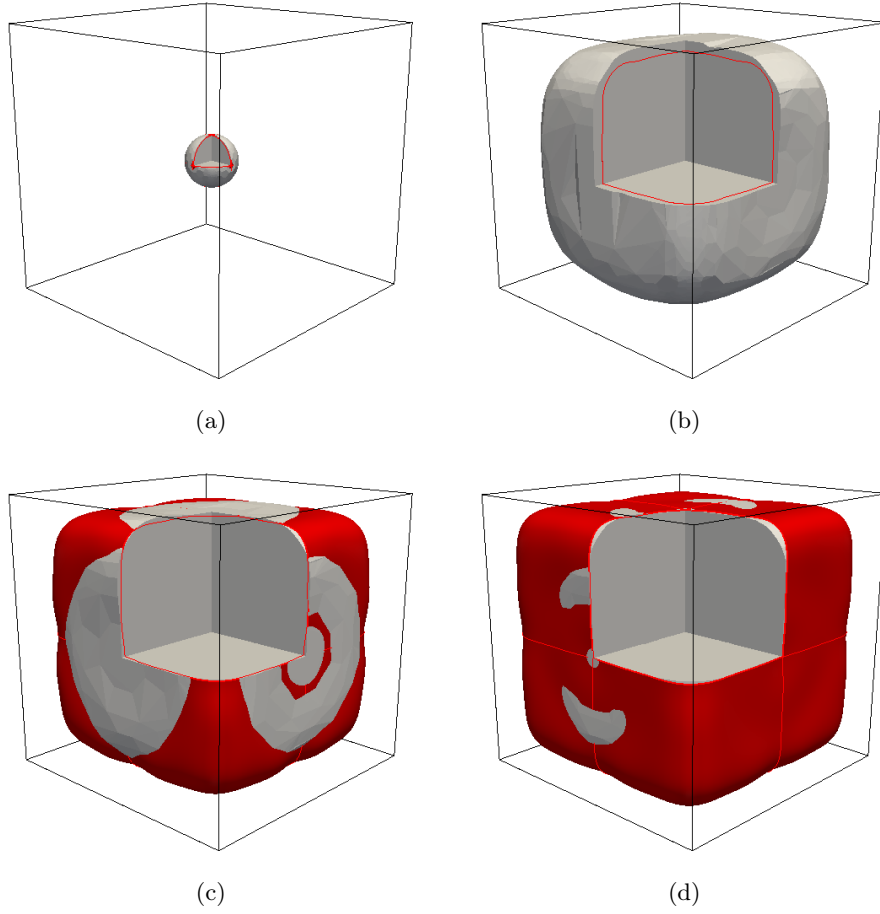


Figure 6.8: Comparison of the mesoscopic model (in gray) and the multiphase-field model (in red) for different times of a single 3D grain growing in a cubic box.

6.3.3 Sensitivity to diffusion in the liquid

As shown in the previous section, the grain shape predictions of the mesoscopic model and of the multiphase-field model are in good agreement. Nevertheless, it is important to assess the importance of the diffusion in the liquid (mainly diffusion parallel to the interface) with respect to the diffusion in the solid (only back-diffusion perpendicularly to the interface), which are the two main phenomena driving the last-stage coalescence. The calculations were performed with the parameters and condition given in Tables 6.1 and 6.3, except that the diffusion coefficient in the liquid D_ℓ in Eq. (5.15) (or in Eq. (5.16) in 3D) was changed to D_ℓ^{mod} .

6.3. Validation of the mesoscopic model

Table 6.3: Parameters used for the evaluation of the sensitivity to diffusion in the liquid of the mesoscopic model (both in 2D and 3D).

Model or physical parameter	2D and 3D models
$\delta_{s\ell}$	1.0 nm
\dot{T}	-1.0°C/s
grain size	$100\mu\text{m}$

Figure 6.9 shows the evolution of a single grain growing in a square/cubic box in which the diffusion coefficient used for the calculation of lateral diffusion corresponds to the most realistic physical value ($D_\ell^{mod} = D_\ell$). This reference case was then compared with

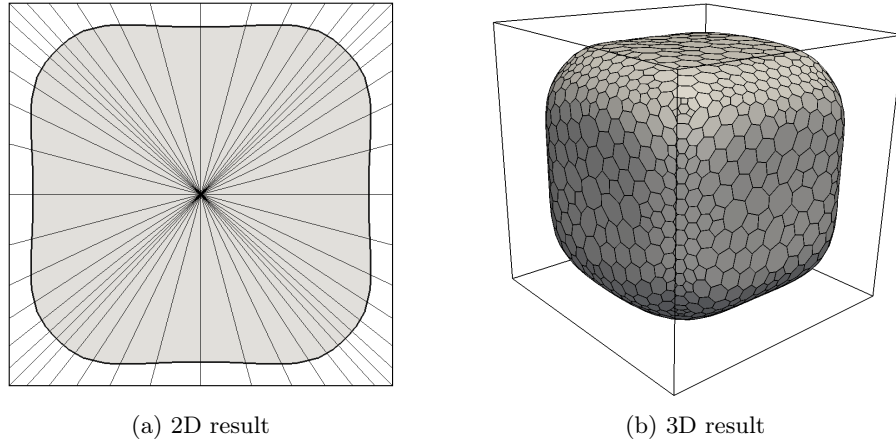


Figure 6.9: Simulation of a single grain growing in (a) a square 2D domain and (b) a 3D cube with $D_\ell^{mod} = D_\ell$ (reference treatment of lateral diffusion in the liquid) at $t = 8\text{s}$.

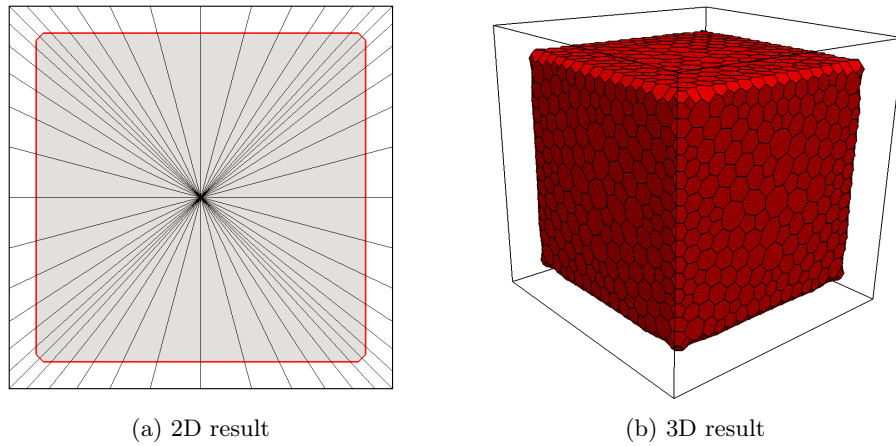


Figure 6.10: Simulation of a single grain growing in (a) a square 2D domain and (b) a 3D cube with $D_\ell^{mod} = 0$ (no lateral diffusion in the liquid) at $t = 8\text{s}$.

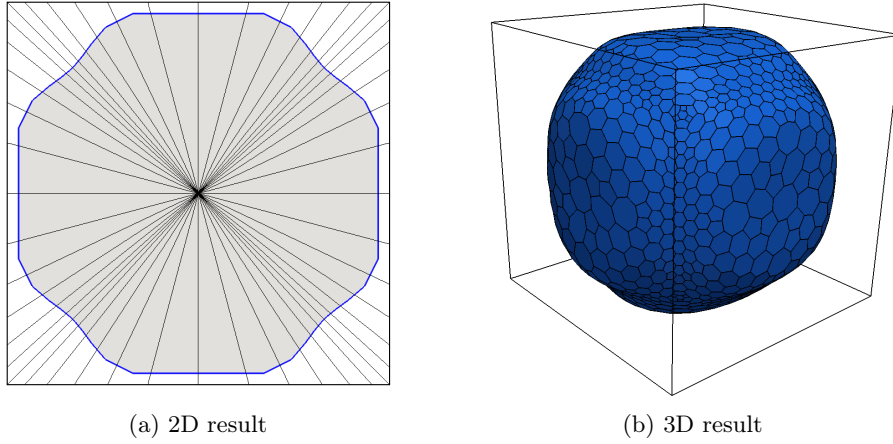


Figure 6.11: Simulation of a single grain growing in (a) a square 2D domain and (b) a 3D cube with $D_\ell^{mod} = 3D_\ell$ (reference treatment of lateral diffusion in the liquid) at $t = 8s$.

the same simulation but in which the lateral diffusion was neglected ($D_\ell^{mod} = 0$) as shown in Fig. 6.10. As for the granular model of Phillion *et al.* [55] in which solute exchange between the columns is not considered, the grain shape of the mesoscopic model with $D_\ell^{mod} = 0$ is polygonal (or polyhedral in 3D). Please note that, as shown in Fig. 6.10(b), for the 3D case, the interface has a “jagged” appearance near the edges of the domain due to the surface reconstruction method. In the simulation shown in Fig. 6.11, the lateral diffusion was enhanced by a factor 3 ($D_\ell^{mod} = 3D_\ell$). The fact that the corners are much more pronounced than in Fig. 6.9 shows the high sensitivity of the model with respect to diffusion in the liquid in the direction parallel to the solid-liquid interface.

The comparison of the evolutions of the grain shape for the three different cases are

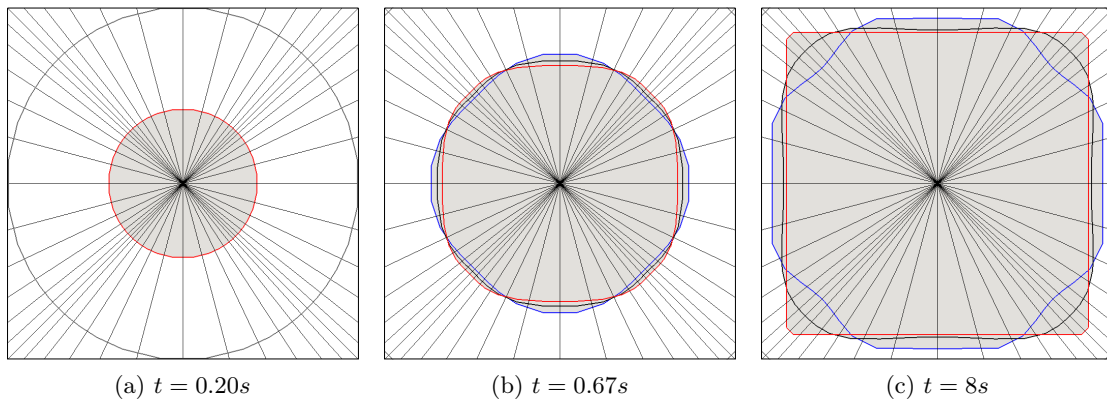


Figure 6.12: Evolution of a single grain growing in a square box. The normal, neglected and enhanced lateral diffusion in the liquid cases are shown by the black, red and blue lines, respectively. The diffusion boundary layer is shown by a solid gray line.

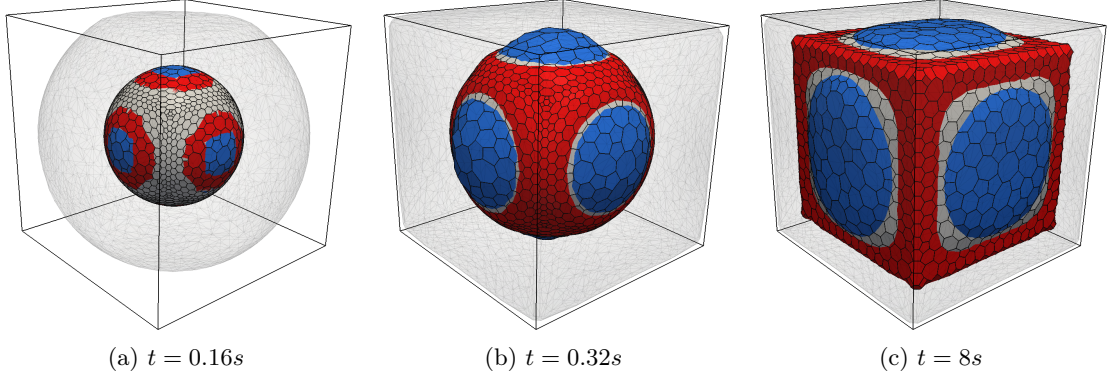


Figure 6.13: Evolution of a single grain growing in a cubic box. The normal, neglected and enhanced lateral diffusion in the liquid cases are shown by the gray, red and blue surfaces, respectively. The diffusion boundary layer is shown by a shaded gray surface.

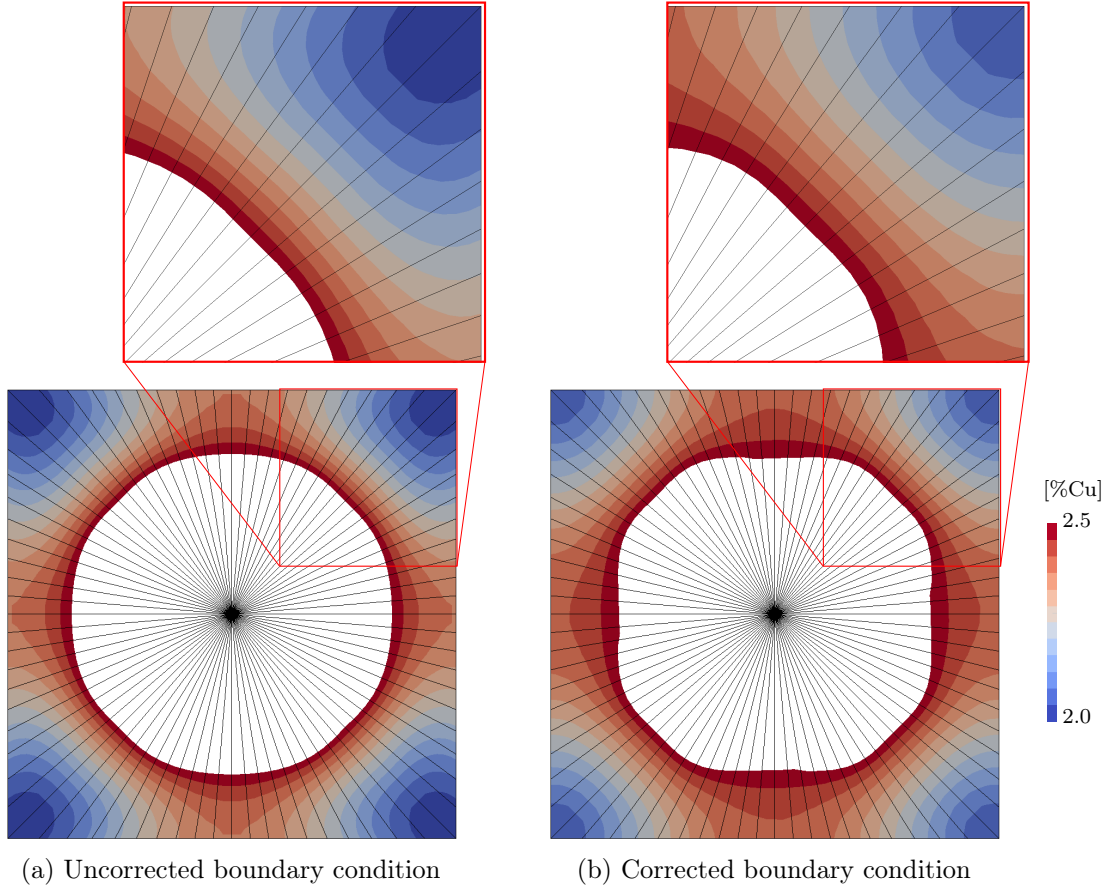
shown in Fig. 6.12 and Fig. 6.13. As long as the diffusion boundary layer does not reach the Voronoi boundary, the grain grows as a circle (or a sphere in 3D). Afterwards, the shape begins to depart from a circle (or a sphere). It is thus of crucial importance to have an accurate prediction of the diffusion in the liquid in the direction parallel to the solid-liquid interface, in order to correctly describe the grain shape evolution.

6.3.4 Boundary condition at the Voronoi facet

As explained in Appendix B.2.4, once the solute layer in a column reaches the Voronoi facet, the composition at the Voronoi boundary, c_ℓ^∞ , increases. However, as shown in Fig. B.6, a no-flux condition is applied in the direction of the r -axis (the coordinate of the column) and not perpendicularly to the Voronoi facet. The correction of this issue is explained in appendix B.2.4.

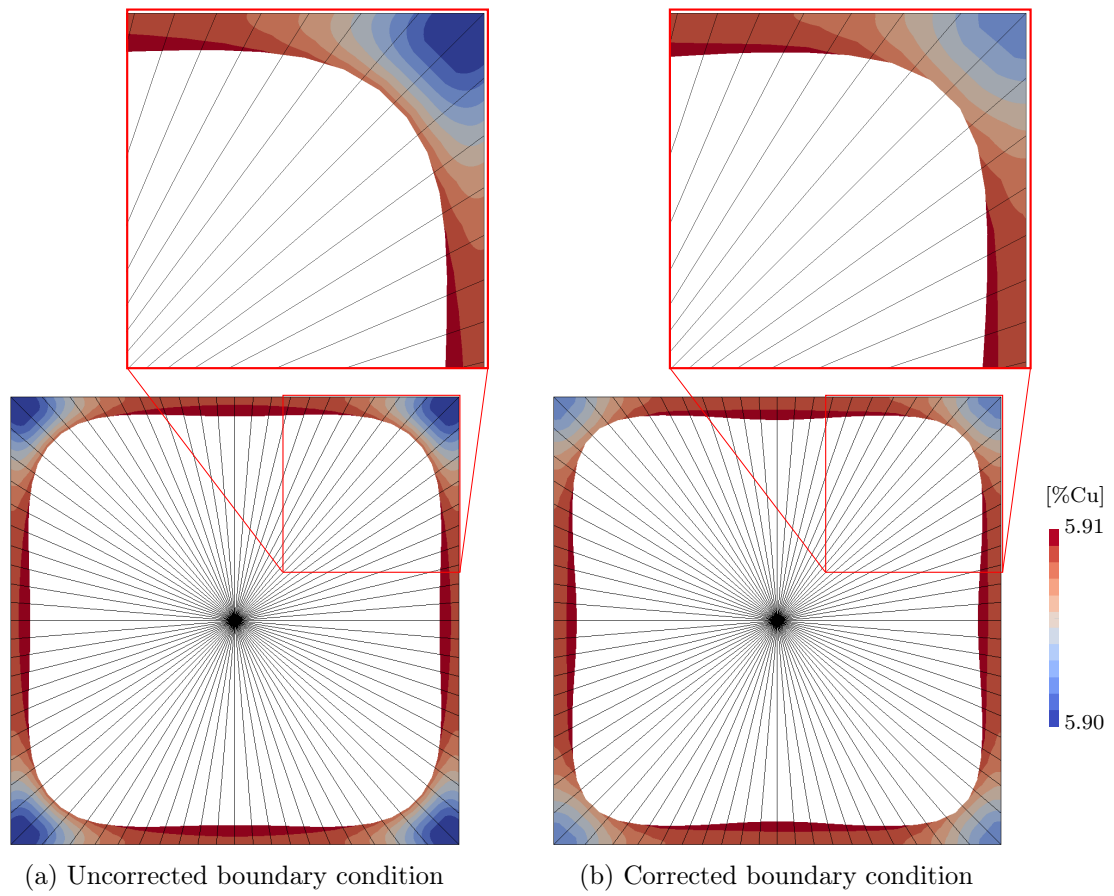
Fig. 6.14 and Fig. 6.15 show the comparison of the solute profile in the liquid phase at different stages of solidification (after 0.75s and 3.0s respectively) for both the non-corrected and corrected Voronoi boundary conditions. The calculations were performed with the parameters and condition given in Tables 6.1 and 6.3. Please note that in this case a regular mesh was chosen.

From the observation of Fig. 6.14 it can be seen that the isoconcentration lines are perpendicular to the Voronoi facet in the calculation performed with the corrected boundary conditions (see Fig. 6.14(b)), while they are aligned with the columns directions near the boundary in the uncorrected calculation (see Fig. 6.14(a)). The grain shape also slightly differs at this stage. The solute profiles observed in Fig. 6.15 near the end of solidification (at $t = 30$ s) seems to be quite different between the uncorrected and corrected boundary conditions. However, as indicated by the small range of the colorscale, the conditions are very close to complete mixing in the liquid and no noticeable difference



in shape between the grains is found.

As a conclusion, for the 2D case there is no noticeable difference in the grain shape between the corrected and uncorrected boundary conditions at the Voronoi facet for sufficiently high solid fraction. In addition, the corrected boundary condition generally requires a regular mesh (does not allow to simulate several grains) and it would be complex to perform a similar correction for the 3D model. All these aspects, as well as the fact that the uncorrected model is still in good agreement with the multiphase-field predictions, ensure that the correction of the boundary condition is not necessary.



7 X-Ray tomography observations

7.1 Introduction

X-ray tomography observations were first performed *ex situ* on samples solidified in the furnace II-sample 2 setup (see section 3.2.1). As shown in section 4.2.3, with such a setup it is possible to achieve near steady-state conditions. It is thus possible to access the temperature of each individual pellet at the moment of the quench. In addition, no further sample preparation is needed before X-ray tomography observations, since it is not necessary to reduce its diameter. This study was complemented with *in situ* experiments, where the temperature was directly controlled by a laser-heated furnace (see section 3.3.3). The cooling conditions used for the experiment were similar to the *ex situ* ones for the purpose of comparison.

Please note that in both *ex situ* and *in situ* X-ray tomography observations, the voxel size is $0.67\text{ }\mu\text{m}$, corresponding to a resolution on the order of $2\text{ }\mu\text{m}$ (estimated to be 3 times larger than the voxel size). We recall that coalescence takes place at the level of the solid-liquid interface thickness δ_{sl} , which is on the order of 2 nm . Therefore, liquid films smaller than $2\text{ }\mu\text{m}$ that are still present cannot be resolved and adjacent grains may appear as coalesced. This can obviously have a strong implication on the percolation analysis of the sample and on the measured solid-liquid interfacial area.

The surface tension of a liquid film, γ_{la} , is approximately 1 J/m^2 . A $2\text{ }\mu\text{m}$ wide liquid film (forming a hemicylindrical meniscus) can resist to a tension of $\frac{\gamma_{la}}{r} \simeq \frac{1\text{ J/m}^2}{1\text{ }\mu\text{m}} = 1\text{ MPa}$. This value is on the order of the elastic limit of Al-Cu alloys at 600°C [103, 104] and indicates that the semisolid material could already partially resist to grain boundary openings when a percolation of the solid phase is indicated by X-ray tomography observations.

7.2 *Ex situ* tomography

X-ray tomography observations were performed on Al-3.0wt.%Cu, Al-4.5wt.%Cu, and Al-6.0wt.%Cu alloys inoculated with 2.0wt% of AlTi5B master alloy. The samples were

Chapter 7. X-Ray tomography observations

solidified in the furnace II-sample 3 setup with a pulling speed of 2 mm/min in an average thermal gradient measured to be $10.4^{\circ}\text{C}/\text{cm}$ (see section 4.2.3). This corresponds to a cooling rate on the order of $-0.035^{\circ}\text{C}/\text{s}$.

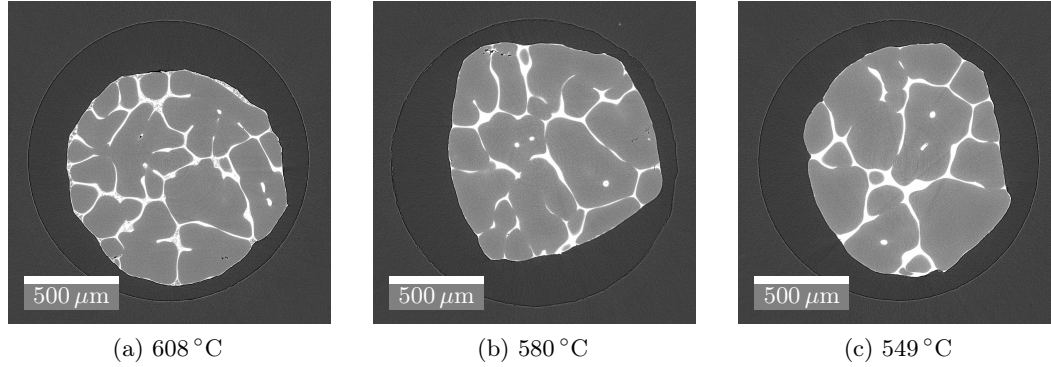


Figure 7.1: *Ex situ* X-ray tomography slice at various temperatures of an Al-6.0wt.%Cu alloy (inoculated with 2.0wt% of AlTi5B master alloy). The solid grains are in gray while the liquid is white.

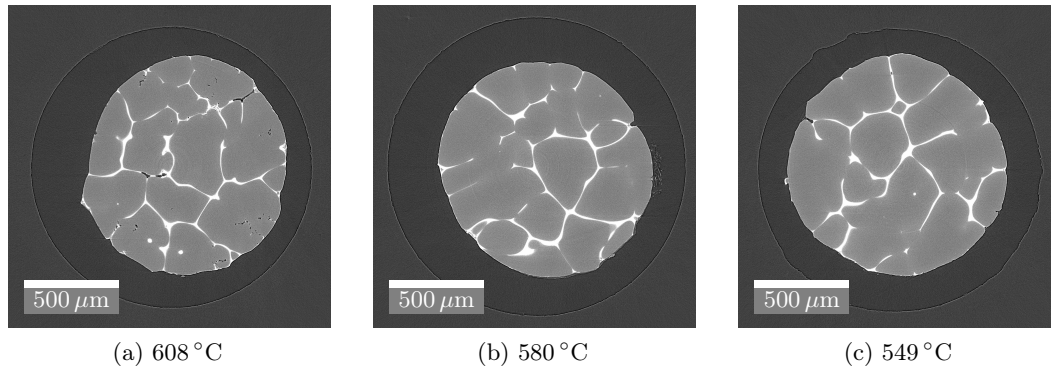


Figure 7.2: Same figure as Fig. 7.1 but for an Al-4.5wt.%Cu alloy (inoculated with 2.0wt% of AlTi5B master alloy).

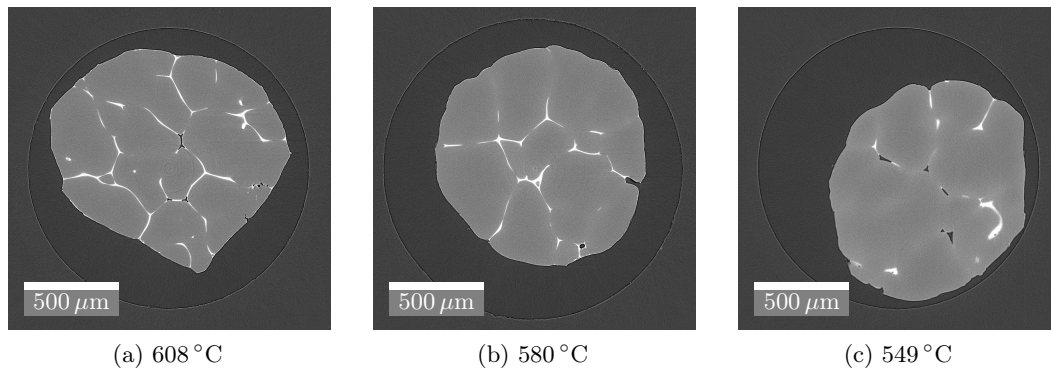


Figure 7.3: Same figure as Fig. 7.1 but for an Al-3.0wt.%Cu alloy (inoculated with 2.0wt% of AlTi5B master alloy).

As shown in Fig. 7.1(a), the microstructure is initially not fully globular, but globulo-dendritic. At lower temperatures (see Fig. 7.1(b) and (c)), the grains become more globular because of coarsening and coalescence of intragranular protrusion (since these are attractive parts). This is shown in the transition between Fig. 7.4(a) and (b). As shown in Fig. 7.2 and Fig. 7.3, for the other compositions, the grains are globular over the full range of solidification. This difference can be explained by observing the results in Table 7.1 in which the grain sizes of different compositions measured by EBSD are compared with the grain size characteristic of the globular-to-dendritic transitions, $2R_{g0,c}$ (see Eq. (2.31)). For all compositions, the measured grain sizes are smaller than $2R_{g0,c}$. However for the Al-6.0wt.%Cu alloy, it is the case for which these values are the closest, explaining why a globulo-dendritic grain structure is observed.

Table 7.1: Measured final average grain size, d_{g0} , (measured by EBSD as shown in table 4.5 and converted to 3D) compared with the grain diameter characteristic of the globular-to-dendritic transition, $2R_{g0,c}$ (calculated with Eq. (2.31) and the parameters given in Table 2.1).

Materials	d_{g0} [μm]	$2R_{g0,c}$ [μm]	$d_{g0}/2R_{g0,c}$
Al-6.0wt.%Cu	353	542	65%
Al-4.5wt.%Cu	305	594	51%
Al-3.0wt.%Cu	280	680	41%

The 3D reconstructed solid and liquid phases and the solid-liquid interface morphologies evolutions of the three alloys are shown in Figs. 7.5, 7.6 and 7.7. Their corresponding ISD plots are also represented.

We first define the the solid-liquid interfacial area per unit volume, $S_V = S_{sl}/V_R$, where

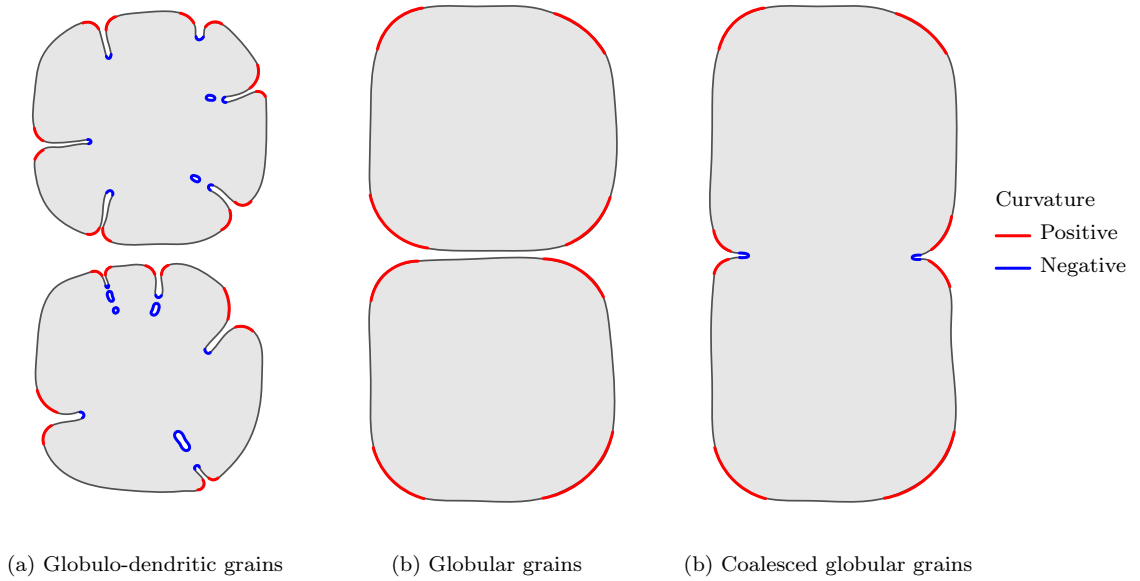


Figure 7.4: Schematic representation of the solid-liquid interface for different morphologies.

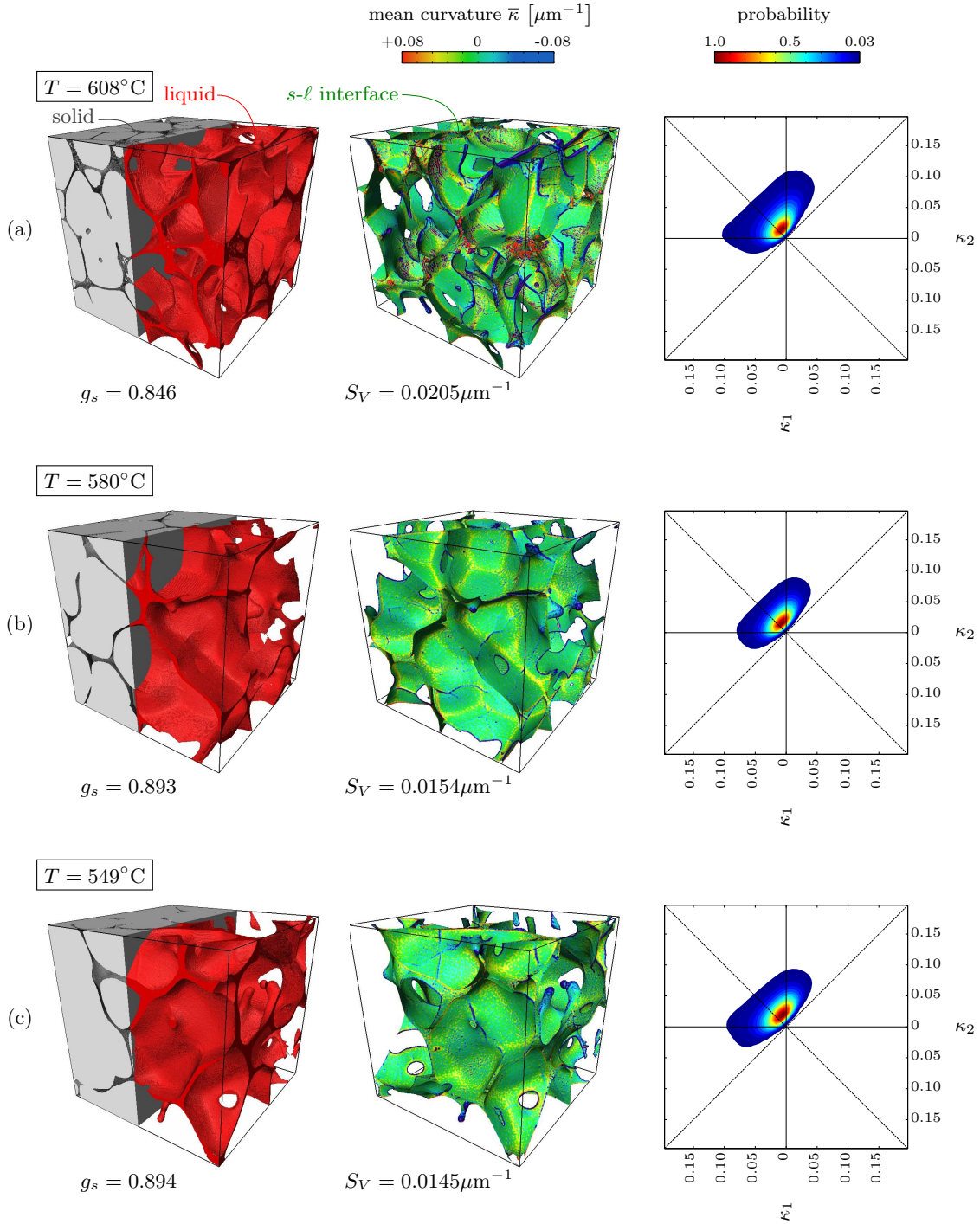


Figure 7.5: *Ex situ* tomography observation of a $600\mu\text{m} \times 600\mu\text{m} \times 600\mu\text{m}$ REV of an Al-6.0wt.%Cu (inoculated with 2.0wt% of AlTi5B master alloy) solidified with a pulling speed of 2mm/min in an average thermal gradient of $10.4^\circ\text{C}/\text{cm}$. On the left pictures are represented the solid (in gray) and liquid (in red) phases for different temperatures, while in the central picture is represented the corresponding solid-liquid interface. Note that the measured g_s and S_v are indicated for each temperature. On the right are plotted their corresponding ISD plots.

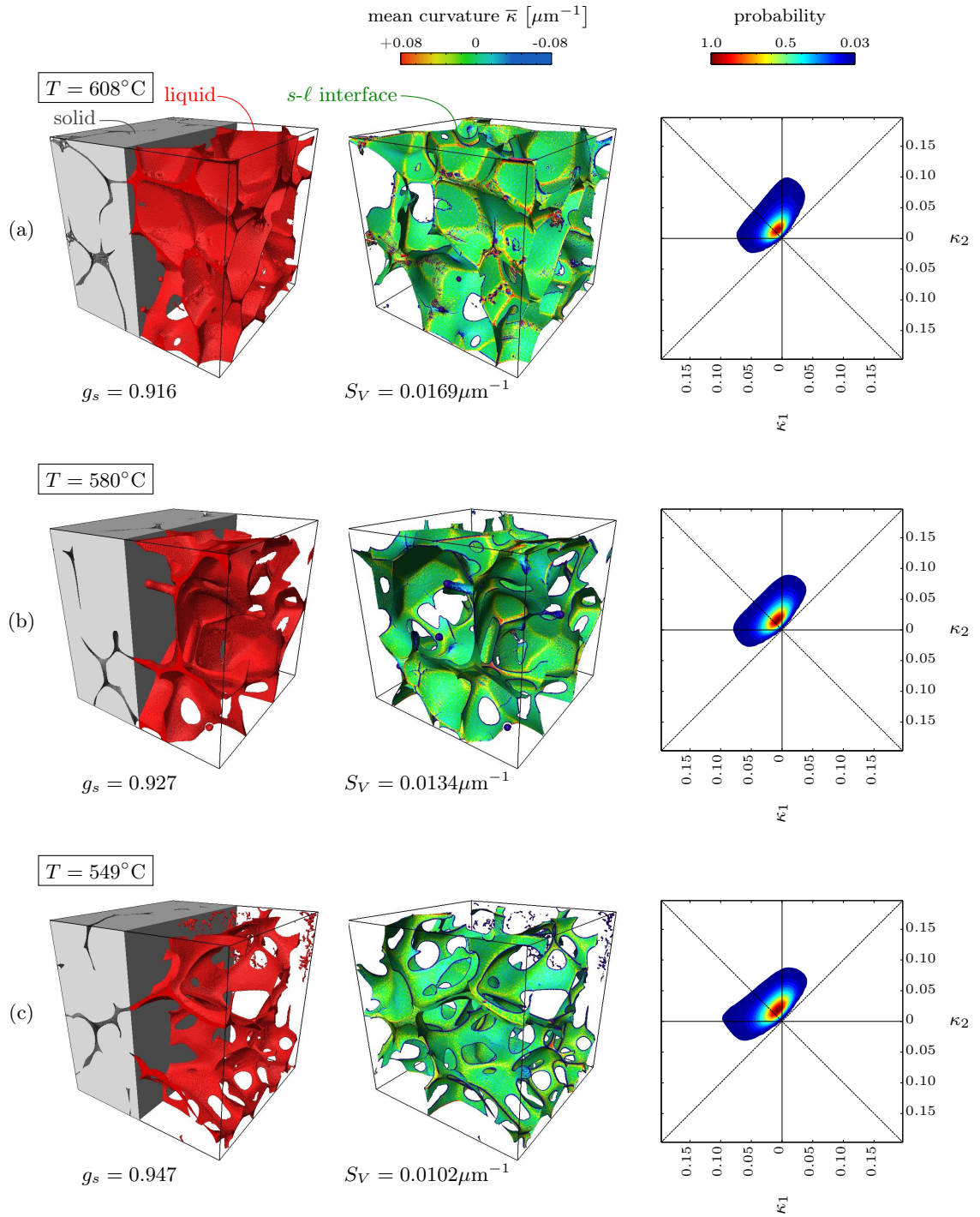


Figure 7.6: Same *ex situ* tomography observation of a $600\mu\text{m} \times 600\mu\text{m} \times 600\mu\text{m}$ REV as in Fig. 7.5 but for an Al-4.5wt.%Cu alloy (inoculated with 2.0wt% of AlTi5B master alloy).

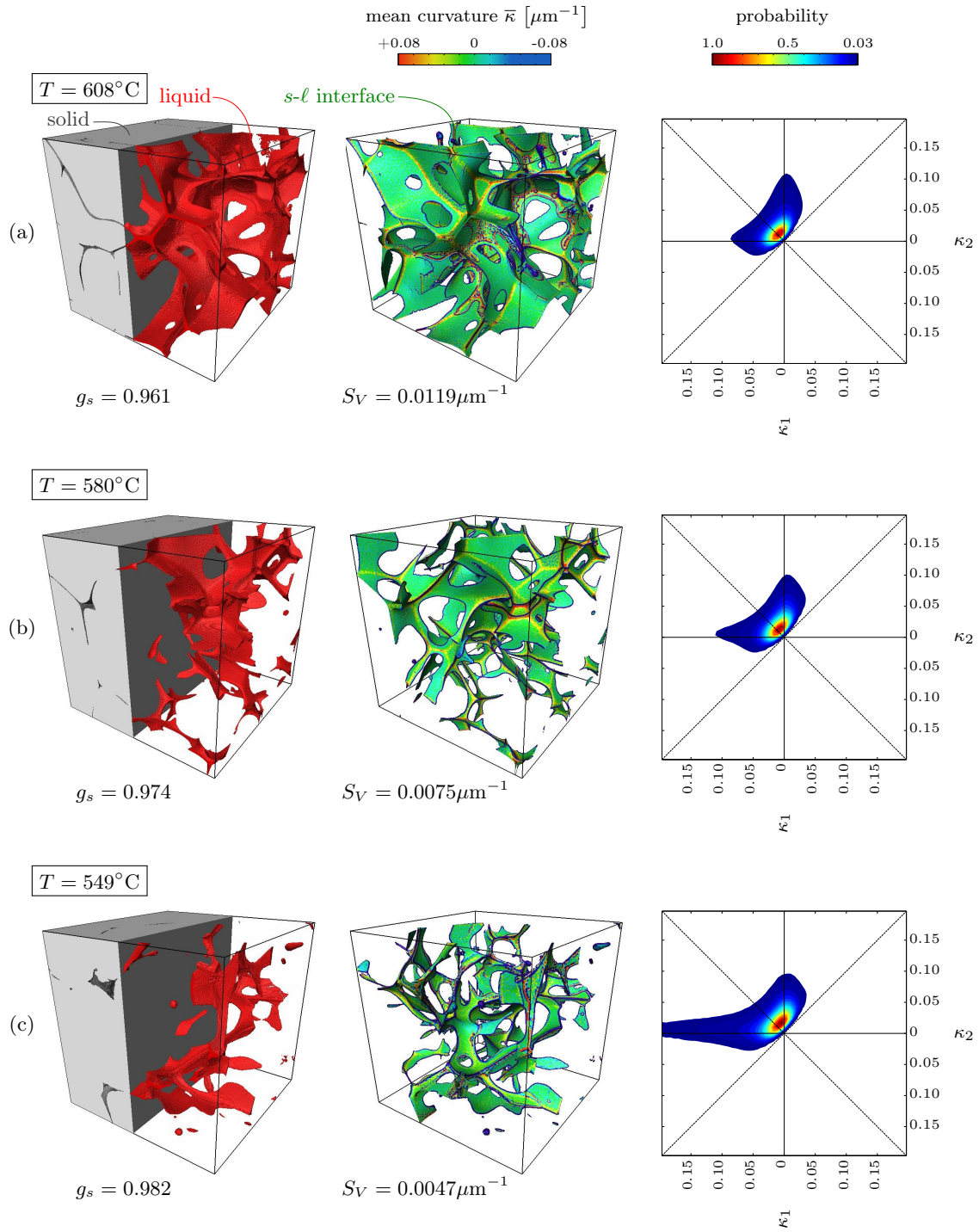


Figure 7.7: Same *ex situ* tomography observation of a $600\mu\text{m}\times 600\mu\text{m}\times 600\mu\text{m}$ REV as in Fig. 7.5 but for an Al-3.0wt.%Cu alloy (inoculated with 2.0wt% of AlTi5B master alloy).

S_{sl} in the area of the solid-liquid interface and V_R the representative elementary volume. As a general trend, as solidification proceeds, S_V initially increases because of grain growth but decreases in the last-stage solidification. This is due to two effects: first the coarsening of dendrite arms (and the consequent transformation of globulo-dendritic grains into fully globular ones) and second the coalescence between two grains (i.e., disappearance of two solid-liquid interfaces to form a grain boundary). The evolution of the solid-liquid interface curvature is schematized in Fig. 7.4. Before coarsening and intragranular coalescence of the protrusion regions with negative mean curvatures are present in the globulo-dendritic morphology, while these negative mean curvature regions disappear in the fully globular structure. In the last-stage solidification, because of grain coalescence (or when two grains are considered as coalesced because the liquid film separating them becomes smaller than the spatial resolution), some regions with mean negative curvature appear. They correspond to liquid pockets at vertices or liquid cylinders along triple lines.

In Fig. 7.8 are shown the envelopes that define the 0.03 probability of the ISD plots for the three alloys. As evidenced by the gray dotted circle in Fig. 7.8(a) for the 6wt%Cu alloy, at higher temperature (608°C), the ISD plot shows the presence of solid-liquid interface patches that possess a cylindrical type of curvature (κ_1 negative and κ_2 equal to zero) because of the globulo-dendritic morphology of the grains. At intermediate temperatures (580°C), the envelope includes less surface of this type because the structure becomes more globular. The effect of coalescence on the curvature distribution is visible in the lower temperature for the Al-3.0wt.%Cu alloy: as evidenced by the gray dotted circle in Fig. 7.8(c), the formation of liquid pocket cylinders is revealed by the shift of the envelope of the ISD plot towards a negative principal curvature κ_1 and κ_2 equal to zero.

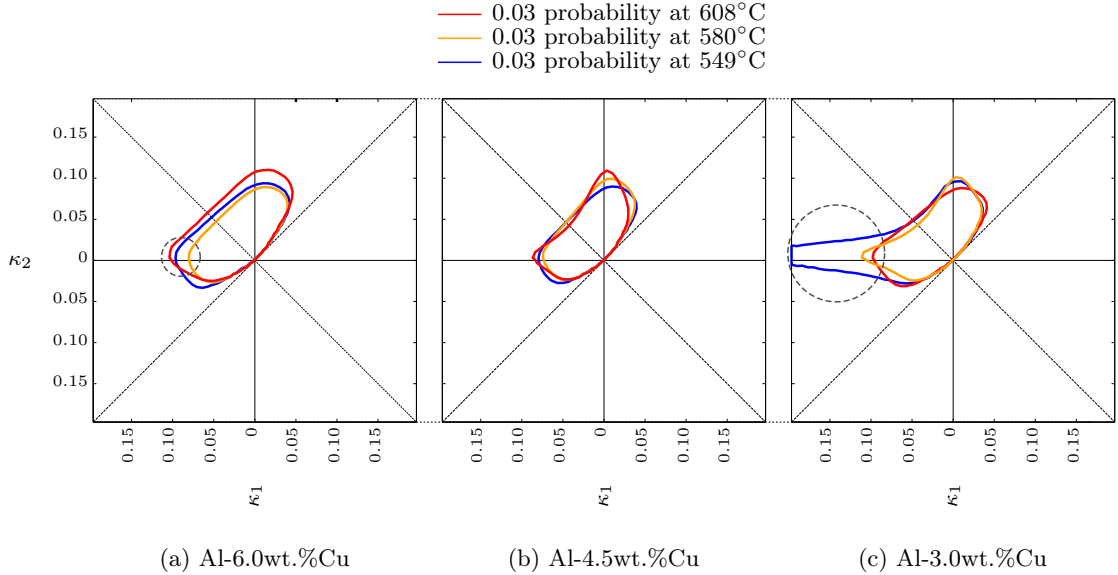


Figure 7.8: 0.03 probability contour of the ISD plots of the *ex situ* X-ray tomography observations, for three alloys.

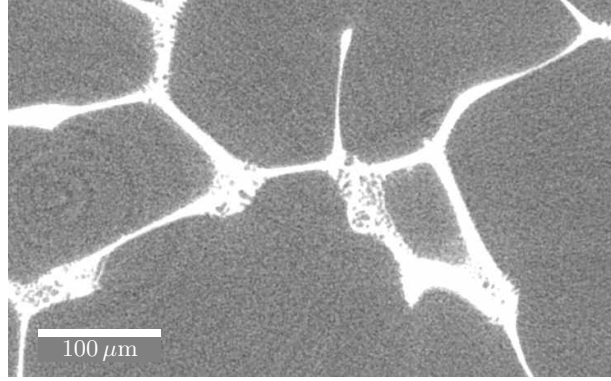


Figure 7.9: Zoom of Fig. 7.1 revealing the presence of small solid grains formed in the liquid during quench and introducing artifacts in the analysis.

It is useful to mention that, for solid fractions lower than approximately 0.85, a quenching artifact is present: as shown in Fig. 7.9, small solid particles form during the quench. For even lower solid fractions, the segmentation of the liquid and solid becomes more difficult because of this artifact. The surface associated to these artifacts is small and thus does have a limited influence on the ISD plots. However, the analysis of the percolation state was not performed in this case since it is biased by these artifacts.

As a conclusion, the ISD plot is a useful tool that allows to indirectly track grain coalescence. However, the limitation of the *ex situ* experiments is the presence of quenching artifacts and, in the present thermal conditions of the furnace II-sample type 3 setup, a relatively large grain size.

7.3 *In situ* tomography

As for the *ex situ* experiments, *in situ* X-ray tomography experiments were performed for various nominal compositions (also Al-3.0wt.%Cu, Al-4.5wt.%Cu, and Al-6.0wt.%Cu alloys inoculated with 2.0wt% of AlTi5B master alloy). For all the experiments, the samples were rapidly heated up to 700°C and held at this temperature for 2min. The samples were then cooled down at -0.05°C/s. This corresponds to the slowest cooling rate achievable with the laser furnace of TOMCAT, while keeping an acceptable temperature control of the laser-heated furnace. This is the reason why the cooling rate of the *in situ* experiments is slightly larger (in absolute value) than those experienced by the samples solidified with furnace II-sample 2 setup and observed *ex situ* (on the order -0.035°C/s). In the *in situ* experiments, solidification occurs during observation. In order to obtain sharp reconstructions, it is thus important to ensure that microstructure evolution remains limited during the observation time. The scan time is on the order of 160s, corresponding to a temperature change of the sample on the order of 8°C. By considering the Brody-Fleming's model (see Eq. (2.10)) with the Clyne and Kurz correction (see Eq. (2.11)), it is possible to estimate the change of solid fraction that occurs during the scan (see Table 7.2).

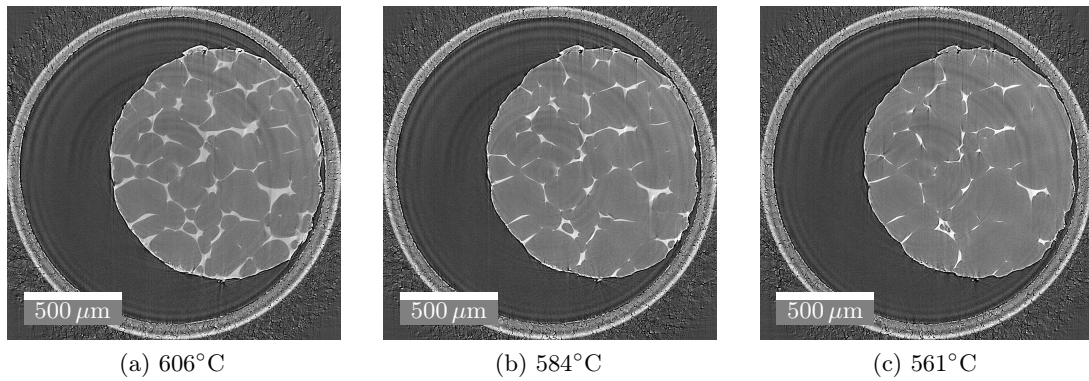


Figure 7.10: *In situ* X-ray tomography slice at various temperatures of an Al-6.0wt.%Cu alloy (inoculated with 2.0wt% of AlTi5B master alloy). The solid grains are in gray while the liquid is white. The temperature was measured by a pyrometer.

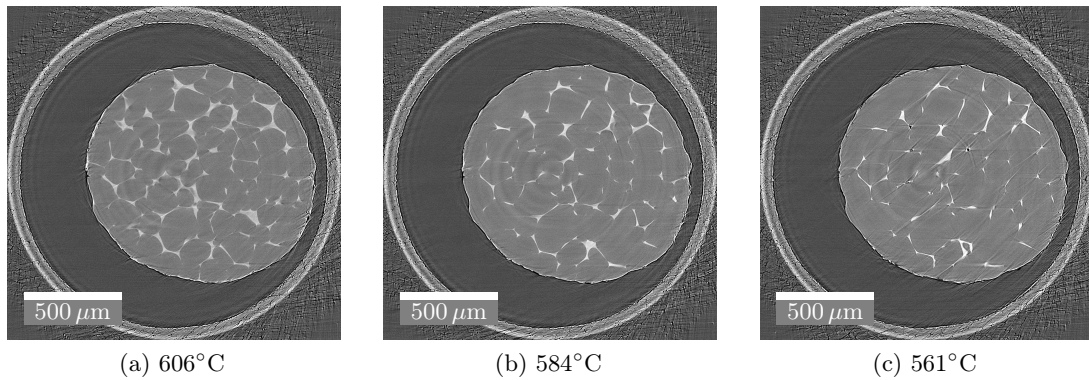


Figure 7.11: Same figure as Fig. 7.10 but of an Al-4.5wt.%Cu alloy (inoculated with 2.0wt% of AlTi5B master alloy).

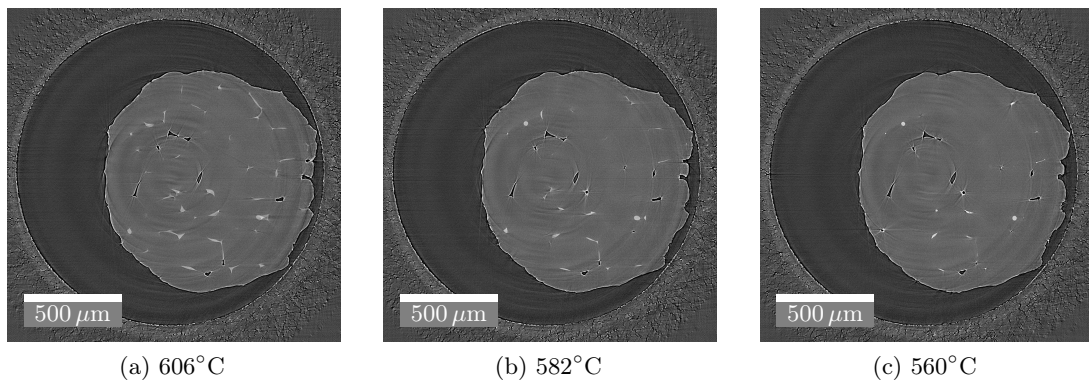


Figure 7.12: Same figure as Fig. 7.1 but of an Al-3.0wt.%Cu alloy (inoculated with 2.0wt% of AlTi5B master alloy).

As shown in Table 7.2, in the observations that were performed (last-stage solidification), the change of solid fraction during an observation is on the order of 0.005-0.02.

Chapter 7. X-Ray tomography observations

Table 7.2: Change of solid fraction during scan estimated from Eqs. 2.10 and 2.11 for various solid fractions and nominal compositions. The temperature change during the scan was on the order of 8°C (scan time on the order of 160s and a cooling rate of -0.05°C/s).

Materials	Solid fraction g_s	Change of g_s during scan
Al-3.0wt.%Cu	0.891	0.022
	0.938	0.013
	0.959	0.009
Al-4.5wt.%Cu	0.922	0.015
	0.952	0.010
	0.965	0.008
Al-6.0wt.%Cu	0.985	0.006
	0.992	0.005
	0.995	0.004

Please note that, even for a fixed temperature, there could be a microstructure evolution during the scans due to the globularization of the grains. However, since the microstructure in this case is fully globular for all the compositions considered (as shown in Figs. 7.10, 7.11 and 7.12), this phenomenon is negligible.

We recall that the grain size was measured to be 130 μm for the Al-6.0wt.%Cu inoculated alloy (see section 4.5). Compared to the *ex situ* ISD plots at a given temperature, the *in situ* ones show a more advanced percolation state. This can be explained by calculating the Fourier number associated with the solid, Fo_s :

$$Fo_s = \frac{D_s \Delta T}{\left(\frac{d_{g0}}{2}\right)^2 |\dot{T}|} \quad (7.1)$$

The ratio between the Fourier number in the *ex situ* case (Fo_s^{ex}) and *in situ* case (Fo_s^{in}) for the Al-6.0wt.%Cu inoculated alloy is the following:

$$\frac{Fo_s^{ex}}{Fo_s^{in}} = \frac{d_{g0}^{in2} |\dot{T}|^{in}}{d_{g0}^{ex2} |\dot{T}|^{ex}} = 0.19 \quad (7.2)$$

where d_{g0}^{ex} , d_{g0}^{in} , $|\dot{T}|^{ex}$ and $|\dot{T}|^{in}$ are the final grain sizes and absolute cooling rates in the *ex situ* and *in situ* experiments, respectively. The fact that $\frac{Fo_s^{ex}}{Fo_s^{in}} = 0.19$ explains why, for the same temperature the solid fraction is higher for the *in situ* experiments, i.e., solidification is more advanced, since the situation is closer to lever-rule.

Since the structure is fully globular, the decrease of S_V as solidification proceeds is exclusively due to grain coalescence. In addition, the initial shift of the ISD plot exhibited by the 6wt% *ex situ* specimen (shown in Fig. 7.8(a) and outlined by the gray dotted circle) is not present in this case.

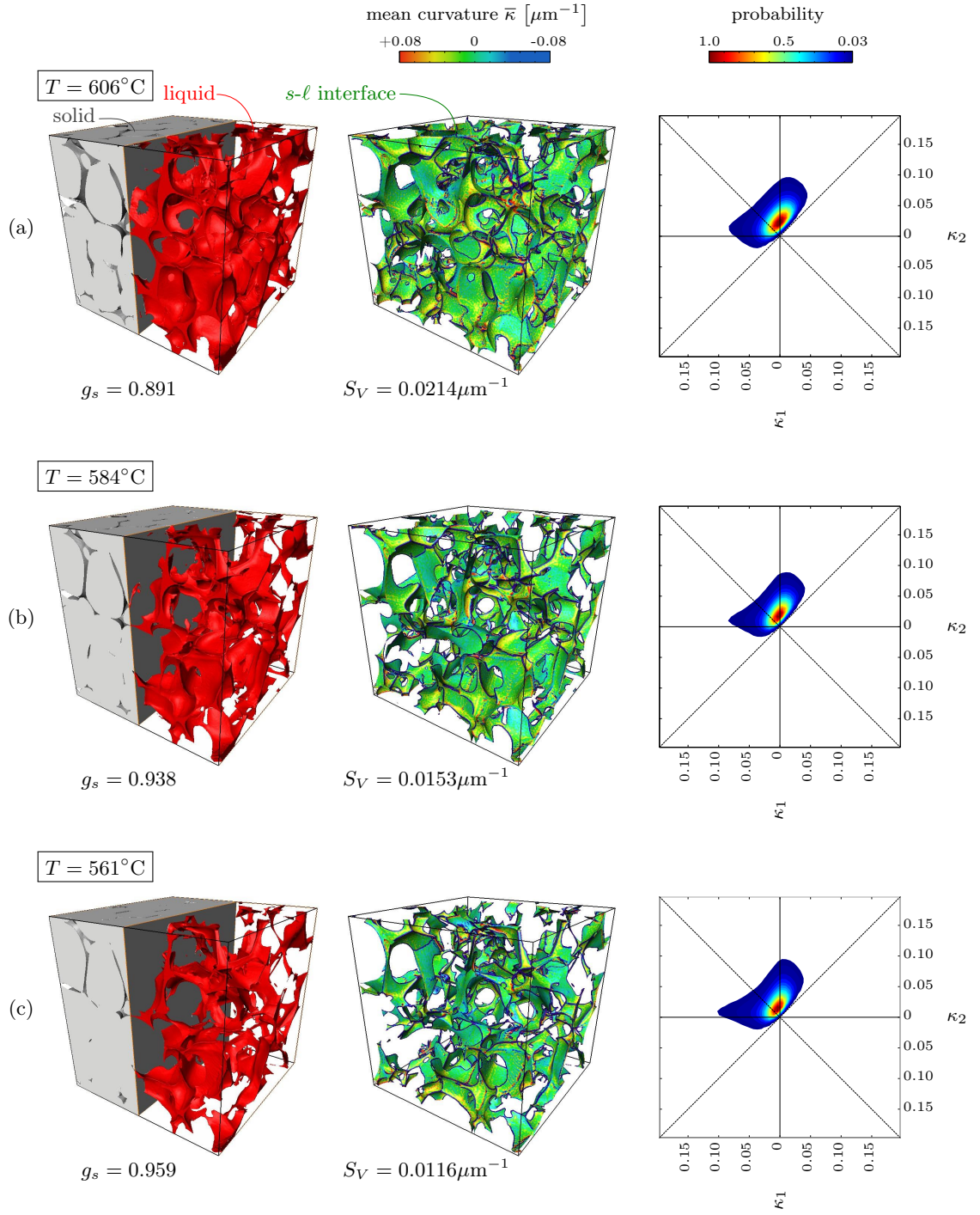


Figure 7.13: *In situ* tomography observation of a $600\mu\text{m} \times 600\mu\text{m} \times 600\mu\text{m}$ REV of an Al-6.0wt.%Cu (inoculated with 2.0wt% of AT5B master alloy) cooled down at -0.05°C/s . On the left pictures are represented the solid (in gray) and liquid (in red) phases for different temperatures, while in the central picture is represented the corresponding solid-liquid interface. Note that the measures g_s and S_v are indicated for each temperature. On the right are plotted the corresponding ISD plots. The temperature was measured by a pyrometer.

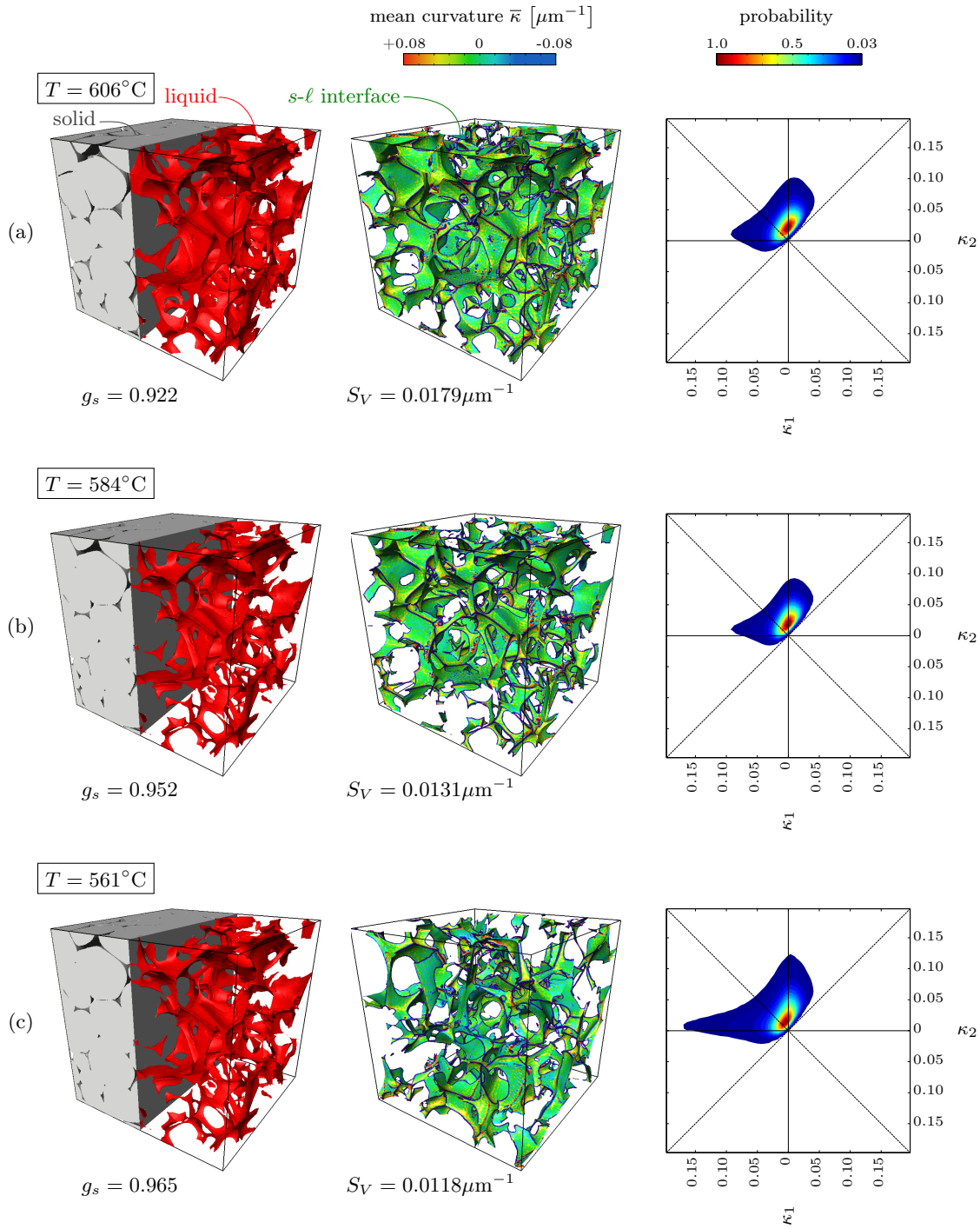


Figure 7.14: Same *in situ* tomography observation of a $600\mu\text{m} \times 600\mu\text{m} \times 600\mu\text{m}$ REV as in Fig. 7.13 but for an Al-4.5wt.%Cu alloy (inoculated with 2.0wt% of AlTi5B master alloy).

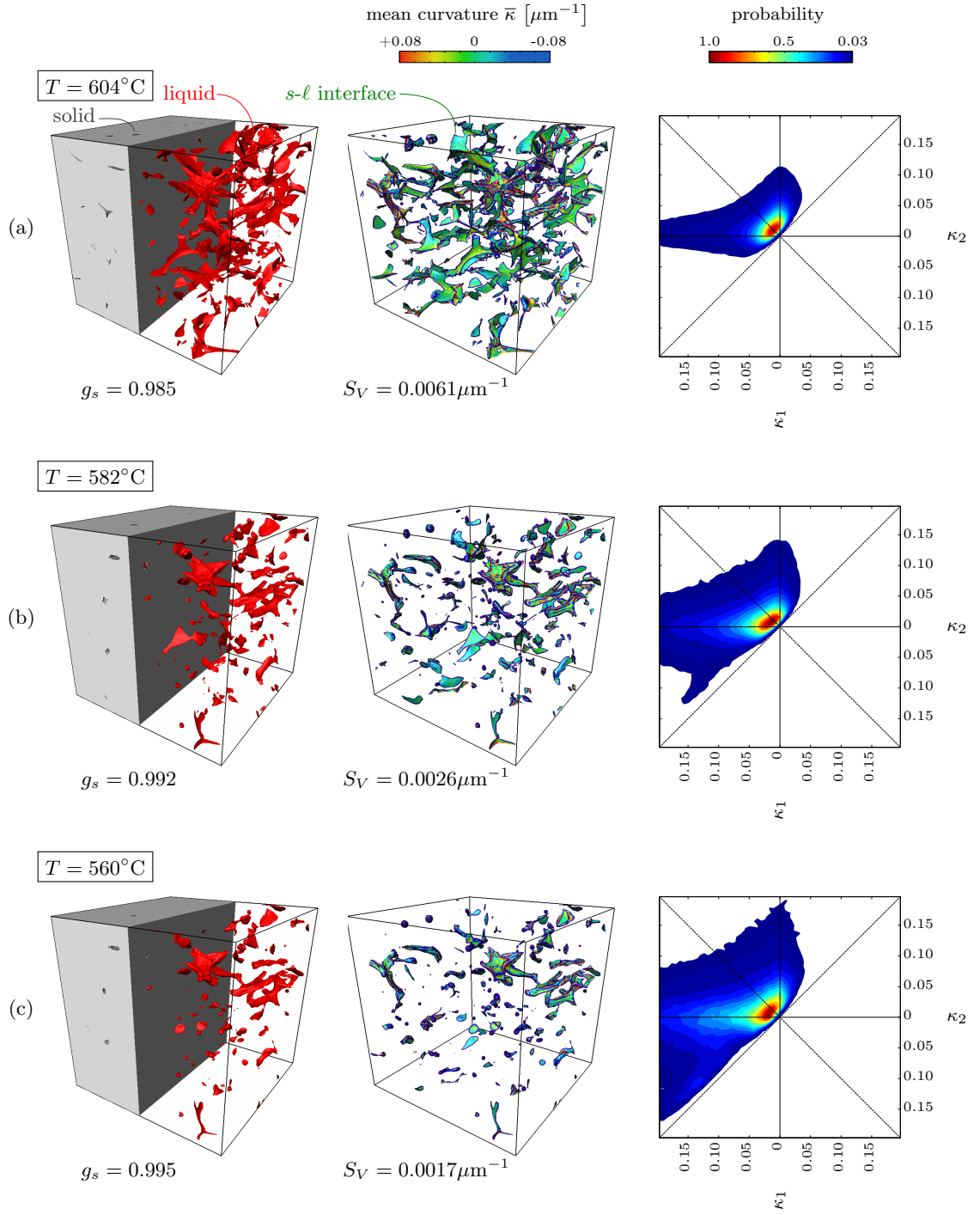


Figure 7.15: Same *in situ* tomography observation of a $600\mu\text{m}\times 600\mu\text{m}\times 600\mu\text{m}$ REV as in Fig. 7.13 but for an Al-3.0wt.%Cu alloy (inoculated with 2.0wt% of AlTi5B master alloy).

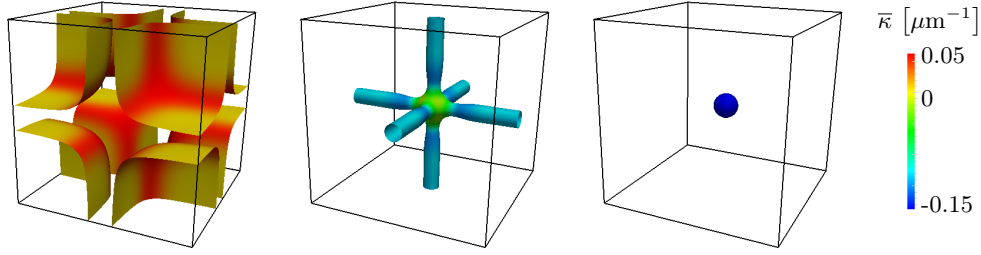


Figure 7.16: Schematic representation of the mean curvature transitions of 8 grains (only 1/8 of each grain is shown) growing in a box of $100\mu\text{m}$ side length. (a) At higher solid fraction, the solid-liquid interfaces consist of flat surfaces and positive curvatures in the corners/edges. (b) The liquid phase consists of cylinders. (c) In the last-stage solidification, some liquid pockets remain.

As evidenced in the gray dotted circles in Figs. 7.17(a) and 7.17(b), the progressive coalescence leads to the formation of liquid cylinders. This is revealed by the shift of the ISD envelope towards a negative principal curvature, the other principal curvature being zero. In Fig. 7.17(c), the region highlighted by the dotted gray circle represents a patch of curvature that possesses two negative principal curvatures, i.e., a liquid pocket. These two transitions are schematized in Fig. 7.16.

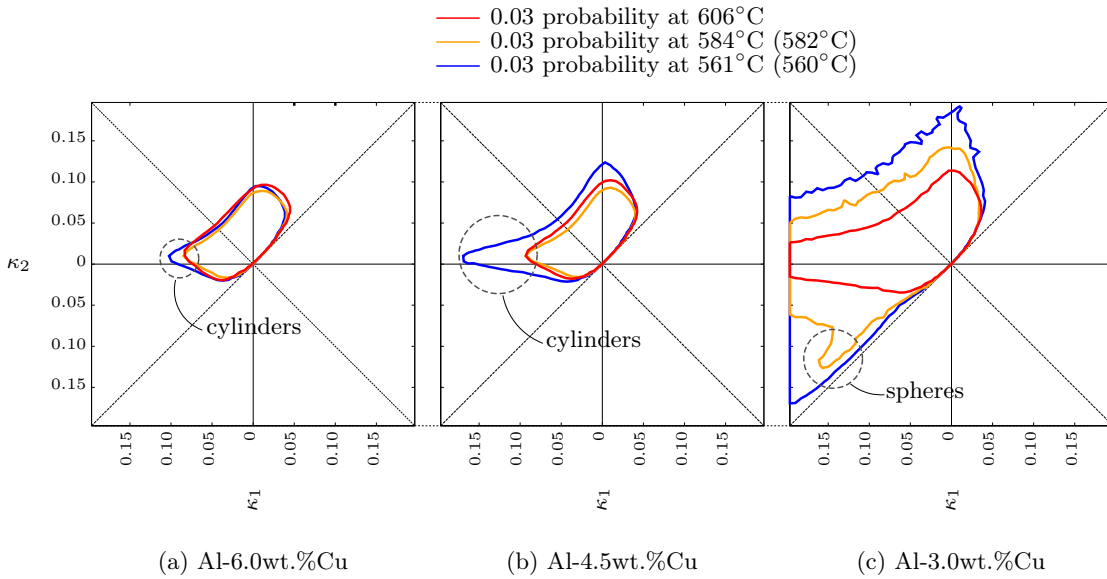


Figure 7.17: Contour at 0.03 probability of the ISD plots of the *in situ* X-ray tomography observations. Please note that the temperatures of the Al-3.0wt.%Cu sample are slightly different and noted in parenthesis in the legend. The regions indicating the presence of cylinders or spheres are shown by a dotted gray circle.

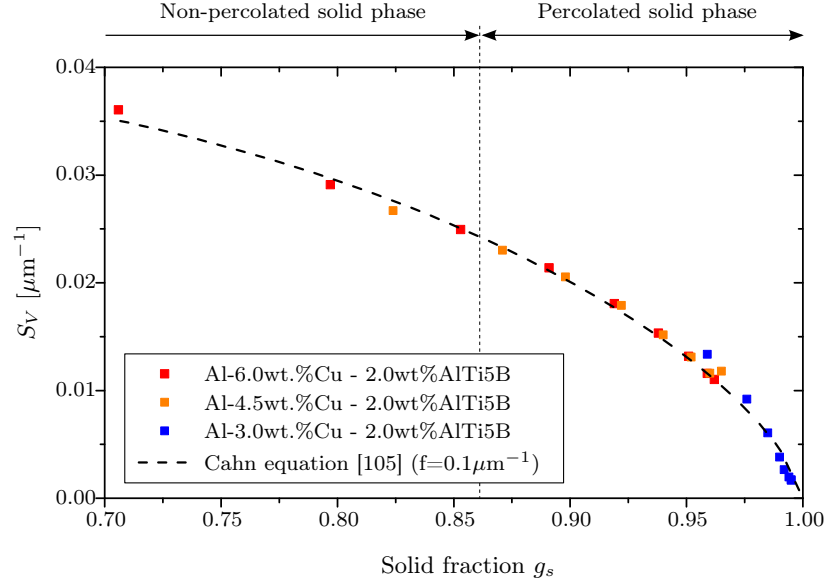


Figure 7.18: Evolution of S_V as a function of the solid fraction, g_s , for various X-ray tomography *in situ* observations. The points are fitted with equation Eq. (7.3) with the constant $f = 0.1\mu\text{m}^{-1}$. The range of solid fractions for which the liquid phase is percolated or not in the *in situ* observations is indicated.

The evolution of S_V as a function of g_s for the various compositions observed by *in situ* X-ray tomography is shown in Fig. 7.18. The points are fitted with the analytical evolution of S_V as a function of g_s for spherical grains given by the following equation [105] (similarly to the analysis performed by Ludwig *et al.* [56]):

$$S_V = f (1 - g_s)^{\frac{2}{3}} g_s^{\frac{2}{3}} \quad (7.3)$$

where f is a constant. At low solid fractions, Eq. (7.3) becomes $S_V = f g_s^{2/3}$. Since $g_s = R_g/R_{g0}$, at low solid fractions S_V can be expressed as follows:

$$S_V = \frac{4\pi R_g^2}{\frac{4}{3}\pi R_{g0}^3} = \frac{3}{R_{g0}} g_s^{\frac{2}{3}} = \frac{6}{d_{g0}} g_s^{\frac{2}{3}} \quad (7.4)$$

indicating that $f = 6/d_{g0}$.

In Fig. 7.18, it was found that the experimental points can be well fitted by Eq. (7.3) with $f = 0.1\mu\text{m}^{-1}$. This would indicate a final grain size of $60\mu\text{m}$, while it was measured to be $184\mu\text{m}$ with the EBSD analysis. This discrepancy can be explained by the fact that Eq. (7.3) describes the impingement of spherical grains, while in reality the grains shape departs from a sphere when the solute layers start to interact.

A percolation analysis of the microstructures observed at different temperatures and for various compositions was performed. This analysis revealed that the solid becomes percolated within the REV at a solid fraction $g_s = 0.86$ (see Fig. 7.18). However, it should be noted that this analysis, performed on images with a limited spatial resolution

on the order of $2\text{ }\mu\text{m}$ (corresponding to three times the voxel size), is not representative of the real percolation state of the sample. The liquid phase remains percolated until a solid fraction $g_s = 0.95$ (we recall that in 3D it is possible to have percolation of the two phases at the same time).

As a conclusion, the analysis of the evolution of S_V and of the shift of the ISD plot envelopes allows to indirectly track grain coalescence. It is also possible to find the solid fraction at which the solid structure is percolated. However, the limited spatial resolution, introduces a bias in the value of solid fraction at which the solid becomes percolated.

The 3D mesoscopic model simulations performed with the correct physical values (see section 8.3) will provide more insight in the values at which the structure is effectively percolated. In addition, by directly comparing the mesoscopic model and the X-ray tomography results, it will be possible to estimate the actual spatial resolution of the X-ray tomography observations.

8 Mesoscopic model results

8.1 Introduction

After the validations performed in section 6.3, this chapter is dedicated to the main results of the mesoscopic model, considering the percolation of several grains.

At first are shown the results of the 2D model, in particular the evolution of the solute profiles, the evolution of the solid-liquid interfacial area per unit volume, S_V , and the various percolation transitions. The calculations were performed on a domain containing typically a few thousands of grains. After that, 3D simulations were performed by considering a few hundreds of grains. For both the 2D and 3D mesoscopic models, the percolation transitions were then mapped for various nominal compositions and solidification conditions.

Finally, the 3D model results are compared with the *in situ* X-ray tomography observations.

In Table 8.1 are summarized the main physical parameter values used for the calculations. The parameters $\gamma_{gb,max}$ and γ_{sl} are the same as those of 2D granular model of Vernède *et al.* for comparison. The choice of these parameters for the 3D model are justified in section 8.3.1.

Table 8.1: Summary of the main physical parameter values used for the calculation, unless otherwise stated.

Parameter	value for 2D model	value for 3D model
$\gamma_{gb,max}$	0.32 J/m ² [36]	Bulatov <i>et al.</i> [34]
γ_{sl}	0.1 J/m ² [1]	0.135 J/m ² [106]
ΔS_f	1.0 10 ⁶ J/(m ³ K) [36]	
D_ℓ	3.0 10 ⁻⁹ m ² /s [107]	
D_s	3.0 10 ⁻¹³ m ² /s	
δ_{sl}	1 nm	

8.2 2D results

8.2.1 Solute diffusion and coalescence

In order to visualize the evolution of the solute profile and how coalescence affects the distribution of solute, the model was run for only a few grains, namely 36, possessing a

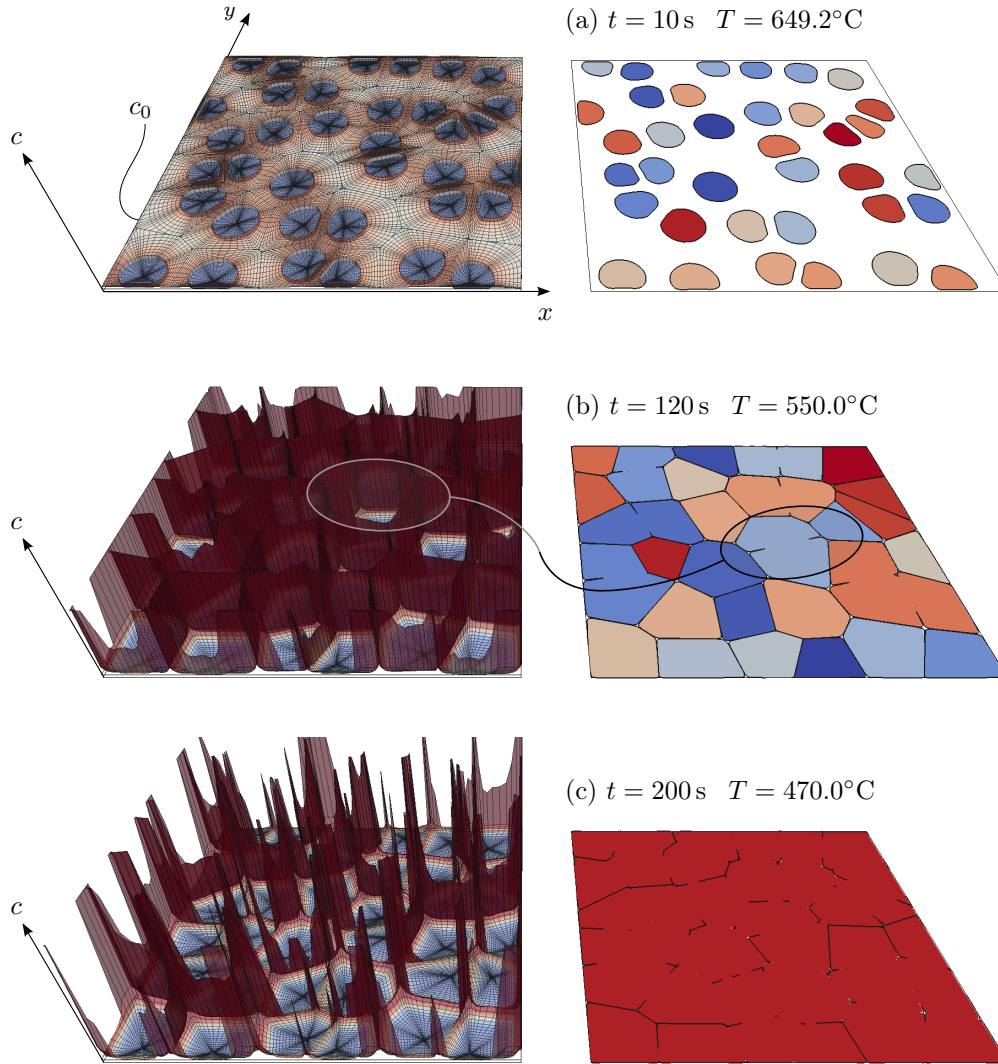


Figure 8.1: Simulation with the 2D mesoscopic model of the progressive percolation of 36 grains of an Al-1.0wt.%Cu alloy for different times. The average grain size was set to $100 \mu\text{m}$ and the cooling rate $\dot{T} = -1^\circ\text{C/s}$. On the left are represented the concentration fields, while on the right each grain cluster has a specific color (note that the solid-liquid interface is traced in black). The gray circles in figure (b) indicate two grains that are coalesced.

random orientation. In the initial stages of solidification, the grains shape starts to depart from a sphere because of the diffusion boundary layers interactions (see Fig. 8.1(a)). However, at this stage, the grains form distinct clusters since coalescence has not yet occurred. As shown in Fig. 8.1(b), at a more advanced stage, the grains begin to be in contact. As highlighted by the gray circle in Fig. 8.1(b), the concentration in the liquid film separating the two impinging grains is reduced until the *coalescence line* on the phase diagram is reached. This is essentially due to solute back-diffusion in the solid perpendicularly to the solid-liquid interface (at this stage, the liquid is in a state of almost complete mixing, i.e., the diffusion of solute parallel to the solid-liquid interface is negligible). At this point, the two grains highlighted by the gray circle in Fig. 8.1(b) are considered to belong to the same cluster and thus possess the same color. We recall that the position of the coalescence line on the phase diagram depends on the coalescence undercooling ΔT_b , which is proportional to $(\gamma_{gb}(\Delta\theta) - 2\gamma_{sl})$ in the repulsive case (see section 5.2.2). The arrangement and the crystallographic orientations of the grains are random, thus generating a liquid film that can possess a complex morphology. As shown in Fig. 8.1(c), at a much lower temperature, only a single solid cluster remains. In this case the solid is percolated, since it is possible to find a path connecting the two opposite sides of the domain, in both x and y directions.

8.2.2 Definition of the percolation transitions

In this section we define the main percolation transitions that the grain structure undergoes.

The progressive formation of grain clusters can be tracked following two different criteria. With the contact criterion, two grains belong to the same cluster when the thickness of the liquid film separating them becomes on the order of the solid-liquid interface thickness, δ_{sl} (*contact clusters*). With the coalescence criterion, two grains belong to the same cluster when they are locally coalesced and are thus connected via a dry grain boundary (*coalescence clusters*). The temperature and solid fraction at which a percolating contact cluster appears (*percolation by contact*) are noted by T_{pcont} and $g_{s,pcont}$, respectively. Considering the coalescence criterion, when *percolation by coalescence* occurs, the temperature and solid fraction are labelled as T_{pcoal} and $g_{s,pcoal}$, respectively. These percolation transitions are shown in Fig. 8.2, in a simulation performed with 1024 grains possessing an average size of $100\ \mu\text{m}$. As shown in Fig. 8.2 and in Fig. 8.3(b), the number of contact clusters decreases faster than the coalescence clusters, since the coalescence criterion is more restrictive. This can be seen in particular at 534°C , where a single contact cluster exists while several coalescence clusters persist. A typical property that exhibits a strong variation close to a percolation transition is the size of the largest non-percolated cluster [39]. For both the contact and coalescence criteria, it initially increases, but, once a percolating cluster exists, it decreases since the percolating cluster fills the remaining space. In Fig. 8.3(a) is represented the ratio between the volume (area) of the largest non-percolating cluster and the total volume of solid. The transitions are

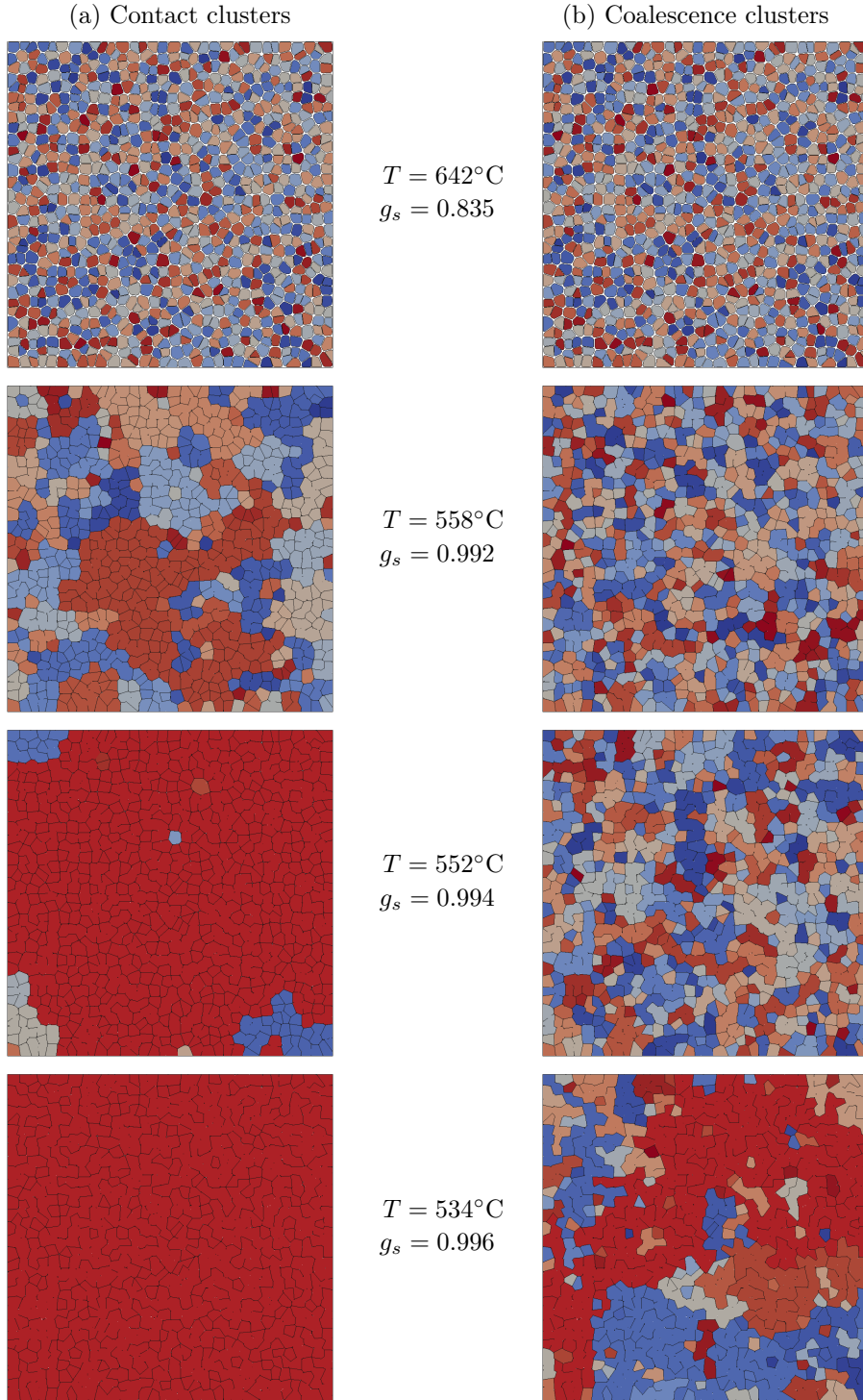


Figure 8.2: Simulation with the mesoscopic model of the progressive percolation of 1024 grains of an Al-1.0wt.%Cu alloy for different times. The average grain size was $100\text{ }\mu\text{m}$ and the cooling rate was set to $\dot{T} = -1^{\circ}\text{C/s}$. The solid clusters are colored following two different criteria: (a) contact clusters, (b) coalescence clusters. For both criteria, the percolating cluster is highlighted in red.

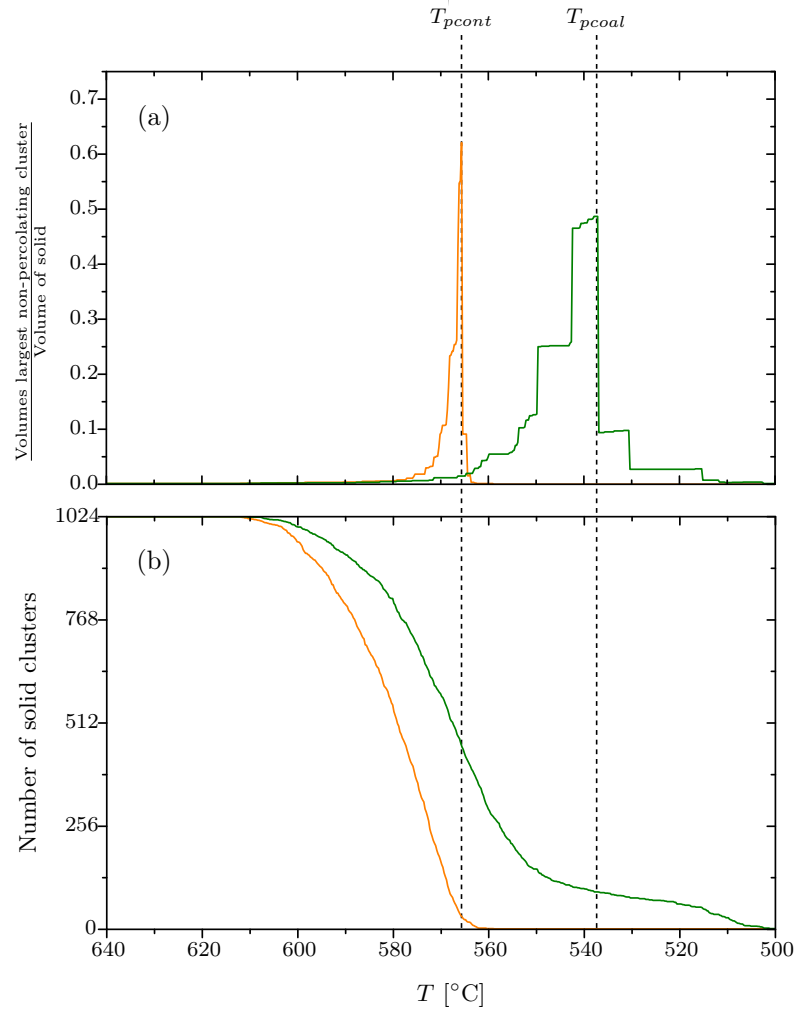


Figure 8.3: (a) Evolution fraction of the largest non-percolating cluster (defined as the ratio between the volume of the largest non-percolating cluster and the solid volume) as a function of temperature for the simulation shown in Fig. 8.2. (b) Number of solid clusters evolution as a function of temperature. For both graphs are indicated the temperatures characteristic of the percolation of the solid structure: T_{pcont} and T_{pcoal} .

clearly visible for both contact and coalescence criteria. Please note that in reality, at 548°C , the eutectic would have filled the remaining liquid space (if the second phase can nucleate), but the model allows to find the solidification of eutectic-free alloys.

When two grains coalesce, part of the solid-liquid interface is substituted with a grain boundary interface. Therefore, in order to track the progressive percolation of grains, one can observe the evolution of the solid-liquid interfacial area per unit volume, S_V . This value has been normalized by the average final grain size, d_{g0} , in order to obtain $\mathcal{S}_V = S_V d_{g0}$. As shown in Fig. 8.4, for the model, the evolution of \mathcal{S}_V as a function of the solid fraction initially increases because of grain growth, but then decreases abruptly

at a solid fraction of approximately $g_s = 0.97$, when grain coalescence becomes significant. The solid fraction/temperature at which the maximum value of S_V (corresponding also to the maximum of S_V) is found are denoted as g_{s,S_Vmax} and T_{S_Vmax} , respectively. It is interesting to note that, until significant coalescence takes place, the evolution of S_V closely follows the predictions of a regular hexagonal arrangement of edgy grains. Please note that for the calculation of S_V in the case of edgy grains, it is assumed that $d_{g0}n_g^{2D} = 1$, where n_g^{2D} is the 2D density of nucleation sites.

These results can be compared with the 2D granular model of Vernède *et al.* [40]. We recall that the latter considers complete mixing in the liquid and polyhedral grains with a correction to smooth the grain corners. For an Al-1.0wt.%Cu alloy and the same cooling rate, the temperatures at which the various transitions occur are in good agreement, the main noticeable difference are g_{s,S_Vmax} , since it is on the order of 0.975 for the present model, while it is on the order of 0.90 for the model of Vernède *et al.*. Because of the assumptions used in the Vernède model, the curvature at the grain corners could be overestimated thus predicting a lower g_{s,S_Vmax} . In addition, we recall that the present mesoscopic model simulates a progressive coalescence of grains, while, in the model of Vernède *et al.*, a grain boundary is either fully coalesced or not. The progressiveness of the coalescence in the mesoscopic model can also explain why a larger g_{s,S_Vmax} is found, since, when coalescence initially takes place, the reduction of S_V is not as drastic as for the granular model of Vernède *et al.*.

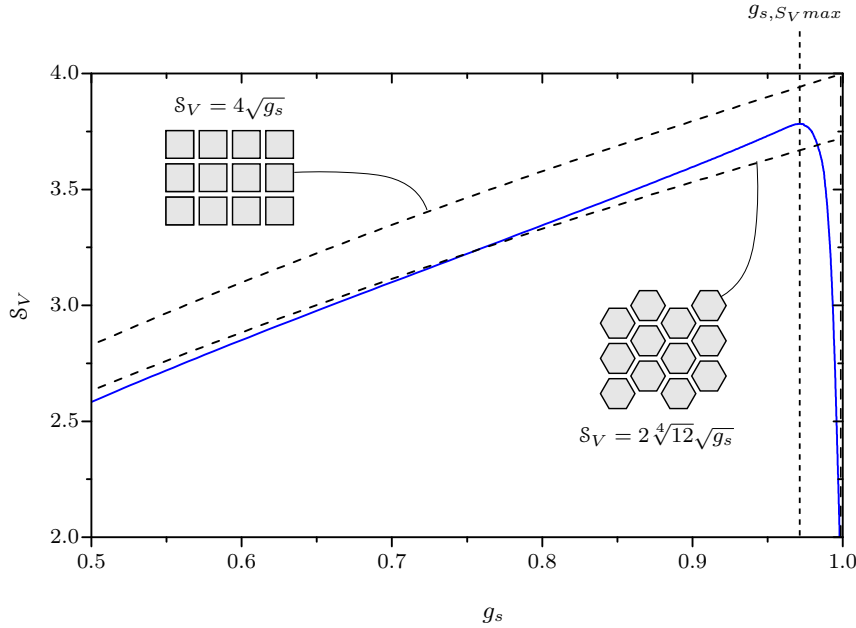


Figure 8.4: Evolution of $S_V = S_V d_{g0}$ as a function of the solid fraction, g_s . The model prediction is compared with the evolution of S_V for a regular square arrangement and a regular hexagonal arrangement of edgy grains. The solid fraction at which S_V is maximum (corresponding also to the solid fraction at which S_V is maximum), g_{s,S_Vmax} , is also indicated.

As pointed out by Vernède *et al.* [40], another important transition can be defined: the solid fraction/temperature at which 1% of the liquid channels become isolated from the feeding network. This value gives an indication of the moment at which feeding in the liquid phase becomes difficult, i.e., when conditions favourable to hot tear formation are present. In the present mesoscopic model, since liquid feeding is not accounted for, we suppose that the feeding network is represented by the largest liquid cluster. The temperature/solid fraction at which 1% of the liquid channels become isolated from the largest liquid cluster are thus considered. They are noted as $T_{iso-\ell}$ and $g_{s,iso-\ell}$, respectively.

As pointed out in section 2.3, the observed percolation threshold in domain of size L , $g_{sc,L}$ (that can be either the solid fraction at which percolation by contact or percolation by coalescence occur) can be expressed as the following scaling law:

$$\sqrt{\langle (g_{sc,L} - \langle g_{sc,L} \rangle)^2 \rangle} \propto L^{-1/\nu} \quad (8.1)$$

where the term $\sqrt{\langle (g_{sc,L} - \langle g_{sc,L} \rangle)^2 \rangle}$ represents the standard deviation of the observed

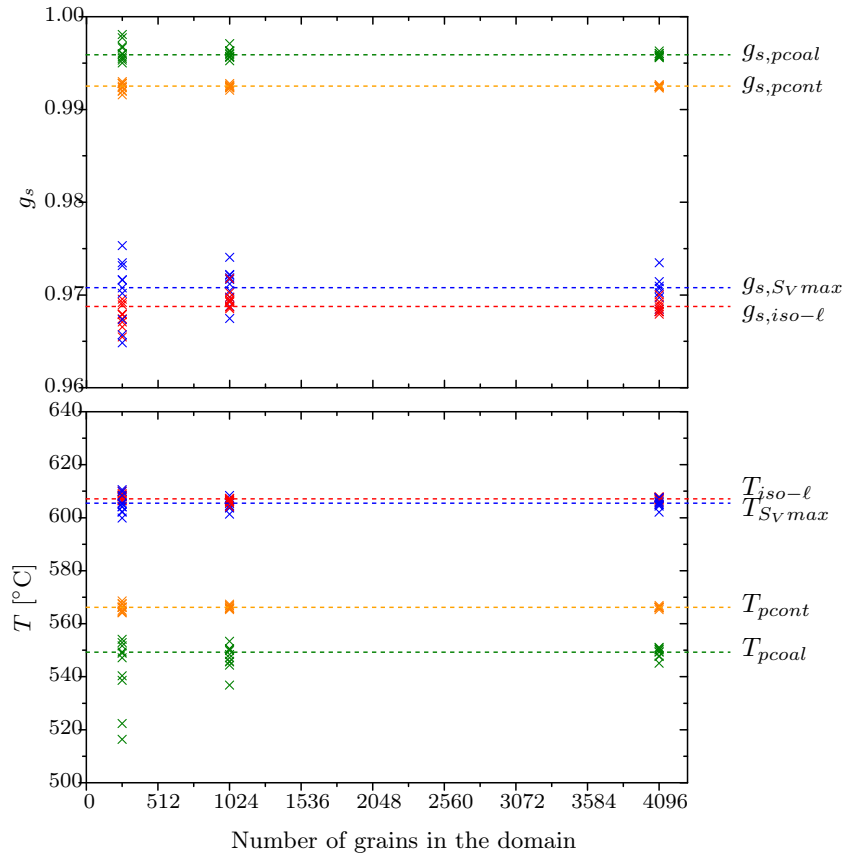


Figure 8.5: Various solid fractions and temperatures transitions as a function of the number of grains in the domain.

percolation threshold in a domain of size L and ν is the correlation length. Ten calculations were performed for each domain size, containing respectively 256, 1024 and 4096 grains (see Fig. 8.5). As expected from Eq. (8.1), Fig. 8.5 shows that the larger the number of grains in the domain, the lower the spread of the percolation thresholds. In order to find an accurate value of percolation threshold it is needed to either perform the simulations on a large domain or several simulations on smaller domains and take the average. With Eq. (8.1), it is possible to find the correlation length for different percolation transitions: for contact percolation the correlation length is found to be $\nu = 0.91 \pm 0.9$, while for the coalescence percolation $\nu = 1.08 \pm 0.9$. Unlike the results of Vernède *et al.* [40], in which 100 simulations for various domain sizes were performed (containing up to 102400 grains), the correlation length values of the simulations performed with the mesoscopic model are not in good agreement with the theoretical values of lattice percolation in 2D (equal to $4/3$). It would be needed to perform a larger number of simulations and also simulations containing more grains. However, due to the computational cost of the present mesoscopic model, the simulations were limited to a maximum number of 4096 grains. The complete solidification of 4096 grains typically requires 12h, when run on the calculation server over 8 processors.

8.2.3 Percolation transitions for several grains

As shown in Fig. 8.6, the temperatures and solid fractions at which the various transitions occur are plotted as a function of nominal composition. In this figure, the regions of temperature/solid fractions at which isolation of liquid pocket starts but no percolation by coalescence or contact happened is highlighted in red. We recall that this region is vulnerable in terms of hot tearing since liquid feeding is not sufficient but the solid structure is not yet percolated and thus cannot resist to grain boundary openings. On the other hand, when percolation by coalescence happens or when the eutectic phase nucleates, the semi-solid material behaves like a ductile solid and can resist to grain boundary openings (green region). An intermediate colored is noted in orange when there is percolation by contact but percolation by coalescence (or by the eutectic) is not yet reached. It is also possible to define $c_{0,HT}$ as the nominal composition range for which the vulnerable region in terms of hot tearing (red region in Fig. 8.6) is explored during solidification. In addition, the nominal composition at which the time spent in the vulnerable region is maximum (or maximum temperature interval of the vulnerable region since a constant cooling rate is considered) is noted as $c_{0,HT}^{max}$.

In figure Fig. 8.7 are compared the various transitions for different cooling rates and values of γ_{sl} . By comparing Fig. 8.7(a) and (b), one can see that, for a given nominal composition, the transitions take place at lower temperatures (or higher solid fractions) when the cooling rate is increased by 10 (in absolute value). This can be explained by the fact that the Fourier number associated to case (b) is lowered by a factor 10 compared to case (a). In addition, by increasing the cooling rate, the curvature of the grain corners

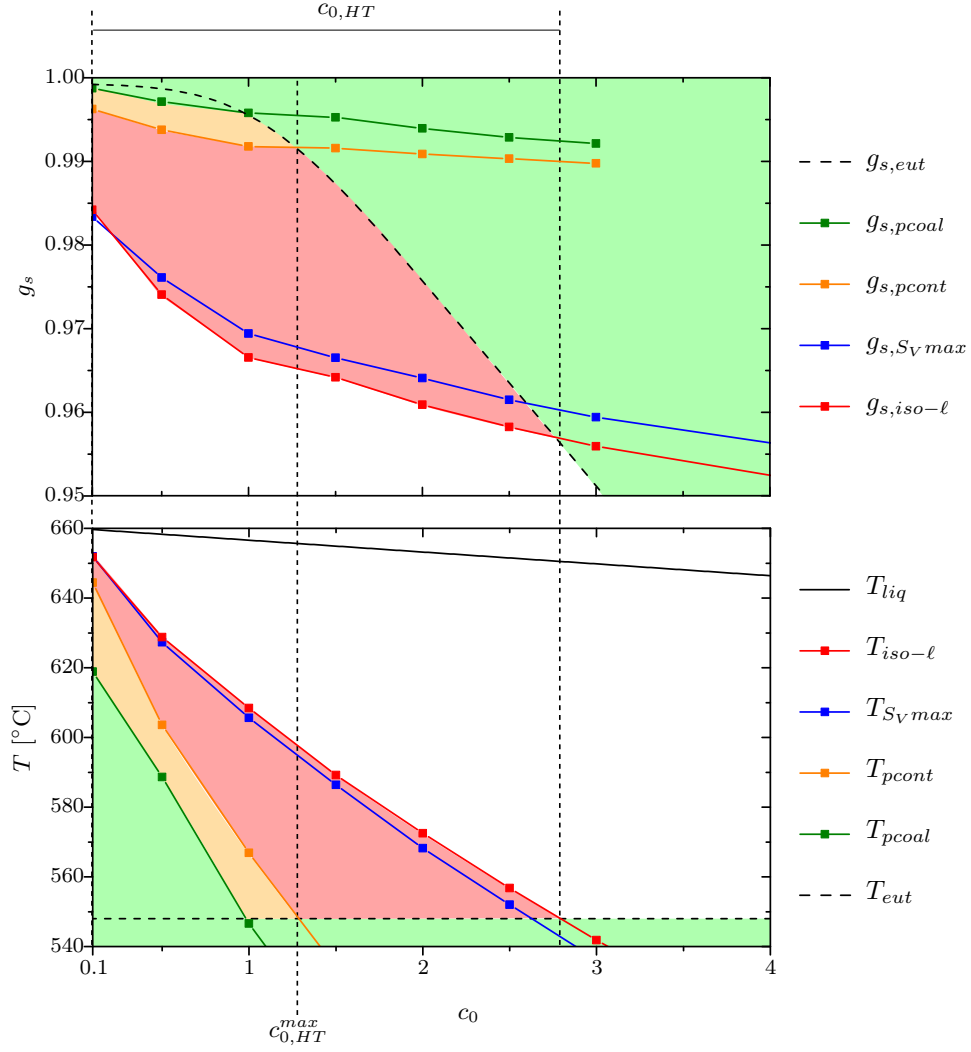


Figure 8.6: Solid fractions and temperatures at which the different transitions take place, as indicated in the legend, for 4096 grains (of $100\ \mu\text{m}$ size) cooled at -1.0°C/s . In addition to these transitions, the liquidus and solidus temperatures, respectively T_{liq} and T_{eut} , as well as the solid fraction at which the model predicts the appearance of the eutectic, T_{eut} , are shown. The regions where $g_{s,iso-l} < g_s < g_{s,pcont}$ (and $T_{iso-l} > T > T_{pcont}$) are shown in red, while the regions where $g_{s,pcont} < g_s < g_{s,pcoal}$ (and $T_{pcont} > T > T_{pcoal}$) are shown in orange. Finally when $g_s > \min(g_{s,pcoal}, g_{s,eut})$ (and $T < \max(T_{pcoal}, T_{eut})$) is shown in green. In addition, are shown the nominal composition range sensitive to hot tearing, $c_{0,HT}$, and the nominal composition at which the time spent in the vulnerable region is maximum, $c_{0,HT}^{max}$.

is more pronounced. This also shifts the transitions to higher solid fractions. It is also noticeable that the temperature interval separating the T_{pcont} and T_{pcoal} is lower for the higher cooling rate case. This can be explained by the fact that, for higher cooling rate simulation, the last-stage solidification is characterized by larger solute gradients in the solid phase. Backdiffusion of solute in the solid is more pronounced and thus the

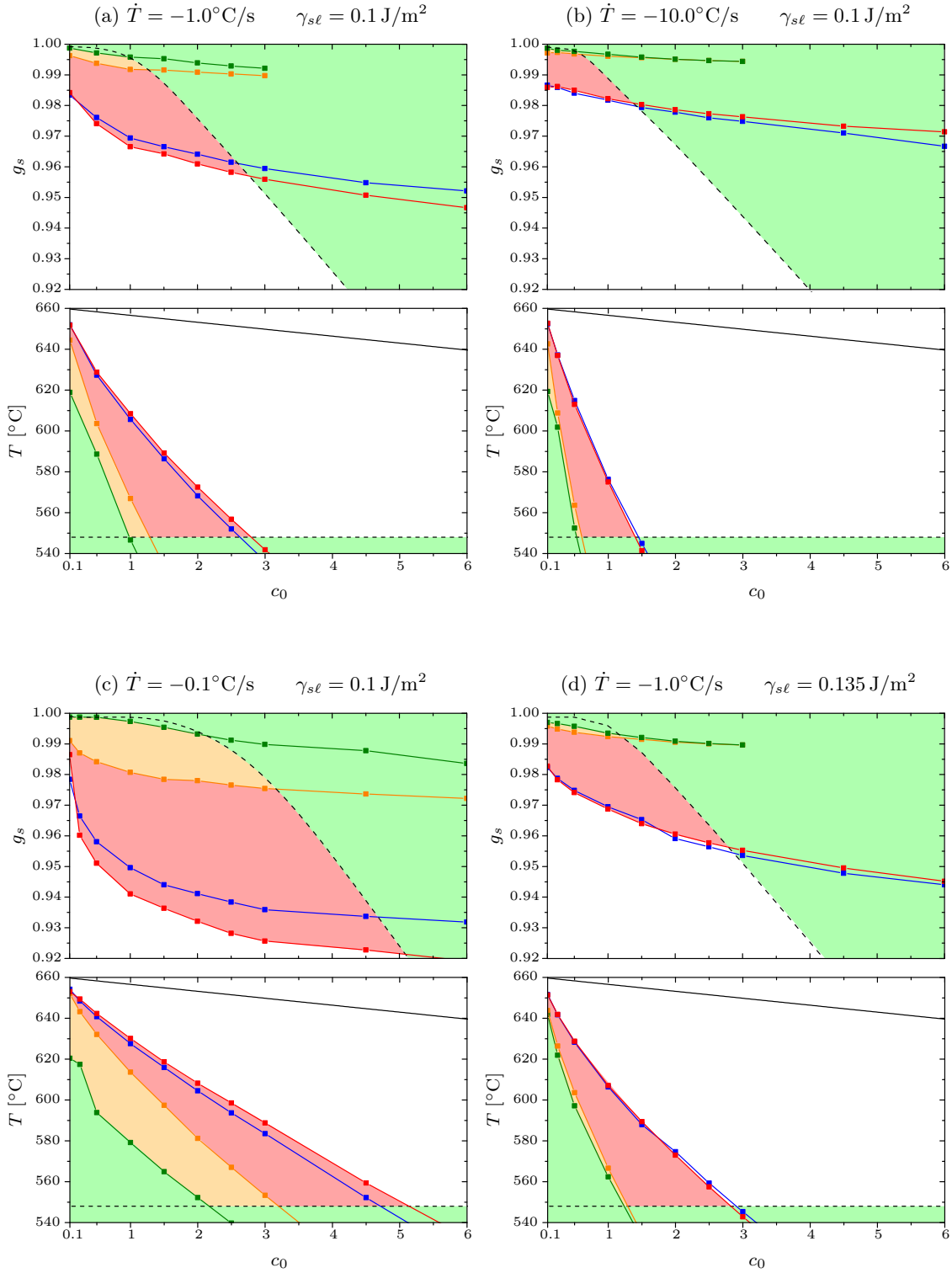


Figure 8.7: Same figure as Fig. 8.6 but for different cooling conditions and values of γ_{sl} . We recall that 4096 grains of $100 \mu\text{m}$ size were considered.

coalescence line is reached more rapidly.

On the other hand, for lower cooling rates (comparison of Fig. 8.7(a) and (c)), since the Fourier number associated to case (c) is larger, the transitions are shifted to higher temperatures and lower solid fractions. Please note that in case (c), since the gradients in the last-stage solidification are reduced compared to case (a), larger temperature differences between T_{pcont} and T_{pcoal} are observed.

There is no strong noticeable differences between cases (d) and (a) of Fig. 8.7, when the interfacial energy is increased. T_{SVmax} is slightly affected since, in the larger γ_{sl} case, the Gibbs-Thompson effect is enhanced (see section 2.1.3) and the grains corners are more pronounced. The main difference between cases (a) and (d) is the fact that in case (d), the coalescence undercooling is reduced because of the increase of γ_{sl} (see section 2.2). Therefore, the orange region (determined by the coalescence undercooling of repulsive grain boundaries) is narrower.

The values $c_{0,HT}$ and $c_{0,HT}^{max}$ for various conditions are shown in Table 8.2.

Table 8.2: Summary of the nominal composition range sensitive to hot tearing, $c_{0,HT}$, and of the nominal composition at which the time spent in the vulnerable region is maximum, $c_{0,HT}^{max}$, for the cases shown in Fig. 8.7. The values $c_{0,HT}$ and $c_{0,HT}^{max}$ are explained in Fig. 8.6.

Case	\dot{T} [°C/s]	γ_{sl} [J/m ²]	$c_{0,HT}$ [wt%]	$c_{0,HT}^{max}$ [wt%]
(a)	-1.0	0.1	[0, 2.8]	1.3
(b)	-10.0	0.1	[0, 1.4]	0.6
(c)	-0.1	0.1	[0, 5.2]	3.2
(d)	-1.0	0.135	[0, 2.8]	1.3

The main tendency is that nominal composition at which the time spent in the vulnerable region is maximum, $c_{0,HT}^{max}$, decreases with increasing cooling rates. This approach is similar to the Clyne and Davies [49] hot tearing criterion in which the time spent in this vulnerable state of the mushy zone normalized by the time during which stress in the mushy zones can be relaxed is considered.

8.3 3D results

The computational cost associated with the 3D mesoscopic model is of course larger than the 2D one: in 2D, a grain is generally subdivided into approximately 40 columns, while in 3D approximately 2000 columns per grain are needed to enmesh the Voronoi tessellation with a similar fineness of the columns. This is the reason why the number of grains considered in the 3D calculation was limited to a few hundreds per simulation.

8.3.1 Grain boundary energy calculation

We recall that the calculation of the grain boundary in the 3D model is performed by assigning a random orientation to each grain (3×3 matrix) and the grain boundary energy is then calculated for each boundary between two Voronoi regions with the code developed by Bulatov *et al.* [34]. The calculation is based on the orientations of two impinging grains and the vector perpendicular to the grain boundary plane. On the other hand, in 2D, the grain boundaries were assumed to be pure symmetric tilt boundaries with the rotation axis parallel to $\langle 100 \rangle$ and a simplified relationship between the grain boundary energy and the misorientation between the impinging grains (see Fig. 5.11(a)).

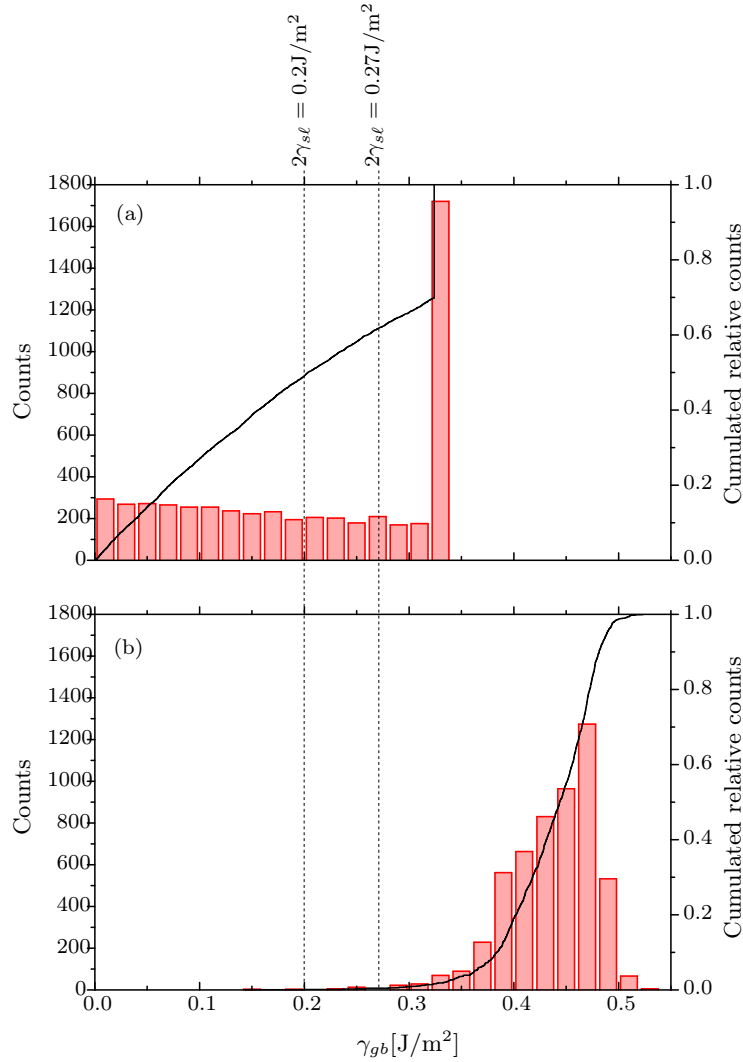


Figure 8.8: Number of counts and cumulated relative counts of the grain boundary energy distributions. (a) Grain boundary energy distribution calculated in the 2D model by assuming a random orientation and simplified pure symmetric tilt boundaries (see Fig. 5.11(a)). (b) 3D grain boundary energy distribution used in the 3D mesoscopic model as proposed by Bulatov *et al.* [34].

Figure 8.8 shows the grain boundary distributions used for the 2D and the 3D. By setting $\gamma_{sl} = 0.1\text{J/m}^2$ in the 2D distribution (Fig. 8.8(a)), approximately 50% of the grain boundaries are attractive (negative value of $(\gamma_{gb} - 2\gamma_{sl})$), the remaining 50% being repulsive. On the other hand, as shown in Fig. 8.8(b), by setting $\gamma_{sl} = 0.1\text{J/m}^2$ in the 3D γ_{gb} distribution of Bulatov *et al.* [34], 99.9% of the grain boundaries are repulsive. Since in the literature there is a wide spread of the values of γ_{sl} , from 0.088J/m^2 to 0.135J/m^2 [106], we arbitrarily chose the value of 0.135J/m^2 , that yields 99.5% of repulsive grain boundaries.

Therefore, in 2D and 3D simulation results will differ not only because of topological reasons (for example in 3D both the solid and the liquid phases can be percolated at the same time, while this is not possible in 2D) but also because of the difference between the grain boundary energy calculation (as shown in Fig. 8.8) and the associated different proportions of repulsive/attractive grain boundaries.

It is interesting to note that the 3D grain boundary energy distribution (see Fig. 8.8) looks similar to the Mackenzie plot (see Fig. 4.17, consisting in the misorientation distribution (between each pair of grains) of randomly oriented grains of cubic symmetry. This indicates that a direct relationship between the misorientation of a pair of grains and their grain boundary energy may be found.

8.3.2 Solute diffusion, coalescence and percolation transitions

Similarly to the result shown in Fig. 8.1 for the 2D model, in Fig. 8.9 the progressive percolation of 125 grains has been simulated with the 3D mesoscopic model. In the initial stages of solidification, the grains shape starts to depart from a sphere because of the diffusion boundary layers interactions (see Fig. 8.1(a) in which the diffusion boundary layers are shown in light gray). However, at this stage, the grains form distinct clusters since coalescence has not yet occurred. In Fig. 8.9(b), two coalesced grains are highlighted by a black circle. At much lower temperature, as shown in Fig. 8.9(c), only one percolated cluster remains, all the opposite faces of the domain being connected. Please note that in Fig. 8.9(c) white regions appear where the solid-liquid interface has disappeared and it is thus possible to see through the coalesced regions. As defined in section 8.2.2, two criteria can be used to characterize the percolation state of the solid phase: the contact and the coalescence criteria. As for the 2D model, since the coalescence criterion is more strict, percolation by coalescence is achieved at a lower temperature (see Fig. 8.10).

In addition, the evolution of S_V as a function of the solid fraction can give useful insight on the percolation state of the sample. The mesoscopic model prediction is compared with the evolution of S_V of regular arrangements of edgy grains. Two extreme cases are considered: a simple cubic arrangement of cubes and face-centered cubic arrangement of rhombic dodecahedra (these polyhedra originates from the Voronoi tessellation of the grain nucleation centers located in a face centered-cubic arrangement as explained in

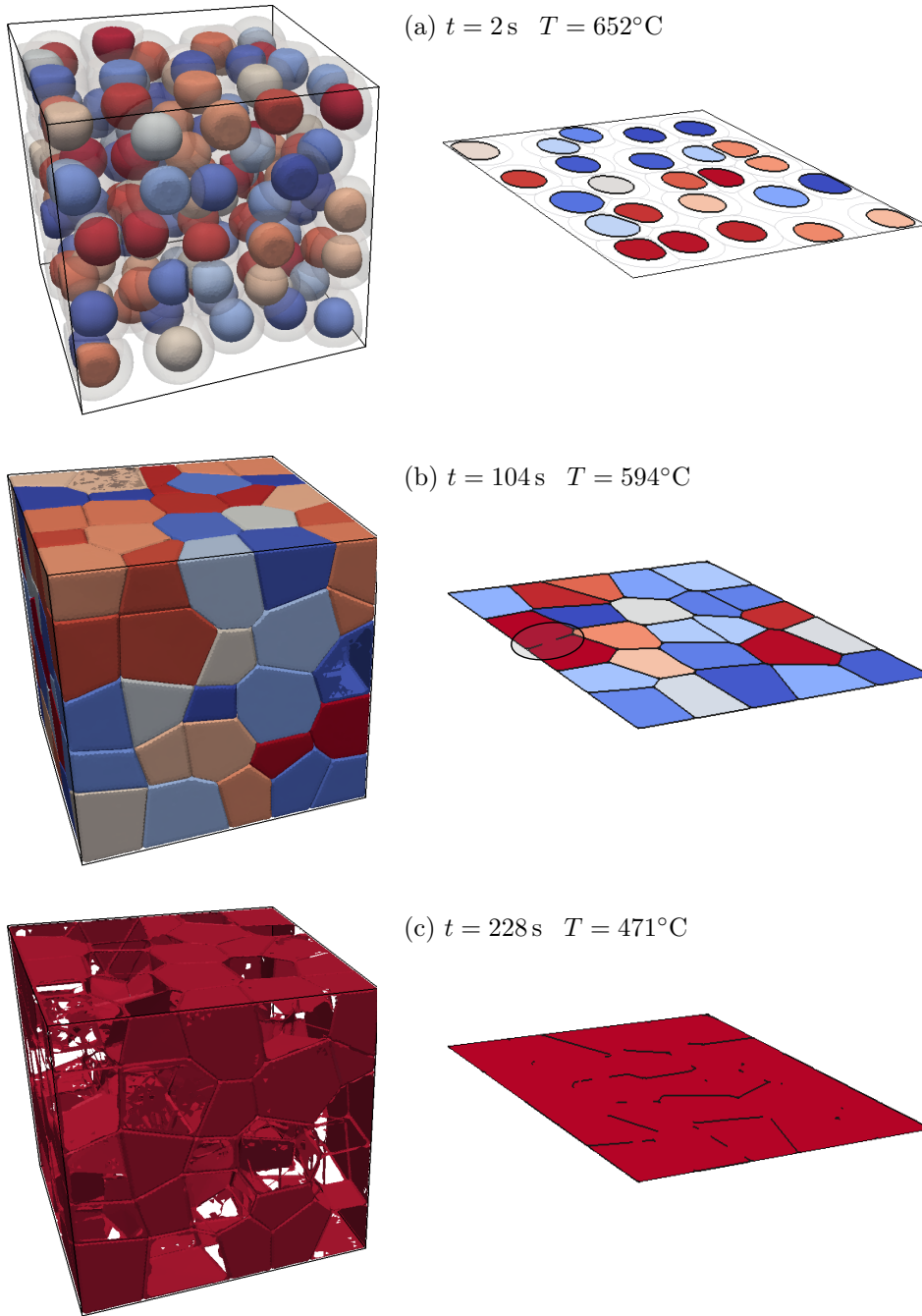


Figure 8.9: Simulation with the 3D mesoscopic model of the progressive percolation of 125 grains of an Al-1.0wt.%Cu alloy for different times. The average grain size was set to $100 \mu\text{m}$ and the cooling rate $\dot{T} = -1^\circ\text{C/s}$. On the left are represented the solid-liquid interfaces (each color represents a different coalescence cluster). On the right side, a slice of the same image is shown. The solid-liquid interface is represented by black lines while each portion of space occupied by a cluster possesses a unique color. Note that in figure (a) the diffusion boundary layer is shown in light gray and that in figure (b) a coalescence cluster is evidenced by a black circle.

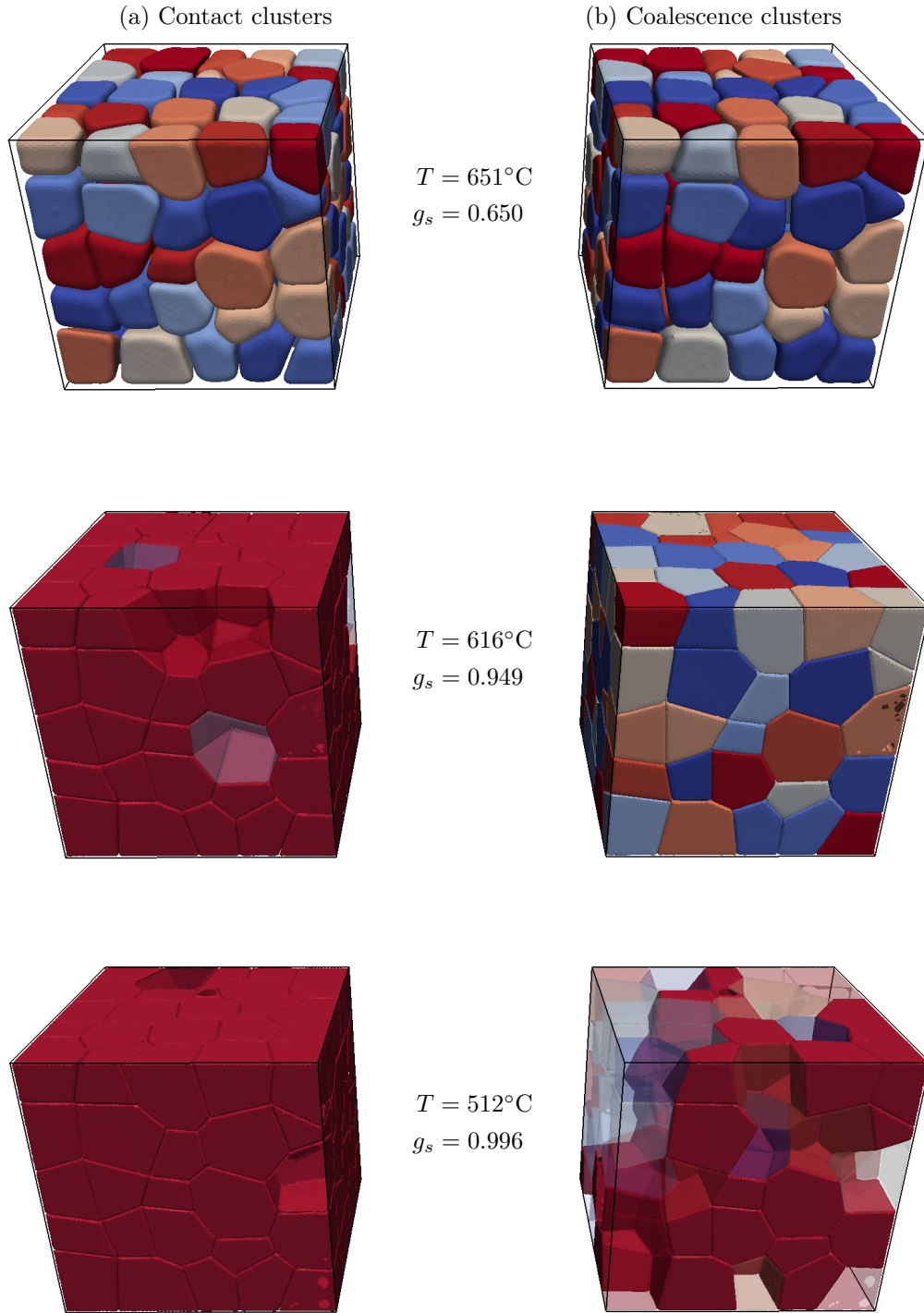


Figure 8.10: Simulation with the 3D mesoscopic model of the progressive percolation of 125 grains of an Al-1.0wt.%Cu alloy for different times. The average grain size was $100\text{ }\mu\text{m}$ and the cooling rate was set to $\dot{T} = -1^{\circ}\text{C/s}$. The solid clusters are colored following two different criteria: (a) contact clusters, (b) coalescence clusters. For both criteria, the percolating cluster is highlighted in red, while the non-percolating clusters are shown in transparency. Please note that in Figure (c) white regions appear where the solid-liquid interface has disappeared and it is thus possible to see through the coalesced regions.

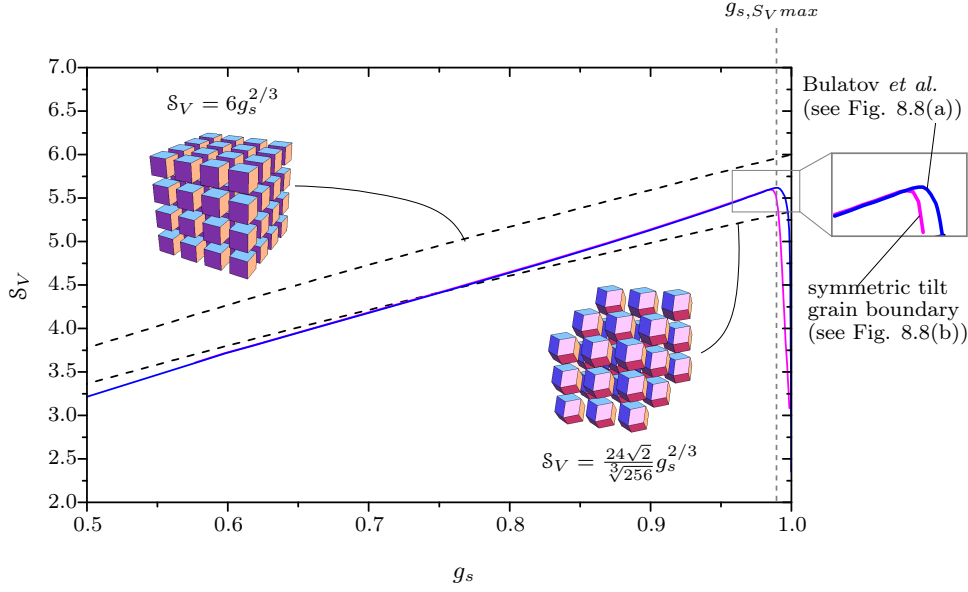


Figure 8.11: Evolution of $S_V = S_V d_{g0}$ as a function of the solid fraction, g_s , for the 3D mesoscopic model. The model prediction is compared with the evolution of S_V for a simple cubic arrangement of cubes and a face-centered cubic arrangement of rhombic dodecahedra (see Appendix B.3). Please note that the blue line represents the evolution of S_V for the 3D mesoscopic model with the grain boundary energies calculated with the expression proposed by Bulatov *et al.*, while the magenta line represents results of the 3D mesoscopic model in which the grain boundary energies are calculated in the same manner as the 2D model. The solid fraction at which S_V is maximum on the blue curve (corresponding also to the solid fraction at which S_V is maximum), g_{s,S_Vmax} , is also indicated.

Appendix B.3). Like for the 2D mesoscopic model, the evolution of S_V closely follows the prediction of the densest arrangement of edgy grains (corresponding to the face centered cubic arrangement of rhombic dodecahedra in 3D, or hexagonal arrangement in 2D). In a similar way compared to the 2D simulation, due to an increase of curvature of the grain corners/edges when a stage of complete mixing is achieved in the liquid, the simulated curve starts to depart from the analytical curve close to $g_s = 0.85$ until g_{s,S_Vmax} is reached.

The value of the solid fraction at which S_V (as well as S_V) is maximum is found at $g_{s,S_Vmax} = 0.989$ (see blue curve in Fig. 8.11). This value is larger than the observed $g_{s,S_Vmax} = 0.975$ of the 2D model. In order to ensure that the difference between the values of g_{s,S_Vmax} found in the 2D and 3D model do not result from the fact that grain boundary energies are calculated differently, another simulation was performed with the 3D model but with the same grain boundary energy calculation as in the 2D model (magenta curve in Fig. 8.11). It indicates a slightly smaller $g_{s,S_Vmax} = 0.985$, which is still larger than the 2D model prediction.

In order to explain the differences between the 2D and the 3D model, one can plot the

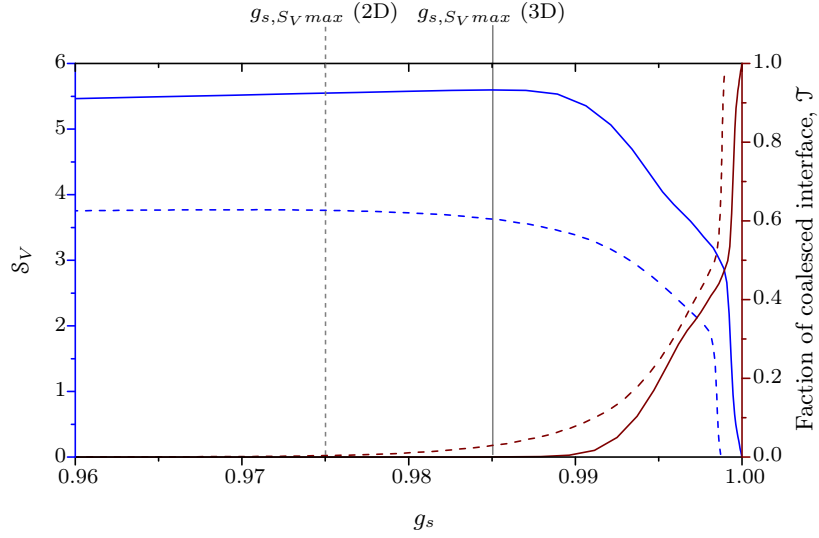


Figure 8.12: Evolution of $S_V = S_V d_{g0}$ as a function of the solid fraction, g_s , for the 2D model (blue dotted line) and for the 3D mesoscopic model in which the grain boundary energies are calculated in the same manner as the 2D model (blue continuous line). The fraction of coalesced interface ($\mathcal{T} = \frac{S_{gb}}{S_{sl} + S_{gb}}$), found by a postprocessing analysis, is also plotted for the 2D (brown dotted line) and 3D (brown continuous line) models.

fraction of coalesced interface which is equal to:

$$\mathcal{T} = \frac{S_{gb}}{S_{sl} + S_{gb}} \quad (8.2)$$

where S_{gb} is the area associated to all the grain boundaries and S_{sl} is the solid-liquid interfacial area. As shown in Fig. 8.12, \mathcal{T} begins to significantly increase at a lower solid fraction for the 2D model compared to 3D (please note that the same grain boundary energy distribution was considered for comparison). This suggests that, in 3D, coalescence is more localized and that the reduction of solid-liquid interface becomes significant only at a larger solid fraction. Therefore, a larger value of $g_{s, S_V max}$ was found for the 3D model.

8.3.3 Percolation of several grains

The various transitions predicted by the 3D mesoscopic model, containing 125 Al-Cu grains, are shown in Fig. 8.13 as a function of the Cu nominal composition. They are compared with the 2D model predictions.

First, the percolation by contact and percolation by coalescence transitions are compared. While the T_{pcont} curves of the 2D and 3D models are nearly superimposed, percolation by coalescence is achieved at lower temperatures for the 3D model. This can be explained by the fact that different grain boundary energy distributions were considered (see 8.3.1). The differences observed between the 2D and 3D models for the $T_{S_V max}$ and the T_{iso-l}

curves are due to topology reasons. As explained in the previous section, since coalescence in 3D is more localized, the solid-liquid liquid interface removal is less pronounced for the 3D model. The maximum of S_V is thus found at larger solid fractions in 3D (see Fig. 8.11), i.e., at lower temperatures. In order to explain the differences between the $T_{iso-\ell}$ curves, we recall that, in 3D, it is possible to have both liquid and solid phases percolated at the same time, while this is not achievable in 2D. Therefore, in 2D, when

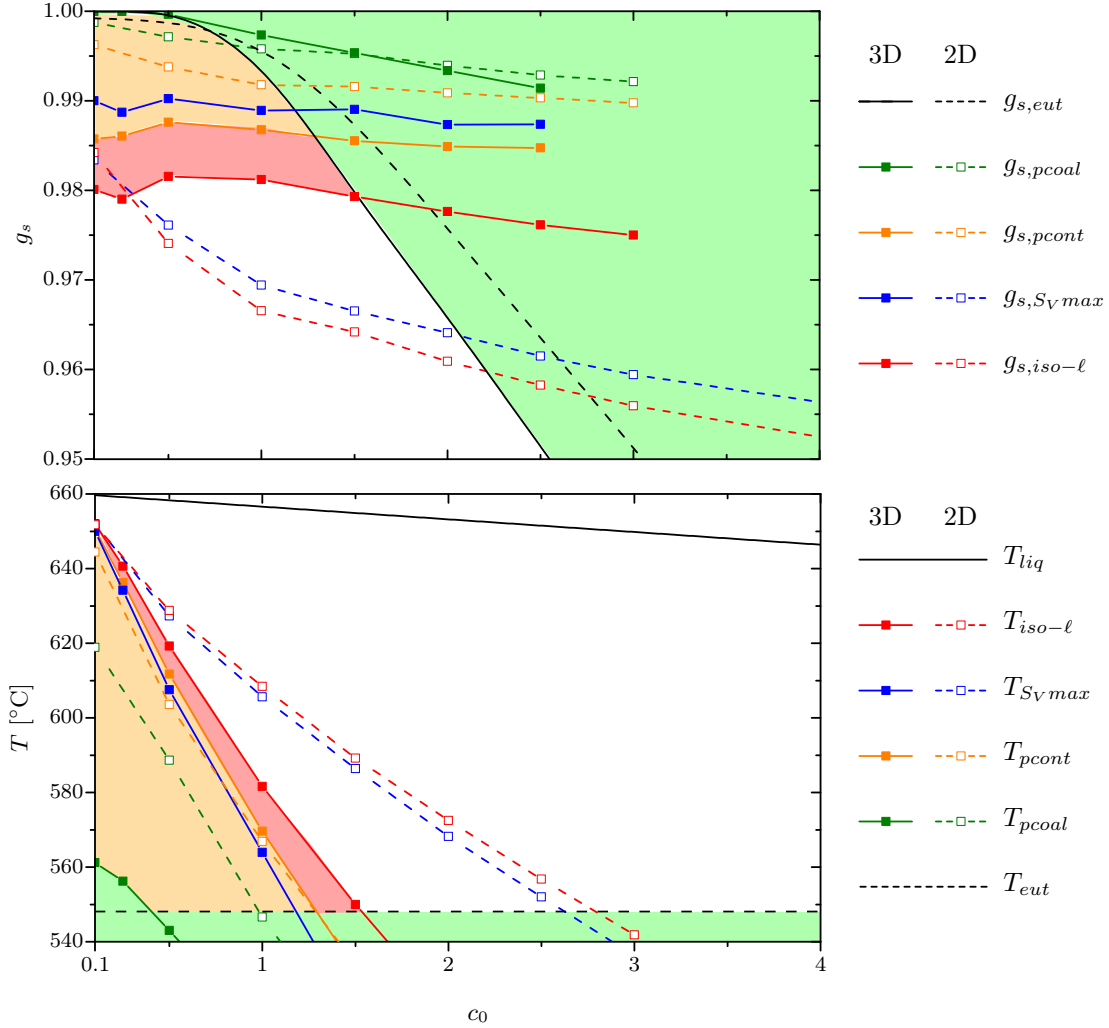


Figure 8.13: Comparison of solid fractions and temperatures at which the different transitions take place as calculated with the 3D (solid lines) and 2D (dotted lines) mesoscopic models. Please note that the different regions (red, orange and green) are only shown for the 3D simulation result. 4096 grains were considered in 2D, but with only 125 grains in 3D. For both simulations the grain size was set to $100\mu\text{m}$ and the cooling rate was -1.0°C/s . As explained in section 8.3.1, the grain boundary energy is calculated differently. Please note also that γ_{sl} was set to 0.1 J/m^2 for the 2D simulation and 0.135 J/m^2 for the 3D simulation as justified in section 8.3.1.

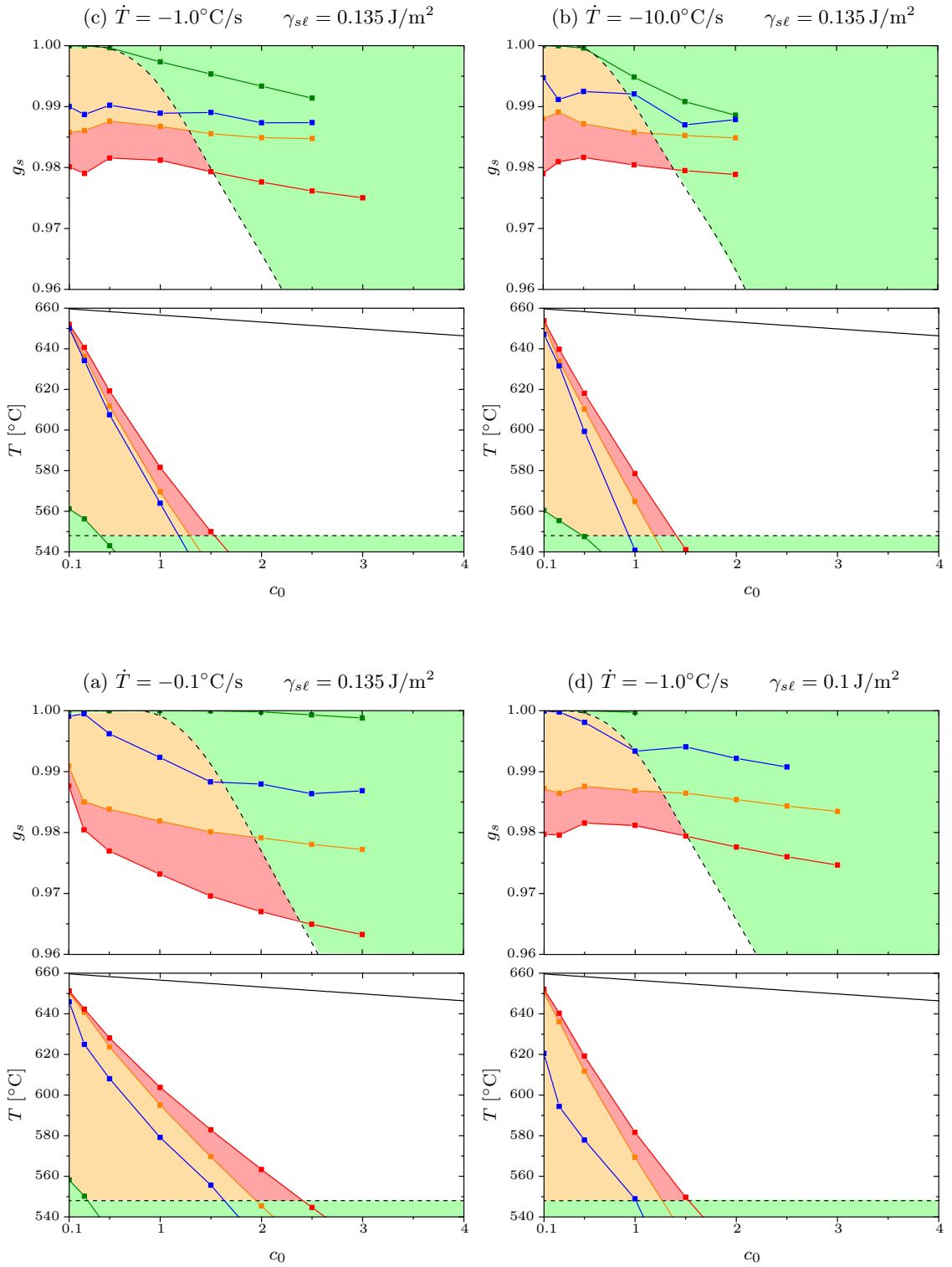


Figure 8.14: Solid fractions and temperatures at which the different transitions take place, as a function of parameters indicated in the legend, for 125 grains (of 100 μm size). Various cases (cooling rates and values of γ_{sl} are considered. Please note that the grain boundary energy shown in Fig. 8.8(b) was considered. The significance of the various transitions are explained in Fig. 8.13 (except the $g_{s,eut}$ line which is dotted instead of continuous).

coalescence of the solid grains starts to occur, the liquid is easily isolated, while in 3D significant coalescence has to take place in order to form isolated liquid pockets. This is the reason why liquid isolation occurs at lower temperatures in 3D. As a consequence, the temperature interval over which the material is considered to be vulnerable in terms of hot tearing (red region in Fig. 8.13) is significantly reduced in 3D compared to 2D.

As shown in Fig. 8.14, various transitions have been mapped for different conditions, namely cooling rate and solid-liquid interfacial energy values, by considering 125 grains in the 3D mesoscopic model. Please note that the g_{s,S_Vmax} and T_{S_Vmax} curves have a jiggered appearance since the S_V values were calculated in the postprocessing analysis of the simulations and thus collected at a much lower frequency. Therefore, these curves do not have the same level of precision as the others.

The values $c_{0,HT}$ and $c_{0,HT}^{max}$ for various conditions are summarized in Table 8.3.

Table 8.3: Summary of the nominal composition range sensitive to hot tearing, $c_{0,HT}$, and of the nominal composition at which the time spent in the vulnerable region is maximum, $c_{0,HT}^{max}$, for the cases shown in Fig. 8.7. The values $c_{0,HT}$ and $c_{0,HT}^{max}$ are explained in Fig. 8.6.

Case	\dot{T} [°C/s]	$\gamma_{s\ell}$ [J/m ²]	$c_{0,HT}$ [wt%]	$c_{0,HT}^{max}$ [wt%]
(a)	-1.0	0.135	[0, 1.5]	1.3
(b)	-10.0	0.135	[0, 1.4]	1.2
(c)	-0.1	0.135	[0, 2.4]	1.9
(d)	-1.0	0.1	[0, 1.5]	1.3

There is a noticeable difference in the observed values of $c_{0,HT}$ and $c_{0,HT}^{max}$ between case (a) and case (c) in Fig. 8.14, in which the cooling rate is reduced by a factor 10 ($\dot{T} = -1.0^\circ\text{C/s}$ versus $\dot{T} = -0.1^\circ\text{C/s}$). In particular, the value of $c_{0,HT}$ is increased in the case of the lower cooling rate. However, when the cooling rate is increased (in absolute values) from -1.0°C/s to -10.0°C/s (comparison between case (a) and (b) in Fig. 8.14), the change of $c_{0,HT}$ and $c_{0,HT}^{max}$ is hardly noticeable.

As a conclusion, the vulnerable region in terms of hot tearing has been found for different conditions with the 3D mesoscopic model. However, we would like to emphasize that, in order to predict the hot tearing susceptibility of an alloy, it is also necessary to know the temperature (or solid fraction) at which the solid starts to be mechanically coherent (coherency point) and is thus able to transmit strains, as determined experimentally by Drezet *et al.* [108] using *in situ* diffraction observations on dog bone tests. However, the final microstructure observed in their experiments was globulo-dendritic. It would be thus interesting to perform the same analysis on a fully globular microstructure and compare the data with predictions of the 3D mesoscopic model.

8.3.4 Comparison between experiments and modeling results

The results of the 3D mesoscopic model were finally compared with the *in situ* X-ray tomography observations (section 7.3). We recall that the resolution of the X-ray tomography experiment is expected to be on the order of $2\mu\text{m}$ (corresponding to three times the voxel size). Therefore, liquid channels smaller than the resolution cannot be resolved. For comparison, the coalescence calculation in the 3D mesoscopic model was modified: when the width of a liquid film separating two grains within a column, h , becomes smaller than the resolution of the X-ray tomography observation, the corresponding columns of

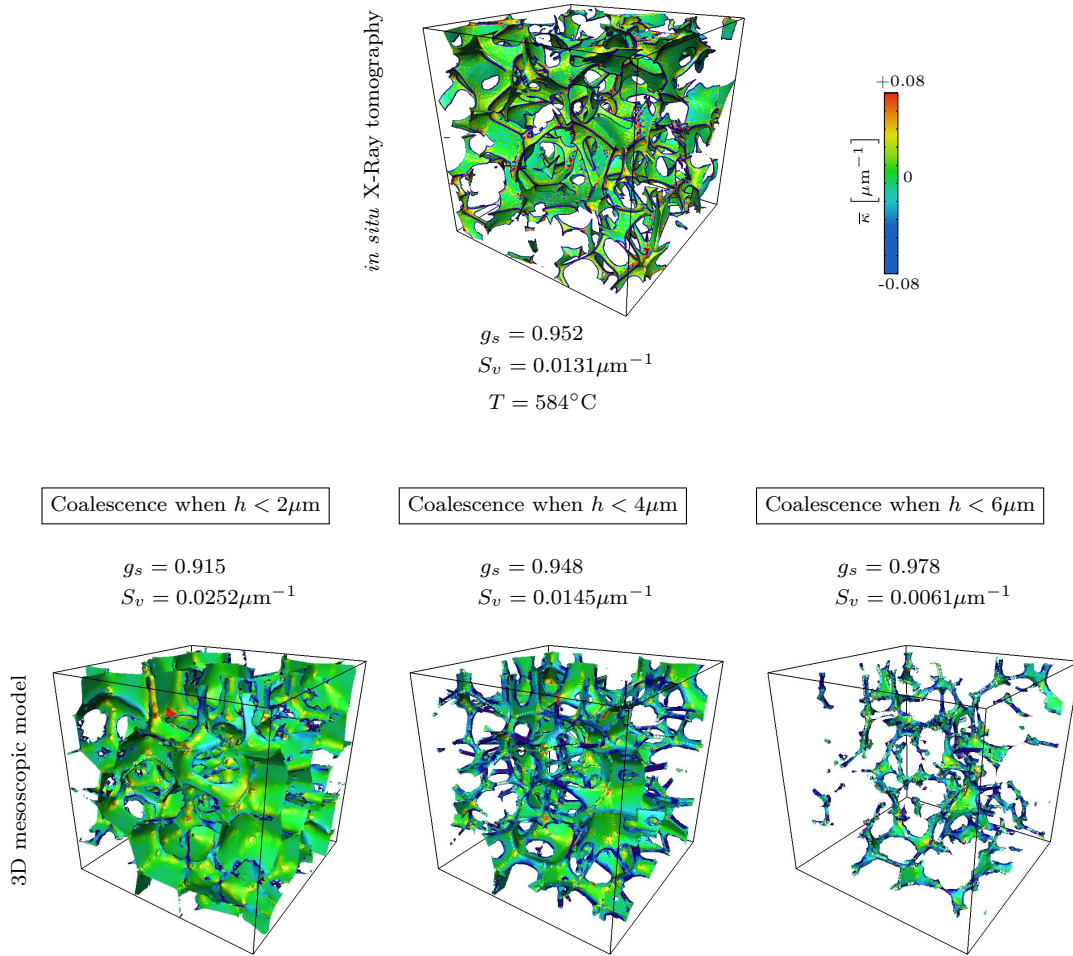


Figure 8.15: Comparison of the *in situ* X-ray tomography observations of an Al-4.5wt.%Cu sample (inoculated with 2.0wt% of master alloy) cooled at -0.05°C/s and the 3D mesoscopic model simulation performed for the same alloy and under the same conditions. The final grain size in the model was set to a value observed in the experiment. Please note that the color of the solid-liquid interface is colored based on the mean curvature value and for each temperature observation, the values of the solid fraction, g_s and the specific solid-liquid interfacial area per unit volume, S_v , are indicated.

the two adjacent grains are considered to be coalesced.

As shown in Fig. 8.15, the experimental result was compared with the 3D mesoscopic model predictions with variable coalescence calculations: coalescence was considered for liquid width lower than $2\mu\text{m}$, $4\mu\text{m}$ and $6\mu\text{m}$, respectively. Please note that the values of g_s and S_V are very sensitive to the liquid width under which coalescence is considered. The model was found to be in good agreement with the experiments if two grains were considered to be coalesced when $h < 4\mu\text{m}$. This indicates that the actual resolution of the X-ray tomography observations is on the order of $4\mu\text{m}$ and thus larger than the expected $2\mu\text{m}$. It is suggested that this is due to the fact that the application of a median filter to the stacks before binarization and the smoothing of the solid-liquid interface in the postprocessing analysis lowers the actual resolution of the X-ray tomography observations.

The *in situ* X-ray tomography observations were compared with the 3D mesoscopic predictions for various alloy compositions as shown in Fig. 8.16, 8.17 and 8.18 by considering coalescence when $h < 4\mu\text{m}$. The model results are in good agreement with the experimental ones, even if, as shown for example in Fig. 8.17, the model underestimates the solid fractions at higher temperatures and slightly overestimates it at lower temperatures.

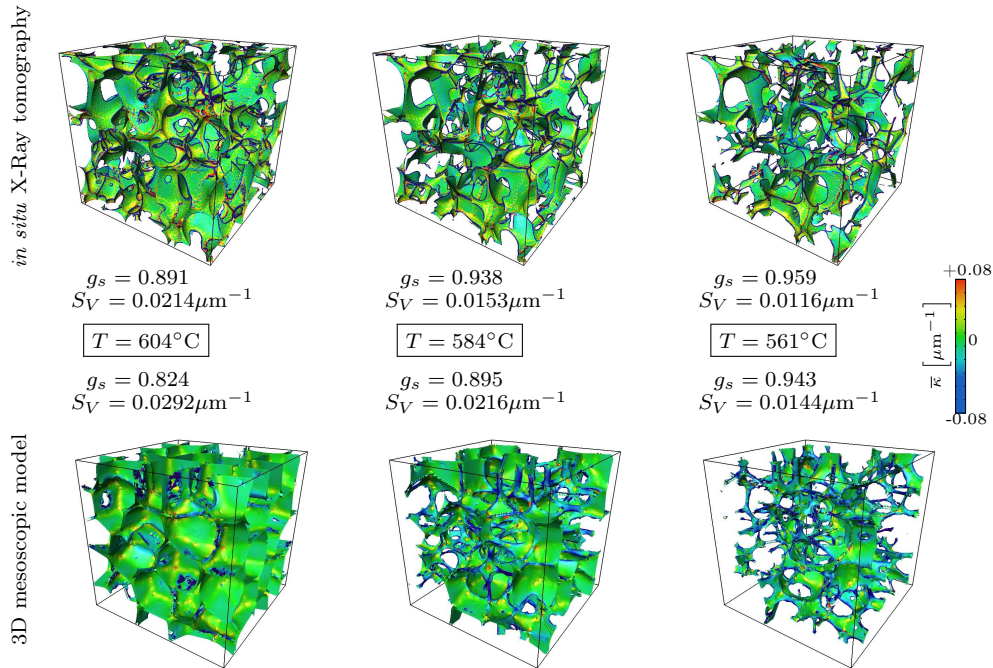


Figure 8.16: Comparison of the *in situ* X-ray tomography observations of an Al-6.0wt.%Cu sample (inoculated with 2.0wt% of master alloy) cooled at -0.05°C/s and the 3D mesoscopic model simulation performed for the same alloy and under the same conditions. The final grain size in the model was set to a value observed in the experiment. Please note that the color of the solid-liquid interface is colored based on the mean curvature value and for each temperature observation, the values of the solid fraction, g_s and the specific solid-liquid interfacial area per unit volume, S_V , are indicated.

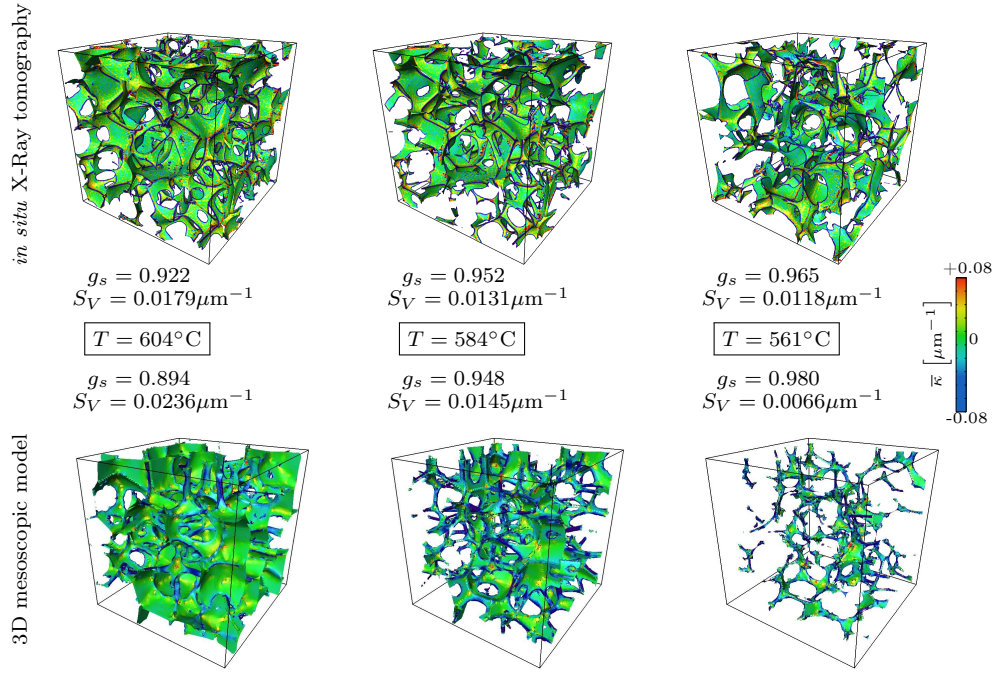


Figure 8.17: Same figure as Fig. 8.16 for an Al-4.5wt.%Cu alloy (inoculated with 2.0wt% of master alloy) cooled at -0.05°C/s .

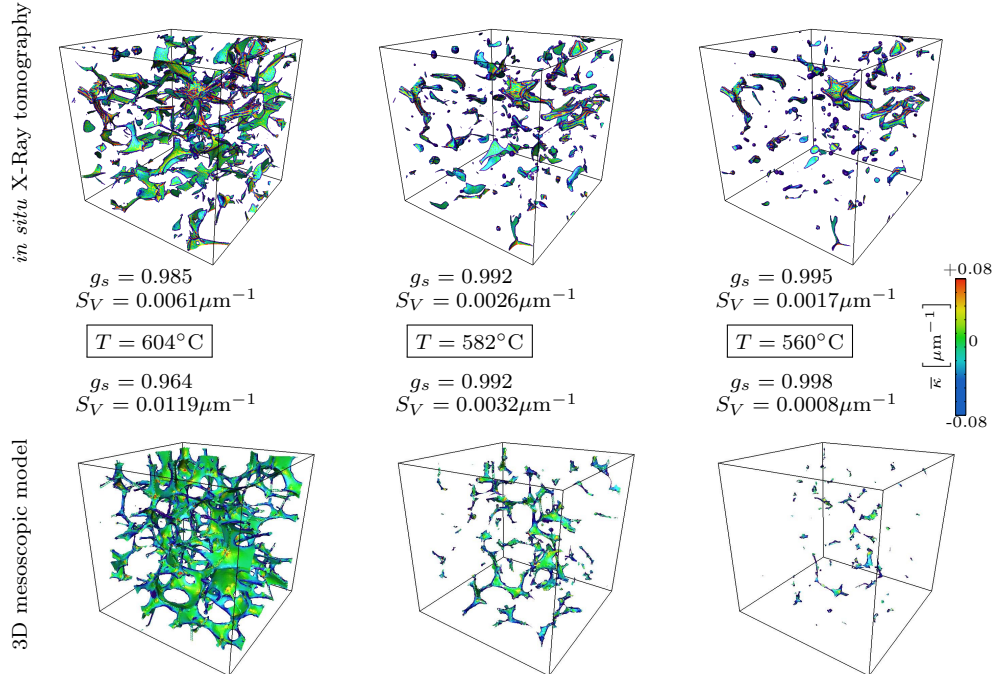


Figure 8.18: Same figure as Fig. 8.16 for an Al-3.0wt.%Cu alloy (inoculated with 2.0wt% of master alloy) cooled at -0.05°C/s .

As a conclusion, the X-ray tomography results can give some useful insights in terms of grain percolation, by analyzing the percolation state of the solid phase, the evolution of S_V and the shift of the ISD plots envelopes. However, X-ray tomography results are biased by the limited resolution of such observations (estimated to be on the order of $4\mu\text{m}$). Therefore, the development of a mesoscopic model was useful in order to obtain more realistic values for the various percolation transitions and thus to quantify the solid fractions/temperatures at which the semi-solid material is vulnerable in terms of hot tearing.

9 Conclusion and perspectives

From the experimental point of view, an innovative method, based on the Bridgman furnace principle, has been developed. The standard Bridgman furnace, generally used in order to obtain the complete solidification history of a single sample, has been substantially modified in order to reduce the thermal gradient and obtain the desired globular-equiaxed grain structure. In addition, a new type of sample was engineered (consisting of alloy pellets separated by ceramic separators) in order to reduce macrosegregation as well as helping to achieve steady-state conditions. Please note that the temperature profile of the furnace was tuned such as that each pellet remains liquid for approximately the same amount of time (avoiding the fading of the inoculant) and then follows the same cooling rate. This method thus allows to obtain the solidification history in a single sample while minimizing macrosegregation. However, due to the thermal arrest experienced by the pellets in the new sample/furnace configuration, larger grain sizes, on the order of $250\mu\text{m}$, were obtained, even for heavily inoculated alloys (addition of 2.0wt% master alloy). Please note that a complete analysis of the final grain size was performed for various compositions, inoculant contents and experimental setups. The thermal arrest observed in the modified sample (pellets separated by ceramics) was not only characterized by thermal measurements performed with thermocouples inserted in the samples, but also complemented by simple thermal simulations performed with the software Calcosoft.

The samples obtained with the modified Bridgman furnace were then observed post-mortem by *ex situ* X-ray tomography. In addition, X-ray tomography experiments have been performed *in situ* with a laser-heated furnace under similar conditions ($\dot{T} = -0.035^\circ\text{C/s}$ for the *ex situ* versus $\dot{T} = -0.05^\circ\text{C/s}$ for the *in situ*). With the *in situ* setup it was possible to obtain the desired globular-equiaxed microstructure, with a grain size on the order of $150\mu\text{m}$, since virtually no thermal arrest is experienced by the sample. A postprocessing analysis of the principal curvature distribution (ISD plots) was performed on both *ex situ* and *in situ* observations for various compositions of inoculated Al-Cu alloys. The ISD plots of the X-ray tomography observations indicated the formation of liquid cylinders along triple lines and, at a more advanced solidification stage, the

formation of liquid pockets at quadruple vertices. In addition, the evolution of the specific solid-liquid interfacial area, S_V , as a function of the solid fraction measured from the *in situ* data, was found to match well the analytical evolution of spherical grains (see Fig. 7.18). However, as emphasized in this work, the resolution of the X-ray tomography setup is on the order of $2\mu\text{m}$. Therefore, liquid films whose thickness is inferior to the resolution were not resolved. This is one of the reasons why the development of a model that is not limited in terms of spatial resolution was needed.

From the modeling point of view, the percolation of a small number of grains has been simulated with a multiphase-field model in 2D. However due to the large computational cost of this technique, a new mesoscopic model has been developed both for 2D and 3D geometries. This model was inspired by the granular model developed by Phillon *et al.* [3] that considers polyhedral grains based on a Voronoi tessellation of space. In the new mesoscopic model, the set of tetrahedra (triangles in 2D) that define the grains are further subdivided into smaller tetrahedra (triangles in 2D) called columns and solute diffusion is considered in both the solid and liquid phases. The mesoscopic model thus accounts for solute diffusion in the liquid parallel to the interface and in the solid perpendicularly to the interface, which are the two main phenomena influencing the last-stage solidification before coalescence. Please note also that the enmeshing of the space into small columns allows to obtain smoother shapes of the grains and to better describe the progressive coalescence of the grains. In addition, the fact of considering smooth grain shapes allows to have liquid cylinders/pockets in the last-stage solidification (which is not possible in the case of polyhedral grains) and thus to correctly describes the solid fraction and temperatures of the various percolation transitions. In addition, while for the 2D model a simple relationship (simplified symmetric tilt grain boundary) was used for the grain boundary energy, for the 3D model the grain boundary energy was found by using the relationship recently proposed by Bulatov *et al.* [34] for FCC crystal structures.

The mesoscopic has been first validated both in 2D and 3D with the multiphase-field predictions in simplified geometries. The assumptions of the model, such as the fact of neglecting diffusion between the solid part of the columns and the choice of conditions at the Voronoi boundary, have been justified. After that, the percolation of several grains has been simulated in 2D. The mesoscopic model results are in good agreement with the results of the granular model of Vernède *et al.* [40] which considers polygonal grains with a correction to smooth the edgy corners. However, the main difference between the two models is the solid fraction at which S_V is maximum: a larger solid fraction was found for the mesoscopic model (0.975 for the mesoscopic model versus 0.90 for the Vernède *et al.* model) which can be explained by the fact that the mesoscopic model allows to have a more progressive coalescence. Therefore, when coalescence takes place, the reduction of S_V is not as drastic as for the model of Vernède *et al.*. Please note that, due to the difference in dimensionality, the 3D mesoscopic model predicts that the maximum of S_V is found at larger solid fractions compared to the 2D mesoscopic model.

The various percolation transitions of the solid phase have been mapped as a function

of the nominal composition with the 2D and 3D mesoscopic models. In addition, by estimating the solid fractions/temperatures at which the liquid starts to become isolated from the largest liquid cluster (by assuming that the largest liquid cluster corresponds to the feeding cluster), it was possible to predict the nominal compositions (and the associated temperature and solid fraction) that are most vulnerable in terms of hot tearing. While percolation by contact takes place at similar temperature for both 2D and 3D models, liquid isolation occurs at lower temperature (i.e., larger solid fractions) for the 3D model. This can be explained by the topological differences, i.e., the fact that in 3D it is possible to have solid and liquid phases percolated at the same time while this is forbidden in 2D. For example, for a cooling rate of -1.0°C/s , the 3D model predicted that Al-1.3wt.%Cu alloys are the most sensitive to hot tearing.

Finally, the 3D mesoscopic model was compared with X-ray microtomography observations. A benchmark of the the simulation results postprocessed with various spatial resolutions indicated that the actual resolution of the X-ray tomography analysis is on the order of $4\mu\text{m}$ due to the postprocessing analysis.

9.1 Perspectives

With the modified Bridgman furnace, it was possible to obtain the desired microstructure under steady-state conditions while drastically limiting macrosegregation. While being limited to equiaxed microstructures (since in columnar ones the solid-liquid interface would be interrupted at each pellet end), this method allows to obtain the full solidification history of an alloy in a single sample. However, the heat extraction in the developed setup is not efficient enough to avoid thermal arrest in the sample. In order to avoid the experienced thermal arrest, the sample could be solidified in a furnace with a design that provides a better heat extraction, while keeping the same sample setup to still limit macrosegregation. Another way of avoiding a thermal arrest, would be to simply increase the thermal gradient that develops in the sample or use a thicker and more conductive crucible in order to significantly increase heat extraction along the axial direction of the sample.

By accounting for diffusion of solute and coalescence, the 3D mesoscopic model can predict the temperatures at which percolation (either by contact or coalescence) occurs and estimate when the material is vulnerable to hot tearing. However, this model does not predict the coherency temperature of the alloy (temperature at which the semi-solid material begins to be able to transmit strains), which is important to predict whether hot tearing will effectively occur. The coherency of Al-Cu alloys was determined experimentally by Drezet *et al.* [108] using *in situ* diffraction on a dog bone test. However, the final microstructure observed in their experiments was globulo-dendritic. It would thus be interesting to perform the same analysis on a fully globular microstructure and compare the data with predictions of the 3D mesoscopic model.

The 3D mesoscopic predictions could also be useful in order to refine the 3D granular

model of Sistaninia *et al.* [18–21] which accounts for stress development and liquid feeding but using edgy polyhedral grains. Because of the large computational cost of the mesoscopic model, a coupling of the two models is not realistic at present. However, a benchmark of several possible grain configurations could be performed in order to correct the solidification calculations of Sistaninia *et al.*'s model. This could be performed by considering a single Voronoi facet and its associated tetrahedron for various geometries and measuring the edges/corners curvatures. In addition, we recall that, in the granular model of Sistaninia *et al.*, a Voronoi facet is either considered as fully coalesced or separated by a liquid channel if coalescence has not yet occurred at that location. The progressivity of coalescence of the 3D mesoscopic model predictions could be taken into account, by considering, for example the surface fraction of the Voronoi boundary that is coalesced. This parameter could be used to better describe the semi-solid deformation calculation performed in Sistaninia *et al.*'s model. In addition, the description of the grain boundary energy as proposed by Bulatov *et al.* [34] could be used in the granular model in order to better describe the repulsive/attractive proportion of grain boundaries, which can significantly affects coalescence.

As a conclusion, the 3D granular models of Sistaninia *et al.* could be improved with the outcomes of the present work in order to create more advanced predictive tools for hot tearing formation.

A Appendix experimental

A.1 Thermal gradient distribution

This section is aimed at deriving simple expressions relating the thermal gradients in the alloy pellets with respect to the ones in the ceramic separators. In addition, the temperature drop at the interface between the two materials is calculated.

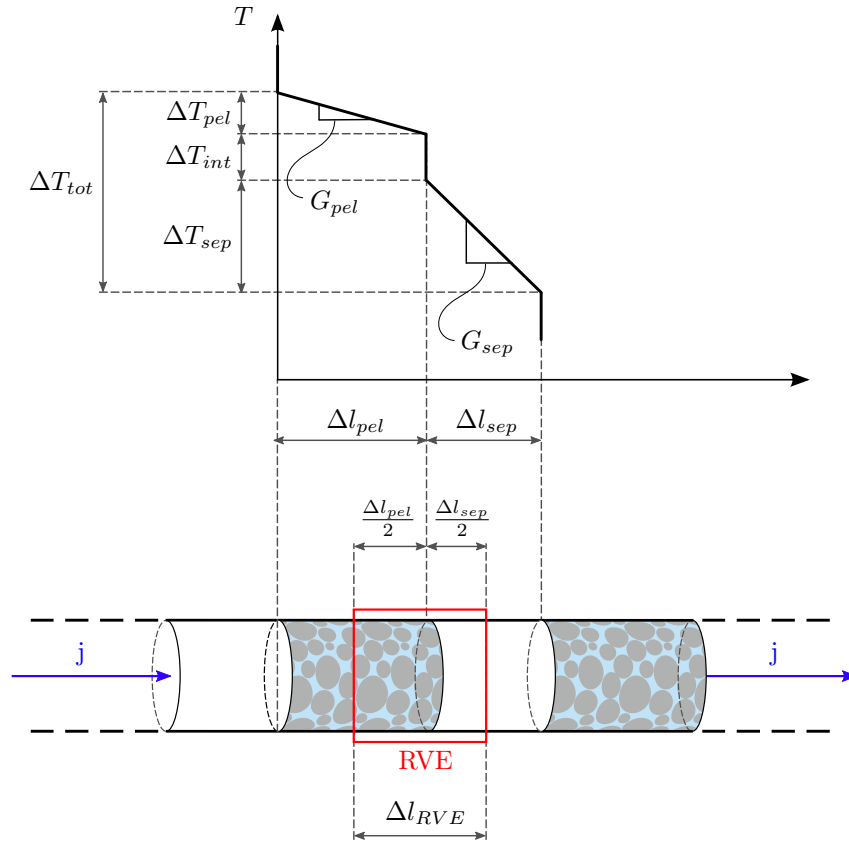


Figure A.1: Schematic representation of the RVE.

Appendix A. Appendix experimental

Let us assume there is a constant flux through in the longitudinal direction. The total drop of temperature in the RVE, ΔT_{tot} can be subdivided as follows:

$$\Delta T_{tot} = \Delta T_{pel} + \Delta T_{int} + \Delta T_{sep} \quad (\text{A.1})$$

where ΔT_{pel} , ΔT_{int} and ΔT_{sep} are the temperature drop respectively in the pellet, at the interface and in the separator. Since the flux is the same in each part:

$$j = \bar{\kappa} \underbrace{\frac{\Delta T_{tot}}{\Delta l_{tot}}}_{\bar{G}} = \kappa_{pel} \underbrace{\frac{\Delta T_{pel}}{\Delta l_{pel}}}_{G_{pel}} = h_{int} \Delta T_{int} = \kappa_{sep} \underbrace{\frac{\Delta T_{sep}}{\Delta l_{sep}}}_{G_{sep}} \quad (\text{A.2})$$

where $\bar{\kappa}$ is the average thermal conductivity of the REV and κ_{pel} and κ_{cer} are the conductivities of the pellet respectively the separator and h_{int} the heat transfer coefficient at the interface. The thermal gradient in the pellet, in the separator as well as the average gradient are designed respectively by G_{pel} , G_{sep} and \bar{G} . The thicknesses associated to the pellet and the separator are indicated by Δl_{pel} respectively Δl_{sep} . As shown in Fig. A.1, the the REV includes half of a pellet and half of a separator as well as their interface. The REV length is thus given by $\Delta l_{RVE} = \frac{1}{2} (\Delta l_{pel} + \Delta l_{sep})$. One can find the following relationship:

$$\boxed{\frac{G_{pel}}{G_{sep}} = \frac{\kappa_{sep}}{\kappa_{pel}}} \quad (\text{A.3})$$

From Eq. (A.2), it is possible to deduce the average conductivity of the REV:

$$\bar{\kappa} = \left(\frac{\frac{\Delta l_{pel}}{2}}{\Delta l_{RVE}} \frac{1}{\kappa_{pel}} + \frac{1}{\Delta l_{RVE}} \frac{1}{h_{int}} + \frac{\frac{\Delta l_{sep}}{2}}{\Delta l_{RVE}} \frac{1}{\kappa_{sep}} \right)^{-1} \quad (\text{A.4})$$

From a given \bar{G} and by knowing the $\bar{\kappa}$ with Eq. (A.4), one can find the temperature drops in the different parts and at the interface:

$$\boxed{\begin{aligned} \Delta T_{pel} &= \frac{\bar{\kappa}}{\kappa_{pel}} \bar{G} \Delta l_{pel} \\ \Delta T_{int} &= \frac{\bar{\kappa} \bar{G}}{h_{int}} \\ \Delta T_{cer} &= \frac{\bar{\kappa}}{\kappa_{cer}} \bar{G} \Delta l_{cer} \end{aligned}} \quad (\text{A.5})$$

A.1. Thermal gradient distribution

Therefore the gradients in the pellet and in the ceramic are the following:

$$\boxed{\begin{aligned} G_{pel} &= \frac{\bar{\kappa}}{\kappa_{pel}} \bar{G} \\ G_{cer} &= \frac{\bar{\kappa}}{\kappa_{cer}} \bar{G} \end{aligned}} \quad (\text{A.6})$$

B Appendix Modeling

B.1 Multiphase-field

B.1.1 Choice of the multiobstacle potential

The choice of the multiobstacle potential presented in section 5.1.2 is explained hereafter. Rappaz *et al.* [16] derived a multiphase-field formulation similar to the one derived in section 5.1.2, but, instead of the multiobstacle potential, they considered a multiwell potential (shown in Fig. B.1):

$$g_{mw}(\phi) = \sum_{i < j} W_{ij} \phi_i^2 \phi_j^2 \quad (\text{B.1})$$

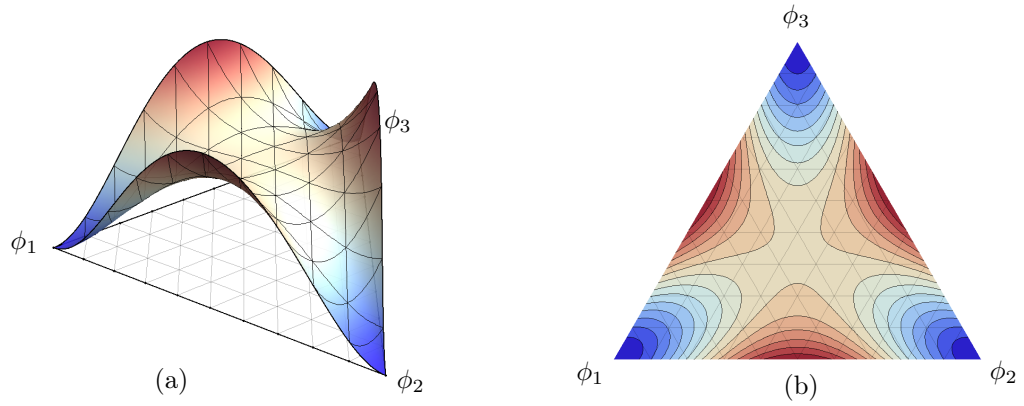


Figure B.1: (a) Ternary plot of the multiwell potential $g_{mw}(\phi)$ for $W_{12} = W_{13} = W_{23} = 1$ and (b) its relative colormap plot.

This formulation would lead to spontaneous formation of ghost phases, since for example for the interface between phase 1 and phase 2 (where $\phi_1 = 0.5$, $\phi_2 = 0.5$ and $\phi_3 = 0$) an increase of ϕ_3 , with the constraint that $\phi_1 = \phi_2$, would cause a decrease of g_{mw} .

In order to avoid the presence of ghost phases, a different shape of the potential is needed.

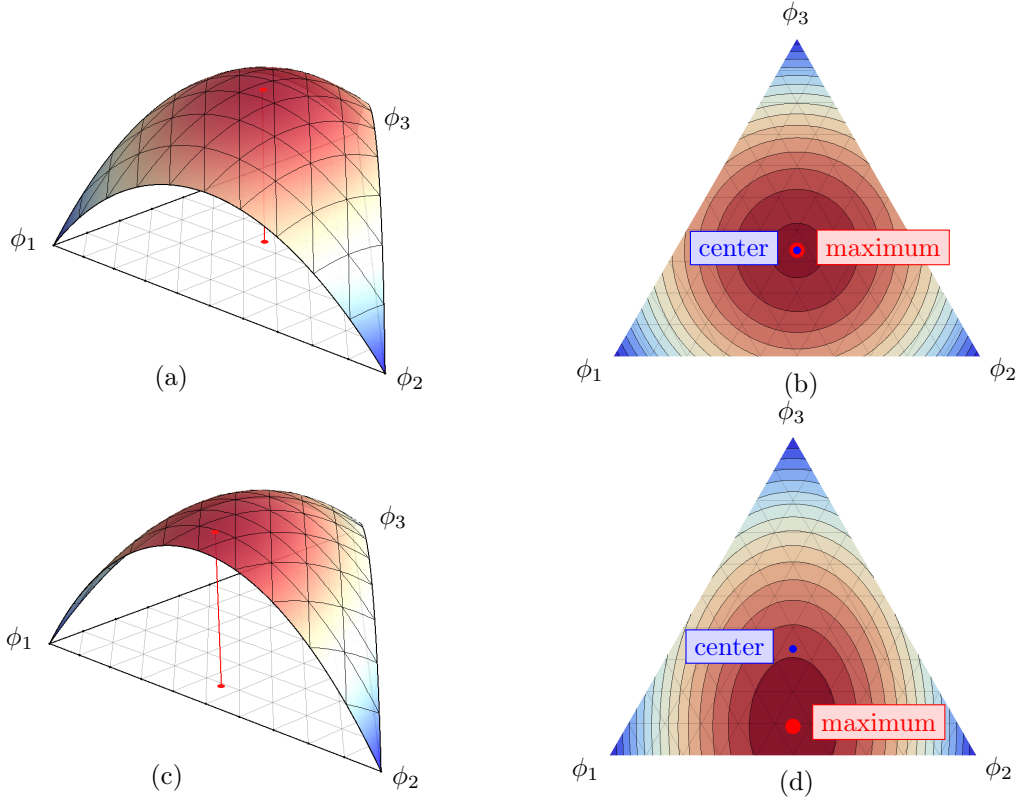


Figure B.2: (a) Ternary plot of the multiobstacle potential $g_{mo,simple}(\phi)$ for $W_{12} = W_{13} = W_{23} = 1$ and (b) its relative colormap plot.

Typically, one can choose a multiobstacle potential:

$$g_{mo,simple}(\phi) = \sum_{i < j} W_{ij} \phi_i \phi_j \quad (\text{B.2})$$

Unlike for the multiwell potential g_{mw} , for example for the interface between phase 1 and phase 2 (where $\phi_1 = 0.5$, $\phi_2 = 0.5$ and $\phi_3 = 0$) an increase of ϕ_3 , with the constraint that $\phi_1 = \phi_2$, would cause an increase of $g_{mo,simple}$. The $g_{mo,simple}$ potential is shown in Fig. B.2(a) and (b), where the maximum of the curve is located in the center of the Gibbs simplex for all equal W_{ij} . However, when the values of W_{ij} are not equal, this is not necessarily true (see Fig. B.2(c) and (d)).

This is the reason why another term, dependent on three phase-fields is added to $g_{mo,simple}$ to obtain (see Fig. B.3):

$$g_{mo}(\phi) = \sum_{i < j} W_{ij} \phi_i \phi_j + \sum_{i < j < k} 9(W_{ij} \phi_k + W_{ik} \phi_j + W_{jk} \phi_i) \phi_i \phi_j \phi_k \quad (\text{B.3})$$

The maximum of the potential is then located at the center of the Gibbs-simplex,

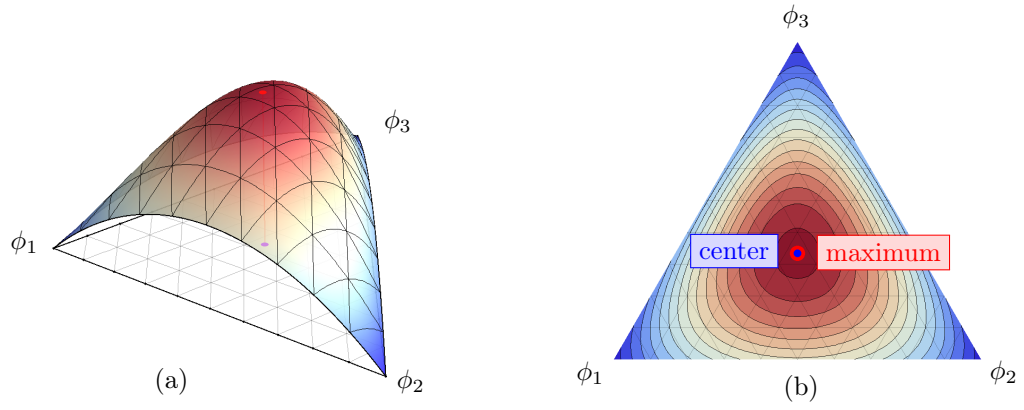


Figure B.3: (a) Ternary plot of the multiobstacle potential $g_{mo}(\phi)$ for $W_{12} = 1.8$ and $W_{13} = W_{23} = 1$ and (b) its relative colormap plot.

independently of the values of W_{ij} .

B.2 Mesoscopic model

B.2.1 Discretization of the diffusion equations in the solid

The diffusion equation in the solid (Eq. (5.10)) is solved with an implicit backward-Euler finite difference formulation. The 1D domain is discretized in $N + 1$ nodes, going from 0 to N , the N th node is used in order to account for the Dirichlet condition in r_i^* (where the concentration is c_s^*). The spacing is $\Delta\eta = 1/N$ and the k th node is positioned at $k\Delta\eta$. The time is discretized with a time step Δt . The actual time t at the j th timestep is thus represented by $j\Delta t$.

Discretization for an internal node

Eq. (5.10) can be discretized as follows for an internal node (note that, for clarity, we omit the subscript s in c_s):

$$\boxed{\frac{c_k^{j+1} - c_k^j}{\Delta t} = \frac{D_s}{r_i^{*2}} \frac{c_{k+1}^{j+1} - 2c_k^{j+1} + c_{k-1}^{j+1}}{\Delta\eta^2} + \left(\frac{k\Delta\eta v_i^*}{r_i^*} + \frac{(P-1)D_s}{k\Delta\eta r_i^{*2}} \right) \frac{c_{k+1}^{j+1} - c_{k-1}^{j+1}}{2\Delta\eta}} \quad (\text{B.4})$$

where c_k^j is the concentration at the node k at the time $j\Delta t$.

Let's first define the mesh Fourier number as being $Fo_\eta = \frac{D_s \Delta t}{\Delta\eta^2}$. Eq. (B.4) can be simplified as follows for an internal node:

$$-A_k c_{k-1}^{j+1} + (1 + A_k + B_k) c_k^{j+1} - B_k c_{k+1}^{j+1} = c_k^j \quad (\text{B.5})$$

where $A_k = \left(\frac{Fo_\eta}{r_i^{*2}} \left(1 - \frac{(P-1)}{2k} \right) - \frac{v_i^* \Delta t}{r_i^*} \frac{k}{2} \right)$ and $B_k = \left(\frac{Fo_\eta}{r_i^{*2}} \left(1 + \frac{(P-1)}{2k} \right) + \frac{v_i^* \Delta t}{r_i^*} \frac{k}{2} \right)$.

Discretization for the central node

At the node 0 (where ν and thus k are equal to zero), because of the no-flux boundary condition in a finite difference scheme one can begin from Eq. (B.4) (with $k=0$) and set $c_{-1}^{j+1} = c_1^{j+1}$:

$$\frac{c_0^{j+1} - c_0^j}{\Delta t} = \frac{2D_s}{r_i^{*2}} \frac{c_1^{j+1} - c_0^{j+1}}{\Delta\eta^2} + \frac{(P-1)D_s}{\eta r_i^{*2}} \frac{\partial c}{\partial \eta} \quad (\text{B.6})$$

where the term $\frac{(P-1)D_s}{\eta r_i^{*2}} \frac{\partial c}{\partial \eta}$ is undetermined. In order to shortcome this issue, instead of evaluating it in $\eta = 0$ with a centered derivative, it is possible to evaluate the term

$\frac{(P-1)D_s}{\eta r_i^{*2}} \frac{\partial c}{\partial \eta}$ in $\eta = \frac{\Delta \eta}{2}$ with an uncentered derivative:

$$\left. \frac{(P-1)D_s}{\eta r_i^{*2}} \frac{\partial c}{\partial \eta} \right|_{\eta=\frac{\Delta \eta}{2}} = \frac{2(P-1)D_s}{\Delta \eta r_i^{*2}} \frac{c_1^{j+1} - c_0^{j+1}}{\Delta \eta} = \frac{2(P-1)D_s}{r_i^{*2}} \frac{c_1^{j+1} - c_0^{j+1}}{\Delta \eta^2} \quad (\text{B.7})$$

A more rigourous way to evaluate the undetermined term is to use the Bernoulli-L'Hospital (B.H.) rule helping to evaluate the following limit:

$$\begin{aligned} \lim_{\eta \rightarrow 0} \frac{(P-1)D_s}{\eta r_i^{*2}} \frac{\partial c}{\partial \eta} &= \lim_{\eta \rightarrow 0} \frac{(P-1)D_s}{r_i^{*2}} \frac{\frac{\partial c}{\partial \eta}}{\eta} \stackrel{B.H.}{=} \lim_{\eta \rightarrow 0} \frac{(P-1)D_s}{r_i^{*2}} \frac{\frac{\partial^2 c}{\partial \eta^2}}{1} \\ &= \frac{(P-1)D_s}{r_i^{*2}} \frac{c_1^{j+1} - 2c_0^{j+1} + c_{-1}^{j+1}}{\Delta \eta^2} \end{aligned} \quad (\text{B.8})$$

again it is possible to set $c_{-1}^{j+1} = c_1^{j+1}$ and Eq. (B.8) becomes:

$$\frac{2(P-1)D_s}{r_i^{*2}} \frac{c_1^{j+1} - c_0^{j+1}}{\Delta \eta^2} \quad (\text{B.9})$$

yielding the same result as with the uncentered derivative method (see Eq. (B.7)).

Finally, the diffusion equation in the solid discretized for the node 0 is given by:

$$\boxed{\frac{c_0^{j+1} - c_0^j}{\Delta t} = \frac{2P D_s}{r_i^{*2}} \frac{c_1^{j+1} - c_0^{j+1}}{\Delta \eta^2}} \quad (\text{B.10})$$

Eq. (B.10) can be simplified as follows:

$$(1 + B_0)c_0^{j+1} - B_0c_1^{j+1} = c_0^j \quad (\text{B.11})$$

where $B_0 = 2P \frac{F_{o\eta}}{r_i^{*2}}$.

Matricial form of the discretized diffusion equation

The set of equation can be written on the following matricial form:

$$[K] \mathbf{c}^{j+1} = \mathbf{c}^j + \mathbf{s} \quad (\text{B.12})$$

where \mathbf{c}^j and \mathbf{c}^{j+1} are column vectors containing the concentrations of the solid at the time steps j and $j+1$. \mathbf{s} and $[K]$ are defined by:

$$\mathbf{s} = \begin{bmatrix} 0 \\ \vdots \\ 0 \\ B_{N-1}c_s^* \end{bmatrix} \quad (\text{B.13})$$

$$[K] = \begin{bmatrix} (1+B_0) & -B_0 & & & \\ -A_1 & (1+A_1+B_1) & -B_1 & & \\ & \ddots & \ddots & \ddots & \\ & -A_{N-2} & (1+A_{N-2}+B_{N-2}) & -B_{N-2} & \\ & & -A_{N-1} & (1+A_{N-1}+B_{N-1}) & \end{bmatrix} \quad (\text{B.14})$$

Estimation of the derivative

In Eq. (5.19), it is needed to estimate the derivative $\left[\frac{\partial c_{s,i}}{\partial r}\right]^*$ numerically. The spacing is given by $\Delta r = r_i^*/N$. In order to estimate $\left[\frac{\partial c_{s,i}}{\partial r}\right]^*$, one can perform a Taylor expansion of $c_{s,i}$ around $c_{s,i}^*$ (for clarity we omit the subscripts and use c instead of $c_{s,i}$):

$$c_{k-1} = c_k + \Delta r c'_k + \frac{\Delta r^2}{2} c''_k - \frac{\Delta r^3}{6} c'''_k + O(\Delta r^4) \quad (\text{B.15})$$

$$c_{k-2} = c_k + 2\Delta r c'_k + 4\frac{\Delta r^2}{2} c''_k - 8\frac{\Delta r^3}{6} c'''_k + O(\Delta r^4) \quad (\text{B.16})$$

$$c_{k-3} = c_k + 3\Delta r c'_k + 9\frac{\Delta r^2}{2} c''_k - 27\frac{\Delta r^3}{6} c'''_k + O(\Delta r^4) \quad (\text{B.17})$$

The second, third and fourth order approximations of the first derivative are given by respectively:

$$\left[\frac{\partial c_{s,i}}{\partial r}\right]^* = \frac{c_N - c_{N-1}}{\Delta r} + O(\Delta r^2) \quad (\text{B.18})$$

$$\left[\frac{\partial c_{s,i}}{\partial r}\right]^* = \frac{3c_N - 4c_{N-1} + 2c_{N-2}}{2\Delta r} + O(\Delta r^3) \quad (\text{B.19})$$

$$\left[\frac{\partial c_{s,i}}{\partial r}\right]^* = \frac{11c_N - 18c_{N-1} + 9c_{N-2} - 2c_{N-3}}{6\Delta r} + O(\Delta r^4) \quad (\text{B.20})$$

In all the calculations the fourth order derivative (Eq. (B.20)) was used.

B.2.2 Numerical integration in triangular/tetrahedral coordinates

In section 5.2, the following integral need to be solved:

$$\langle c_{s,i} \rangle = \frac{P}{r_i^{*P}} \int_0^{r_i^*} c_{s,i} r^{(P-1)} dr \quad (\text{B.21})$$

This corresponds to an integration of c_s in triangular coordinates in 2D and tetrahedral coordinates in 3D. The domain is discretized in $N + 1$ nodes, going from 0 to N and the spacing is $\Delta r = r_i^*/N$. We recall that k th node is positioned at $k\Delta r$.

Numerical integration in triangular coordinates

The integration of Eq. (B.21) in 2D (P=2) yields:

$$\langle c_{s,i} \rangle = \frac{2}{r_i^{*2}} \int_0^{r_i^*} c_{s,i} r dr \quad (\text{B.22})$$

$$\begin{aligned} &= \frac{2}{r_i^{*2}} \left[S_0 c_0 + \sum_{i=1}^{N-1} S_k c_k + S_N c_N \right] \\ &= \frac{2}{r_i^{*2}} \left[\frac{1}{2} \left(\frac{\Delta r}{2} \right)^2 c_0 + \sum_{i=1}^{N-1} \Delta r (k \Delta r) c_k + \frac{1}{2} \Delta r \left(\left(N - \frac{1}{4} \right) \Delta r \right) c_N \right] \\ &= \frac{1}{N^2} \left[\frac{1}{4} c_0 + \sum_{i=1}^{N-1} 2k c_k + \left(N - \frac{1}{4} \right) c_N \right] \end{aligned} \quad (\text{B.23})$$

where S_0 , S_k and S_N are the areas presented in Fig. B.4.

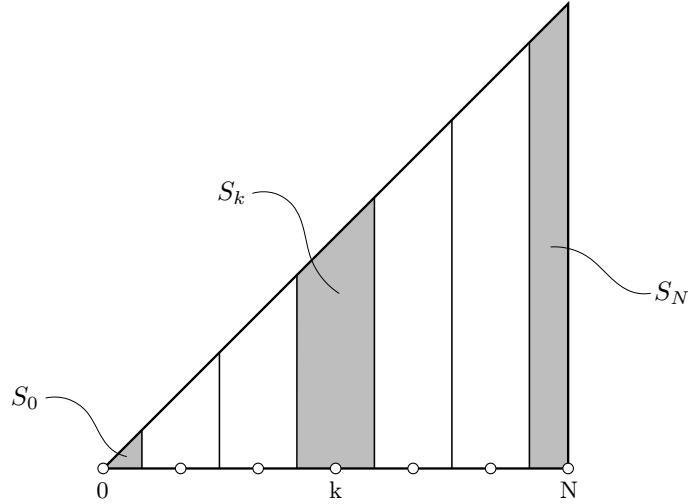


Figure B.4: Triangle associated to the numerical integration in 2D triangular coordinates.

For example, for a constant concentration \bar{c} , Eq. (B.22) becomes:

$$\langle c_{s,i} \rangle = \frac{2}{r_i^{*2}} \int_0^{r_i^*} \bar{c} r dr = \bar{c} \frac{2}{r_i^{*2}} \int_0^{r_i^*} r dr = \bar{c} \quad (\text{B.24})$$

Appendix B. Appendix Modeling

while Eq. (B.23) becomes:

$$\langle c_{s,i} \rangle = \frac{1}{N^2} \left[N + \sum_{i=1}^{N-1} 2k \right] \bar{c} = \frac{1}{N^2} [N + (N-1)N] \bar{c} = \bar{c} \quad (\text{B.25})$$

Numerical integration in tetrahedral coordinates

The integration of Eq. (B.21) in 3D (P=3) yields:

$$\langle c_{s,i} \rangle = \frac{3}{r_i^{*3}} \int_0^{r_i^*} c_{s,i} r^2 dr = \frac{6}{r_i^{*3}} \int_0^{r_i^*} c_{s,i} \frac{r^2}{2} dr \quad (\text{B.26})$$

$$\begin{aligned} &= \frac{6}{r_i^{*3}} \left[V_0 c_0 + \sum_{i=1}^{N-1} V_k c_k + V_N c_N \right] \\ &= \frac{6}{r_i^{*3}} \left[\frac{1}{6} \left(\frac{\Delta r}{2} \right)^3 c_0 + \sum_{i=1}^{N-1} \frac{1}{6} \Delta r^3 \left(\left(k + \frac{1}{2} \right)^3 - \left(k - \frac{1}{2} \right)^3 \right) c_k \right. \\ &\quad \left. + \frac{1}{6} \Delta r^3 \left(N^3 - \left(N - \frac{1}{2} \right)^3 \right) c_N \right] \\ &= \frac{1}{N^3} \left[\frac{1}{8} c_0 + \sum_{i=1}^{N-1} \left(3k^2 + \frac{1}{4} \right) c_k + \left(\frac{3}{2} N \left(N - \frac{1}{2} \right) + \frac{1}{8} \right) c_N \right] \end{aligned} \quad (\text{B.27})$$

where V_0 , V_k and V_N are the volumes presented in Fig. B.4.

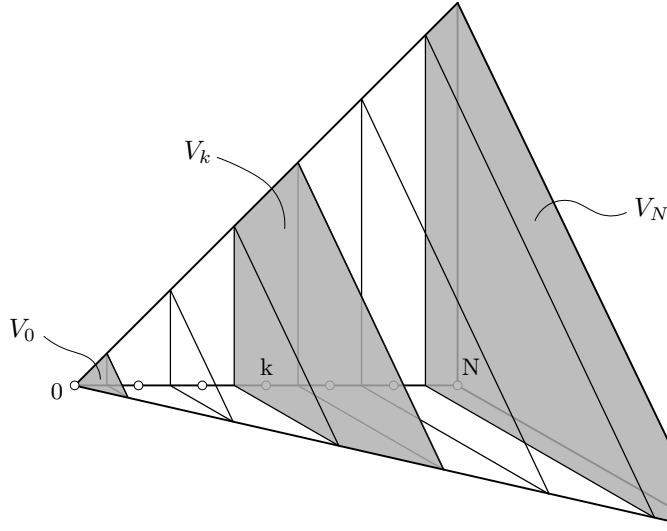


Figure B.5: Tetrahedron associated to the numerical integration in 3D tetrahedral coordinates.

For example, for a constant concentration \bar{c} , Eq. (B.26) becomes:

$$\langle c_{s,i} \rangle = \frac{3}{r_i^{*3}} \int_0^{r_i^*} \bar{c} r^2 dr = \bar{c} \frac{3}{r_i^{*3}} \int_0^{r_i^*} r^2 dr = \bar{c} \quad (\text{B.28})$$

while the RHS becomes:

$$\begin{aligned} \langle c_{s,i} \rangle &= \left(\frac{1}{N} \right)^3 \left[\frac{1}{8} + \sum_{i=1}^{N-1} \left(3k^2 + \frac{1}{4} \right) + \left(\frac{3}{2} N \left(N - \frac{1}{2} \right) + \frac{1}{8} \right) \right] \bar{c} \\ &= \left(\frac{1}{N} \right)^3 \left[N \left(N - \frac{1}{2} \right) \left(N + \frac{1}{2} \right) + \frac{N}{4} \right] \bar{c} = \bar{c} \end{aligned} \quad (\text{B.29})$$

B.2.3 Solute conservation equations in the liquid part of the columns

In section 5.2, it is needed to calculate the following integral:

$$\int_{r_i^*}^{L_i} \langle c_{\ell,i} \rangle r^{(P-1)} dr = \int_{r_i^*}^{L_i} c_{\ell,i}(r) r^{(P-1)} dr \quad (\text{B.30})$$

with $c_{\ell,i}(r)$ assumed to be a piecewise parabolic-linear function (see Eq. (5.14)), Eq. (B.30) becomes:

$$\begin{aligned} \int_{r_i^*}^{L_i} \langle c_{\ell,i} \rangle r^{(P-1)} dr &= \int_{r_i^*}^{r_i^* + \lambda_i} \left[c_{\ell,i}^\infty + (c_{\ell,i}^* - c_{\ell,i}^\infty) \left(\frac{\lambda_i - (r - r_i^*)}{\lambda_i} \right)^2 \right] r^{(P-1)} dr \\ &\quad + \int_{r_i^* + \lambda_i}^{L_i} c_{\ell,i}^\infty r^{(P-1)} dr \end{aligned} \quad (\text{B.31})$$

$$\int_{r_i^*}^{L_i} (\langle c_{\ell,i} \rangle - c_{\ell,i}^\infty) r^{(P-1)} dr = \int_{r_i^*}^{r_i^* + \lambda_i} (c_{\ell,i}^* - c_{\ell,i}^\infty) \left(\frac{\lambda_i - (r - r_i^*)}{\lambda_i} \right)^2 r^{(P-1)} dr \quad (\text{B.32})$$

Solution in 2D

In 2D (with $P = 2$), the left hand side of Eq. (B.32) becomes:

$$\int_{r_i^*}^{L_i} (\langle c_{\ell,i} \rangle - c_{\ell,i}^\infty) r dr = (\langle c_{\ell,i} \rangle - c_{\ell,i}^\infty) \frac{L_i^2 - r_i^{*2}}{2} \quad (\text{B.33})$$

while the right hand side of Eq. (B.32) becomes:

$$\begin{aligned} &\int_{r_i^*}^{r_i^* + \lambda_i} (c_{\ell,i}^* - c_{\ell,i}^\infty) \left(\frac{\lambda_i - (r - r_i^*)}{\lambda_i} \right)^2 r dr \\ &= (c_{\ell,i}^* - c_{\ell,i}^\infty) \int_0^{\lambda_i} \left(\frac{\lambda_i - r'}{\lambda_i} \right)^2 (r' + r_i^*) dr' \\ &= (c_{\ell,i}^* - c_{\ell,i}^\infty) \left(- \left[\frac{\lambda_i}{3} \left(\frac{\lambda_i - r'}{\lambda_i} \right)^3 (r' + r_i^*) \right]_0^{\lambda_i} + \int_0^{\lambda_i} \frac{\lambda_i}{3} \left(\frac{\lambda_i - r'}{\lambda_i} \right)^3 dr' \right) \\ &= (c_{\ell,i}^* - c_{\ell,i}^\infty) \left(\frac{r_i^* \lambda_i}{3} + \frac{\lambda_i^2}{12} \right) \\ &= (c_{\ell,i}^* - c_{\ell,i}^\infty) \frac{\lambda_i (\lambda_i + 4r_i^*)}{12} \end{aligned} \quad (\text{B.34})$$

the result was obtained with the change of variable $r' = r - r_i^*$ and by using an integration by parts.

- Until $\lambda_i < L_i - r_i^*$, Eq. (B.32) gives:

$$\left(\langle c_{\ell,i} \rangle - c_{\ell,i}^\infty \right) \frac{L_i^2 - r_i^{*2}}{2} = (c_{\ell,i}^* - c_{\ell,i}^\infty) \frac{\lambda_i(\lambda_i + 4r_i^*)}{12} \quad (\text{B.35})$$

and Eq. (B.35) can then be solved for λ_i .

- Once the solute layer reaches the Voronoi facet (i.e., when $\lambda_i > L_i - r_i^*$), the composition $c_{\ell,i}^\infty$ will increase since a no-flux condition should apply at this location (i.e., due to the rejected solute of the symmetric neighbour grain). λ_i is then known and fixed to $L_i - r_i^*$ in Eq. (B.35):

$$\left(\langle c_{\ell,i} \rangle - c_{\ell,i}^\infty \right) \frac{L_i^2 - r_i^{*2}}{2} = (c_{\ell,i}^* - c_{\ell,i}^\infty) \frac{(L_i - r_i^*)(L_i + 3r_i^*)}{12} \quad (\text{B.36})$$

and Eq. (B.36) can then be solved for $c_{\ell,i}^\infty$.

Solution in 3D

In 3D (with $P = 3$), the left hand side of Eq. (B.32) becomes:

$$\int_{r_i^*}^{L_i} (\langle c_{\ell,i} \rangle - c_{\ell,i}^\infty) r^2 dr = (\langle c_{\ell,i} \rangle - c_{\ell,i}^\infty) \frac{L_i^3 - r_i^{*3}}{3} \quad (\text{B.37})$$

while the right hand side of Eq. (B.32) becomes:

$$\begin{aligned} & \int_{r_i^*}^{r_i^* + \lambda_i} (c_{\ell,i}^* - c_{\ell,i}^\infty) \left(\frac{\lambda_i - (r - r_i^*)}{\lambda_i} \right)^2 r^2 dr \\ &= (c_{\ell,i}^* - c_{\ell,i}^\infty) \int_0^{\lambda_i} \left(\frac{\lambda_i - r'}{\lambda_i} \right)^2 (r' + r_i^*)^2 dr' \\ &= (c_{\ell,i}^* - c_{\ell,i}^\infty) \left(- \left[\frac{\lambda_i}{3} \left(\frac{\lambda_i - r'}{\lambda_i} \right)^3 (r' + r_i^*)^2 \right]_0^{\lambda_i} + \int_0^{\lambda_i} \frac{2\lambda_i}{3} \left(\frac{\lambda_i - r'}{\lambda_i} \right)^3 (r' + r_i^*) dr' \right) \\ &= (c_{\ell,i}^* - c_{\ell,i}^\infty) \left(\frac{\lambda_i r_i^{*2}}{3} - \left[\frac{\lambda_i^2}{6} \left(\frac{\lambda_i - r'}{\lambda_i} \right)^4 (r' + r_i^*) \right]_0^{\lambda_i} + \int_0^{\lambda_i} \frac{\lambda_i^2}{6} \left(\frac{\lambda_i - r'}{\lambda_i} \right)^4 dr' \right) \\ &= (c_{\ell,i}^* - c_{\ell,i}^\infty) \left(\frac{\lambda_i r_i^{*2}}{3} + \frac{\lambda_i^2 r_i^*}{6} + \frac{\lambda_i^3}{30} \right) \\ &= (c_{\ell,i}^* - c_{\ell,i}^\infty) \frac{\lambda_i(\lambda_i^2 + 5r_i^* \lambda_i + 10r_i^{*2})}{30} \end{aligned} \quad (\text{B.38})$$

the result was obtained with the change of variable $r' = r - r_i^*$ and by using two integration by parts.

- Until $\lambda_i < L_i - r_i^*$, Eq. (B.32) gives:

$$\left(\langle c_{\ell,i} \rangle - c_{\ell,i}^\infty \right) \frac{L_i^3 - r_i^{*3}}{3} = (c_{\ell,i}^* - c_{\ell,i}^\infty) \frac{\lambda_i(\lambda_i^2 + 5r_i^*\lambda_i + 10r_i^{*2})}{30} \quad (\text{B.39})$$

and Eq. (B.39) can then be solved for λ_i .

- Once the solute layer reaches the Voronoi facet (i.e., when $\lambda_i > L_i - r_i^*$), the composition $c_{\ell,i}^\infty$ will increase since a no-flux condition should apply at this location (i.e., due to the rejected solute of the symmetric neighbour grain). λ_i is then known and fixed to $L_i - r_i^*$ in Eq. (B.39):

$$\left(\langle c_{\ell,i} \rangle - c_{\ell,i}^\infty \right) \frac{L_i^3 - r_i^{*3}}{3} = (c_{\ell,i}^* - c_{\ell,i}^\infty) \frac{(L_i - r_i^*)(L_i^2 + 3L_i r_i^* + 6r_i^{*2})}{30} \quad (\text{B.40})$$

and Eq. (B.40) can then be solved for $c_{\ell,i}^\infty$.

Derivative of the liquid profile

In Eq. (5.19), it is needed to have an analytical expression of the gradient in the liquid. The solute profile in the proximity of the interface is given by:

$$c_{\ell,i}(r) = c_{\ell,i}^\infty + (c_{\ell,i}^* - c_{\ell,i}^\infty) \left(\frac{\lambda_i - (r - r_i^*)}{\lambda_i} \right)^2 \quad (\text{B.41})$$

Its derivative in r_i^* (in both 3D and 2D) is thus:

$$\left[\frac{\partial c_{\ell,i}}{\partial r} \right]^* = \frac{c_{\ell,i}^* - c_{\ell,i}^\infty}{\frac{\lambda_i}{2}} \quad (\text{B.42})$$

Once the solute layer reaches the Voronoi facet, λ_i is then known and fixed to $L_i - r_i^*$ and thus:

$$\left[\frac{\partial c_{\ell,i}}{\partial r} \right]^* = \frac{c_{\ell,i}^* - c_{\ell,i}^\infty}{\frac{L_i - r_i^*}{2}} \quad (\text{B.43})$$

B.2.4 Voronoi boundary conditions

As explained in section B.2.3, once the solute layer reaches the Voronoi facet (i.e., when $\lambda_i > L_i - r_i^*$), the composition $c_{\ell,i}^\infty$ will increase due to the rejected solute of the symmetric neighbour grain. However, due to the way the calculation is performed, the solute gradient is zero in $r = L_i$ in the r -axis coordinates and the profile (once the solute layer has reached the facet) has the following form:

$$c_{\ell,i}(r, t) = c_{\ell,i}^\infty(t) + (c_{\ell,i}^*(t) - c_{\ell,i}^\infty(t)) \left(\frac{L_i - r}{L_i - r_i^*(t)} \right)^2 \quad (\text{B.44})$$

and it can be checked that:

$$\left. \frac{\partial c_{\ell,i}}{\partial r} \right|_{r=L_i, t} = 0 \quad (\text{B.45})$$

In fact, there should be a no-flux condition in the direction perpendicular to the Voronoi boundary. In order to implement such a condition without substantially modifying the principles of the model, one can first introduce a vector \mathbf{v} tangential to the Voronoi boundary. The tangential gradient of the liquid concentration at the position $r = L_i$ of a

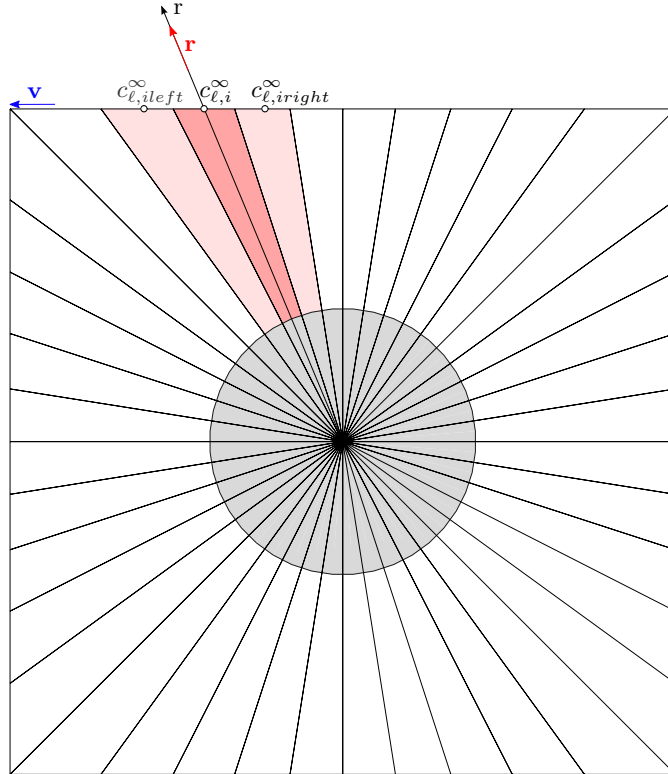


Figure B.6: Meshed Voronoi domain with the liquid part of column i and respective neighbours highlighted in red.

Appendix B. Appendix Modeling

column i , $\frac{\partial c_{\ell,i}}{\partial v}$, can be estimated from the previous time step concentration $c_{\ell,i}^\infty$ and the corresponding values of the neighbouring columns. For the column i represented in Fig. B.6, this gradient can be estimated as follows:

$$\left. \frac{\partial c_{\ell,i}}{\partial v} \right|_{r=L_i,t} = \frac{c_{\ell,i_{right}}^\infty(t) - c_{\ell,i_{left}}^\infty(t)}{\Delta d_v} \quad (\text{B.46})$$

Since the projected gradient on the r -axis is given by $\left. \frac{\partial c_{\ell,i}}{\partial v} \right|_{r=L_i,t} \mathbf{v} \cdot \mathbf{r}$, the modified profile in order to cope with correct boundary conditions is thus given by:

$$c_{\ell,i}^{mod}(r,t) = c_{\ell,i}(r,t) + \left[\left. \frac{\partial c_{\ell,i}}{\partial v} \right|_{r=L_i,t-\Delta t} \mathbf{v} \cdot \mathbf{r} \right] (r_i^* - r) \frac{L_i - r}{L_i - r_i^*} \quad (\text{B.47})$$

and it can be checked that:

$$\left. \frac{\partial c_{\ell,i}^{mod}}{\partial r} \right|_{r=L_i,t} = \left[\left. \frac{\partial c_{\ell,i}}{\partial v} \right|_{r=L_i,t-\Delta t} \mathbf{v} \cdot \mathbf{r} \right] \quad (\text{B.48})$$

The gradient along the r -axis is corrected by evaluating the gradient in the v direction at the previous time step. Provided that the time step is small enough, this introduces a no-flux boundary condition perpendicularly to the Voronoi boundary.

Instead of using Eq. (B.36) for the 2D case, the new $c_{\ell,i}^\infty$, when the solute layer has reached the boundary of the column, can be found with the following relationship:

$$\boxed{\begin{aligned} (\langle c_{\ell,i} \rangle - c_{\ell,i}^\infty) \frac{L_i^2 - r_i^{*2}}{2} &= (c_{\ell,i}^* - c_{\ell,i}^\infty) \frac{(L_i - r_i^*)(L_i + 3r_i^*)}{12} \\ &+ \left[\left. \frac{\partial c_{\ell,i}}{\partial v} \right|_{r=L_i,t-\Delta t} \mathbf{v} \cdot \mathbf{r} \right] \frac{(L_i - r_i^*)^2 (L_i + r_i^*)}{12} \end{aligned}} \quad (\text{B.49})$$

Please note that it is possible to find a similar expression for the 3D case. However, the calculation of the gradient at the Voronoi boundary is more complex. Here only the 2D case is used in order to evaluate the importance of the no-flux condition at the Voronoi boundary.

B.2.5 Meshing of the interface

In 2D, the meshing of the solid-liquid interface is straightforward since each column has two neighbours. The meshing becomes slightly more complicated when coalescence occurs (see section 5.2.4).

In 3D the meshing of the solid-liquid interface is much more complex. As a consequence of the way the columns were constructed, it is known that each column has three neighbours, the positions representing the solid-liquid interface position within one column (red points in Fig. B.7) can thus be connected (red lines in Fig. B.7). However, as shown in Fig. B.7, various polygons (squares, pethagons, hexagons, etc.) have to be created in order to form a closed surface.

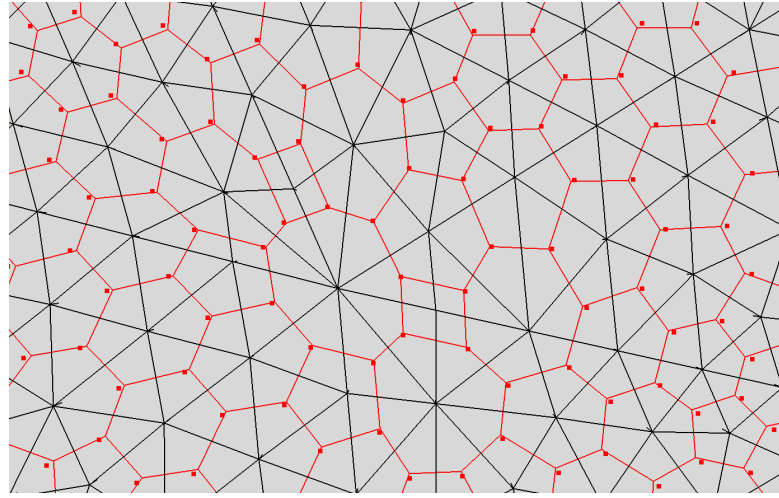


Figure B.7: Subdivision of the domain in tetrahedral columns (in the figure only the column triangular basis is shown in black). The points at the center of the columns (thus representing the position of the interface within one column) are shown in red and are connected by red lines.

Since no algorithm performing a mesh from such a configuration was found in the literature, we developed a new one.

This algorithm, explained in Fig. B.8, is the following:

1. Let us start from point 1 and connect it to point 2.
2. After that, in order to create a polygon, point 2 can be either connected to point 3 or 10. With the help of the normal to point 2, \mathbf{n} , it is possible to chose the point that yields the smaller angle (α_1 in this case). The pentagon 1-2-3-4-5 can be thus constructed with this method.
3. After that, another pair of connected points (which has not previously been “explored” in a given direction to form a polygon) is chosen, for example the pair 5-6 to create the hexagon 6-7-8-9-1-5.

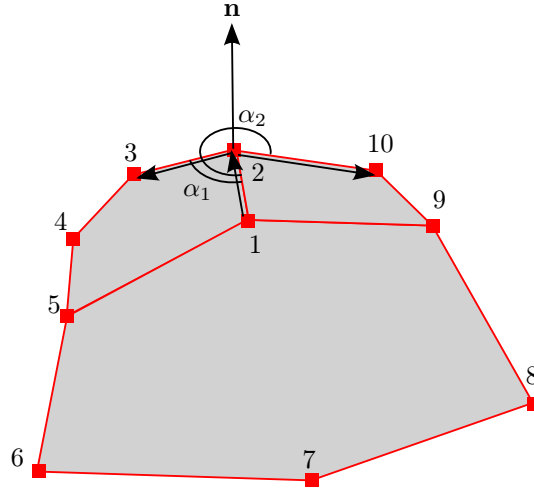


Figure B.8: Representation of the mesh when no coalescence occurred.

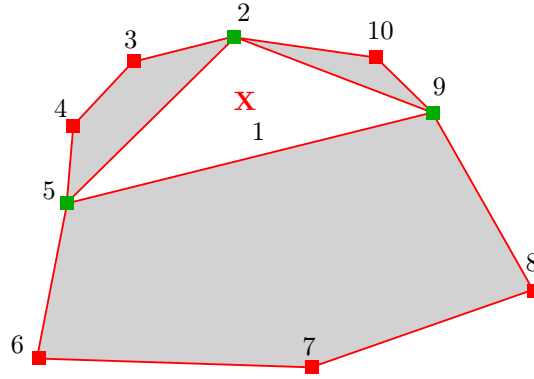


Figure B.9: Representation of the mesh when coalescence occurred in point 1. The nodes that were originally connected to the coalesced point are highlighted in green.

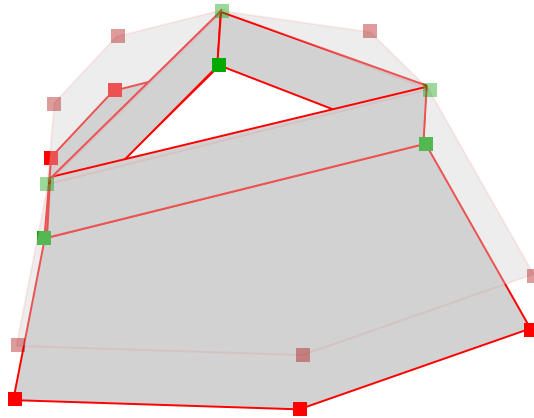


Figure B.10: Same figure as Fig. B.9 but the green point are connected to their symmetric counterparts (shown in transparency) by creating quadrilaterals.

As shown in Fig. B.9, the coalesced points (point 1 in this case) are not considered. The algorithm starts from the pair formed by point 2 and 3 to create the quadrilateral 2-3-4-5, the other polygons are created in the same way. The green points represent the points that were originally connected to the coalesced point(s). In order to create a closed surface the green points are then connected to their symmetric counterparts by creating quadrilaterals. For green points located at the boundary of the calculation domain, the segments connect these points to their orthogonal projections on the boundary, similarly to what was performed in 2D and shown in Fig. 5.14. The final mesh for a typical case of two coalescing grains is shown in Fig. B.11 (where the blue points are correspond to the projection of the green points that are at the Voronoi boundary).

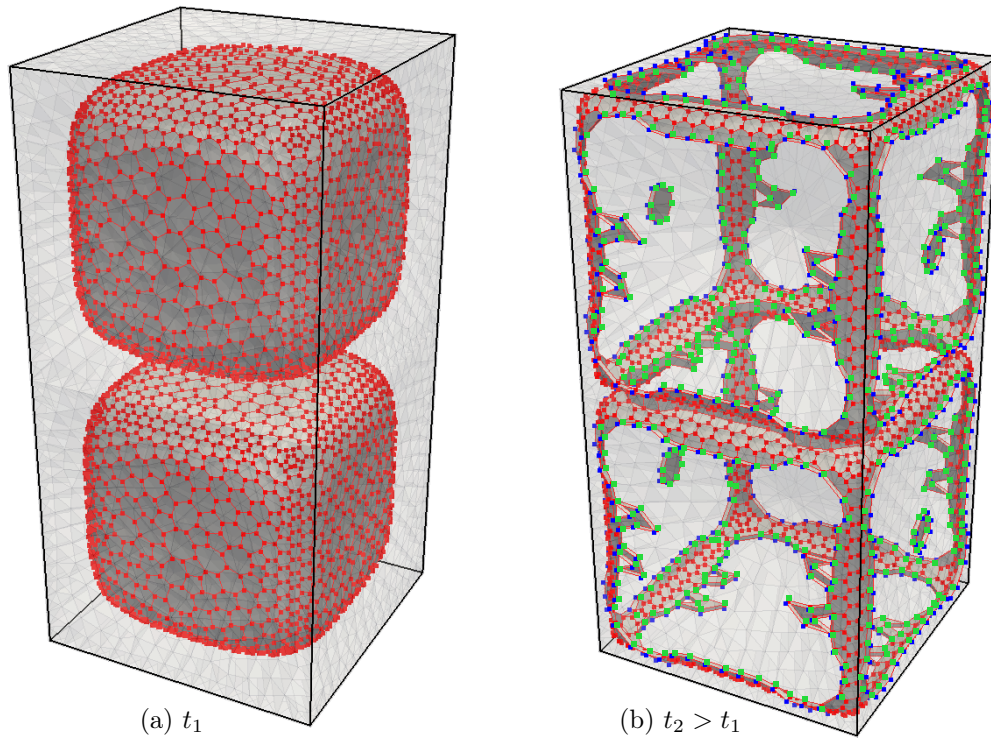


Figure B.11: Final mesh for two coalescing grains.

B.2.6 Evaluation of the curvature

In this section are presented the calculations necessary to determine the curvature in 2D and 3D.

Curvature of a circle in 2D

The general equation of a circle is given by:

$$ax^2 + ay^2 + bx + cy + e = 0 \quad (\text{B.50})$$

If we consider that the interface position in the column i is given by $P_1(x_1, y_1)$, while in the neighbouring columns is given by $P_2(x_2, y_2)$ and $P_3(x_3, y_3)$ (see Fig. 5.16), one can solve a set of equations summarized in the following determinant:

$$\det(\mathbf{A}) = \begin{vmatrix} x^2 + y^2 & x & y & 1 \\ x_1^2 + y_1^2 & x_1 & y_1 & 1 \\ x_2^2 + y_2^2 & x_2 & y_2 & 1 \\ x_3^2 + y_3^2 & x_3 & y_3 & 1 \end{vmatrix} = 0 \quad (\text{B.51})$$

and thus:

$$a = \det(\mathbf{A}_{11}), \quad b = \det(\mathbf{A}_{12}), \quad c = \det(\mathbf{A}_{13}), \quad e = \det(\mathbf{A}_{14}) \quad (\text{B.52})$$

where \mathbf{A}_{ij} are the cofactors of the matrix \mathbf{A} .

The equation of the circle possessing a center $P_R(x_0, y_0)$ and a radius R can be written as:

$$(x - x_0)^2 + (y - y_0)^2 = R^2 \quad (\text{B.53})$$

By combining Eq. (B.50) and Eq. (B.53), one can find the center and radius of the circle:

$$P_R(x_0, y_0) = \left(-\frac{b}{2a}, -\frac{c}{2a}\right) \quad (\text{B.54})$$

$$R = \sqrt{\frac{b^2 + c^2}{4a} - e} \quad (\text{B.55})$$

The mean local curvature is thus given by:

$$\bar{\kappa} = \frac{1}{2}(\kappa_1 + \kappa_2) = \frac{1}{2}\left(\frac{1}{R} + 0\right) = \frac{1}{2R} \quad (\text{B.56})$$

Curvature of a sphere in 3D

The general equation of a sphere is given by:

$$ax^2 + ay^2 + az^2 + bx + cy + dz + e = 0 \quad (\text{B.57})$$

If we consider that the interface position in the column i is given by $P_1(x_1, y_1)$, while in the neighbouring columns is given by $P_2(x_2, y_2)$, $P_3(x_3, y_3)$ and $P_4(x_3, y_3)$ (see Fig. 5.17), one can solve a set of equation summarized in the following determinant:

$$\det(\mathbf{A}) = \begin{vmatrix} x^2 + y^2 + z^2 & x & y & z & 1 \\ x_1^2 + y_1^2 + z_1^2 & x_1 & y_1 & z_1 & 1 \\ x_2^2 + y_2^2 + z_2^2 & x_2 & y_2 & z_2 & 1 \\ x_3^2 + y_3^2 + z_3^2 & x_3 & y_3 & z_3 & 1 \\ x_4^2 + y_4^2 + z_4^2 & x_4 & y_4 & z_4 & 1 \end{vmatrix} = 0 \quad (\text{B.58})$$

and thus:

$$a = \det(\mathbf{A}_{11}), \quad b = \det(\mathbf{A}_{12}), \quad c = \det(\mathbf{A}_{13}), \quad d = \det(\mathbf{A}_{14}), \quad e = \det(\mathbf{A}_{15}) \quad (\text{B.59})$$

where \mathbf{A}_{ij} are the cofactors of the matrix \mathbf{A} .

The equation of the sphere possessing a center $P_R(x_0, y_0, z_0)$ and radius R can be written as:

$$(x - x_0)^2 + (y - y_0)^2 + (z - z_0)^2 = R^2 \quad (\text{B.60})$$

By combining Eq. (B.57) and Eq. (B.60), one can find the center and radius of the sphere:

$$P_R(x_0, y_0, z_0) = \left(-\frac{b}{2a}, -\frac{c}{2a}, -\frac{d}{2a}\right) \quad (\text{B.61})$$

$$R = \sqrt{\frac{b^2 + c^2 + d^2}{4a} - e} \quad (\text{B.62})$$

The mean local curvature is thus given by:

$$\bar{\kappa} = \frac{1}{2}(\kappa_1 + \kappa_2) = \frac{1}{2} \left(\frac{1}{R} + \frac{1}{R} \right) = \frac{1}{R} \quad (\text{B.63})$$

B.3 Polyhedron associated to regularly arranged edgy grains in 3D.

In this section we explain the polyhedra associated to regularly arranged edgy grains in 3D.

It is straightforward that, by setting the nucleation points in a simple cubic lattice, the associated polyhedra consist of cubes. However, in a face-centered cubic arrangement, it is more complex to visualize it. As shown in Fig. B.12, a cuboctahedron is created by the connections of the nearest nucleation centers, forming a so-called Delaunay triangulation. The polyhedron associated to a FCC arrangement is a rhombic dodecahedron (in geometrical terms, it corresponds to the dual of the cuboctahedron).

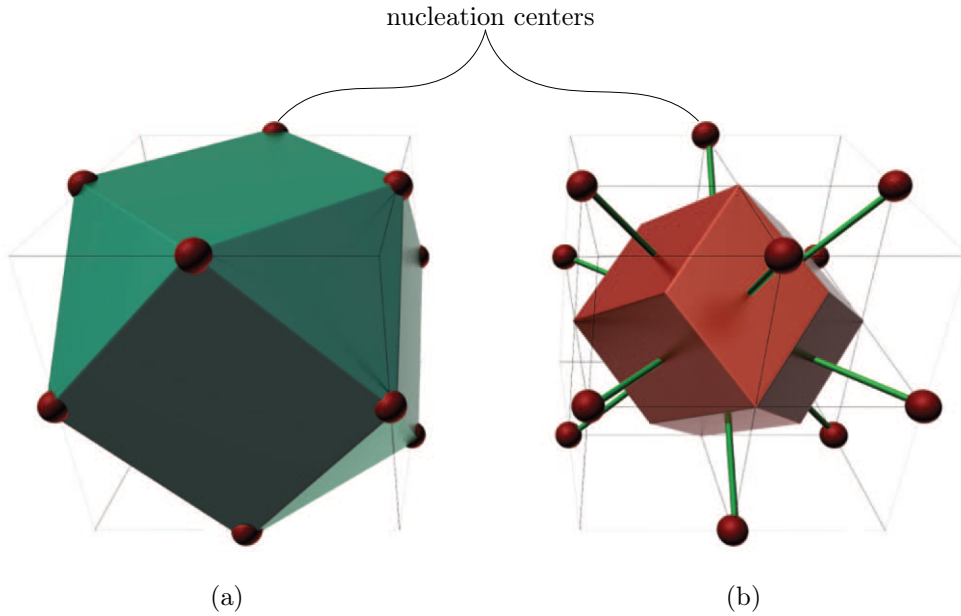


Figure B.12: (a) Cuboctehedron created by the junction by the nearest nucleation points arranged in a FCC arrangement (Delaunay triangulation). (b) Rhombic dodecahedron representing the Voronoi diagram of the FCC arrangement (after [109]).

Bibliography

- [1] S. Vernède, *A granular model of solidification as applied to hot tearing*. PhD thesis, EPFL, Lausanne, 2007.
- [2] M. Sistaninia, *Prediction of Hot Tearing Formation in Metallic Alloys Using a Granular Approach*. PhD thesis, EPFL, 2013.
- [3] A. Phillion, J.-L. Desbiolles, and M. Rappaz, “A 3D granular model of equiaxed-granular solidification,” in *Modeling Of Casting, Welding, And Advanced Solidification Processes - XII*, pp. 353–360, Minerals, Metals & Materials Soc, 184 Thorn Hill Rd, Warrendale, Pa 15086-7514 Usa, 2009.
- [4] J. W. Richard, *Aluminium; its history, occurrence, properties, metallurgy and applications, including its alloys*. Philadelphia, H. C. Baird & co., 1896.
- [5] C. Hall, “Process of reducing aluminium from its fluoride salts by electrolysis,” 1889.
- [6] P. Héroult, “Procédé électrolytique pour la préparation de l’aluminium,” 1886.
- [7] J. G. Kaufman, *Aluminum alloy castings. Properties, processes and applications*. ASM International, 2004.
- [8] J. A. Dantzig and M. Rappaz, *Solidification*. EPFL Press, 2009.
- [9] V. Mathier, S. Vernède, P. Jarry, and M. Rappaz, “Two-phase modeling of hot tearing in aluminum alloys: Applications of a semicoupled method,” *Metallurgical and Materials Transactions A*, vol. 40, pp. 943–957, 2009.
- [10] J.-M. Drezet, “Crack-free aluminium alloy welds using a twin laser process,” in *61st Inter. Conf. of the Inter. Institute of Welding*, 2008.
- [11] S. Vernède and M. Rappaz, “A simple and efficient model for mesoscale solidification simulation of globular grain structures,” *Acta Materialia*, vol. 55, no. 5, pp. 1703 – 1710, 2007.
- [12] V. Mathier, *Two-phase modelling of hot tearing in aluminium alloys using a semi-coupled method*. PhD thesis, EPFL, 2007.

- [13] S. J. Fensin, D. Olmsted, D. Buta, M. Asta, A. Karma, and J. J. Hoyt, "Structural disjoining potential for grain-boundary premelting and grain coalescence from molecular-dynamics simulations," *Phys. Rev. E*, vol. 81, p. 031601, Mar 2010.
- [14] J. Campbell, *Castings (second edition)*. Elsevier, 2003.
- [15] M. Rappaz, J.-M. Drezet, and M. Gremaud, "A new hot-tearing criterion," *Metallurgical and Materials Transactions A*, vol. 30, pp. 449–455, 1999.
- [16] M. Rappaz, A. Jacot, and W. Boettinger, "Last-stage solidification of alloys: Theoretical model of dendrite-arm and grain coalescence," *Metallurgical and Materials Transactions A: Physical Metallurgy and Materials Science*, vol. 34 A, no. 3, pp. 467–479, 2003.
- [17] S. Vernède and M. Rappaz, "Transition of the mushy zone from continuous liquid films to a coherent solid," *Philosophical Magazine*, vol. 86, no. 24, pp. 3779–3794, 2006.
- [18] M. Sistaninia, A. Phillion, J.-M. Drezet, and M. Rappaz, "Simulation of semi-solid material mechanical behavior using a combined discrete/finite element method," *Metallurgical and Materials Transactions A*, vol. 42, pp. 239–248, 2011.
- [19] M. Sistaninia, A. Phillion, J.-M. Drezet, and M. Rappaz, "Three-dimensional granular model of semi-solid metallic alloys undergoing solidification: Fluid flow and localization of feeding," *Acta Materialia*, vol. 60, no. 9, pp. 3902–3911, 2012.
- [20] M. Sistaninia, A. Phillion, J.-M. Drezet, and M. Rappaz, "A 3D coupled hydro-mechanical granular model for the prediction of hot tearing formation," *IOP Conference Series: Materials Science and Engineering*, vol. 33, no. 1, p. 012070, 2012.
- [21] M. Sistaninia, A. Phillion, J.-M. Drezet, and M. Rappaz, "A 3-D coupled hydromechanical granular model for simulating the constitutive behavior of metallic alloys during solidification," *Acta Materialia*, vol. 60, no. 19, pp. 6793–6803, 2012.
- [22] L. Bennett, J. M. T.B. Massalski, and H. Baker, *Binary Alloy Phase Diagrams*. American Society for Metals, 1986.
- [23] E. Scheil, "Bemerkungen zur schichtkristallbildung," *Zeitschrift für Metallkunde*, vol. 1, p. 1383, 1942.
- [24] G. Gulliver *Journal of the Institute of Metals*, vol. 9, p. 120, 1913.
- [25] H. Brody and M. C. Flemings, "Solute redistribution in dendritic solidification," *Transaction of the metallurgical society of AIME*, vol. 236, pp. 615–624, 1966.
- [26] T. Clyne and W. Kurz, "Solute redistribution during solidification with rapid solid state diffusion," *Metallurgical and Materials Transactions A*, vol. 12, pp. 965–971, 1981.

-
- [27] I. Ohnaka, "Mathematical analysis of solute redistribution during solidification with diffusion in solid phase," *Transactions of the Iron and Steel Institute of Japan*, vol. 26, no. 12, pp. 1045–1051, 1986.
- [28] S. Kobayashi, "Mathematical analysis of solute redistribution during solidification based on a columnar dendrite model," *Transactions of the Iron and Steel Institute of Japan*, vol. 28, no. 9, pp. 728–735, 1988.
- [29] V. R. Voller and S. Sundarraaj, "Modelling of microsegregation," *Materials Science and Technology*, vol. 9, no. 6, pp. 474–482, 1993.
- [30] D. Kammer and P. Voorhees, "The morphological evolution of dendritic microstructures during coarsening," *Acta Materialia*, vol. 54, no. 6, pp. 1549 – 1558, 2006.
- [31] C. Herring, "Surface tension as a motivation for sintering," in *Fundamental Contributions to the Continuum Theory of Evolving Phase Interfaces in Solids* (J. Ball, D. Kinderlehrer, P. Podio-Guidugli, and M. Slemrod, eds.), pp. 33–69, Springer Berlin Heidelberg, 1999.
- [32] L. Priester, *Les joints de grains - de la théorie à l'ingénierie*. Matériaux. Métallurgie, EDP Sciences, 2006.
- [33] G. Rohrer, "Grain boundary energy anisotropy: a review," *Journal of Materials Science*, vol. 46, pp. 5881–5895, 2011.
- [34] V. V. Bulatov, B. W. Reed, and M. Kumar, "Grain boundary energy function for fcc metals," *Acta Materialia*, vol. 65, no. 0, pp. 161 – 175, 2014.
- [35] W. T. Read and W. Shockley, "Dislocation models of crystal grain boundaries," *Physical Review*, vol. 78, no. 3, pp. 275–289, 1950.
- [36] V. Mathier, A. Jacot, and M. Rappaz, "Coalescence of equiaxed grains during solidification," *Modelling and Simulation in Materials Science and Engineering*, vol. 12, no. 3, pp. 479–490, 2004.
- [37] D. A. Porter and K. E. Easterling, *Phase Transformations in Metals and Alloys*. CRC Press, second ed., 2004.
- [38] D. Stauffer and A. Aharon, *Introduction To Percolation Theory*. CRC Press, second ed., 1994.
- [39] K. Christensen, "Percolation theory," *Imperial college, London*, vol. lecture notes, 2002.
- [40] S. Vernède, P. Jarry, and M. Rappaz, "A granular model of equiaxed mushy zones: Formation of a coherent solid and localization of feeding," *Acta Materialia*, vol. 54, no. 15, pp. 4023 – 4034, 2006.

Bibliography

- [41] B. I. Halperin, S. Feng, and P. N. Sen, “Differences between lattice and continuum percolation transport exponents,” *Phys. Rev. Lett.*, vol. 54, pp. 2391–2394, Jun 1985.
- [42] I. Farup, J.-M. Drezet, and M. Rappaz, “In situ observation of hot tearing formation in succinonitrile-acetone,” *Acta Materialia*, vol. 49, no. 7, pp. 1261–1269, 2001.
- [43] V. Mathier, P.-D. Grasso, and M. Rappaz, “A new tensile test for aluminum alloys in the mushy state: Experimental method and numerical modeling,” *Metallurgical and Materials Transactions A*, vol. 39, pp. 1399–1409, 2008.
- [44] O. Ludwig, J.-M. Drezet, C. Martin, and M. Suéry, “Rheological behavior of Al-Cu alloys during solidification constitutive modeling, experimental identification, and numerical study,” *Metallurgical and Materials Transactions A*, vol. 36, pp. 1525–1535, 2005.
- [45] O. Ludwig, J.-M. Drezet, P. Ménéès, C. Martin, and M. Suéry, “Rheological behavior of a commercial AA5182 aluminum alloy during solidification,” *Materials Science and Engineering: A*, vol. 413-414, no. 0, pp. 174 – 179, 2005.
- [46] D. Eskin, Suyitno, and L. Katgerman, “Mechanical properties in the semi-solid state and hot tearing of aluminium alloys,” *Progress in Materials Science*, vol. 49, no. 5, pp. 629 – 711, 2004.
- [47] P.-D. Grasso, *Coalescence and mechanical behaviour of semi-solid aluminium alloys in relation to hot tearing*. PhD thesis, EPFL, 2004.
- [48] S. Terzi, L. Salvo, M. Suéry, N. Limodin, J. Adrien, E. Maire, Y. Pannier, M. Bornert, D. Bernard, M. Felberbaum, M. Rappaz, and E. Boller, “In situ x-ray tomography observation of inhomogeneous deformation in semi-solid aluminium alloys,” *Scripta Materialia*, vol. 61, no. 5, pp. 449 – 452, 2009.
- [49] T. Clyne and G. Davies, “The influence of composition on solidification cracking susceptibility in binary alloy systems,” *J. Brit. Foundry*, vol. 74, pp. 65–73, 1981.
- [50] U. Feurer, “Mathematisches modell der warmrißneigung von binaren aluminium-legierungen,” *Giessereiforschung*, vol. 28, no. 2, pp. 75–80, 1976.
- [51] M. M’Hamdi, A. Mo, and C. Martin, “Two-phase modeling directed toward hot tearing formation in aluminum direct chill casting,” *Metallurgical and Materials Transactions A*, vol. 33, pp. 2081–2093, 2002.
- [52] V. Mathier, J.-M. Drezet, and M. Rappaz, “Two-phase modelling of hot tearing in aluminium alloys using a semi-coupled approach,” *Modelling and Simulation in Materials Science and Engineering*, vol. 15, no. 2, p. 121, 2007.

-
- [53] D. J. Lahaie and M. Bouchard, "Physical modeling of the deformation mechanisms of semisolid bodies and a mechanical criterion for hot tearing," *Metallurgical and Materials Transactions B*, vol. 32, pp. 697–705, 2001.
- [54] S. Vernède, J. A. Dantzig, and M. Rappaz, "A mesoscale granular model for the mechanical behavior of alloys during solidification," *Acta Materialia*, vol. 57, no. 5, pp. 1554 – 1569, 2009.
- [55] A. Phillion, S. Vernède, M. Rappaz, S. Cockcroft, and P. D. Lee, "Prediction of solidification behaviour via microstructure models based on granular structures," *International Journal of Cast Metals Research*, vol. 22, no. 1-2, pp. 240–243, 2009.
- [56] O. Ludwig, M. DiMichiel, L. Salvo, M. Suéry, and P. Falus, "In-situ three-dimensional microstructural investigation of solidification of an Al-Cu alloy by ultrafast x-ray microtomography," *Metallurgical and Materials Transactions A*, vol. 36, pp. 1515–1523, 2005.
- [57] J. Hunt, "Steady state columnar and equiaxed growth of dendrites and eutectic," *Materials Science and Engineering*, vol. 65, no. 1, pp. 75 – 83, 1984.
- [58] M. Rappaz, C. Charbon, and R. Sasikumar, "About the shape of eutectic grains solidifying in a thermal gradient," *Acta Metallurgica et Materialia*, vol. 42, no. 7, pp. 2365 – 2374, 1994.
- [59] W. W. Mullins and R. F. Sekerka, "Morphological stability of a particle growing by diffusion or heat flow," *Journal of Applied Physics*, vol. 34, no. 2, pp. 323–329, 1963.
- [60] D. Turnbull, "Kinetics of heterogeneous nucleation," *The Journal of Chemical Physics*, vol. 18, no. 2, pp. 198–203, 1950.
- [61] P. Schumacher and A. Greer, "Enhanced heterogeneous nucleation of α -al in amorphous aluminium alloys," *Materials Science and Engineering: A*, vol. 181-182, no. 0, pp. 1335–1339, 1994. Proceedings of the Eighth International Conference on Rapidly Quenched and Metastable Materials: Part 2.
- [62] A. Greer, A. Bunn, A. Tronche, P. Evans, and D. Bristow, "Modelling of inoculation of metallic melts: application to grain refinement of aluminium by Al-Ti-B," *Acta Materialia*, vol. 48, no. 11, pp. 2823 – 2835, 2000.
- [63] J. Spittle and S. Sadli, "Effect of alloy variables on grain refinement of binary aluminium alloys with al-ti-b," *Materials Science and Technology*, vol. 11, no. 6, pp. 533–537, 1995.
- [64] A. Greer, P. Cooper, M. Meredith, W. Schneider, P. Schumacher, J. Spittle, and A. Tronche, "Grain refinement of aluminium alloys by inoculation," *Advanced Engineering Materials*, vol. 5, no. 1-2, pp. 81–91, 2003.

Bibliography

- [65] E. Gebhardt, M. Becker, and S. Dorner, “Diche und viscositaet von schmelzen aus aluminium un aluminiumlegierungen,” *Aluminium*, vol. 231, pp. 315–321, 1955.
- [66] S. K. Seshadri and D. B. Downie, “High-temperature lattice parameters of copper-aluminium alloys,” *Metal Science*, vol. 13, no. 12, pp. 696–698, 1979.
- [67] S. Ganesan and D. Poirier, “Densities of aluminum-rich aluminum-copper alloys during solidification,” *Metallurgical and Materials Transactions A*, vol. 18, pp. 721–723, 1987.
- [68] B. Appolaire and H. Combeau, “Modelling of the settling of equiaxed crystals during the solidification of large steel ingots,” in *International Symposium on Liquid Metal Processing and Casting, Nancy, France*, 2003.
- [69] E. C. Ellwood and J. M. Silcock *Journal of Institute of Metals*, vol. 74, pp. 457–467, 1948.
- [70] Calcom SA, Lausanne, Switzerland, *calcosoft3D User manual*.
- [71] B. Appolaire, H. Combeau, and G. Lesoult, “Modeling of equiaxed growth in multicomponent alloys accounting for convection and for the globular/dendritic morphological transition,” *Materials Science and Engineering: A*, vol. 487, no. 1-2, pp. 33 – 45, 2008.
- [72] J. L. Fife, M. Rappaz, M. Pistone, T. Celcer, G. Mikuljan, and M. Stampanoni, “Development of a laser-based heating system for in-situ synchrotron-based x-ray tomographic microscopy,” *Journal of Synchrotron Radiation*, vol. 19, pp. 352–358, May 2012.
- [73] G. Petzow, *Metallographic etching (2nd edition)*. ASM International, 1999.
- [74] A. Kak, M. Slaney, G. Wang, C. Kak, and M. Slaney, “Principles of computerized tomography,” *IEEE Press*, 1987.
- [75] J. Radon, “On determination of functions by their integral values along certain multiplicities,” *Ber. der Sachische Akademie der Wissenschaften Leipzig, (Germany)*, vol. 69, pp. 262–277, 1917.
- [76] J. Radon, “Mengen konvexer körper, die einen gemeinsamen punkt enthalten,” *Mathematische Annalen*, vol. 83, no. 1-2, pp. 113–115, 1921.
- [77] E. Maire, J. Buffière, L. Salvo, J. Blandin, W. Ludwig, and J. Létang, “On the application of X-ray microtomography in the field of materials science,” *Advanced Engineering Materials*, vol. 3, no. 8, pp. 539–546, 2001.
- [78] H. Meidani, *Phase-field modeling of micropore formation in a solidifying alloy*. PhD thesis, EPFL, 2013.

-
- [79] T. Clyne, “Heat flow in controlled directional solidification of metals: I. experimental investigation,” *Journal of Crystal Growth*, vol. 50, no. 3, pp. 684 – 690, 1980.
- [80] T. Clyne, “Heat flow in controlled directional solidification of metals: II. mathematical model,” *Journal of Crystal Growth*, vol. 50, no. 3, pp. 691 – 700, 1980.
- [81] J. Mackenzie, “Second paper on statistics associated with the random disorientation of cubes,” *Biometrika*, vol. 45, no. 1-2, pp. 229–240, 1958.
- [82] J. A. Warren, R. Kobayashi, and W. C. Carter, “Modeling grain boundaries using a phase-field technique,” *Journal of Crystal Growth*, vol. 211, no. 1-4, pp. 18 – 20, 2000.
- [83] R. Kobayashi, J. A. Warren, and W. C. Carter, “A continuum model of grain boundaries,” *Physica D: Nonlinear Phenomena*, vol. 140, no. 1-2, pp. 141 – 150, 2000.
- [84] A. E. Lobkovsky and J. A. Warren, “Phase field model of premelting of grain boundaries,” *Physica D: Nonlinear Phenomena*, vol. 164, no. 3-4, pp. 202 – 212, 2002.
- [85] J. A. Warren, R. Kobayashi, A. E. Lobkovsky, and W. C. Carter, “Extending phase field models of solidification to polycrystalline materials,” *Acta Materialia*, vol. 51, no. 20, pp. 6035 – 6058, 2003.
- [86] T. Pusztai, G. Bortel, and L. Gránásy, “Phase field theory of polycrystalline solidification in three dimensions,” *EPL (Europhysics Letters)*, vol. 71, no. 1, p. 131, 2005.
- [87] M. Plapp, “Remarks on some open problems in phase-field modelling of solidification,” *Philosophical Magazine*, vol. 91, no. 1, pp. 25–44, 2011.
- [88] I. Steinbach, F. Pezzolla, B. Nestler, M. Seeßelberg, R. Prieler, G. Schmitz, and J. Rezende, “A phase field concept for multiphase systems,” *Physica D: Nonlinear Phenomena*, vol. 94, no. 3, pp. 135 – 147, 1996.
- [89] H. Garcke, B. Nestler, and B. Stoth, “A multiphase field concept: Numerical simulations of moving phase boundaries and multiple junctions,” *SIAM Journal on Applied Mathematics*, vol. 60, no. 1, pp. 295–315, 1999.
- [90] B. Nestler and A. A. Wheeler, “Phase-field modeling of multi-phase solidification,” *Computer Physics Communications*, vol. 147, no. 1-2, pp. 230–233, 2002.
- [91] H. Meidani and A. Jacot, “Phase-field simulation of micropores constrained by the dendritic network during solidification,” *Acta Materialia*, vol. 59, no. 8, pp. 3032 – 3040, 2011.

Bibliography

- [92] D. Cogswell and W. Carter, “Thermodynamic phase-field model for microstructure with multiple components and phases: The possibility of metastable phases,” *Phys. Rev. E*, vol. 83, p. 061602, 2011.
- [93] W. Boettinger, J. Warren, C. Beckermann, and A. Karma, “Phase-field simulation of solidification,” *Annual Review of materials Research*, vol. 32, pp. 163–194, 2002.
- [94] Y.-T. Kim, N. Provatas, N. Goldenfeld, and J. Dantzig, “Universal dynamics of phase-field models for dendritic growth,” *Phys. Rev. E*, vol. 59, pp. R2546–R2549, Mar 1999.
- [95] A. Karma, “Phase-field formulation for quantitative modeling of alloy solidification,” *Phys. Rev. Lett.*, vol. 87, p. 115701, Aug 2001.
- [96] M. Snir, S. Otto, S. Huss-Lederman, D. Walker, and J. Dongarra, *MPI-The Complete Reference, Volume 1: The MPI Core*. Cambridge, MA, USA: MIT Press, 2nd. (revised) ed., 1998.
- [97] C. Barber, Bradford, D. P. Dobkin, and H. Huhdanpaa, “The quickhull algorithm for convex hulls,” *ACM Trans. Math. Softw.*, vol. 22, pp. 469–483, Dec. 1996.
- [98] P. L. George, *Modulef : génération automatique de maillages*. Collection didactique, Rocquencourt: INRIA, 1986. Résumé en français et anglais.
- [99] M. Bernadou, P. L. George, and A. Hassim, *Modulef : une bibliothèque modulaire d’éléments finis*. Rocquencourt: INRIA, 1988.
- [100] B. Chapman, G. Jost, and R. van der Pas, *Using OpenMP: Portable Shared Memory Parallel Programming*. No. vol.10 in Scientific Computation Series, MIT Press, 2008.
- [101] H. Garcke, B. Nestler, and B. Stoth, “A multiphase field concept: Numerical simulations of moving phase boundaries and multiple junctions,” *SIAM Journal on Applied Mathematics*, vol. 60, no. 1, pp. 295–315, 1999.
- [102] H.-J. Diepers and A. Karma, “Globular-dendritic transition in equiaxed alloy solidification,” in *Solidification Processes and Microstructures: A Symposium in Honor of Prof. W. Kurz* (M. Rappaz, R. Trivedi, and C. Beckermann, eds.), p. 369, TMS, 2004.
- [103] B. Magnin, L. Maenner, L. Katgerman, and S. Engler, “Ductility and Rheology of an Al-4.5%Cu Alloy from room temperature to coherency temperature,” *Materials Science Forum*, vol. 217-222, pp. 1209–1214, 1996.
- [104] W. van Haaften, B. Magnin, W. Kool, and L. Katgerman, “Constitutive behavior of as-cast aa1050, aa3104, and aa5182,” *Metallurgical and Materials Transactions A*, vol. 33, no. 7, pp. 1971–1980, 2002.

- [105] J. W. Cahn, “The significance of average mean curvature and its determination by quantitative metallography,” *TMS AIME*, vol. 239, p. 610, 1967.
- [106] A. Fallet, G. Chichignoud, L. Martin, M. Suery, and P. Jarry, “Influence of barium addition on the microstructure and the rheological behavior of partially solidified Al-Cu alloys,” *Materials Science and Engineering A*, vol. 426, pp. 187–193, 2006.
- [107] O. V. Lapshin, “Diffusion parameters in liquid phase sintering of the Al-Cu system,” *Science of sintering*, vol. 34, pp. 203–213, 2002.
- [108] J. Drezet, B. Mireux, Z. Szaraz, and T. Pirling, “In situ neutron diffraction during casting: Determination of rigidity point in grain refined al-cu alloys,” *Materials*, vol. 7, no. 2, pp. 1165–1172, 2014.
- [109] K. Petkov, Q. Feng, F. Zhe, A. Kaufman, and K. Mueller, “Efficient lbm visual simulation on face-centered cubic lattices,” *Visualization and Computer Graphics, IEEE Transactions on*, vol. 15, pp. 802–814, Sept 2009.

C List of symbols

Roman alphabet

A'	constant relating the velocity of the isotherms with the columnar front undercooling
c_0	nominal composition of an alloy
$c_{0,HT}$	range of nominal compositions of alloys sensitive to hot tearing
$c_{0,HT}^{max}$	nominal composition of the alloy for which the time spent in the vulnerable region (in the context of hot tearing) is maximum
c_s, c_ℓ	solite concentration in the solid and liquid phases of a binary alloy
c_s^*, c_ℓ^*	solite concentration in the solid and liquid phases of a binary alloy at the solid-liquid interface
c_ℓ^∞	solite concentration at the Voronoi facet (mesoscopic model)
$\langle c \rangle, \langle c_s \rangle, \langle c_\ell \rangle$	average concentration, average solid concentration, average liquid concentration
c_{liq}	liquidus concentration
c_{sol}	solidus concentration
c_p, c_V	specific heat at constant pressure and at constant volume
D_s, D_ℓ	diffusion coefficients in the liquid and solid phases
d	diameter of a sphere
d_g, d_{g0}, d_{g0}^{2D}	grain size, final grain size, final grain size measured on a section
d_f	diameter of the substrate (assuming a disk-shape form)
\mathcal{F}	free energy functional in phase-field model
$f(\theta)$	shape factor
G, G_{pel}, G_{sep}	temperature gradient, temperature gradient in the alloy pellet, temperature gradient in the ceramic separator
G, G^m	total and molar ibbs free energy
G_C	composition gradient
g	acceleration due to gravity, 9.82 m s^{-2}

Appendix C. List of symbols

g_g, g_{ge}	grain volume fraction, extended grain volume fraction
g_{mo}	term related to the multiobstacle potential between two phases (multiphase-field)
g_s	volume fraction of solid
$g_{sc}, g_{sc,L}, \langle g_{sc,L} \rangle$	volume fraction of solid at percolation, finite lattice solid fraction percolation threshold, average finite lattice solid fraction percolation threshold
$g_{s,iso-\ell}$	solid fraction at which isolation of the liquid occurs
$g_{s,pcoal}$	solid fraction at which percolation by coalescence occurs
$g_{s,pcont}$	solid fraction at which percolation by contact occurs
$g_{s,S_V max}$	solid fraction at which S_V is maximum
g_{ge}	extended grain fraction
h	liquid film width
h_{mesh}	mesh size
h_{ext}	heat transfer coefficient with the exterior
h_{int}	interface heat transfer coefficient
k_0, k_0^m	partition coefficient (mass), partition coefficient(molar)
L_f	latent heat of fusion per unit mass
M_{ij}	mobility between phase i and j (multiphase-field model)
m	disturbance mode
m_ℓ, m_s	slopes of the liquidus and solidus curve (mass fractions)
n	number of moles
$\mathbf{n}, (n_x, n_y, n_z)$	unit vector normal to a surface and its Cartesian components
n_g, n_g^{2D}	grain density in volume, grain density measured on a section
p, p_a, p_ℓ	pressure, atmospheric pressure, pressure in the liquid
$p_{\ell,max}^C$	cavitation pressure in the liquid
$p, p_c, p_{c,L}, \langle p_{c,L} \rangle$	probability, percolation threshold, finite lattice percolation threshold, average finite lattice percolation threshold
Q	growth restriction factor
R	radius
$R_g, R_{g0}, R_{g0,c}$	radius of grain, final grain radius, critical grain radius
R_c	radius of a critical nucleus
r^*	position of the interface in the mesoscopic model (and when a Landau transformation is performed)
S	average number of sites per cluster
$S_{s\ell}$	solid-liquid interfacial area
S_V	solid-liquid interfacial area per unit volume ($= S_{s\ell}/V_R$)
S_V	normalized solid-liquid interfacial area per unit volume ($= S_V d_{g0}$)
T	temperature
\dot{T}	cooling rate
\dot{T}_c	critical cooling rate of the globular-to-dendritic transition
T^*	solid-liquid interface temperature
T_{col}	temperature of a columnar front
T_{eut}	eutectic temperature

T_{ext}	external temperature of the furnace
T_m	equilibrium melting temperature of pure material
T_m^∞	melting point of a pure material possessing considering a flat surface
T_m^R	melting point of a pure material possessing an interface of curvature R
T_{liq}	liquidus temperature
T_{sol}	solidus temperature
$T_{iso-\ell}$	temperature at which isolation of the liquid occurs
T_{pcoal}	temperature at which percolation by coalescence occurs
T_{pcont}	temperature at which percolation by contact occurs
$T_{S_V max}$	temperature at which S_V is maximum
t	time
t_{col}	time at which the columnar front arrives
t_f	local solidification time
t_n	time of nucleation
V_R	volume of representative volume element
v	scalar velocity
v^*	velocity of the interface in the mesoscopic model (and when a Landau transformation is performed)
v_g	velocity normal to the surface of a grain
v_T	isotherm velocity
x^*	position of the interface in 1D problems

Appendix C. List of symbols

Greek alphabet

Γ_{sl}	Gibbs-Thomson coefficient ($= \gamma_{sl}T_f/\Delta S_f$)
γ_{fl}	surface energy between foreign substrate and liquid
γ_{fs}	surface energy between foreign substrate and solid
γ	percolation exponent constant
γ_{gb}	grain boundary surface energy
γ_{gb}^{max}	grain boundary surface energy for a highly disordered grain boundary
γ_{sl}	surface energy between solid and liquid
γ_{la}	surface energy between liquid and air
ΔG	free energy difference
$\Delta G_n^{homo}, \Delta G_n^{hetero}$	free energy barrier for homogeneous or heterogeneous nucleation
ΔS_f	volumetric entropy of fusion of species ($= L_f/T_f$)
ΔT	undercooling
ΔT_b	undercooling for bridging or coalescence
ΔT_0	Equilibrium freezing range or solidification interval ($= T_{liq} - T_{sol}$)
ΔT_{int}	temperature drop at the interface between two materials
ΔT_{col}	undercooling of the columnar front
ΔT_n	nucleation undercooling
ΔT_R	curvature undercooling
Δt	time step
$\Delta \theta$	misorientation
δ_{sl}	thickness of the diffuse solid-liquid interface
ϵ_{ij}	first interfacial energy contribution (multiphase-field)
η	dimensionless coordinate in Landau transformation; paraboloidal coordinate
θ	angular coordinate; wetting angle
κ	thermal conductivity
$\bar{\kappa}, \kappa_G$	mean and Gaussian curvature of a surface
κ_1, κ_2	principal curvatures
λ	diffusion layer thickness in mesoscopic model
λ_1, λ_2	primary, secondary dendrite arm spacing
ν	percolation exponent constant
ξ	correlation length
ρ	density
$\rho_s, \rho_l, \rho_s^{eut}, \rho_l^{eut}$	density of solid, liquid, solid eutectic and liquid eutectic
σ_{fail}	tensile strength
Φ_i^*	flow of solute at the interface in column i during one time step in the mesoscopic model
Φ_i^j	flow of solute between column i and j during one time step in the mesoscopic model
ϕ	vector containing all the phase-field variables ϕ_i
ϕ_i	phase-field variable ($i = 1$: liquid, $i > 1$: solid grain)

Classical dimensionless numbers

Name	Expression	Physical Meaning
Fourier	$\text{Fo} = \frac{\alpha t_c}{L_c^2}$	ratio of characteristic time t_c to the time for conduction L_c^2/α

Mathematical operators

Symbol	Meaning	Representation
$\mathbf{A} \cdot \mathbf{B}$	dot product of two vectors	$a_i b_i$
\mathbf{A}^T	transpose of a second rank tensor	a_{ji}
$\text{tr} \mathbf{A}$	trace of a second rank tensor	a_{ii}
∇A	gradient of a scalar	$\frac{\partial A}{\partial x_i}$
$\nabla \cdot \mathbf{A}$	divergence of \mathbf{A}	$\frac{\partial a_i}{\partial x_i}$
$\nabla^2 A$	Laplacian of A	$\frac{\partial^2 A}{\partial x_i \partial x_i}$
$\ \mathbf{A}\ $	L_2 norm of a vector	$\sqrt{a_i a_i}$

Christophe Mondoux

chemin des rosiers 1
1004 Lausanne
Vaud, Suisse
☎ +41 (0)79 376 53 45
✉ christophe.mondoux@epfl.ch
in christophe.mondoux
Swiss citizenship



Work experience

2011-2015 **PhD thesis Materials Science and Engineering**, *Laboratoire de simulation des matériaux (LSMX), Ecole Polytechnique Fédérale de Lausanne (EPFL), under supervision of Prof. M. Rappaz*,
Title: “Mesoscopic Modeling and Experimental Investigations of the Last-Stage Solidification of Globular-Equiaxed Grains Microstructures: Application to the Al-Cu system”.

Education

2010-2011 **Master in Materials Science and Engineering**, *EPFL and Imperial College*.
○ **Master project**, LSMX-EPFL, “Studying the effect of solidification on the growth of micropores using phase-field method”
○ **Imperial College, London**: One year ERASMUS exchange program (2009-2010), *First class honours*.
2006-2010 **Bachelor in Materials Science and Engineering**, *EPFL*.
2002-2006 **School leaving diploma**, *Liceo cantonale di Locarno*.

Languages

Italian	Mother tongue	English	Fluent (C1)
French	Mother tongue	German and Swiss-German	Good understanding (B1)

Computer skills

Languages	C/C++, Matlab, Mathematica, L ^A T _E X, HTML
Systems	Windows XP/7, Mac OSX
Softwares	Microsoft office, Paraview, Avizo, Thermo-Calc, Calcosoft, Inkscape

Extra-professional activities and Hobbies

Coaching EPFL Member of the coaching team of EPFL
Piano Praticice of classical piano music for 12 years at the “Scuola Popolare di Musica” of Locarno (1993-2006).
Tennis Playing tennis at the Lausanne-Sports tennis club and tennis club Losone.

Conferences

Poster presentation

Junior Euromat 23-27 July 2012, Lausanne (CH), Modeling of percolation of globular-equiaxed grains.

Oral presentation

MCWASP, 21-26 June 2015, Awaji Island (JP), Modeling of percolation of globular-equiaxed grains in Al-Cu alloys.

ICASP, 8-11 July 2014, Old Windsor (UK), Experimental study and modelling of percolation of globular-equiaxed grains in inoculated Al-Cu alloys.

Euromat 8-13 September 2013, Sevilla (ES), Experimental study and modeling of percolation of globular-equiaxed grains.

CCMX summer school 26-30 August 2012, Modeling percolation of globular-equiaxed grains with multiphase-field method.

Publications

Ch. Mondoux, H. Combeau, J.-L. Desbiolles, and M. Rappaz, “Modeling of percolation of globular-equiaxed grains in Al-Cu alloys,” *IOP Conference Series: Materials Science and Engineering*, vol. 84, no. 1, p. 012081, 2015.

Ch Mondoux, H. Combeau and M.Rappaz. Development of a innovative Bridgman setup to form globular-equiaxed grains. (to be published)

Ch Mondoux, J.-L. Desbiolles and M.Rappaz. A new mesoscopic model for simulating percolation in the context of hot tearing: development of a 2D model and validations. (to be published)

Ch Mondoux, J.-L. Desbiolles, J. Fife and M.Rappaz. Last-stage solidification investigations of globular-equiaxed microstructures in inoculated AlCu alloys in the context of hot tearing: 3D mesoscopic model simulations and comparison with *in situ* X-ray tomography observations. (to be published)